Photoelectrochemical kinetics of visible-light driven water splitting at Rh SrTiO3 based electrodes

Manuel Antuch Cubillas

NNT : 2018SACLS084

Photoelectrochemical kinetics of visible-light driven water splitting at Rh:$SrTiO_3$ based electrodes

Thèse de doctorat de l'Université Paris-Saclay
préparée à L'Université Paris Sud

École doctorale n°571 Sciences chimiques : molécules, matériaux, instrumentation et biosystèmes (2MIB)
Spécialité de doctorat: Chimie

Thèse présentée et soutenue à Orsay, le 23 Avril 2018, par

Manuel Antuch Cubillas

Composition du Jury :

Hynd Rémita DR CNRS, Université Paris-Sud	Président
Julien Bachmann Professeur, Friedrich-Alexander Universität, Erlangen	Rapporteur
Jean-François Guillemoles DR CNRS, Institut Photovoltaïque d'Île de France	Rapporteur
Claude Heller DR R&D H_2-énergie, Air Liquide	Examinateur
Christian Beauger CR, Mines ParisTech, Sophia Antipolis	Examinateur
Pierre Millet Professeur, Université Paris Sud	Directeur de thèse

Thèse de doctorat

… A mis padres.

… A mi esposa.

Université Paris-Saclay
Espace Technologique / Immeuble Discovery
Route de l'Orme aux Merisiers RD 128 / 91190 Saint-Aubin, France

ACKNOWLEDGEMENTS

There are many people who contributed to the conclusion of this thesis and I have multiple reasons to be thankful. I would want to thank my Ph.D. supervisor Prof. Dr. Pierre Millet for his efforts and comprehension that allowed my research in France. Even though he had not met me and all our contact was a phone call back in 2015, he pursued the collaboration and it is because of him that I could make the thesis in France. I'll always keep in my mind the scientific discussions we had. I learned his way to analyze results, to patiently listening to my frequent (sometimes bizarre) theoretical disquisitions and wisely putting them in practical ground through smart questions, thank you very much… for all. I also want to thank Mme. Annie Millet for her kindness to me and her permanent availability for poster printing and link with Pierre.

I would want to thank Prof. Dr. Akihiko Kudo and Prof. Dr. Yan Z. Voloshin for precious scientific collaboration.

I want to thank the Directors of the École Doctorale 2MIB, who acceded to an unusual Ph.D. contest by phone and still giving me the grant. I also thank Dr. Loïc Assaud and Dr. Alireza Ranjbari, because of innumerable pleasant days in the laboratory, and their help with personal affairs, such as changing home and full support in everyday life. I am also thankful to Prof. Dr. Sylvain Franger for his refined sense of humor and for always answering my frequent doubts regarding electrochemical impedance spectroscopy.

Thanks a lot too to my Ph.D. partners, Dr. Ángel Villagrá and Joumada Al-Cheikh, who worked next to me and shared the curious world of experimental electrochemistry. I am also grateful to Nicolas Gautier and Jean-Pierre Baltaze for all the tennis we played together and moments of much fun. I am further grateful to Anshuman Agrawal, who has always been nice and invited me several times to hang out with his numerous friends.

I should also mention the personal of the experimental platform at the Institute, who were always available to fulfill my frequent and continuous measurement requirements. These are, Jean-Pierre Baltaze (NMR), Diana Dragoë (XPS), Romuald Saint-Martin (powder XRD), Jérémy Forté (thin film XRD), Sandra Mazérat (AFM), Cristian Herrero (EPR), François Brisset (SEM). Many thanks too to Rodolphe Adam and Bernard Massot for precious help for establishing good computational conditions.

I also appreciate the help of Mme. Corinne Ruello, who introduced me (joined to Ángel Villagrá as well) to the new world of French administration.

I am grateful to Prof. Dr. Julien Bachmann who received me one month in his research

group at Friedrich-Alexander Universität (Erlangen-Nürnberg), where I learned useful experimental procedures that were completely new for me.

I am thankful to my Cuban Professors of Chemistry at the University of Havana and to the Cuban educational system, who contributed to my early formation as a chemist; I am indebted to them because of my ground studies.

From the family side, I am thankful to my grandparents for their love, also to all my uncles and aunts, my brother, some dozes of cousins, and all my friends. I am thankful too to my mother-in-law, father-in-law and sister-in-law, who received me in a happy family.

A particular place in my acknowledgements is for my Mother Mery and my Father Manolo. I will never forget their hard work and sacrifice for me to have a happy childhood during the tough 90s in Cuba: the chickens grown inside the house for eating and the bicycle rides to the school. Their permanent encouragement to study and prepare myself for the future, their profound love and support has been very important. This thesis is devoted to them.

Finally, to my person, my wife Karen, my love for her came in a thunder at the first sight. Ever since, all my goals and wishes are for her to be happy, and for us, to build a family. This thesis is devoted to you.

Most sincerely,

Manuel

TABLE OF CONTENTS

List of Abbreviations

T	Absolute temperature
k_B	Boltzmann's constant
C_{HF}	Capacitance associated to the high frequency relaxation in PEIS
C_{LF}	Capacitance associated to the low frequency relaxation in PEIS
C_{SC}	Capacitance associated to the space charge
α	Charge transfer coefficient
k_t	Charge transfer rate constant
CV	Cyclic voltammetry
DW	Debye-Wäller factor (in EXAFS spectroscopy)
DFT	Density Functional Theory
EPR	Electron Paramagnetic Resonance
EDS	Energy Dispersive Spectroscopy
g	g tensor in EPR spectroscopy
A	Hyperfine interaction tensor in EPR spectroscopy
Z"	Imaginary component of the impedance
Z	Impedance
IMPS	Intensity Modulated Photocurrent Spectroscopy
IMVS	Intensity Modulated Photovoltage Spectroscopy
LSV	Linear Sweep Voltammetry
LSV	Linear Sweep Voltammetry
β	Non-ideality factor associated to the semiconductor|electrolyte interface
OCPD	Open-Circuit Photovoltage Decay
R	Path distance (in EXAFS spectroscopy)
PEIS	Photoelectrochemical Impedance Spectroscopy

I_0	Photogenerated flux of minority carriers
rds	rate determining step
Z’	Real component of the impedance
k_r	Recombination rate constant
R_{HF}	Resistance associated to the high frequency relaxation in PEIS
R_{LF}	Resistance associated to the low frequency relaxation in PEIS
SEM	Scanning Electron Microscopy
$\boldsymbol{\beta}$	Spin down
$\boldsymbol{\alpha}$	Spin up
H	Strain tensor in EPR spectroscopy
H	Transfer function of IMVS
XRD	X-ray Diffraction
XPS	X-ray Photoelectron Spectroscopy
UV-Vis	Ultraviolet-Visible Spectroscopy
EXAFS	Extended X-ray Absorption Spectroscopy
XANES	X-ray Near Edge Spectroscopy

ABSTRACT

The **Chapter 1** of this thesis is aimed to provide an overview of the state of the art regarding nowadays photoelectrochemical research. In this chapter, the theoretical foundations of the models existing so far are presented, in order to determine the charge transfer and recombination kinetics at illuminated semiconducting photoelectrodes. Furthermore, a detailed theoretical presentation of the electrochemical techniques used to determine the dynamics characteristics in photoelectrodes is provided. Additionally, an overview of the main characterization techniques used throughout the thesis is presented. Finally, comments on the methods regarding the computations carried out by DFT and the fitting of EXAFS spectra is also provided.

In **Chapter 2**, the materials and methods are presented. The procedures for the preparation of photoelectrodes and details on the experimental parameters to perform the photoelectrochemical determinations are explained. The apparatus employed and their particular experimental setup are commented. Furthermore, the necessary detailed explanations on the DFT computations, EXAFS fitting and Matlab treatment of photoelectrochemical data is provided, joined to the presentation of representative input files that would allow the reproduction of the work presented herein. On the other hand, the kinetics of the hydrogen evolution reaction (HER) and the oxygen evolution reaction (OER) at the surface of semiconducting electrodes is of wide interest nowadays. These reactions are known to be multistep. There is a need to identify the rate-determining step (rds) and to develop alternative electrocatalysts to overcome the observed severe kinetic limitations in order to promote the use of clean fuels.

Rh:$SrTiO_3$ was selected as an interesting semi-conducting material in view of water photo-dissociation. Results are reported in **Chapter 3**. Rh:$SrTiO_3$ is a p-type semiconductor with a band-gap of 2.4 eV. The semiconductor was surface-modified by

addition of catalytic species, e.g. sorption of the $Co(Cl_2Gm)_3(B\text{-}CH_3)_2$ clathrochelate, or deposition of metallic Cu and Pt. The unmodified and surface-modified $Rh:SrTiO_3$ samples were characterized by X-ray Photoelectron Spectroscopy, X-ray Diffraction analysis and other techniques, in order to determine the chemical nature of each element. Scanning Electron Microscopy was also used to assess the rough morphology of the surface of each photoelectrode. The heterogeneous hydrogen evolution reaction (HER) and the oxygen evolution reaction (OER) on unmodified and surface-modified $Rh:SrTiO_3$ samples were initially studied by Open Circuit Photovoltage Decay (OCPD), Linear Sweep Voltammetry (LSV) and Photoelectrochemical Impedance Spectroscopy (PEIS). The potential range of investigation was from -1.30 up to -1.00 V (vs. SCE) for the HER, and from +1.50 V down to +1.00 V (vs SCE) for the OER. Light intensities varied from 60 mW/cm^2 to 530 mW/cm^2. The behavior of the photoelectrodes could be classified into two groups: the first one contains pristine $Rh:SrTiO_3$, and $Rh:SrTiO_3$ – $Co(Cl_2Gm)_3(B\text{-}CH_3)_2$. For this group, kinetic parameters were found independent of light intensity and electrode potential. The second group contains the $Rh:SrTiO_3$ – Cu and $Rh:SrTiO_3$ – Pt photoelectrodes: they exhibited a Tafel-like behavior for the charge transfer and the recombination processes. From such dependence, it was possible to calculate a transfer coefficient, suggesting that either the Volmer step or the Heyrovsky step (in the high surface coverage region, i.e. $\theta_H > 0.6$) are the rds for the HER mechanism. When these photoelectrodes were used for the OER, they all exhibited very slow charge transfer kinetics.

Results reported in **Chapter 4** pertain to the hydrogen evolution reaction (HER) in the homogeneous phase. The HER mechanism is analyzed using the $Co(Cl_2Gm)_3(B\text{-}CH_3)_2$ clathrochelate (considered as a model catalyst of the clathrochelate family) dissolved in an electrolyte as electrocatalyst. The study was made by Density Functional Theory

analysis. Indeed the HER is the focus of much attention by the scientific community because hydrogen of electrolytic grade is considered as the energy carrier of the future. Molecular complexes of 3d-transition metals, such as cobalt, are potential alternative candidates to platinum for the HER in acidic media. Among these, cage complexes such as tris-dioximate metal clathrochelates have shown high HER catalytic properties. However, a full theoretical mechanistic study of such reaction has not been undertaken yet. This is why in this chapter, we report on a DFT study of the HER mechanism catalyzed by the model cobalt clathrochelate. For all species involved, high spin and low spin configurations were calculated. The structure of the clathrochelate was determined by Extended X-ray Absorption Fine Structure Spectroscopy (EXAFS). For the fitting of EXAFS spectra, the XRD and the DFT geometries were employed. Both geometries differed slightly, but EXAFS proved to be highly sensitive to these small structural variations because the adequate fitting of EXAFS employing the DFT optimized geometry needed more variables than the XRD geometry. In order to study the mechanism of the HER, several protonation sites located in the cage formed by the ligand framework and in the metal, were investigated. Protonation was found to be possible in various positions of the ligand structure, but direct protonation of cobalt was found to be the most energetically favored, enabling partial electron transfer to the coordinated proton. Several combinations of double protonation were further calculated. However, a structural and energetic analysis of relevant protonated intermediates and the calculated transition state for HER, with a η^2 character, suggested that the proposed ECCE mechanism was not favored. Instead, an ECEC mechanism was considered, but a transition state connecting reactants and products could not be found, which lead to a proposition of a Proton Coupled Electron Transfer for the last step of the HER mechanism.

Results reported in **Chapter 5** are related to the dynamic characterization of Rh:$SrTiO_3$ and Rh:$SrTiO_3$ – Pt photoelectrodes performed by Intensity Modulated Photovoltage Spectroscopy (IMVS). The IMVS response obtained for these photoelectrodes was completely unexpected, when compared to previous results reported in the scientific literature. Indeed, instead of recording conventional IMVS responses (that would resemble to typical electrochemical impedance spectra), spiral-like shapes were observed in the complex plane (Nyquist representation). To the best of our knowledge, this thesis constitutes a first report of such observation in semiconducting photoelectrodes studied in a photoelectrochemical cell. As a matter of fact, it is notable that after 30 years after the invention of light modulated photoelectrochemical spectroscopy, there is only one report of water splitting studied by IMVS. In order to provide an explanation for such experimental finding, the classical model of heterogeneous photoelectrochemical kinetics at the surface of illuminated semiconducting electrodes was implemented and solved numerically in Matlab. Such calculations allowed us to reproduce all the features observed in the experimental IMVS response, leading us to the conclusion that such spiral-like observations are due to non-steady state dynamics at the photoelectrode|electrolyte interfaces. These findings open new understanding on the complex dynamic behavior of illuminated semiconducting photoelectrodes.

.

RÉSUMÉ

Dans le **Chapitre 1** de cette thèse, nous présentons une analyse bibliographique relative à l'état actuel des connaissances en photo-électrochimie. Dans ce chapitre, nous présentons la théorie et les modèles qui permettent d'expliquer les dynamiques de transfert de charge et de recombinaison à la surface d'électrodes semi-conductrices sous illumination. Nous présentons également une description théorique détaillée des techniques électrochimiques utilisées et une description des méthodes de caractérisation employées lors de cette thèse. Finalement, nous décrivons les procédés de calcul utilisés pour les analyses DFT et EXAFS.

Dans le **Chapitre 2**, nous décrivons les matériaux et les méthodologies utilisées au cours de notre travail. Les procédés de préparation des photo-électrodes sont décrits et les détails des paramètres expérimentaux utilisés pour les mesures électrochimiques sont fournis. Des explications détaillées sont fournies à propos de l'appareillage utilisé pour la caractérisation des matériaux, et au sujet de la mise en œuvre pratique des calculs DFT et EXAFS. De même, les méthodes utilisées pour le traitement des données électrochimiques sous Matlab sont décrites, de manière à faciliter la reproduction de ce travail de recherche. Les réactions de dégagement d'hydrogène (HER pour l'acronyme anglais) et de dégagement d'oxygène (OER pour l'acronyme anglais) présentent un fort intérêt sociétal. Ces réactions possèdent des mécanismes complexes, à étapes multiples, et les étapes cinétiquement limitantes présentent des limitations cinétiques sévères. Ces caractéristiques doivent être étudiées en détail afin de guider la recherche de catalyseurs plus performants. Rh:$SrTiO_3$ a été sélectionné en tant que matériau semi-conducteur performant pour la photo-dissocation de l'eau. Les résultats rapportés dans le **Chapitre 3** concernent l'étude de ce matériau, qui possède une conduction de type p et une énergie de bande interdite de 2,4 eV. Ce semi-conducteur a été modifié en surface par addition de co-catalyseurs destinés à améliorer la cinétique de transfert de charge, par

exemple par sorption d'un clathrochélate tel que $Co(Cl_2Gm)_3(B\text{-}CH_3)_2$, ou par déposition de nanoparticules métalliques de Cu ou du Pt. Les matériaux obtenus ($Rh:SrTiO_3$ non-modifié ou modifié) ont été caractérisés par Spectroscopie de Photoélectrons X (XPS pour l'acronyme anglais), par Diffraction des Rayons X (XRD, pour l'acronyme anglais) et par d'autres techniques qui ont permis leur caractérisation chimique et structurale. La morphologie de la surface a été déterminée par Microscopie à Balayage Électronique (SEM pour l'acronyme anglais) : elle révèle la rugosité de tous ces matériaux. Les réactions d'HER et d'OER ont été étudiées par la méthode dite de la Chute du Photo-potentiel Libre (OCPD, pour l'acronyme anglais), par Voltammetrie à Balayage Linéaire de Potentiel (LSV, pour l'acronyme anglais) et par Spectroscopie d'Impédance Photo-électrochimique (PEIS, pour l'acronyme anglais). Les mesures ont été réalisées dans le domaine de potentiel allant de -1.30 à -1.00 V (vs. SCE) pour l'HER, et de +1.50 V et +1.00 V pour l'OER. L'intensité lumineuse utilisée varie entre 60 mW/cm^2 et 530 mW/cm^2. Le comportement des photo-électrodes vis-à-vis de l'HER nous a permis de les classer en deux groupes. Le premier groupe rassemble $Rh:SrTiO_3$ et $Rh:SrTiO_3 - Co(Cl_2Gm)_3(B\text{-}CH_3)_2$. Dans ce cas, les paramètres cinétiques mesurés sont indépendants du potentiel d'électrode et de l'intensité de la source lumineuse utilisée. Le second groupe rassemble $Rh:SrTiO_3$ – Cu et $Rh:SrTiO_3$ – Pt, deux photoélectrodes pour lesquelles les constantes de vitesse suivent un comportement de type plutôt métallique. Cette observation nous a permis de calculer le coefficient de transfert de la réaction qui suggère que l'étape cinétiquement limitante (rds) est soit l'étape de Volmer, soit l'étape de Heyrovsky (à haute densité de courant, lorsque le taux de recouvrement en surface en ad-atomes d'hydrogène adsorbés est tel que $\theta_H > 0,6$). En ce qui concerne l'OER, toutes les photo-électrodes utilisées ont une cinétique très lente. Les résultats rapportés dans le **Chapitre 4** concernent la réaction de dégagement

d'hydrogène en phase homogène : il s'agit d'une étude mécanistique utilisant la Théorie du Fonctionnel de la Densité (DFT, pour l'acronyme anglais), et portant sur un clathrochélate de cobalt dissout en solution. En effet, l'HER est l'objet de nombreuses recherches au sein de la communauté scientifiques car l'hydrogène électrolytique issu de l'eau est considéré comme le vecteur énergétique de l'avenir. Les complexes des métaux de transition 3-d, comme le cobalt, présentent des alternatives intéressantes au platine pour l'HER en milieux acide. Parmi une grande variété de complexes possibles, les complexes de type cage (le cation métallique actif est placé au centre d'une cage ligantaire) utilisant des ligands tris-dioximate, connus sous le nom de clathrochélates, ont montré propriétés électrocatalytiques très intéressantes vis-à-vis de l'HER. Pourtant, une étude théorique complète du mécanisme d'HER n'a pas encore été réalisée. C'est la raison pour laquelle nous nous sommes attaqués à ce problème. Dans ce Chapitre, nous présentons une description théorique du mécanisme d'HER, catalysé par le clahtrochélate modèle $Co(Cl_2Gm)_3(B\text{-}CH_3)_2$. Pour toutes les espèces chimiques possibles, les configurations bas-spin et haut-spin ont été calculées. La structure du clathrochélate a été déterminée par Spectroscopie d'Absorption X (EXAFS, pour l'acronyme anglais). Pour parvenir à effectuer le calcul EXAFS, la géométrie déterminée par XRD et par optimisation DFT a été employée. Les deux géométries sont légèrement différentes, mais l'EXAFS est sensible à ces petites différences puisque la simulation du spectre EXAFS expérimental à partir de la géométrie DFT a nécessité plus de paramètres. Dans le but d'étudier le mécanisme de l'HER, l'énergie de plusieurs sites de protonation (sur le ligand organique et sur le centre métallique) a été calculée. Nos calculs montrent que la protonation du ligand est possible à plusieurs endroits, mais que la protonation directe du cobalt reste énergétiquement favorisée. Plusieurs combinaisons de double protonation ont été calculées. Cependant, l'analyse structurelle

et énergétique, et l'état de transition (avec des caractéristiques η^2) suggèrent que le mécanisme ECCE n'est pas favorisé. Il a été donc considéré un mécanisme ECEC. Toutefois, il n'a pas été possible d'identifier un état de transition, ce qui pourrait signifier que la dernière étape du mécanisme pourrait être concertée. Les résultats présentés dans le **Chapitre 5** concernent la caractérisation dynamique des photo-électrodes à base de $Rh:SrTiO_3$ et de $Rh:SrTiO_3$ – Pt, par IMVS (Intensity Modulated photoVoltage Spectroscopy). Les réponses expérimentales obtenues par IMVS sont très différentes de celles auxquelles nous nous attendions compte tenu des résultats disponibles dans la littérature. En effet, au lieu d'obtenir des réponses typiques d'IMVS (c'est-à-dire des diagrammes habituels qui ressemblent ceux de spectroscopie d'impédance électrochimique), nous avons mesuré des diagrammes ayant une forme en spirale (graphe tracés dans le plan complexe en coordonnées de Nyquist) inattendue. Après avoir regardé en détail la littérature disponible à ce sujet, nous sommes arrivés à la conclusion que c'est la première fois qu'un comportement de ce type est rapporté pour des photo-électrodes semi-conductrices illuminées à l'aide de cellules photo-électrochimiques. Environ 30 ans après l'invention de la spectroscopie photo-électrochimique de lumière modulée, il est étonnant de réaliser qu'il n'existe dans la littérature qu'un seul article discutant de la photo-dissociation de l'eau par IMVS. Pour expliquer nos observations expérimentales, nous avons résolu sous Matlab les équations différentielles classiques, qui rendent compte de la dynamique de transfert et de recombinaison de charge dans les photo-électrodes semi-conductrices sous illumination. Ces calcules nous ont permis de simuler complètement des caractéristiques en spirale observées expérimentalement par IMVS. Cela nous a permis de tirer la conclusion que ce comportement est dû à une dynamique non-stationnaire de l'interface semi-conducteur|électrolyte.

RESUMEN

El **Capítulo 1** de esta tesis presenta la revisión del estado del arte en foto-electroquímica. Dicho capítulo presenta los fundamentos teóricos necesarios para comprender los modelos existentes para determinar la cinética de transferencia y recombinación de carga en fotoelectrodos iluminados. Además, se describen detalladamente las técnicas electroquímicas empleadas con este fin. Adicionalmente, se presenta una visión general de las técnicas de caracterización más importantes que fueron empleadas en esta tesis. Finalmente, se realizan comentarios acerca de los métodos de cómputo relacionados con los cálculos DFT y el ajuste de espectros EXAFS.

En el **Capítulo 2** se describen los materiales y métodos. Se explican los procedimientos de preparación de los fotoelectrodos, así como detalles que conciernen los parámetros experimentales empleados para realizar las determinaciones fotoelectroquímicas. Los equipos de caracterización y sus particularidades de trabajo se explican además. Se tratan también en detalle (i) la metodología de cálculo DFT, (ii) el tratamiento para ajustar los espectros EXAFS, (iii) y el tratamiento de los datos fotoelectroquímicos realizados en Matlab. Se proveen también los ficheros de entrada típicos, con el propósito de facilitar una eventual repetición del trabajo presentado a continuación.

La cinética de la reacción de evolución de hidrógeno (HER, por sus siglas en inglés) y de la reacción de evolución de oxígeno (OER, por sus siglas en inglés) en la superficie de fotoelectrodos sometidos a iluminación es de vital importancia en la actualidad. Se conoce que estas reacciones poseen un mecanismo complejo de múltiples pasos, y por ello presentan grandes limitaciones cinéticas que deben estudiarse para desarrollar fuentes alternativas y renovables de energía. Precisamente, el **Capítulo 3** trata sobre el estudio del material semiconductor Rh:$SrTiO_3$, que posee conductividad tipo p y un band-gap de 2.4 eV. El semiconductor se modificó con especies catalíticas, como el clatroquelato $Co(Cl_2Gm)_3(B\text{-}CH_3)_2$, y con Pt y Cu metálicos. Los materiales se

caracterizaron mediante Espectroscopía de Fotoelectrones X (XPS, por sus siglas en inglés), Difracción de Rayos X (XRD, por sus siglas en inglés), que permitieron su identificación química. Adicionalmente, se realizaron mediciones de Microscopía Electrónica de Barrido (SEM, por sus siglas en inglés) que permitieron poner en evidencia la naturaleza rugosa de la superficie de todos los materiales. Los estudios fotoelectroquímicos de la HER y la OER se realizaron mediante Caída del Fotopotencial a Circuito Abierto (OCPD, por sus siglas en inglés), Voltametría de Barrido Lineal (LSV, por sus siglas en inglés), y Espectroscopía de Impedancia Fotolectroquímica (PEIS, por sus siglas en inglés). Los estudios se realizaron en el rango de -1,30 V a -1,00 V (vs. SCE) para la HER, y de 1.50 V a 1.00 V (vs SCE) para la OER, y con intensidades de luz desde 60 mW/cm^2 hasta 530 mW/cm^2. El comportamiento de los fotoelectrodos se pudo clasificar en dos grupos, uno formado por $Rh:SrTiO_3$ y el otro por $Rh:SrTiO_3$ – $Co(Cl_2Gm)_3(B\text{-}CH_3)_2$. En este caso, los parámetros cinéticos no dependieron del potencial de electrodo ni de la intensidad de iluminación. En cambio, los parámetros cinéticos de los fotoelectrodos formados por $Rh:SrTiO_3$ – Cu and $Rh:SrTiO_3$ – Pt exhibieron un comportamiento tipo Tafel. Dicha dependencia permitió calcular el coeficiente de transferencia, que sugirió ya sea la reacción de Volver, o la reacción de Heyrovsky en el límite de alta densidad de hidrógeno adsorbido, como posible paso determinante en el mecanismo de HER.

En el **Capítulo 4** se estudió la HER electrocatalizada por el clatroquelato modelo $Co(Cl_2Gm)_3(B\text{-}CH_3)_2$, mediante métodos relacionados con la Teoría de los Funcionales de la Densidad (DFT, por sus siglas en inglés). De hecho, la HER recibe gran atención por la comunidad científica debido a la demanda social por nuevas fuentes de energía limpia y renovable. Los complejos moleculares de metales de transición 3-d, como el cobalto, son candidatos potenciales al platino para la HER en medio ácido. Entre esos

complejos, los clatroquelatos metálicos han mostrado propiedades catalíticas respecto a la HER. Sin embargo, un tratamiento teórico completo del mecanismo de dicha reacción no se ha realizado aún. Es por ello que en este capítulo se realizó un cálculo DFT para estudiar el mecanismo de la HER catalizada por un clatroquelato modelo. Para todas las especies involucradas, se calcularon las configuraciones de alto espín y de bajo espín. La estructura del clatroquelato se determinó por espectroscopía EXAFS. El ajuste de los espectros EXAFS se realizó mediante el empleo de las geometrías obtenidas por XRD y por DFT. Ambas geometrías fueron ligeramente diferentes, pero el EXAFS demostró ser muy sensible a estas pequeñas variaciones estructurales pues el ajuste adecuado de la señal EXAFS con la geometría obtenida mediante optimización DFT, necesitó más variables de las que se emplearon con la geometría XRD. Para estudiar el mecanismo de la HER, se calcularon varios sitios de protonación en el ligando orgánico y en el centro metálico. Los resultados mostraron que la protonación fue posible en varios sitios del ligando, sin embargo, la protonación directa en el cobalto fue la más favorecida energéticamente. Varias combinaciones de doble protonación se calcularon además. Sin embargo, el análisis estructural y energético de los diversos intermediarios permitió concluir que dicho mecanismo no estaba favorecido. En su lugar, se exploró un mecanismo ECEC, que llevó a proponer que la última etapa en la evolución de dihidrógeno es un paso concertado.

Por otra parte, el **Capítulo 5** está consagrado a determinaciones dinámicas en fotoelectrodos compuestos por $Rh:SrTiO_3$ y $Rh:SrTiO_3$ – Pt, realizados por Espectroscopía de Fotovoltaje de Intensidad Modulada (IMVS, por sus siglas en inglés). La respuesta obtenida en IMVS fue completamente inesperada, si se le compara con los resultados esperados según la literatura científica. De hecho, en lugar de la respuesta típica en IMVS, que parece la de un espectro de impedancia electroquímcia, se obtuvo

una respuesta en forma de espiral en la representación de Nyquist. Hasta donde sabemos, esta tesis constituye el primer reporte de dicha observación, en fotoelectrodos semiconductores estudiados en una celda fotoelectroquimica. De hecho, es interesante como después de 30 años de invención de las espectroscopías fotoelectroquímicas de luz modulada, solo existe un reporte de IMVS en un sistema fotoelectroquímico para la disociación del agua. Con el propósito de dar una explicación para esta observación experimental, el modelo clásico de cinética fotoelectroquímica heterogénea en la superficie de electrodos semiconductores iluminados, se implementó en Matlab. Esos cálculos permitieron reproducir todas las características observadas en la respuesta experimental de IMVS. Ello permitió concluir que dicho patrón en espiral se debió a la dinámica no estacionaria de la interfase fotoelectrodo|electrolito. Este descubrimiento abriría una nueva puerta en la comprensión del comportamiento dinámico en fotoelectrodos semiconductores iluminados.

INTRODUCTION AND OBJECTIVES OF THE DOCTORAL THESIS

The context of the 21st century demands for a rapid change of the energetic matrix which is currently based on fossil non-renewable fuels, towards renewable sources that will not harm the ecosystem and will be available indefinitely.

Hence, a widely explored alternative is the transformation of solar energy into electric energy by means of photovoltaic devices, which comprises semiconducting p-n junction cells, or more recently Dye Sensitized Solar Cells.

Another possibility is the use photoelectrochemical cells that can harvest solar energy to transform chemicals into other chemicals that could be used as renewable fuels. For example, water splitting into both dihydrogen and dioxygen. Indeed, the whole body of this work is devoted to the thorough study of photoelectrochemical cells for water splitting based on the Rh:$SrTiO_3$ semiconducting material.

In a photoelectrochemical cell, a common approach is to employ semiconductors that can absorb visible light. However, to find an adequate semiconducting material is not a straightforward task because not only its band gap should be less than 3 eV (to harvest visible light), but also the band edges must be satisfactorily placed so that the targeted reaction can proceed from a thermodynamic perspective.

A material that has been shown to be active for water splitting is Rh-doped $SrTiO_3$. Pristine $SrTiO_3$ is an n-type material with a rather large band-gap lying in the UV region of the electromagnetic spectrum. However, doping with Rh changes the conductivity type of the material to p-type, and therefore has been applied successfully as a photocathode in a water splitting cell, to target the hydrogen evolution reaction (HER).

Another important issue to address in photoelectrochemical systems is the kinetics of charge transfer and recombination at the surface of photoelectrodes. Indeed, water splitting is a heterogeneous multistep processes that has revealed serious kinetic

limitations. Hence, co-catalysts should be incorporated at the surface of semiconductors, with the ideal purpose to accelerate the rate of charge transfer, and decrease the rate of recombination of charge carriers.

The chemical nature of such catalysts is wide since it may be either metallic nanoparticles or appropriate molecular complexes. As a matter of fact, there is a family of organometallic compounds that have been shown to be active molecular catalysts for the HER, but have never been tested as heterogeneous catalysts in the surface of semiconducting photoelectrodes. Such family is known as clathrochelates, which consist in a polymacrocyclic cage of organic ligands that encapsulate a central metal atom (typically Fe or Co).

Consequently, the need to find efficient photoelectrochemical systems for water splitting, that can function assisted by visible light was the main scientific problem that motivated this thesis.

Therefore, the **main objective** of this thesis was to determine the dynamic behavior for heterogeneous visible-light driven water splitting at the surface of Rh:$SrTiO_3$ photoelectrodes, modified with suitable catalysts comprising metallic Pt and Cu and the $Co(Cl_2Gm)_3(B\text{-}CH_3)_2$ molecular clathrochelate, in order to provide insights that could allow to build efficient photoelectrochemical devices.

The **specific objectives** of this thesis can be summarized as follows:

- To characterize by means of spectroscopic and microscopic techniques the Rh:$SrTiO_3$ semiconducting material.
- To characterize by spectroscopic techniques the $Co(Cl_2Gm)_3(B\text{-}CH_3)_2$ molecular clathrochelate.

- To obtain and to characterize photoelectrodes based on the Rh:$SrTiO_3$ semiconductor, modified with metallic Pt and Cu, and with the molecular $Co(Cl_2Gm)_3(B\text{-}CH_3)_2$ clathrochelate.
- To obtain kinetic parameters for charge transfer and recombination by means of Open Circuit Photovoltage Decay, for photoelectrodes based on the Rh:$SrTiO_3$ semiconducting material, modified with metallic Pt and Cu, and with the molecular $Co(Cl_2Gm)_3(B\text{-}CH_3)_2$ clathrochelate.
- To determine the polarization curves without and with controlled illumination, under both anodic and cathodic applied potentials, in photoelectrodes based on the Rh:$SrTiO_3$ semiconducting material, modified with metallic Pt and Cu, and with the molecular $Co(Cl_2Gm)_3(B\text{-}CH_3)_2$ clathrochelate.
- To determine Tafel slopes for both the HER and the OER for the four photoelectrodes, thereby proposing possible rate determining steps in the multistep mechanisms of these reactions.
- To determine the kinetic parameters of the hydrogen evolution reaction (HER) at different cathodic applied electrode potentials and illumination levels, by means of Photoelectrochemical Impedance Spectroscopy (PEIS), for photoelectrodes based on the Rh:$SrTiO_3$ modified with metallic Pt and Cu, and with the molecular $Co(Cl_2Gm)_3(B\text{-}CH_3)_2$ clathrochelate.
- To determine the kinetic parameters of the oxygen evolution reaction (OER) at different anodic applied electrode potentials and illumination levels, by means of Photoelectrochemical Impedance Spectroscopy (PEIS), for photoelectrodes based on the Rh:$SrTiO_3$ modified with metallic Pt and Cu, and with the molecular $Co(Cl_2Gm)_3(B\text{-}CH_3)_2$ clathrochelate.

- To simulate the electrocatalytic mechanism of the hydrogen evolution reaction (HER) in the homogeneous phase of the molecular $Co(Cl_2Gm)_3(B\text{-}CH_3)_2$ clathrochelate, by means of Density Functional Theory (DFT) analysis.
- To determine the non-steady state photoelectrochemical response of $Rh:SrTiO_3$ and $Rh:SrTiO_3$ – Pt photoelectrodes, by means of Intensity Modulated Photovoltage Spectroscopy (IMVS).
- To solve a system of differential equations and to perform numeric simulations in Matlab, in order to describe the non-steady state photoelectrochemical response of $Rh:SrTiO_3$ and $Rh:SrTiO_3$ – Pt photoelectrodes observed in IMVS.

CHAPTER 1. Bibliographic overview

1.1. Introduction

Contemporary energetic and climatic context has urged the scientific community to find clean and renewable energy sources that could solve the growing needs of modern societies. In particular, water splitting[1–5] has attracted much attention, as demonstrated by the large amount of research efforts aiming to transform scientific fundamental knowledge into useful, reasonably cheap, and therefore widely available technologies.[6–24] Another widely explored alternative is related to the development of photovoltaic devices able to transform photon energy into electricity.[25–36]

In a recent book related to water splitting,[12] extensive considerations were made regarding "The Potential Contribution of Photoelectrochemistry in the Global Energy Future".[37] The authors commented on the commercial viability of carbon dioxide reduction and water photoelectrolysis, and reached the conclusion that the most promising target for solar energy conversion is the development of water splitting systems, but there is still a long way to travel to improve materials for effective photoelectrolysis.

The current challenge is to move forward in the development of materials with adequate properties for light harvesting and the development of catalysts, preferably without the use of precious metals, which would allow for the scaling of this technology aiming to realistic practical applications. The strong scientific interest in photoelectrocatalysis in contemporary research is undisputed,[1–5,38–50] and such research rhythm should guarantee on the mid to long term the necessary progress required for a transition towards alternative and renewable energy sources.

1.2. Dye sensitized solar cells (DSSC) vs. Photoelectrochemical cells (PEC)

There are several configurations for systems that convert light into useful electrical or chemical energy.[51] In order to illustrate the underlying principles, we shall comment here two of the most important ones.

In the first place, we shall consider the Dye Sensitized Solar Cells (DSSC, Fig. 1-1).[29,34–36,52,53] Such cells are composed by two electrodes that are put face-to-face and close together (the distance is in the μm range), while the void space in-between is filled by a solution containing a solvent (usually water) and a dissolved redox active electrolyte. In such cells, there is usually one photoelectrode and one conventional metallic electrode. The working photoelectrode is composed by a mesoporous semiconducting material with photoactive particles at the nanometer size, with TiO_2 being by far the most extensively used semiconducting material. However, TiO_2 has a large band-gap, slightly larger than 3 eV, which lies in the UV region of the electromagnetic spectrum, and therefore does not absorb visible light. In order to obtain

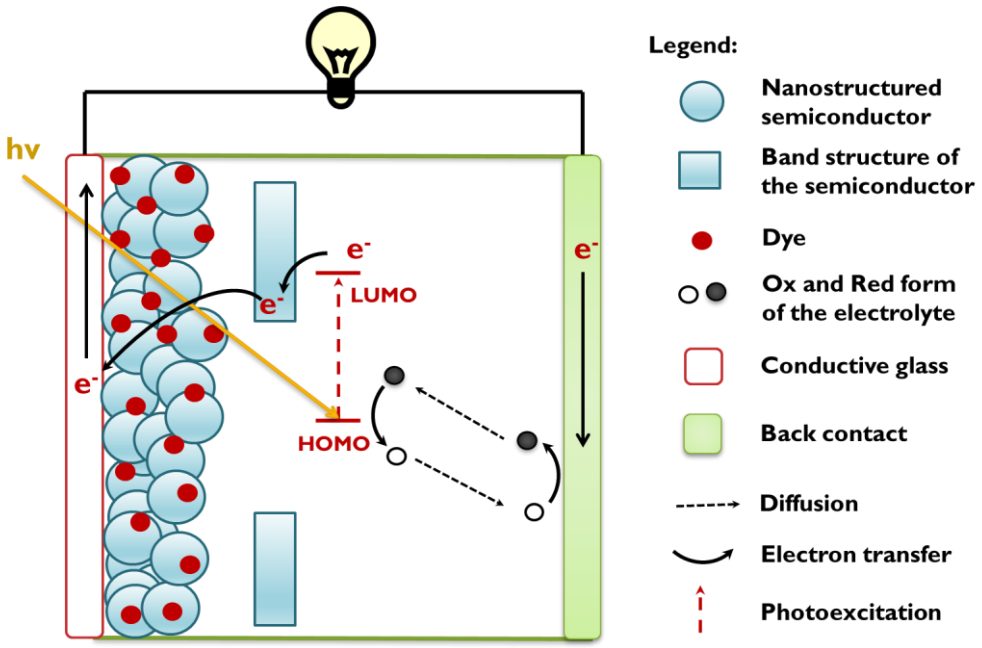

Fig. 1-1 a) Schematic representation of a Dye Sensitized Solar Cell (DSSC). Main processes occurring during illumination are explained in the main text.

visible light excitation, a monolayer of a specific dye that absorbs in the visible region is sorbed at the surface of the semiconducting particles. Thus, upon light excitation of the DSSC, the dye absorbs light and consequently electrons from the HOMO are excited to the LUMO of the molecule (photons must have an energy at least equal to the difference of energy between the LUMO and the HOMO of the dye). Energetically, the LUMO of the molecule must have a higher energy level than the conduction band of the semiconducting material, so that charge injection from the excited dye to the conduction band of the semiconductor can occur. When this is achieved, then the electrons diffuse through the nanoparticles of the semiconductor to reach a transparent conducting substrate (typically Indium Tin Oxide, ITO), and the electrons are transported through an external circuit down to the cathode (also known as back-contact). At the cathode, the electrons reduce the oxidized form of the electrolyte (typically I_3 to I^-), then the reduced form of the electrolyte diffuses towards the working photo-electrode and reacts with the cationic dye, to regenerate the dye (Fig. 1-1). Extensive research has been done in the domain of DSSC, and still continues. DSSCs offer a promising alternative to harvest light and thus profit from the electric energy these devices can generate.

A second device of interest for light energy conversion is the Photoelectrochemical Cells (PEC). The experimental setup based on a conventional three electrode configuration, comprising a working photoelectrode (photoanode or photocathode, sometimes both), a counter electrode and a reference electrode, as depicted in Fig. 1-2. The purpose of the PEC is usually to obtain H_2 and O_2 separately from water photo-dissociation. In the PEC, the absorbing material is often the semiconductor itself.[54,55] However, it is worth noting that photoelectrode architectures exhibiting a dye as the absorber have been reported,[24] for example, the recent report on NiO-dye Mo_3S_4 catalyst PEC for the HER,[56] where light absorption is not performed by the

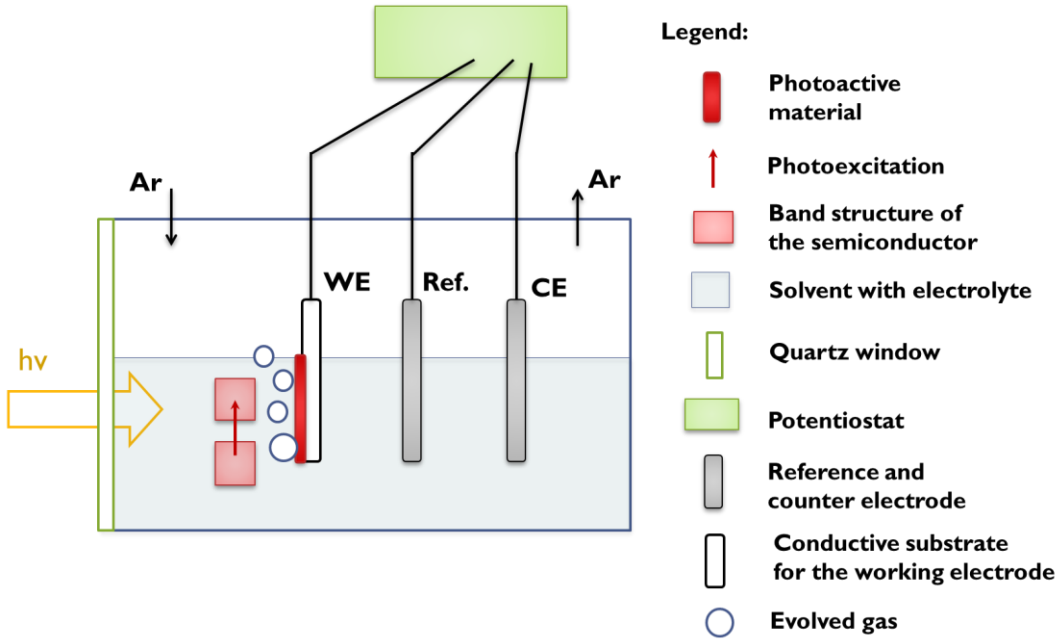

Fig. 1-2. a) Schematic representation of a Photoelectrochemical Cell (PEC).

semiconductor but by an organic dye. Another possibility is the surface modification of semiconducting materials with molecular organometallic catalysts having adequate band gap for visible light excitation,[57] aiming to the HER.

Depending on the conductivity type of the semiconductor used in the PEC, the photoelectrode is either the seat of the OER that forms O_2 by water oxidation (in such cases n-type semiconductors, such as hematite[17,55,58] or $BiVO_4$ [59–62] as typical examples, are required), or the seat of the HER that forms H_2 from water reduction (in such cases, p-type semiconductors such as Rh:$SrTiO_3$,[9] for example, are required). Usual laboratory measurements are performed in cells specially designed for photoelectrochemistry. These cells contain a visible light permeable quartz window, form where illumination goes to the photoelectrode. Besides, the cell is a closed volume and the determinations are constantly performed under inert atmosphere of argon.

In PEC cells, the semiconductor may be in the bulk solid form, and not necessarily in the form of nanoparticles as in DSSC. Bulk semiconductors, when in contact with an electrolyte solution, develop a space charge inside the semiconductor, where an electric

field is developed. This is because the concentration of charge carriers is significantly less than in metals. Consequently, after light excitation, the photogenerated exciton separates into electron/hole pairs which are driven apart by the electric field inside the semiconductor. The process is therefore different from the charge separation processes in DSSC, where the nano-size of the semiconducting particles does not allow the development of a space charge, and therefore charge separation occurs by diffusion of photogenerated carriers.[12]

This thesis is completely devoted to the analysis of PEC systems, and not to the development of DSSC. Given the importance of heterogeneous processes in PEC for this thesis, a detailed discussion of these issues shall be developed in the next section.

1.3. Electrochemistry of bulk semiconducting photoelectrodes

In this section, the behavior of p-type semiconductors shall be described (the behavior of n-type semiconductors is analogous in an opposite manner). When an interface between a semiconducting electrode and a solution is formed, the Fermi levels (E_F) in both phases are not equal. This is the driving force that leads to charge transfer, in order to equalize the E_F (equilibrium). Consequently, there is a bending of the energy bands in the semiconductor close to the interface. In the case of a p-type semiconductor, the E_F of the semiconductor is usually lower than the E_F of electrons in solution (determined by the redox couple in solution), causing an electron transfer from the solution to the semiconductor. The excess of electrons at the surface of the p-type semiconductor causes a downwards band bending. In these conditions, the surface of the semiconductor is depleted from majority carriers (holes for p-type semiconductors) and the region where this happens is commonly called the depletion layer. In the depletion layer there is an electric field. The region inside the semiconductor where an electric field exists is known as the space charge region, and has an associated capacitance (C_{sc}).

On the other hand, the region of the solution close to the interface where the electric potential drops is called the Helmholtz layer and has an associated capacitance (C_H). Excluding heavily doped semiconductors, C_H is much higher than C_{sc}. Therefore, most of the overall applied potential across the interface, drops in the space charge region and not in the solution side of the interface, i.e. $\phi_{sc} \gg \phi_H$, where ϕ_{sc} stands for the potential drop within the space charge, and ϕ_H represents the potential drop in the Helmholtz layer.

When an external electric bias is applied to a semiconductor|electrolyte interface, the band-edges in contact with the electrolyte are pinned (phenomenon referred to as Fermi level pinning), while the bands in the bulk of the material move depending on the applied bias. Therefore, band bending can be modified depending on the applied electrode potential.

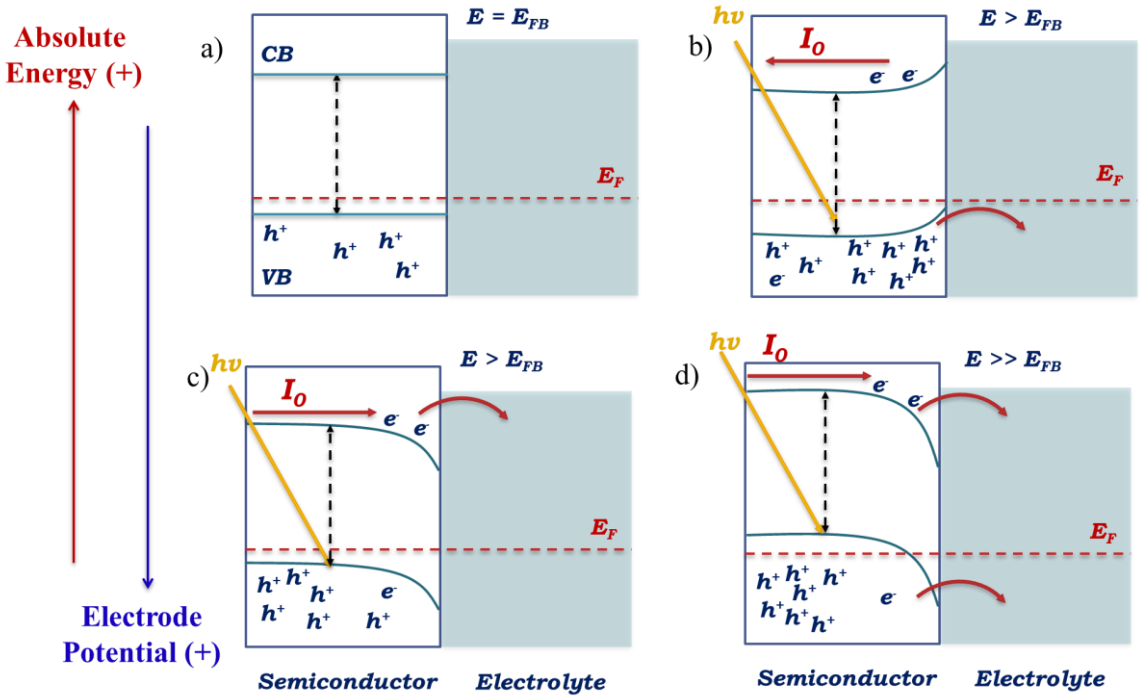

Fig. 1-3. Schematic energetic diagram of a p-type semiconducting photoelectrode under a) flat-band conditions b) accumulation conditions at applied electrode potentials more positive than the flat-band potential, c) depletion conditions at applied potentials more negative than the flat-band potential; d) inversion conditions applied potentials much more negative than the flat-band potential

When a semiconducting electrode is illuminated by light with energy $h\nu$ higher than its band gap, charge separation occurs and an electron-hole pair is consequently generated.[21–23,63] The direction of the photoexcited electrons depends on band bending. For example, at the electrode potential where there is no net electric field inside the semiconductor, the material is in flat-band conditions (Fig. 1-3 a) and no photocurrent is observed because there is no electric field to drive electron-hole separation. Conversely, if a positive potential is applied, there is an accumulation of majority carriers at the interface (holes for a p-type semiconductor) and an accumulation layer is formed. Under these conditions, p-type semiconductors behave as dark anodes.[64] Photoexcitation by light with energy larger than the band-gap is possible, but the photogenerated current of minority carriers (electrons for p-type semiconductors) flows to the bulk due to band bending. On the other hand, at electrode potentials more negative than the flat-band potential, there is a depletion of majority carriers (holes for p-type semiconductors) and a downwards band bending. Consequently, minority carriers (electrons for p-type semiconductors) can tranfer to the electrolyte to react with redox species in the nearby (Fig. 1-3 c). There is another possibility (Fig. 1-3 d), when very negative potentials are applied to the photoelectrode, beyond the extrinsic level, the depletion of majority carriers is so strong, that minority carriers themselves can promote charge transfer reactions, in addition to the characteristic photocurrents under illumination. Such condition is known as inversion layer, and has the particularity that the surface of a p-type semiconductors behaves like an n-type semiconductor.[65] This fact shall be extensively discussed during the presentation of the results of Chapter 3.

1.4. Kinetic model of Photoelectrochemical Impedance Spectroscopy (PEIS) to study the heterogeneous charge transfer at illuminated semiconducting electrodes

Electrochemical and photo-electrochemical interfaces are usually the seat of multi-step reaction paths. Each step has its own kinetics and a characteristic time constant. The determination of these different time constants provides a detailed description of the underlying microscopic processes. The purpose of Electrochemical Impedance Spectroscopy (EIS) is to measure the impedance of such interfaces over an extended range of frequencies. Each reaction step is excited individually at a characteristic frequency and in favorable cases, all time constants are obtained. From a practical viewpoint, the measures are made by applying to the electrochemical interface a sinusoidal voltage (or current) perturbation of varying frequency, and recording the sinusoidal current (or voltage) output. The amplitudes and phase shifts of both excitation/response signals are determined on a frequency-to-frequency basis and the resulting impedance diagram is plotted in the complex plane, usually in either Nyquist or Bode coordinates. The transfer functions thus obtained are electrical impedances (Z), calculated as the ratio between the oscillating voltage ($\tilde{U}$) and the current ($\tilde{I}$) as depicted in eq. 1-1

$$Z = \frac{\tilde{U}}{\tilde{I}} \qquad (1\text{-}1)$$

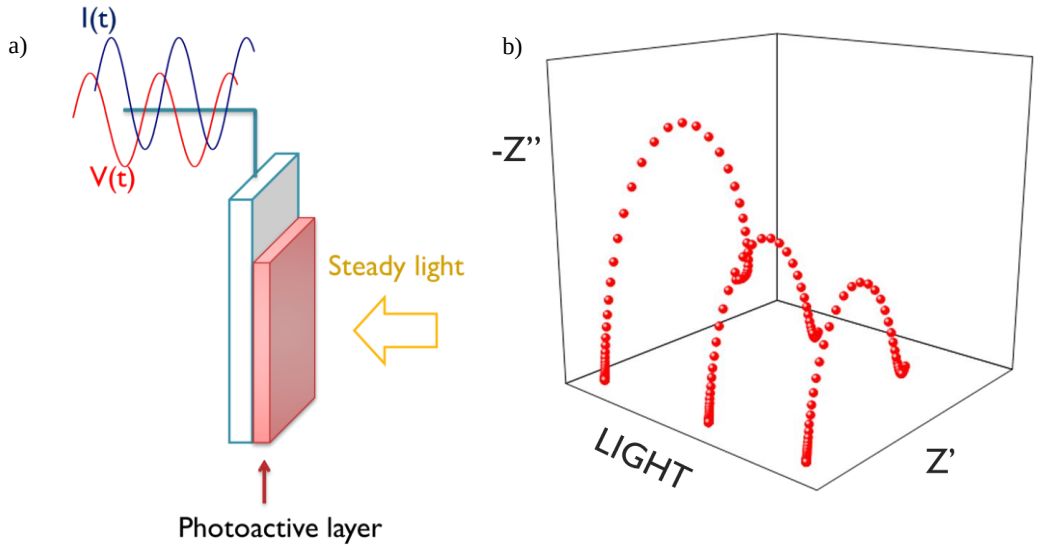

Fig. 1-4. a) Scheme displaying the measurement of PEIS. Such technique consists in recording a usual EIS response under constant illumination. In this drawing, the counter electrode and the reference electrode have not been represented; b) Scheme showing that, besides the usual real and imaginary part of the impedance, light is another relevant variable in PEIS.

EIS analysis has been extended to photo-electrochemical interfaces. The heterogeneous kinetics of charge transfer in semiconducting photoelectrodes can be analyzed by Photoelectrochemical Impedance Spectroscopy (PEIS) which is also a powerful technique. The purpose of PEIS is to record a usual EIS spectrum at a constant level of illumination (Fig. 1-4 a). Therefore, besides the real and imaginary parts of the impedance, light intensity is another experimental variable to control.

In the case where $C_{sc} \ll C_H$, PEIS spectra may be fitted to eq. 1-2 and therefore to obtain semiquantitative evaluation of relevant charge transfer and recombination kinetic parameters (Fig. 1-5).[66,67]

$$Z(\omega) = R + \frac{1}{i\omega C_{sc} + \left(\frac{q}{k_B T}\right) I_0 \left(\frac{k_r}{k_r + k_t}\right)\left(\frac{k_t + i\omega}{k_r + k_t + i\omega}\right)} \qquad (1\text{-}2)$$

In eq. 1-2 $Z(\omega)$ represents the impedance, R corresponds to the solution resistance, i is the imaginary unit, ω stands for the angular frequency of the ac perturbation, C_{sc} is the

space-charge capacitance, q is the elemental charge, k_B stands for Boltzman's constant, T is the absolute temperature, I_0 is the photogenerated flux of minority carriers (electrons in the case of a *p*-type semiconductor), k_r and k_t stand for the pseudo first order rate constants for recombination and charge transfer, respectively.

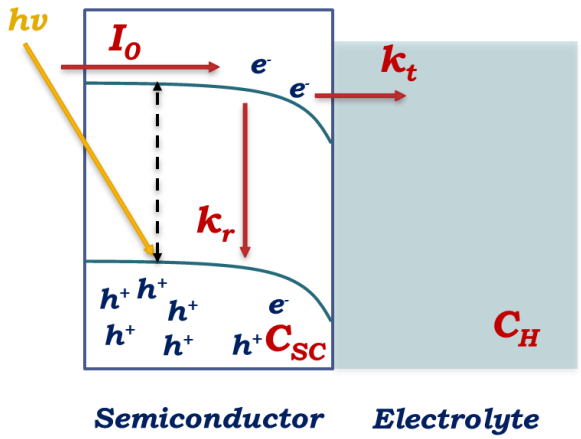

Fig. 1-5. Illuminated p-type photoelectrode under reverse bias. Main kinetic and parameters discussed in the text are presented

These parameters are illustrated in Fig. 1-5. It is worth noting that this model only considers recombination as a surface reaction, while neglecting other recombination paths, such as bulk recombination.

Equation 1-2 describes a system with two relaxation times (Fig. 1-6 a). The relaxation occurring at high frequencies (HF) can be fitted to an RC circuit, thus providing a direct measure of the space charge capacitance (C_{sc}). Conversely, the relaxation occurring at low frequencies (LF) is associated with charge transfer and recombination. In the LF relaxation, the frequency at which the maximum of the imaginary component occurs, permits to determine the charge transfer rate constant k_t (eq. 1-3; Fig. 1-6 b, left panel)

$$f_{LF}^{MAX} = k_t \qquad (1\text{-}3)$$

The low and high frequency limits of the impedance in the low frequency relaxation are given by eqs. 1-4 and 1-5, respectively (Fig. 1-6 b, right pannel).

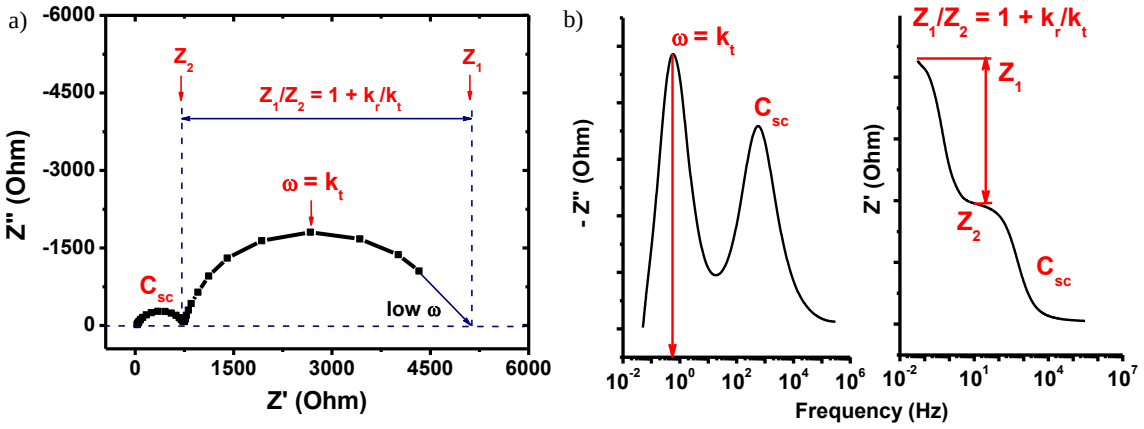

Fig. 1-6. Typical photoelectrochemical impedance spectrum (PEIS), shown as Nyquist (a) and Bode (b) plots, for an illuminated semiconductor. The figure highlights the relation between PEIS the relevant kinetic parameters discussed in the text.

$$\lim_{\omega \to 0} Z(\omega) = Z_1 = R + \frac{k_t + k_r}{\left(\frac{q}{k_B T}\right) I_0 k_r \left(1 + \frac{k_r}{k_t}\right)} \qquad (1\text{-}4)$$

$$Z_2 = R + \frac{k_r + k_t}{\left(\frac{q}{k_B T}\right) I_0 k_r} \qquad (1\text{-}5)$$

Therefore, the ratio $(Z_1 - R)/(Z_2 - R)$ (eq. 1-6) allows the determination of k_r once k_t is known.

$$\frac{Z_1 - R}{Z_2 - R} = 1 + \frac{k_r}{k_t} \qquad (1\text{-}6)$$

Rate constants allow to estimate the fraction of photogenerated minority carriers that are actually transferred towards the solution (eq. 1-7), and therefore to give an estimation of the efficiency of the photoelectrode[68]

$$\eta = \frac{k_t}{k_t + k_r} \qquad (1\text{-}7)$$

1.5. Electric vs. Kinetic models to study the dynamics at illuminated semiconducting photoelectrodes

Besides the kinetic description of heterogeneous charge transfer at illuminated semiconducting electrodes described in the prvious section, the analysis of PEIS spectra can be performed by means of electric (equivalent circuit). In general, it is possible to find analogies between kinetic and electric treatments of PEIS data because the value of a circuit element (a resistance or capacitance, for example) can be composed of several charge transfer and recombination parameters.[12,69–71] Current literature regarding the interpretation of PEIS in the framework of illuminated semiconducting photoelectrodes does not show preferences for a particular approach. Therefore, both kinetic and electric treatments are completely valid and can offer a coherent interpretation of the complex phenomena regarding heterogeneous charge transfer kinetics.

Some equivalent circuit models available in the literature are shown in Fig. 1-7.[17,69–72] A detailed discussion of each equivalent circuit is outside the scope of this thesis, because the analysis of PEIS was performed using a kinetic model only. Nevertheless, the meaning of each of the equivalent circuits shall be commented succinctly. Fig. 1-7 a represents an equivalent circuit which is entirely alike to the kinetic model presented in the previous section. The relation between kinetic and electric parameters is given by the following equations.[12]

$$R_{LF} = \frac{k_B T}{q^2 I_0}\left(\frac{k_t + k_r}{k_t}\right) \quad (1\text{-}8)$$

$$C_{LF} = \left[\frac{k_B T (k_t + k_r)}{q^2 I_0}\right]^{-1} \quad (1\text{-}9)$$

$$R_{HF} = \frac{k_B T}{q^2 I_0}\left(\frac{k_t + k_r}{k_r}\right) \quad (1\text{-}10)$$

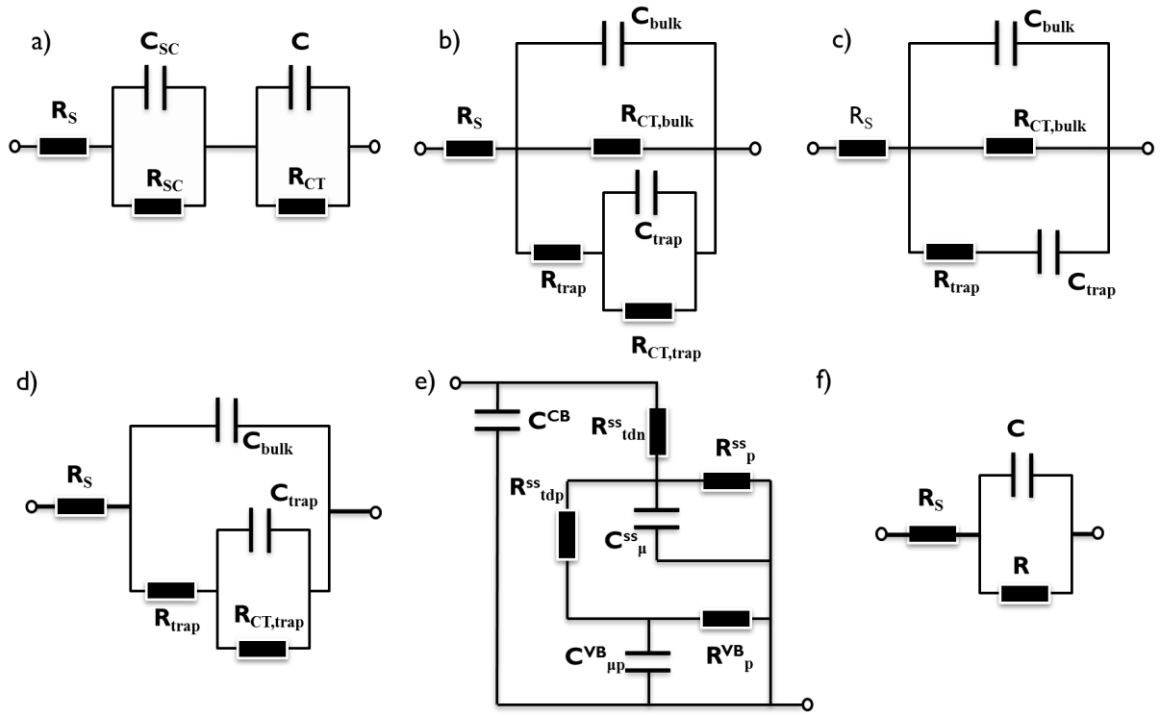

Fig. 1-7. Some equivalent circuit models employed for the treatment of photoelectrochemical impedance data. In this figure, the subscripts CT stand for charge transfer; trap, represents surface states or trap states, bulk represents the bulk of the semiconducting material, SS stands for surface states, S represents the solution, and μ is a chemical resistance or capacitance.

$$C_{HF} = C_{SC} \qquad (1\text{-}11)$$

Where R_{LF} and C_{LF} represent the resistance and capacitance associated to the low frequency relaxation; R_{HF} and C_{HF} stand for the resistance and capacitance associated to the high frequency relaxation. The meaning of all other symbols was discussed in the previous section. A Nyquist plot showing the high and low frequency relaxations is depicted in Fig. 1-8.

It is important to note that the capacitance associated to the low frequency relaxation does not correspond to the capacitance of the Helmholtz layer (C_H). However, the seminal work of Scheffold makes such association,[72] an interpretation that has been abandoned today.[12,66,71]

Fig. 1-7 b to d aims to model illuminated photoelectrodes where the presence of surface

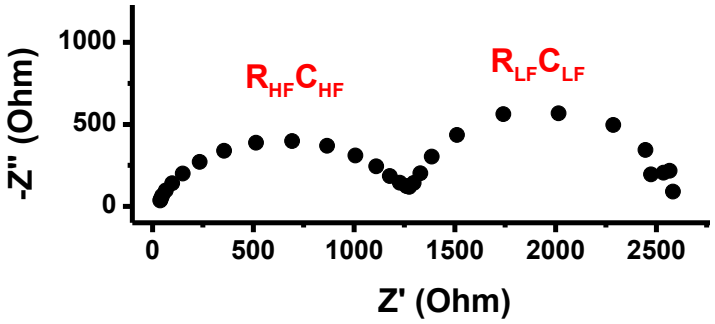

Fig. 1-8. Typical photoelectrochemical impedance spectrum (PEIS) shown as Nyquist plot. High frequency and low frequency relaxations are highlighted.

states is relevant.[17] Fig. 1-7 b represents a photoelectrode where charge transfer can occur from both the valence band (represented with the superscript "bulk") and from surfaces states (also called traps, and depicted with the superscript "trap"). Fig. 1-7 c neglects charge transfer from surface states, while Fig. 1-7 d neglects charge transfer from the valence band.

The equivalent circuit shown in Fig. 1-7 e describes three relaxations instead of two.[70] The relaxation at the highest frequencies has been attributed to the reversible trapping-detrapping process of holes and electrons by surface states, while the middle and low frequency relaxations were associated to charge transfer and recombination from the surface states band and valence band, respectively.[70]

The equivalent circuit depicted in Fig. 1-7 f is the Randles circuit, and has also been employed to treat illuminated semiconducting photoelectrodes.[64] However, such circuit is far too simplistic to obtain a global view of heterogeneous charge transfer and recombination processes occurring at illuminated semiconductors.

From a chemical perspective, it is easier and more intuitive to make a kinetic analysis based on rate constants than based on resistances. Furthermore, several equivalent circuits can produce the same relaxation pattern. Thus, the same PEIS data can be treated in several manners, which contributes to the richness, flexibility, and perhaps ambiguity in electric analysis of PEIS. Consequently, the choice of an electric model is

crucial to make a consistent interpretation of experimental results. A typical example of this can be appreciated in a recent publication,[69] where the authors discuss two different (but related) interpretations of the same circuit model, to describe heterogeneous dynamics in thin film semiconducting photoelectrodes.

The equivalent circuit interpretation of PEIS is so rich that, in a short period of time, the same authors analyze their data with similar electric models while giving different names to the fitting parameters.[69,70] For example, some interfacial capacitances have been referred to as chemical capacitance (C_μ)[69] or bulk capacitances (C_{bulk}).[17] Such wide possibilities of electric models to analyze PEIS can make puzzling the comparison among different photoelectrochemical works.

On the other hand, kinetic models offer the advantage of a straightforward interpretation of the fitting parameters in PEIS (k_t, k_r, C_{sc} and I_0, Fig. 1-5) in a unified manner.

1.6. Open Circuit Photovoltage Decay (OCPD) to study the heterogeneous kinetics at illuminated semiconducting photoelectrodes

Another technique to study the dynamics of illuminated semiconducting photoelectrodes is the open circuit photovoltage decay (OCPD). In such technique, the photoelectrode is kept at open circuit conditions and illuminated for a certain time. Then the light source is switch off and the time evolution of the open circuit voltage is recorded (Fig. 1-9). This technique has been employed to determine the kinetics of the HER at open circuit conditions, at the surface of p-type Si.[73]

Certainly, the kinetics of charge transfer and recombination can be estimated through the following equations[73,74]

$$\left(\frac{1}{U_0}\frac{dU}{dt}\right)_{t=0} = k_t \frac{C_{SC}}{C_H} - k_r \qquad (1\text{-}12)$$

$$\frac{U_f}{U_0} = \frac{k_t}{k_t + k_r} \qquad (1\text{-}13)$$

Where U_0 is the photopotential when the light is switched off, U_f is the final potential after the decay with the light switched off, and $\frac{dU}{dt}$ denotes the time derivative of the open circuit potential when the light is off. C_{SC} and C_H represent the space charge and the Helmholtz capacitance, respectively. Excepting heavily doped semiconductors, the capacity of the space charge is much lower than the capacity of the Helmholtz capacitance (C_H), and therefore $1/C_H$ is actually neglected in front of $1/C_{SC}$.

A complete discussion of the differential equations leading to these results is not the purpose of this work, and the interested reader may consult the original publications.[73,74] It is sufficient to say that the kinetic scheme discussed for PEIS (Fig. 1-5) is the same employed for this derivation.

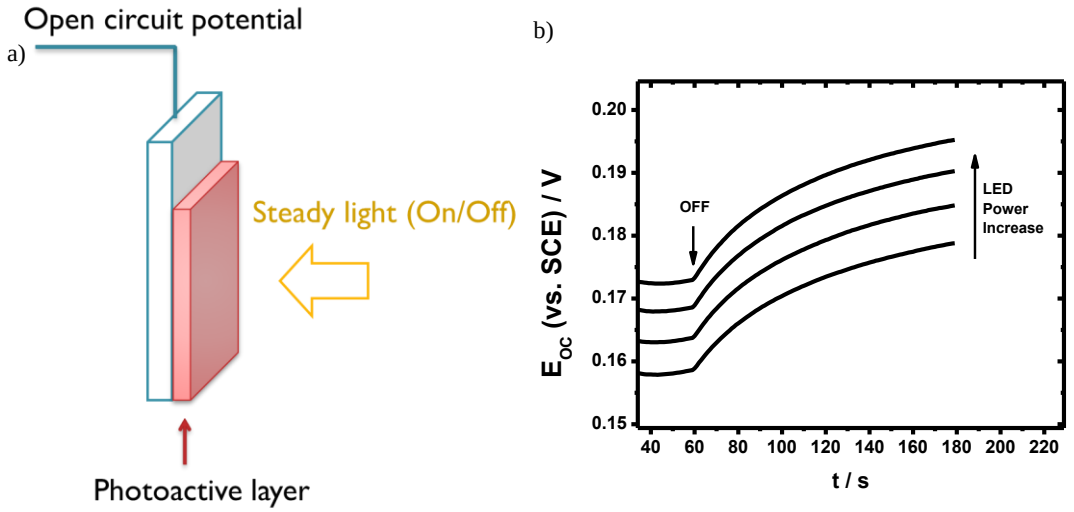

Fig. 1-9. a) Schematic representation of a photoelectrode being measured under open circuit conditions and constant level of light. In this drawing, the counter electrode and the reference electrodes have not been represented; b) Typical OCPD transient for a Rh:$SrTiO_3$ photoelectrode modified with a Co clathrochelate, obtained in this thesis.

It is interesting to note that the OCPD method has not been frequently employed to unravel the photoelectrochemical kinetics at open circuit conditions for illuminated semiconducting electrodes in a PEC configuration. In contrast, photopotential decays have been much more employed to study the carrier dynamics in DSSC.[27,32,75]

1.7. Intensity Modulated Photovoltage Spectroscopy (IMVS)

Intensity modulated photovoltage spectroscopy (IMVS) has been a ubiquitous technique used mostly for the characterization of dye-sensitized solar cells.[27,32,75–77]

IMVS consists in illuminating a photoelectrode, kept at open-circuit, with constant bias light while a small level of illumination is periodically modulated ($\widetilde{\Phi}$) at different frequencies. Such periodic irradiation causes the development of an oscillating photopotential ($\widetilde{U}$). IMVS data is thus analyzed through a transfer function as shown in eq. 1-14

$$H = \frac{\widetilde{U}}{\widetilde{\Phi}} \qquad (1\text{-}14)$$

Where H stands for the transfer function for IMVS, $\widetilde{U}$ is the modulated photovoltage, and $\widetilde{\Phi} = I_0\left(1 + e^{-i\omega t}\right)$ is the modulation of light, while I_0 represents the current of photoexcited minority carriers, which depends on the width of the space charge and the level of illumination.

A scheme of the experimental setup used to perform IMVS measurements is depicted in Fig. 1-10 a. Indeed, there is a led that is connected to an ac generator that allows the modulation of light. The modulated light arrives to a beam splitter that splits the light intensity, and delivers half for the PEC and half for a photodetector that is located outside the PEC. Note that the light intensity that is actually being measured is at the

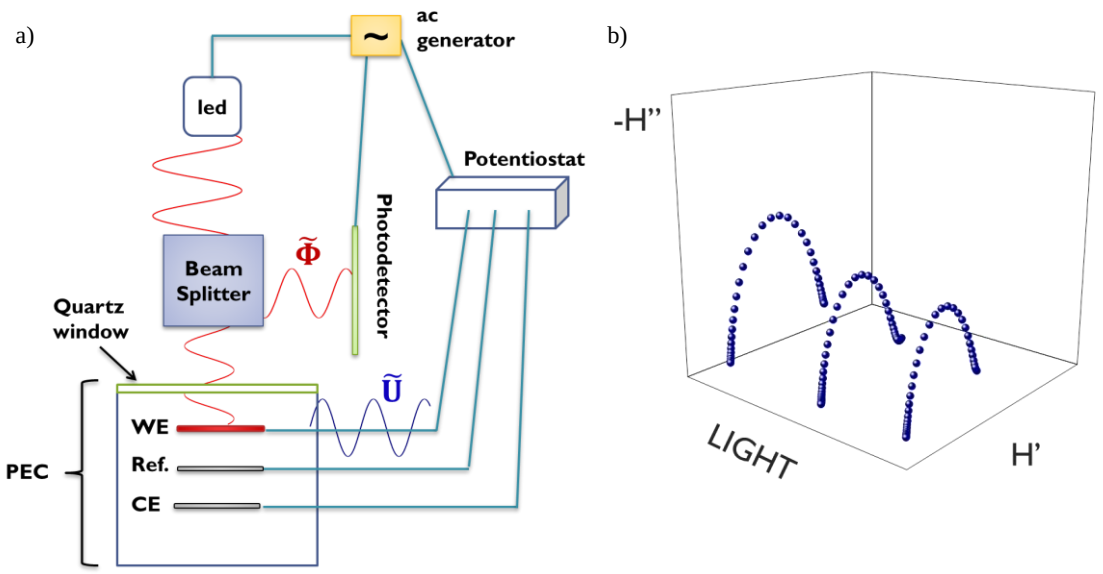

Fig. 1-10. a) Schematic drawing of a photoelectrode in a PEC configuration being measured by IMVS. Light modulation is the applied perturbation and the oscillating photovoltage is thus generated. IMVS is analyzed through a transfer function, as explained in the text. In this drawing, the counter electrode and the reference electrode have not been represented; b) Scheme of the typical IMVS response in the Nyquist representation. The data for this figure were obtained in our laboratory, with the *solaronix* DSSC test cell. Note that the experimental data depicted in (b) were not obtained with an electrode setup as depicted in (a).

photodetector, and not at the photoelectrode surface. Therefore, it is expected that the light intensity actually felt by the working photoelectrode will be lower, due to reflection losses caused by the quartz window of the PEC.

Inside the PEC, the photosensitive working electrode then receives the modulated light, and therefore an oscillating photovoltage ($\widetilde{U}$) is thus measured through the external wiring.

Fig. 1-10 b depicts a scheme of a typical IMVS response, obtained in our laboratory with a *solaronix* test cell.[78–80] Observe how the IMVS response is very similar to a PEIS response, at least for DSSC.

In the context of DSSC systems, IMVS offers information regarding the electron life-time in the cell (τ_n, Fig. 1-11). The electron life-time is numerically equal to the reciprocal of the maximum of the imaginary component in IMVS. It is necessary to note

that the photoinduced processes in DSSC and PEC are so different, that the models of the former cannot be used in the latter, and *vice versa*, which means that the analysis of IMVS in the context of a PEC cell has no relation with the analysis of DSSC.

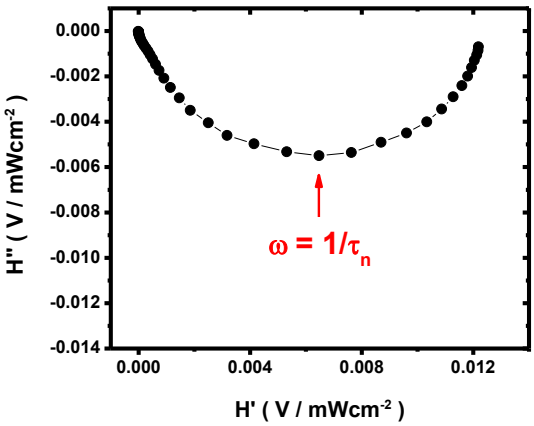

Fig. 1-11. Typical IMVS response in the Nyquist representation. The data for this figure were obtained in our laboratory, with the *solaronix* DSSC test cell. Note that the experimental data depicted in were not obtained with an electrode setup as in a PEC.

Surprisingly, the use of IMVS in the framework of PEC has been very limited over the last 30 years of development of light modulated photoelectrochemical spectroscopy. To the best of our knowledge, there is only one report of IMVS applied to PEC for water oxidation with hematite photoelectrodes.[55] In such study, the authors employed an empirical method to analyze IMVS, called Distribution of Relaxation Times (DRT). In this bibliographic overview we shall no devote further space to describe such DRT theory because we did not employ this method to analyze our experimental data.

Advancing some of the results obtained in this thesis with IMVS, it is worth to comment that our results are completely different to those reported up until now, and its explanation and theoretical justification was performed by using the classical kinetic model based on differential equations.

1.8. Heterogeneous mechanisms of the Hydrogen Evolution Reaction (HER) and the Oxygen Evolution Reaction (OER)

Photoelectrodes in PEC cells are used mainly for two reactions of utmost interest,

namely, the Hydrogen Evolution Reaction (HER) and the Oxygen Evolution Reaction (OER).

At neutral pH, the HER has been proposed to proceed via a discharge step (Volmer reaction) followed either by an electrochemical desorption step (Heyrovsky reaction) or a recombination step (Tafel reaction).[81]

Volmer reaction

$$H_2O + e^- + M = M - H + OH^- \quad (1\text{-}15)$$

Heyrovsky reaction

$$M - H + H_2O + e^- = H_2 + OH^- + M \quad (1\text{-}16)$$

Tafel reaction

$$2M - H = H_2 + 2M \quad (1\text{-}17)$$

Where M represents an active site at the surface, and all other symbols have their usual meaning.

If the Volmer reaction is the rate determining step (rds), then the observed Tafel slope shall be of 120 mV/dec. However, if the rds is the Heyrovsky reaction, the displayed Tafel slope will be 40 mV/dec, and if the Tafel reaction is the rds, the appreciated Tafel slope will be 30 mV/dec. Currently, the scientific community has a general agreement regarding the heterogeneous mechanism for the HER. Though, the recent microkinetic analysis has shown that a Tafel slope of 120 mV/dec may be also obtained when the Heyrovsky reaction is rate determining,[81] and there is a high surface density of adsorbed H atoms. As a consequence, a slope of 120 mV/dec may originate either if the Volmer reaction is the rds, or if the Heyrovsky reaction, in the high coverage region of H ($\theta_H > 0.6$), is the rds.

Conversely, the OER has been studied for over 70 years.[81–88], and still recently there are contributions regarding the multistep mechanism of the OER. For example, two recent publications present different mechanisms for this multistep reaction.[81,87]

One of these publications proposes the following sequence in alkaline solutions[81]

$$M + OH^- = MOH + e^- \quad (1\text{-}18)$$

$$MOH + OH^- = MO + H_2O + e^- \quad (1\text{-}19)$$

$$MO + OH^- = MOOH + e^- \quad (1\text{-}20)$$

$$MOOH + OH^- = MOO^- + H_2O \quad (1\text{-}21)$$

$$MOO^- = M + O_2 + e^- \quad (1\text{-}22)$$

This mechanism is complex, and it has been clearly shown through simulation that the observed Tafel slopes depend on the surface coverage of the intermediates and on the applied overpotential. Simulation results show that Tafel plots may have 21, 22, 30, 40 or 120 mV/dec, depending on the overpotential and the rds of the reaction, as depicted in Figure 4 (a) to (f) of reference 81. For its relevance to the analysis of the OER in this thesis, it is worth to mention that this model is also able to account for a Tafel slope of 60 mV/dec, but in very specific conditions and within a multi-slope current-voltage curve, as depicted in Figure 4 d of reference 81.

In the other recent publication[87] the authors based their analysis on a seminal publication of John Bockris.[82] In such study[87] the following steps are proposed without mentioning the pH. Though, the presence of water in the reactants of the chemical equations suggests that this mechanism applies for neutral pH.

$$M + H_2O = MOH + H^+ + e^- \quad (1\text{-}23)$$

$$MOH = MO + H^+ + e^- \quad (1\text{-}24)$$

$$2MO = O_2 + 2M \quad (1\text{-}25)$$

In this case, the simulation study revealed that a Tafel slope of 120 mV/dec is obtained when reaction 1-23 is rds, while a slope of 40 mV/dec is appreciated when reaction 1-24 is rds. Also, dual Tafel slopes can be observed, when the rds switches from reaction 1-24 at low overpotentials to reaction 1-23 at higher overpotentials (see Figure 1 in reference 87). On the other hand, when reaction 1-25 is the rds, the observed Tafel slope depends on the surface coverage of the intermediates. Indeed, when θ_{OH} and $\theta_O \approx 0$, simulation predicts a Tafel slope of 30 mV/dec, but when $\theta_{OH} \approx 1$ and $\theta_O \approx 0$, a Tafel slope of 60 mV/dec is predicted. This mechanism has many other subtleties, for example, depending on the rate parameters a dual Tafel slope of 30 and 60 mV/dec can be obtained if surface coverages give θ_{OH} and $\theta_O \approx 0$ at low overpotentials and $\theta_{OH} \approx 1$ and $\theta_O \approx 0$ at high overpotentials. The authors further note that it is possible to obtain a Tafel slope of 40 mV/dec (which is more typical when the rds is reaction 1-24, if reaction 1-23 is rds and θ_{OH} is high. For the cases where reaction 1-25 is the rds and $\theta_O \approx 1$, a limiting current was observed in the simulations.

Table 1-1 presents a brief summary of experimental Tafel slopes encountered at various electrodes. The main conclusion extracted is that quite often reality is richer than available mathematical models. Considering this, Tafel analysis should be assumed as information allowing to suggest possible rate determining steps.

Table 1-1. Succinct compendium of Tafel slopes for the HER and the OER at various materials. These data are summarized in reference 81 with further examples.

Hydrogen Evolution Reaction (HER)			
Material	Tafel slope	Conditions	Reference
Pt (bulk)	36-68 (low η)	H_2SO_4 0.5 M	89
	125 (high η)		
Pt (110)	55 (low η)	KOH 0.1 M	90
	150 (high η)		
Pt (111)	140-150		
Pt/C	30	H_2SO_4 0.1 M	91,92
Pt/C	125	NaOH 0.5 M	89
Ni	121-142	NaOH 1 M	93,94
Mo	126		
NiMo	132		
CoP	50	H_2SO_4 0.5 M	91
Ni_2P	75		92
C (graphite)	206		95
Oxygen Evolution Reaction (OER)			
Material	Tafel slope	Conditions	Reference
Pt (bulk)	110	$HClO_4$ 1 M	96
Pt (bulk)	60 (low η)	KOH 1 M	
	120 (high η)		
Ir	85	H_2SO_4 1 M; 80°C	97
Ir-Pt	210		
$Ni(OH)_2$	65	KOH 0.1 M	98
$LnBaCo_2O_{5+\delta}$*	60		99
$NiCo_2O_4$ (nanoneedle)	292	KOH 1 M	100
$NiCo_2O_4$ (nanosheet)	393		
$SrVO_3$	235	NaOH 1 M	88
$LaCoO_3$	70 (low η)		
	135 (high η)		

* Ln = Pr, Sm, Gd, Ho.

1.9. General characteristics of $SrTiO_3$ and Rh:$SrTiO_3$ semiconducting materials

The $SrTiO_3$ material, thoroughly employed in this thesis, presents cubic perovskite structure, as shown in Fig. 1-12 a and b (space group P m -3 m; a = b = c = 3.905 Å; α = β = γ = 90°, cell volume = 59.547 $Å^3$).[101] Non-doped $SrTiO_3$ possesses n-type conductivity and has a band gap of 3.2 eV.[102–104]

Such band gap lies in the UV region of the electromagnetic spectrum, therefore, much experimental and theoretical work can be found in current literature concerning the photocatalytic properties of $SrTiO_3$ with different dopants[9,13,16,102–112] with the purpose to decrease the band gap of the material. To the best of our knowledge, there is no previous study devoted to the determination of the photoelectrochemical kinetics of the heterogeneous reaction occurring at the surface of $SrTiO_3$ – based photoelectrodes. These facts prompted us to utilize in this thesis the novel advanced semiconducting material (Rh doped $SrTiO_3$) that absorbs visible light, and has been shown to act as a hydrogen evolving photo-catalyst[9,13–15] because the absolute energy of its conduction band is around 0.7 eV higher than the redox potential of the couple $H_2|H_2O$ (see Figure 10 within reference 104).

Interestingly, it has been shown that doping changes not only the band gap of the material, but also can tune the type of conductivity in the material. For example, doping

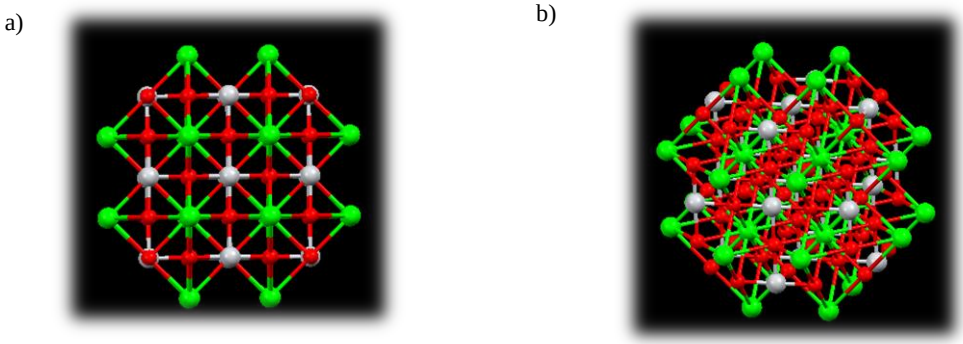

Fig. 1-12. a) Crystallographic structure of $SrTiO_3$, front view; b) Crystallographic strcture of $SrTiO_3$, perspective view. Color codes: green, Sr; red, O, white, Ti.

of $SrTiO_3$ with Ir keeps n-type conductivity with the characteristic anodic photocurrent,[102] while doping with Rh switches the properties of the $SrTiO_3$ material to display p-type conductivity and therefore cathodic photocurrents.[9] This behavior is due to the fact that in-band Ir energetic levels are around 0.5 eV higher in energy than Rh in-band states. Consequently, the Fermi level of Ir:$SrTiO_3$ is closer to the conduction band, thereby the n-type conductivity in the material.[102]

In this thesis, the Rh:$SrTiO_3$ material shall be employed extensively. In such material the energy difference between Rh in-gap states and the conduction band is 2.4 eV, as observed before in soft X-ray spectroscopy,[103] which lies well in the visible region of the electromagnetic spectrum. In the resting state, Rh:$SrTiO_3$ material possesses Rh in the +4 oxidation state in the form of a dark grey solid,[103,112] but during the HER, a photoreduction occurs and Rh exists therefore in the +3 oxidation state, which is a yellow solid that is more active towards the HER.[102,103]

In the context of this work it is instructive to review previously published EIS results of $SrTiO_3$ – based photoelectrodes.[113,114] In both studies a relaxation was fully observed at high frequencies while at low frequencies the authors observed an increase in the impedance but the LF semicircle did not appear. Unfortunately, the reported EIS data[113,114] are depicted only in the Nyquist representation and with no frequency indications, and Bode plots were not represented. An inspection of the experimental part revealed that in reference 113 the frequency window was between 100 kHz and 10 mHz. However in reference 114 the authors did not provide the range of frequencies tested. The extraction of qualitative conclusions from these two studies is further troubling since the axes in the Nyquist representations (Figure 8 b within reference 113 and Figure 3 b within reference 114) are not orthonormal.

These studies did not apply neither a kinetic model nor an electric model to fit the EIS

responses. The authors limited their conclusions about EIS to the interpretation of the usual Randles circuit. Such interpretation, as recognized by Rüdiger Memming, is valid in the context of semiconducting electrodes,[64] but is far too limited to exploit all the information that EIS can give regarding the heterogeneous processes occurring at the interface of illuminated semiconductors.[17,54,55,66,67,70–72,115] In any case, if EIS results already reported[113] were to be analyzed in the framework of a kinetic model (Fig. 1-5), it could be said that the LF relaxation did not fully develop in a frequency sweep down to 10 mHz, and therefore the phenomenological charge transfer rate constant reflects a slow process and should be smaller than 0.01 s^{-1}. Certainly, in order to fully observe the LF relaxation, it should be necessary to descend to lower frequencies to fully appreciate the LF relaxation, as will be shown in Chapter 3.

1.10. General characteristics of clathrochelates

Molecular electrocatalysis aiming at energy relevant reactions is nowadays a hot research topic due to the urgent need to find clean and renewable sources of energy. [116] The possible utilization of dihydrogen as an energy carrier is tempting and promising. So far, a truly efficient process to evolve dihydrogen from acidic electrolytes without platinum-based electrocatalysts has not been discovered. That is the cause of the numerous efforts devoted to develop electrocatalysts based on diverse materials such as Fe, Ni, Ru, Re, Mo etc. [117–123] Among the various alternatives explored as possible molecular catalysts for the hydrogen evolution reaction (HER) in the homogeneous phase, there are several Co, Ni and Fe based diglyioxyme complexes[124] or Ni dithiolenes [125] that demonstrated interesting properties.

Tris-dioximate metal clathrochelates such as the cobalt species shown in Fig. 1-13 are a family of metal complexes that have been shown to be efficient homogeneous electrocatalysts for the HER, and have been shown to be pre-catalysts for the deposition of active Co-based particles in glassy carbon electrodes under bulk electrolysis conditions. [126–129] Clathrochelates are basically polymacrocyclic cage compounds which are able to stabilize the low oxidation states of transition metals (e.g. Co or Fe), thereby offering interesting possibilities to act as hydrogen-producing catalysts with an appealing potential as molecular electrocatalysts.[126,127]

In this context, the clathrochelate family of organometallic compounds is very versatile from a chemical and electrochemical perspective. [130–133] The physical nature of clathrochelates at room temperature is in the form of a stable brown-red solid. This has allowed its analysis by XRD. For example, the molecule $Co(Cl_2Gm)_3(B\text{-}CH_3)_2$ crystalizes in the space group P21/c, as can be appreciated in Fig. 1-14.

Formally, Co clathrochelates may exist in three different oxidation states, namely III, II

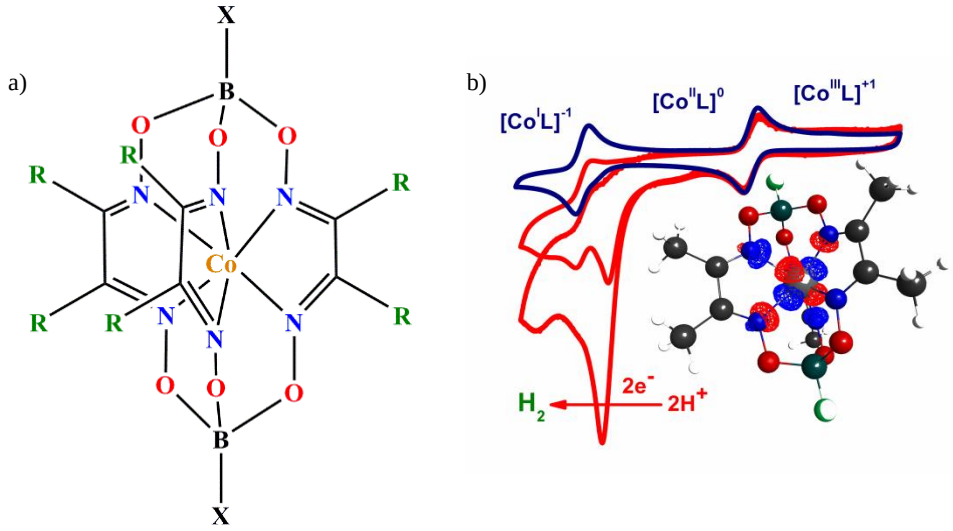

Fig. 1-13. a) Drawing of the Lewis structural motive of clathrochelates. X and R represent apical and ribbed substituents, respectively; b) graphical abstract for a recently published work of our group. The figure highlights two redox couples present in clathrochelates (blue voltammogram) along with the HER electrocatalysis (red voltammograms).

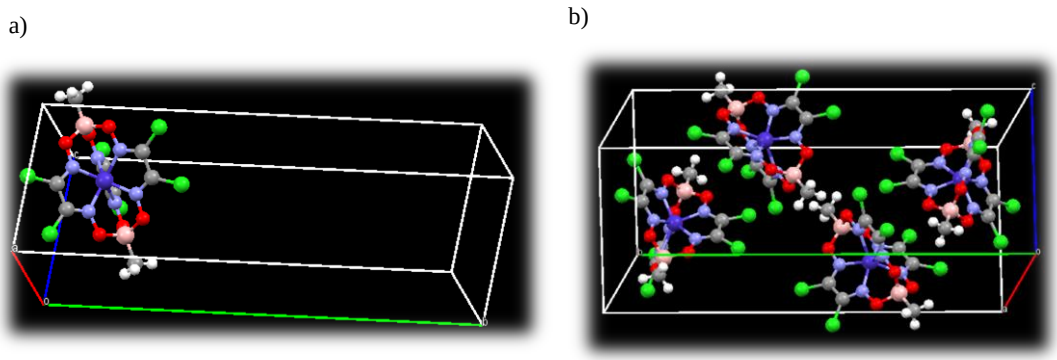

Fig. 1-14. a) Structure of the $Co(Cl_2Gm)_3(B\text{-}CH_3)_2$, the unit cell is indicated; b) Packing of $Co(Cl_2Gm)_3(B\text{-}CH_3)_2$ in the solid state, within the unit cell.

and I. Nevertheless, it has been long recognized that the Co^I species is catalytically active and responsible for the observed hydrogen evolution activity.[127,130] These facts have led to their successful implementation in practical devices such as polymer exchange membrane (PEM) cells.[134–136]

Though, a systematic approach to elucidate the impact of different substituents in the organic cage upon the electrochemical characteristics of the clathrochelates is still somewhat incomplete. Even though DFT studies of the geometric and electronic structures of these molecules have already been reported in the literature,[129,137] a thorough exploration of the HER mechanism has received scarce attention from a theoretical perspective. The only attempt to rationalize HER catalyzed by cobalt clathrochelates was presented few years ago.[129] In such study, DFT calculations on the reduced form of a model complex was reported, considering single protonation either on Co or on the iminic C, while neglecting other possible protonation sites, double protonation, or bimolecular pathways.

In summary, the qualitative prove for the electrocatalytic capabilities of clathrochelates is well established.[126–128] Some previous experimental work has been performed with inorganic acids dissolved in water,[126,128] consequently, any mechanistic analysis is

obscured by the two proton sources present in the system. Future experimental mechanistic studies on clathrochelates should be performed with defined organic acids of varying strength, in order to provide experimental support for the mechanistic possibilities discussed in this thesis.

1.11. Overview of the most important experimental techniques employed for the characterization of photoelectrochemical systems used in this thesis

1.11.1. X-ray photoelectron spectroscopy

X-ray Photoelectron spectroscopy consists in probing a surface with X-ray electromagnetic radiation, which is able to eject electrons from core-levels in the atoms. Such photoelectrons are analyzed according to the distribution of their kinetic energy in order to assess the chemical composition and electronic states present at the surface of the sample. The kinetic energy of the photoelectron satisfies the following equation[138]

$$E_k = h\nu - E_b - W \qquad (1\text{-}26)$$

Where E_k represents the kinetic energy of the photoelectron, $h\nu$ is the energy of the X-rays, E_b is the binding energy of the core-electron that was ejected by the X-ray, and W is a work function that is characteristic of the instrument.

The XPS technique is sensitive to the element type, because each element has a characteristic binding energy, which permits its identification in the sample. Furthermore, X-rays are able to penetrate deeply in the sample, however, the photoelectrons that are actually able to escape from the sample come from no deeper than around 10 nm,[138] therefore, XPS is a technique for surface analysis and does not provide information of the chemical composition in the bulk.

Trends in binding energy (BE) can be established. For example, an electron in an atom shall be more strongly bound (i.e., will possess higher BE) if it is closer to the nucleus. Consequently, for the same element, photoelectrons coming from a K shell will have a greater BE than photoelectrons coming from L shells. Moreover, for different elements and equal atomic shell, the greater BE shall be observed in the element with larger atomic number (Z), due to the greater electrostatic interaction between the nucleus and the electrons in the shell. Furthermore, when a certain atom is bound to another atom of greater electronegativity, then the molecular orbitals localized in the former will be stabilized, and the observed BE will be larger. Therefore, oxidation and reduction are easily observed in XPS because when an atom is oxidized, it loses electron density and the remaining electrons feel the nuclear charge to a greater extent, which is observed by an increase in BE. The opposite holds for reduction.

X-ray photoelectron spectroscopy has been performed on powders of several clathrochelates in order to analyse their chemical composition.[130,139] For those complexes, the spectrum was dominated by the prominent Co2p peak in the 775–815 eV binding energy region. For the Co^{II} complexes, the binding energy was fitted with the $Co2p_{1/2}$ and $Co2p_{3/2}$ signals located circa 796 and 781, respectively.[130] The spin-orbit splitting (SOS) was around 15 eV, which was in agreement for Co^{II} complexes reported in several other publication.[130,140–143] It should be noted that values of SOS depend on the oxidation state of the encapsulated Co ion center in the ligand cage.[130] Furthermore, the XPS spectra of all the studied Co clathrochelates contained weak additional peaks assigned to the shake-up satellites associated with molecular paramagnetism.[144] These results indicated that the studied clathrochelates contained an encapsulated Co^{II} ion as the central atom.

1.11.2. X-ray diffraction

Crystalline solid materials possess a structure where the atoms are set in periodic spatial positions. The periodic arrangement defines various planes of atoms that are identified by means of Miller indices. Miller indices are the reciprocals of the axis intercept of the plane. For example, if the *x*-intercept of the plane is in the length of the unit cell in such direction, the first Miller index shall be the reciprocal of a/a, which equals 1. If the *y*-intercept of a plane is in the half of the length of the unit cell in such direction, the second Miller index shall be the reciprocal of b/2b which equals 2. Miller indices are written in parentheses and are not separated by commas. This information is summarized in Fig. 1-15 a.

Miller indices are relevant, because they can be used to define the inter-planar distances by means of geometric considerations. For example, in the case of a cubic lattice, where the three dimensions of the unit cell are equal (a = b = c) and all angles are of 90 ° (α = β = γ), the relation between planar spacing and Miller indices is given by[145]

$$d_{hkl} = \frac{a}{\sqrt{h^2+k^2+l^2}} \qquad (1\text{-}27)$$

X-ray diffraction is the main means to determine the structure of crystalline materials. The simplest model to explain X-ray diffraction was proposed by Bragg in 1913. Bragg assumed that the X-rays were scattered by a set of parallel planes of atoms. Each plane is a source of scattered radiation and the diffraction pattern is observed when the spacing between planes is in the order of the wavelength of the radiation. Indeed, when the phases of scattered X-rays coming from different planes differ in an integer number of X-ray wavelengths, these two scattered beams interfere in a constructive manner and a diffraction peak is thus observed. Following geometric considerations, the path

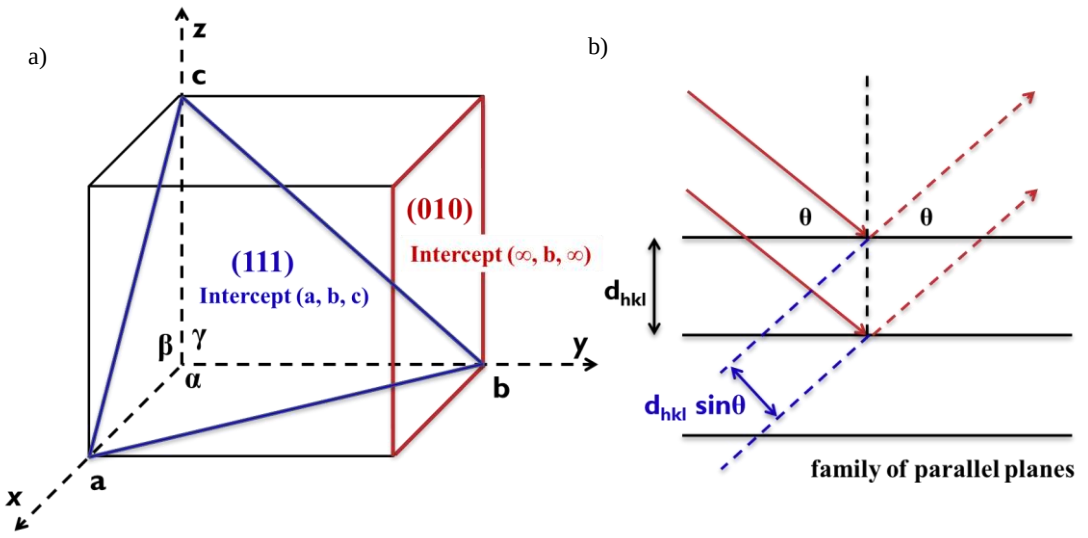

Fig. 1-15. a) Drawing to represent the Miller indices, and its relation to different planes in crystals; b) geometric justification of Brag's law.

difference between two scattered X-rays waves is given by $2d_{hkl}sin\theta$ (Fig. 1-15 b)

Thus, the Bragg equation governs the scattering of X-rays from a crystal lattice

$$d_{hkl} = \frac{\lambda}{2sin\theta_{hkl}} \qquad (1\text{-}28)$$

Where d_{hkl} is the distance between parallel planes in the lattice, defined by (hkl) Miller indices, λ corresponds to the wavelength of the X-ray, while θ_{hkl} corresponds to the angle of the scattered radiation.

In summary, different sets of planes in a particular crystal lattice, cause a unique diffraction patter, which is typical of the compound.

1.11.3. X-ray absorption spectroscopy (XAS)

X-ray absorption spectroscopy comprises several techniques, the most common being X-ray Absorption Near Edge Structure (XANES) and Extended X-ray Absorption Fine

Structure (EXAFS), as depicted in Fig. 1-16 a.

XAS is analogous to UV-Vis optical spectroscopy, in the sense that in both cases the absorption coefficient $\mu(E)$, which is a function of the energy of the electromagnetic wave, is experimentally measured. In XAS, there is a Lambert-Beer type relation, analogous to UV-Vis spectroscopy (eq. 1-29)

$$\frac{I}{I_0} \propto \exp(-\mu(E)) \qquad (1\text{-}29)$$

Where I is the transmitted photon flux, I_0 stands for the incident photon flux, $\mu(E)$ represents the energy dependent absorption coefficient. In is worth noting that XAS can be also measured in fluorescence mode, but the treatment described here does not change.

Optical UV-Vis spectroscopy and X-ray Absorption Near Edge Structure (XANES) have a similar ground since the absorption coefficient is determined by Fermi's golden

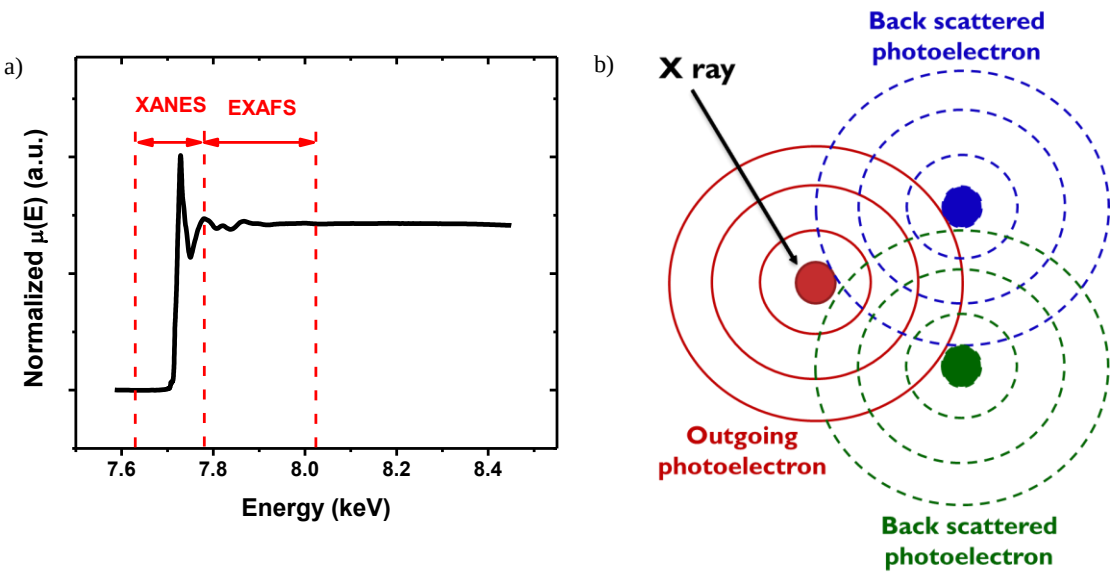

Fig. 1-16. a) Normalized XAS spectrum of the Co K-edge for $Co(Cl_2Gm)_3(B\text{-}CH_3)_2$, that shall be discussed further in this work; b) Scheme illustrating the quantum interference occurring during EXAFS, between the outgoing photoelectron and its scattering caused by the neighboring atoms.

rule (eq. 1-30)[146]

$$\mu \propto \left| < \Psi_f | \hat{\varepsilon} \cdot \vec{r} \cdot \exp(\vec{k}\vec{r}) | \Psi_i > \right|^2 \delta(E_f - E_i - \hbar\omega) \qquad (1\text{-}30)$$

Where μ is the absorption coefficient, Ψ_f represents the wave-function for the final state, Ψ_i stands for the wave-function of the initial state, $\hat{\varepsilon} \cdot \vec{r} \cdot \exp(\vec{k}\vec{r})$ represents the oscillating electromagnetic wave and $\delta(E_f - E_i - \hbar\omega)$ is Dirac's jump function, with E_f being the energy of the final state, E_i the energy of the initial state, and $\hbar\omega$ the energy of the X-ray.[146]

Conversely, in EXAFS spectroscopy the electromagnetic wave spans various keV beyond the absorption edge. Therefore, such high energies are able to excite core electron levels (commonly K (1s), L1 (2s) or L2 (2p) shells), which is the initial bounding state Ψ_i. Certainly, the X-ray energy is large enough so that the electron is ejected from the molecule and travels through the material in the form of a photoelectron wave that is not a bound level, but continuum levels with large kinetic energy (Ψ_f), furthermore a core vacancy remains, which interacts with the photoelectron.

Thus, the main difference between UV-Vis and EXAFS spectroscopy is the nature of the initial and final states. Indeed, in UV-Vis spectroscopy the energy of the electromagnetic wave is never higher than around 3.4 eV, which determines that both Ψ_i and Ψ_f are bound molecular states close to the valence orbitals. Therefore, UV-Vis and XANES spectroscopies possess similar selection rules.

In the case of EXAFS, the outgoing photoelectron travels through the material as a wave, and scatters back toward the photoabsorber atom when it strikes nuclei of neighboring atoms. The complex quantum interference between the outgoing

photoelectron wave and the back-scattered photoelectron wave originates an oscillatory behavior of the absorption coefficient μ.

The travel of the photoelectron wave can be from the photoabsorber directly to a neighbor, and then back to the photoabsorber. In such case, the path is referred to as single scattering. Moreover, the travel of the photoelectron wave can be from the photoabsorber, to a neighbor 1, then to a neighbor 2, and then back to the photoabsorber. Those scattering paths, involving more than one neighbor, are referred to as multiple scattering paths.

Thus, oscillatory signal that occurs at around 0.1 keV beyond the edge step is the actual EXAFS signal χ, which is extracted from the absorption coefficient according to eq. 1-31

$$\chi(E) = \frac{\mu(E) - \mu_0(E)}{\Delta\mu} \qquad (1\text{-}31)$$

Where $\chi(E)$ is the normalized oscillatory part of the absorption coefficient is, $\mu(E)$ is the measured absorption coefficient, $\mu_0(E)$ stands for the absorption coefficient without the contribution of scattering by neighboring atoms (this quantity is approximated by a spline function), and $\Delta\mu$, which is the edge step.

The EXAFS spectrum is analyzed according to the general EXAFS equation (eq. 1-32)[147]

$$\chi(k) = S_0^2 \sum_R N \frac{|f_{eff}(k)|}{kR^2} \sin(2kR + \phi_k) \exp(-2kR/\lambda_k) \exp(-2\sigma^2 k^2) \qquad (1\text{-}32)$$

Where $\chi(k)$ is the EXAFS amplitude; k is the wave-vector calculated according to $k =$

$\sqrt{(2m_e(E-E_0))/\hbar^2}$, with m_e being the mass of the electron, E_0 the energy of the edge and E the energy of the X-ray; S_0^2 represents the amplitude factor, the summation Σ_R extends over all scattering paths, N stands for the number of scatterers for a given scattering path, $|f_{eff}(k)|$ represents the effective scattering amplitude, R is the distance between the absorber atom and the back-scatterer neighbor, σ^2 stands for the Debye-Wäller (DW) factor, λ_k is the mean free path of the photoelectron, ϕ_k is the total phase shift, whose origin resides in the interaction of the photoelectron wave with the absorber and the scatterer.

The transformation of the EXAFS signal in k-space towards the R-space is performed by means of Fourier transform analysis using equation 1-33

$$\chi(R) = FT\{\chi(k)\} = \frac{1}{\sqrt{2\pi}}\int_{-\infty}^{\infty} \exp(2kiR)k^w\chi(k)\Omega(k)dk \qquad (1\text{-}33)$$

Where $\chi(R)$ is the EXAFS signal in the R-space (after Fourier transform), $\chi(k)$ is the EXAFS oscillating data in k-space, FT represents the Fourier transform, applied to $\chi(k)$, i is the imaginary number, k stands for the wave vector, $\Omega(k)$ is a window function, and w is the k-weight.

However, the actual numerical implementation employs the discrete Fast Fourier Transform equation (1-34)[146]

$$\chi(R) = \frac{i\delta k}{\sqrt{\pi N_{fft}}}\sum_{n=1}^{N_{fft}} \exp\left(2\pi in/N_{fft}\right)k_n^w\,\chi(k_n)\Omega(k_n) \qquad (1\text{-}34)$$

Where $\chi(k)$ is put in a uniform k-grid with a spacing δk of 0.05 Å^{-1}; $\chi(k)$ is filled with zeros beyond the real data range; N_{fft} equals 2^{11} = 2048, and $\chi(k)$ can expand till 102.4

Å which is around 40 keV beyond the edge step. These settings provide an R-grid spacing of around 0.031 Å, and R can span until 31.4 Å.

For EXAFS data analysis, the ATHENA code is used in beamline data, then allowing pre-edge subtraction, the determination of the edge position (E_0), atomic background subtraction, edge step determination and normalization of the absorption in order to subtract the atomic background from the absorption spectrum to yield the oscillating $\chi(k)$ EXAFS. ATHENA further allows k-weight, Fourier Transform, simple data plotting, and to merge data sets.

In order to analyze EXAFS, the FEFF code[148,149] generates theoretical signals that are used after, in the fitting stage. The main actions performed by FEFF are the calculation of atomic potentials in the Muffin-Tin approximation from the given atomic geometry (x y z Cartesian coordinates). The Muffin-Tin potential approximation considers all atoms as neutral and perfectly spherical, and the interstitial region between atoms has a constant (flat) potential, thus, there is no chemical bonding. The Muffin-Tin approximation is far too simplistic; nevertheless it works very well to calculate scattering paths. With these presumptions, FEFF calculates the total phase shift ϕ_k and the effective scattering amplitude $|f_{eff}(k)|$ for all possible single-scattering and multiple-scattering paths, according to the input geometry, and finally FEFF proceeds to the calculation of the signals.

Finally, the ARTEMIS code takes the experimental EXAFS $\chi(k)$ and compares it with a theoretical EXAFS $\chi_{theo}(k)$ built with the scattering paths calculated previously in FEFF. The fitting proceeds by minimization of equation 1-35, where ϵ is the level of noise in the data and $\chi_{theo}(k)$ is a function of structural parameters as $\chi_{theo}(k) = \chi_{theo}(w, N, R, \sigma, \Delta E_0)$, where w is the k-weight, N is the coordination number, R is the length of the scattering path, σ is the DW factor, and ΔE_0 energy is the origin of the

photoelectron.

$$\Xi = \sum_k \frac{\left(\chi(k) - \chi_{theo}(k)\right)^2}{\epsilon^2} \qquad (1\text{-}35)$$

Further details on the goodness of fit, involving the statistical variables chi-squared χ^2 (do not confuse with the EXAFS signal χ) and correlation coefficient R can be read in the specialized literature.[146]

The above comments clearly show that EXAFS is a local probe spectroscopy. Indeed, the nature of the initial state Ψ_i, usually K or L edges is highly localized in the photoabsorber atom. Furthermore, the electron mean free path (λ_k) and the dependence of $\chi(k)$ with R^{-2}, determine that the useful EXAFS analysis is restricted, at most, to 5 Å from the photoabsorber.

Considering the physical interpretation of the parameters obtained through the fitting of EXAFS data, the most important are R and σ^2. It may be said that R values, for single scattering paths, corresponds to the photoabsorber – neighbor distance. Actually, ARTEMIS provides a value of ΔR, which is the difference between the atomic distances in the input model, and the effective length of the single scattering path. The DW factor (σ^2) represents both thermal and static disorder present in the sample. The static disorder refers to multiple atoms of the same nature being located at effectively the same distance of the photoabsorber. The thermal disorder is related to atomic vibrations of atoms around their equilibrium positions.[147] Therefore, the DW factor is the standard deviation in the determination of R.

Typical values for ΔR should be less than 0.5 Å, ΔE should be less than 10 eV, S_0^2 should be within the 0.80 and 1.10 range and DW factors usually in the range from 0.003 to 0.020 Å^2.

To the best of our knowledge, there is only one study devoted to the study of the XANES spectra of a series of clathrochelates, in a combined study with XPS determinations.[130] The XANES results already published and those analyzed in this thesis shall be analyzed and compared during the results and discussion. However, it is worth noting that currently there is no published report regarding the EXAFS analysis of clathrochelates.

1.12. Density Functional Theory (DFT) calculations of molecular structure

Density Functional Theory (DFT) is very useful to predict the behavior of molecular systems. DFT is based on the fact that the electronic energy of the ground states is determined by the electron density ρ.[150]

In the first place, it is worth to comment what a functional is. For example, in mathematics, a function usually takes as the input a number, and gives another number as the output. For the function $f(x) = 2x$, if $x = 3$ the output result is $f = 6$. Conversely, a functional *F* takes as the input variable a function, and gives a number as the output. Indeed, a simple functional may be written in the following way: $F[y(x)] = \int_0^3 y(x)dx$, in this case, the input variable is the function $y(x)$, consequently, if $y(x) = 2x$, then $F[2x] = 9$. In this way, it may be appreciated that a functional is the function of another function. According to DFT, the energy of the system is a functional of the electronic density (ρ) (eq. 1-36), and the properties of the molecular system are univocally determined if ρ is known.

$$F[\rho] = E \qquad (1\text{-}36)$$

The DFT foundations reside in the Hohenberg – Kohn theorems.[150,151] Hohenberg – Kohn treatment was developed for an electron cloud in the presence of an external potential. For its application to molecular modeling, the electrons are treated as a charged gas, while the external potential is originated by the fields of the nucleus.

The Hohenberg – Kohn theorems can be stated as follows: (i) for molecules with a non-degenerate ground state, the molecular energy of the ground state, the wave function, and all other electronic properties are determined univocally by the electron density of the ground state $\rho(x, y, z)$, which is a function of only three variables; therefore, the electronic energy of the ground state is a functional of the electron density; (ii) there is a universal and exact functional $F[\rho]$ that establishes the dependence of observables from the electron density, nevertheless, the form of such universal and exact functional is unknown; (iii) the exact energy of the ground state can be obtained only if the exact electronic density is substituted in the functional of the total energy, while any other electron density that is substituted in the functional of the electronic energy shall give a greater energy than the real, so that $F[\rho_{true}] = E_{true} < F[\rho] = E$, where the subscript "true" indicates the true electron density and electronic energy. In other words, the true electron density of the ground state minimizes the functional of the electronic energy. The application of DFT to computational chemistry came with the introduction of orbitals to DFT, as proposed by Kohn and Sham.[150,151]

A disadvantage of DFT is that the actual form of the functional linking ρ with E is not known, therefore, approximate functionals should be used. The actual form of the functionals may be intimidating; a thorough discussion of it is not the purpose of this thesis. The interested reader is referred to the specialized literature.[150,151]

Another approximation used in *ab-initio* and DFT calculations is related to the wave function. Considering that ψ is unknown, it is assumed that the wave function of a

molecule may be written as a linear combination of an appropriate basis set of functions.

$$\psi = \sum_i c_i \chi_i \qquad (1\text{-}37)$$

Where c_i are coefficients that are optimized during the calculation, χ_i stands for hydrogenoid orbitals, i.e., atomic orbitals (s, p, d, f) known as Slater Type Orbitals (STO). STO possess the following mathematical form (eq. 1-38) [150]

$$\chi_{n,l,m}(r,\theta,\varphi) = NY_{l,m}(\theta,\varphi)r^{n-1}e^{-\zeta r} \qquad (1\text{-}38)$$

Where $\chi_{n,l,m}(r,\theta,\varphi)$ represents a STO, n l and m are the principal, angular and magnetic quantum numbers, (r,θ,φ) are spherical coordinates, N is a normalization factor, $Y_{l,m}(\theta,\varphi)$ represents a spherical harmonic function and ζ is an orbital exponent.

In the equation of the STO, the spherical harmonic describes the angular dependence of the orbital. Conversely, the radial part reveals an exponential dependence on the nucleus-electron distance ($\chi_i \sim e^{-r}$). Such type of function is quite inefficient for computational implementation.

In order to accelerate computation, the exponential function is substituted by Gaussian functions (eq. 1-39)

$$\chi_{n,l,m}(r,\theta,\varphi) = NY_{l,m}(\theta,\varphi)r^{2n-2-1}e^{-\zeta r^2} \qquad (1\text{-}39)$$

Whose dependence on the nucleus-electron distance is $e^{-\zeta r^2}$, and a the molecular orbital is approximated by a linear combination of GTO.

In addition to spatial functions, a spin function should be added to the description of

molecular orbitals. Therefore, when the electron spin is included in the calculation, the function describing the electron is called spin-orbital, and can be written as $\phi = \chi\vartheta$, where ϕ is the spin-orbital, χ represents the Cartesian part of the wave function, as expressed by equation 1-38 or 1-39, and ϑ represents here the electron spin, which can be either $\boldsymbol{\alpha}$or $\boldsymbol{\beta}$.

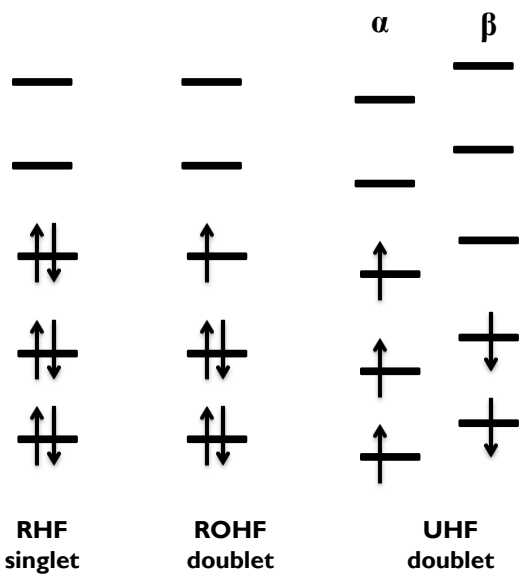

Fig. 1-17. Difference in restricted, restricted open-shell, and unrestricted wave-functions. Observe how for restricted and restricted open-shell wave functions there is a single spatial function for α and β spins.

The spin-orbitals can be "restricted", when only one type of spatial function χ is employed, irrespective of the electron spin. That means that each spatial orbital possesses one electron $\boldsymbol{\alpha}$ and one $\boldsymbol{\beta}$, and the wavefunction is called "restricted Hartree-Fock" (RHF) in the framework of HF calculations, and "restricted Kohn Sham" (RKS) if the framework of DFT.[152] Likewise, if the molecule has unpaired electrons, the spatial part of the spin-orbital can be forced to be the same, and the wavefunction is called "restricted open-shell Hartree-Fock" (ROHF) for the HF method, and "restricted open-shell Kohn Sham" (ROKS) for DFT. Finally, there is another possibility, where different spins are allowed to be described by different spatial functions, which is called "unrestricted Hartree-Fock" (UHF) in the context of HF calculations, and "restricted Kohn Sham" (UKS) if the context of DFT (Fig. 1-17).

In particular, the use of UHF spin-orbitals has a drawback known as "spin contamination". The extent of spin contamination can be assessed through the expectation value of the $\boldsymbol{S^2}$ operator, $\langle \boldsymbol{S^2} \rangle$. Theoretically, $\langle \boldsymbol{S^2} \rangle = S_Z(S_Z + 1)$, therefore,

for a singlet $S_Z = 0$ and $\langle \boldsymbol{S^2} \rangle = 0$, for a triplet $S_Z = 1$ and $\langle \boldsymbol{S^2} \rangle = 2$. For its relevance to this thesis, it is interesting to mention that clathrochelates have been treated theoretically by means of unrestricted wave functions,[137] in particular the reduced form of a clathrochelate in the triplet state presented important spin contamination, as expressed by a value of $\langle \boldsymbol{S^2} \rangle = 2.51$.[137] There are few studies where it is considered whether spin contamination is important or not, in the study of mechanisms of electron transfer.[153] However, most current studies regarding DFT calculations regarding electrocatalytic mechanisms involving open-shell transition metal complexes, employ UKS methodology and do not consider the effect of spin contamination.[152,154–157] ROHF and ROKS wavefunctions do not present spin contamination.

1.12.1. Density Functional Theory as a tool to investigate electrocatalytic mechanisms

Quantum chemical calculations have found a vast application in the study of electrocatalytic mechanisms, both in the homogeneous phase, where organometallic compounds are the protagonist,[124,125,152,155,156,158–161,161–170] and in heterogeneous photoelectrodes based on $SrTiO_3$.[16,104,106,108,109]

Concerning coordination compounds as catalysts for the hydrogen evolution reaction, DFT investigations have aimed to find the most stable pathways for various reaction mechanisms. This approach is fully thermodynamic, and does not give information on the kinetics of various paths. Certainly, it has been recognized that the whole picture to address a catalytic mechanism should be given by a combined thermodynamic and kinetic analysis.[169]

In this respect, Brian H. Solis and Sharon H. Schiffer have outlined the methodology to perform a kinetic analysis of the homogeneous electrocatalytic mechanisms.[163] An

electrocatalytic mechanism comprises several electron transfer and proton transfer reactions, and the activation energy for each step has to be calculated. In the case of electron transfer reactions, the activation barrier is given by the Marcus relation[171–173]

$$\Delta G^{\neq} = \frac{(\Delta G^0 + \lambda)^2}{4\lambda} \qquad (1\text{-}40)$$

Where $\Delta G^{\neq}$ is the activation barrier for electron transfer, ΔG^0 is the driving force, and λ is the reorganization energy.

The calculation of ΔG^0 for an electron transfer reaction is equivalent to calculating the standard redox potential because $\Delta G^0 = -nF\Delta E^0$, where n is the amount of exchanged electrons, F represents the Faraday's constant and ΔE^0 stands for the standard redox potential.

There are several alternatives described in the literature aiming to estimate the redox potential from ab-initio quantum chemistry.[163,169,174–177] The most usual manner is through the calculation of Born-Haber cycles, consisting in optimizing the relevant redox states in gas phase and in a certain solvent. In another manner, the relevant redox states may be directly optimized in the relevant solvent.[169] In that manner, through Hessian calculations, the thermodynamic quantities of the calculated molecules can be estimated, thereby giving access to the value of ΔG^0_{abs} and ΔE^0_{abs}. However, redox potentials are experimentally obtained against a reference electrode. To solve this, a common approach is to employ a reference electrochemical reaction (e.g. the ferrocene|ferrocenium redox couple), that is calculated at the same level of theory than the molecule of interest, and the ΔE^0_{abs} is referred to such reference reaction, thus providing a means to compare calculations with experiments.

Moreover, there are theoretical approaches to calculate the reorganization energies for

electron transfer based on DFT.[178–190] In order to calculate the barrier for proton transfer, the possibility of hydrogen tunneling must be treated, and when water is present (besides a Brønsted acid), proton transfer from the solvent should be taken into account. Additionally, the overall rates of each reaction path shall depend additionally on the concentrations of the acid and the molecular electrocatalyst.

CHAPTER 2. Experimental section

2.1. Synthesis of Rh doped strontium titanate (Rh:$SrTiO_3$)

$SrTiO_3$ powder doped with 1 mol % Rh at Ti sites was prepared by a solid-state reaction. The starting materials, $SrCO_3$ (Kanto Chemical; 99.9%), TiO_2 (Soekawa Chemical; 99.9%), and Rh_2O_3 (Wako Pure Chemical), were mixed in a Sr:Ti:Rh ratio of 1.07:(1 - x):x. The mixture was calcined in air at 1173 K for 1 h and then at 1373 K for 10 h in an aluminum crucible.[9] This material was kindly supplied by Prof. Dr. Akihiko Kudo, from the Tokyo University of Science.

2.2. Synthesis of Rh doped strontium titanate modified with Pt (Rh:$SrTiO_3$ – Pt)

The Rh:$SrTiO_3$ – Pt photocatalyst was prepared by a photodeposition method. 500 mg of Rh:$SrTiO_3$ were dispersed in an aqueous methanol solution (10 vol. %, 120 mL) in an ultrasonic bath. Subsequently, 0.385 mL of an aqueous solution of H_2PtCl_6 (20 mM) was added to the suspension. After removing dissolved air by evacuation through N_2 bubbling, the suspension was irradiated for 3 hours with visible light ($\lambda > 420$ nm) using a 300 W-Xe lamp and a cutoff filter. The resulting Rh:$SrTiO_3$ – Pt photocatalyst was then collected by filtration and washed with abundant water. This material was kindly supplied by Prof. Dr. Akihiko Kudo, from the Tokyo University of Science.

2.3. Synthesis of the clathrochelate hexachlorine containing cobalt(II) tris-dioximate ($Co(Cl_2Gm)_3(B\text{-}CH_3)_2$)

The procedure for the synthesis of $Co(Cl_2Gm)_3(B\text{-}CH_3)_2$ has been reported elsewhere.[132] Briefly, dichloroglyoxime (2.78 mmol), methylboronic acid (1.85 mmol), and $CoCl_2$ (0.93 mmol) were dissolved/suspended in dry nitromethane (20 mL) under argon, and

then the solvent (10 mL) was partially distilled off. The reaction mixture was cooled down to room temperature, and the dark-brown precipitate was filtered off and successively washed with 4 M aqueous hydrochloric acid, water, ethanol, diethyl ether, and hexane. The product was recrystallized from hot chlorobenzene and then extracted with chlorobenzene, and the extract was flash-chromatographically separated on silica gel (0.035−0.070 mm, 30-mm layer). The filtrate was evaporated to a small volume and precipitated with hexane. The precipitate was washed with hexane and dried in vacuo. Yield: 0.55 g (60%). This solid was kindly supplied by Prof. Dr. Yan Z. Voloshin, from the Russian Academy of Sciences in Moscow.

2.4. X-ray Photoelectron spectroscopy

XPS measurements were performed at ICMMO in a Thermo Fisher Scientific apparatus with base pressure in the low 10^{-9} mbar range. The spectrometer was equipped with a monochromatic aluminium source (Al K_α, 1486.7 eV) using a spot size of 400 µm (corresponding to an irradiated zone of approximately 1 mm^2). The hemispherical analyzer was operated at 0° take off angle in the constant analyzer energy mode, with a step of 1 eV for the acquisition of survey scans and a step of 0.1 eV for the acquisition of narrow windows.

2.5. Electron Paramagnetic Resonance spectroscopy

X-band EPR measurements were performed at ICMMO (Institut de Chimie Moléculaire et des Matériaux d'Orsay) using a Bruker Elexsys E 500 EPR spectrometer equipped with an Oxford ESR9 liquid helium flow cryostat. A gold-chromel thermocouple was placed directly below the sample position. The complexes were dissolved to a concentration of 1 mM and transferred to an EPR tube. Dioxygen was purged 5 times

under vacuum. The EPR tube was then cooled down to 77 K in liquid nitrogen before being transferred to the resonance chamber.

2.6. Optical spectroscopy

Ultraviolet Visible (UV-Vis) spectra were obtained at ICMMO using a Perkin Elmer precisely Lambda 35 instrument.

Emission spectrum of the LED was obtained with an Avantes Starline instrument, model Avaspec-204L-USB2-BB-50.

2.7. Scanning Electron Microscopy

Scanning Electron Microscopy images and Energy Dispersive spectra were recorded at ICMMO using a SEM-EDS Cambridge equipment and electron microprobe measurements (EPMA) (microprobe SX 100 CAMECA).

2.8. Powder X-ray Diffraction

Powder X-ray Diffraction measurements were carried out at ICMMO in a Panalytical PW3040/60 X'Pert MPD Pro diffractometer (θ-2θ Bragg-Brentano type). The apparatus contained a monochromator (Johansson type), equipped with a Ge (111) monocrystal in order to select the $K_{\alpha 1}$ (λ = 1.54059 Å) line of the Cu emission spectrum. Detection was performed by a fast X'Celerator PW 3015/20 detector of Real Time Multiple Strip technology. The sample, in powder form, was carefully deposited in the sample-holder with a spinner type "Spinner PW3064", thus allowing to average the intensity of the diffracted signal. Measurements were performed between 20 ° and 100 ° with a step of 0.0167 °, and a global acquisition time of 217 s per step.

2.9. Photoelectrode preparation

Photoelectrodes of Rh:$SrTiO_3$ were prepared at ICMMO by drop-casting 10 μL of an isopropanol suspension containing Rh:$SrTiO_3$ (30 mg in 0.5 mL) on top of an ITO surface. Next, 10 μL of Nafion (50 μL to a final volume of 1 mL in isopropanol) were put on top of the surface through the same methodology, and let dry for three hours. In all cases, the solvent was let to evaporate at room temperature. Before measurements, photoelectrodes were put into Na_2SO_4 (0.1 M) solution and allowed to wet and equilibrate overnight.

For the incorporation of the clathrochelate $Co(Cl_2Gm)_2(B\text{-}CH_3)_2$ (M = 575.81 g/mol), after the drop-casting of Rh:$SrTiO_3$, 0.5 mL of 10^{-2} M mother solution of the clathrochelate was prepared in DMF, then 10 μL of this solution was dropped immediately onto the surface. The total amount of clathrochelate at the surface of the Rh:$SrTiO_3$ photoelectrode was thus 10^{-2} μmol (5.8 μg). The evaporation of DMF was performed with the aid of a vacuum primary pump for two hours. The dissolution of the clathrochelate in DMF was not preserved, and was freshly prepared any time the photoelectrodes were prepared. Next, 10 μL of Nafion (50 μL to a final volume of 1 mL in isopropanol) were added onto the surface using the same methodology, and let dry for one hour. In all cases, the solvent was allowed to evaporate slowly at room temperature. Before measurements, photoelectrodes were put into an electrolyte solution and allowed to wet and equilibrate overnight.

For the electrodeposition of Cu, a copper wire was connected to the working electrode (ITO-Rh:$SrTiO_3$-Nafion), and the electrode potential was alternatively polarized in the anodic region in decreasing potential steps from +1.5 down to +1.0 V (steps of 0.1 V vs. SCE) and in the cathodic region (from -1.3 up to +1.0 V, steps of 0.1 V vs. SCE).

Rh:$SrTiO_3$ – Pt photoelectrodes were prepared by drop-casting 10 μL of an isopropanol

suspension containing Rh:$SrTiO_3$ – Pt (30 mg in 0.5 mL) on top of an ITO surface. Next, 10 μL of Nafion (50 μL to a final volume of 1 mL in isopropanol) were put on top of the surface using the same methodology, and let dry at ambient conditions for three hours. In all cases, the solvent was let to evaporate at room temperature. Before measurements, photoelectrodes were put into Na_2SO_4 (0.1 M) solution and allowed to wet and equilibrate overnight.

The geometric area of all these photoelectrodes was always set to ≈ 1.5 cm^2.

2.10. Electrochemical measurements

All electrochemical measurements were performed in aqueous Na_2SO_4 (0.1 M) in a three electrode cell configuration employing Indium Tin Oxide (ITO) surfaces modified with the semiconducting materials and the catalysts as the working electrodes. Saturated calomel electrode (SCE) and a carbon plaque were employed as reference and counter electrodes, respectively. MilliQ water (remaining resistivity of ≈ 10 MΩ.cm) was used for all tests, and was obtained from a Merck Millipore device.

All photoelectrochemical measurements were performed using a Modulab Solartron Analytical potentiostat, model 2100A. The light source was controlled with a calibrated optical bench (Thorlabs Inc. DC2100), equipped with a 450 nm LED light source. The intensity of light (in mW/cm^2) was measured with a calibrated silicon detector coupled to the optical bench, as provided by Thorlabs Inc.

2.11. Open circuit photovoltage decay

For the open-circuit photovoltage decay measurements, the photoelectrodes were kept at open-circuit conditions throughout the whole experiment. Initially, the photoelectrodes were illuminated for 60 s, then the LED was switched off and the open-circuit

photopotential decay was recorded for further 120 s. Different light intensities were tested, in the power density range of 150 to 400 mW/cm^2 (values of light power employed in each experiment are specified in each particular plot).

2.12. Intensity modulated photovoltage spectroscopy

IMVS determinations were performed at open-circuit conditions. The small ac perturbation of light was always 10 % of the dc bias light. The frequency range explored was typically between 20 Hz and 10 mHz (the detailed frequency ranges are carefully specified in the Bode representations of IMVS spectra reported during the discussion), as provided in the discussion chapters. Likewise, the precise light intensities employed for these determinations are indicated in each particular graph.

An important experimental parameter to adjust in order to clearly observe the non-steady state spiral pattern in IMVS was the number of points per decade being measured. The default value of 10 must be increased to at least 60, so that clean IMVS non-steady state spectra can be obtained.

2.13. Linear potential sweep voltammetry

Cyclic Voltammetry and Linear Sweep Voltammetry experiments were performed at the scan rate of 1 mV/s. The potential and the light power ranges over which each experiment was performed are specified in each particular case in the results and discussion Chapters.

2.14. Photoelectrochemical Impedance Spectroscopy

Photoelectrochemical impedance (PEIS) determinations were performed using a quartz photoelectrochemical cell from Pine Research Instrument Company. PEIS spectra were recorded under potentiostatic control. The amplitude of the sinusoidal potential perturbation was 10 mV in all cases. The frequency range explored was comprised between the kHz to the mHz region. Further specific details concerning LED powers are given in each particular case during the discussion of the results. Fitting of experimental PEIS spectra was performed using Peter's kinetic model,[66] which was implemented in Matlab R2014b using home-made code.

2.15. Matlab treatment of photoelectrochemical data

The treatment of all photoelectrochemical data obtained in this thesis was automatized with Matlab codes. A thorough explanation of the functioning of the scripts is secondary in the context of this thesis, because the main scientific results are in the domain of photoelectrochemistry and the programs to import, simulate, and fit photoelectrochemical data are common programming routines. Examples of a working Matlab program, developed during the thesis in order to import data from the potentiostat output, and then perform all the treatment in the case of OCPD measurements are provided below.

These codes can be useful for other interested researchers or PhD students who might need either a template or some guidance in Matlab programming, oriented to rather simple physical chemistry problems.

Just below, a script is provided that allows all kinetic treatment of OCPD, and finally, there is a Matlab function that works concomitantly with the script for the numerical estimation of time derivatives. The script and the function operate in different .m files.

The Matlab codes for fitting PEIS are much more tangled. These are composed by five different programs that work simultaneously, and all together comprise slightly more than 1200 lines of codes. Likewise, the numerical simulation of IMVS is composed by four different Matlab programs that function as an ensemble, and comprise around 600 lines of codes. For space reasons, these programs are not given explicitly in this Chapter.

2.16. Theoretical calculations on clathrochelates

All calculations made to study clathrochelates were performed in GAMESS.[191] Visualization of molecular orbitals was performed with Macmolplt.[192] Main geometry optimizations and Hessian calculations were accomplished with the B3LYP exchange correlation functional. Other functionals, such as M06-L, TPSS, BP86, PBE and PBE0, were also tested for geometry optimizations, which is discussed in the next section. Basis sets were included manually after being downloaded from the Basis Set Exchange website.[193] For geometry optimizations the LANL2DZ basis set was employed, with effective core potentials for Co and Cl.[194–196] Electronic energies and molecular orbitals were further refined by the all-electron basis cc-pVTZ for Co and cc-pVDZ for all other atoms.[197,198] For the single point calculations, the group $dft and the keyword nrad=125 were included. This is related to the grid selection in DFT calculations (nrad governs the number of radial grid points in Euler-Maclaurin quadrature whose default value is 96). Such value was largely increased to 125 in order to increase the accuracy of the energy estimations. Restricted open-shell Kohn-Sham (ROKS) wave functions were employed for open-shell species (species with unpaired electrons), and restricted Kohn-Sham (RKS) for closed-shell species (species with all electrons paired).

Solvent effects were taken into account through the PCM-SMD model.[199] Harmonic

vibrational frequencies were computed for all the species reported in this work. All the minimum energy structures possessed positive eigenvalues of the Hessian matrix, and the transition state had a unique imaginary frequency. Self-Consistent Field (SCF) convergence was controlled through the group $scf. Pulay's Direct Inversion in the Iterative Subspace (DIIS) and Davidson’s damping of the Fock matrix were used in order to accelerate and stabilize SCF convergence. DIIS was forced from the beginning of the calculation by increasing the energy threshold for its triggering from the default 0.5 Hartree to 10 Hartree (ethrsh keyword).

Below, a typical GAMESS input to perform geometry optimization for a molecule of water is presented. In order to clarify different parts of the input file, these are highlighted with different colors. For example, the main instructions of the input described just above, are put at the beginning of the file, and highlighted here in black-bold letters.

```
$contrl runtyp=optimize scftyp=rhf
icharg=0 mult=1 MAXIT=200 dfttyp=b3lyp $end
$SYSTEM MWORDS=850 MEMDDI=800 $END
$scf dirscf=.f. diis=.t. damp=.t.
ethrsh = 10 $end
$STATPT OPTTOL=0.0005 NSTEP=99 HSSEND=.T. $END
$pcm solvnt=WATER smd=.t. $end

$DATA
BASIS LANL2DZ, this line is a commentary
C1
O     8.0     0.92352     1.76975     0.02449
S   7
1   7817.0000000              0.0011760
2   1176.0000000              0.0089680
3    273.2000000              0.0428680
4     81.1700000              0.1439300
5     27.1800000              0.3556300
6      9.5320000              0.4612480
7      3.4140000              0.1402060
S   2
1      9.5320000             -0.1541530
2      0.9398000              1.0569140
S   1
1      0.2846000              1.0000000
P   4
1     35.1800000              0.0195800
2      7.9040000              0.1242000
3      2.3050000              0.3947140
4      0.7171000              0.6273760
P   1
1      0.2137000              1.0000000

H     1.0     1.91285     1.77931    -0.01729
S   3
1     19.2384000              0.0328280
2      2.8987000              0.2312040
3      0.6535000              0.8172260
S   1
1      0.1776000              1.0000000

H     1.0     0.63415     1.98086    -0.89872
S   3
1     19.2384000              0.0328280
2      2.8987000              0.2312040
3      0.6535000              0.8172260
S   1
1      0.1776000              1.0000000
$END
```

The $contrl group governs (among other things):

- The type of calculation to be performed (an optimization, as expressed in runtyp=optimize)
- The kind of "self-consistent field" wavefunction to be used (in this example, it is scftyp=rhf, which stands for "restricted hartree-fock")
- The charge and the multiplicity of the molecule (this is specified through the keywords **icharg=0 mult=1)**
- The maximum number of allowed iterations (in our calculations we set MAXIT=200, which is the maximum allowed by GAMESS).
- The DFT functional to be used (dfttyp=b3lyp).

The $SYSTEM group governs (among other things):

- The amount of memory allocated to each calculation (MWORDS=850 MEMDDI=800).

The $scf group is related to the "self-consistent field" calculation, for example:

- The keyword dirscf=.f. has been set to "false" (.f.), which stores the numeric integrals on disk. Instead, if its value were set to "true" (.t.), then the integrals would not have been stored, but calculated each time. The impact of this on the speed of calculation depends on the specific hardware, i.e., if it is faster to for GAMESS to calculate an integral, or to find it on the computer's memory.
- The keywords diis (Direct Inversion in the Iterative Subspace) damp (Davidson's damping of the Fock matrix), directly affect the rate of convergence. It was observed that without inclusion of these keywords, the scf

calculations on clathrochelates did not converge. Therefore, these were included in all calculations.

- The keyword ethrsh = 10 forces diis when the energetic difference between two iterations is less than 10 Hartrees. 10 Hartrees is an enormous amount of energy, equivalent to 272.114 eV. In practical terms, this forces diss almost from the beginning of the calculation, thus speeding and stabilizing scf convergence.

The group $STATPT controls the parameters for the search of a stationary point. For example:

- The keyword OPTTOL=0.0005 is the tolerance for the gradient convergence in units of Hartree/Bohr. The default is 0.0001, but this is indeed a strict condition, and was enlarged given the structural complexity of clathrochelates.
- The keyword NSTEP=99 specifies the maximum number of steps to make the geometry optimization.
- The keyword HSSEND=.T. set to "true" (.T.) is essential in each geometry optimization because it instructs the calculation of the Hessian matrix (or the normal vibrational modes) at the end of the optimization process. All calculated frequencies must be real and positive, otherwise the stationary point is not a minimum and the calculation should be restarted to find a true minimum.

The group $pcm sets the use of a solvent during the calculation

- The specific solvent is specified trhough solvnt=WATER
- The smd flag set to true (.t.) selects the "Solvation Model Density", which has a database of 178 organic and inorganic solvents.

Note that GAMESS is not case-sensitive, so keywords may be written in capital letters

or not. A broader description of all keywords and groups may be found in the GAMESS website, in reference 200.

Next, in the $DATA section, it is observed a commentary line, then the symmetry group of the molecule. Rigorously speaking, water is known to belong to the C_{2v} symmetry group, however, if the symmetry is specified, then GAMESS forces the geometry optimization to follow the indicated symmetry, which is not a problem for water whose geometry is well known. Commonly, no symmetry constrains are set through a C_1 group, with the intention to evaluate whether the theoretical model gives the adequate geometry without pre-established constraints. In the next line, this is the oxygen element symbol (O) followed by the atomic number (8.0) and the Cartesian coordinates, highlighted in bold-red letters. Just below, written in blue, the LANL2DZ basis set may be observed, as it was manually introduced. In the same manner, the two hydrogen atoms along with its basis set are also specified.

The following lines specify the input for a single-point energy calculation. The $DATA group is similar to the one just presented for the geometry optimization of water, and it is not fully included here because, for the $Co(Cl_2Gm)_2(B\text{-}CH_3)_2$ clathrochelate, the basis set specification spans over 24 pages in a word document (Times New Roman, 10, single spacing).

```
$CONTRL SCFTYP=ROHF RUNTYP=ENERGY MAXIT=200
ICHARG=0 MULT=2 dfttyp=b3lyp $END
$SYSTEM MWORDS=250 MEMDDI=100 $END
$scf dirscf=.f. diis=.t. damp=.t. ethrsh=10 $end
$dft nrad=125 $end
$pcm solvnt=dmf smd=.true. $end

$DATA
```

```
$END
```

In order to find a transition state, a saddle point search has to be performed, and a single imaginary frequency needs to be found to assess its correct determination. Saddle point searches may be performed in GAMESS, specifying RUNTYP=SADPOINT.

2.17. Cartesian coordinates of the optimized molecules at B3LYP/LANL2DZ level with effective core potentials for Co, Cl and Fe

The reproduction of the theoretical results reported in this thesis cannot be performed with ease without the Cartesian coordinates of the complexes. Therefore, we present them in (x,y,z) format, after geometry optimization. Having this information, any interested reader can view the molecules referred in Chapter 4 directly in any molecular modeling program and to run other calculations based on the molecules reported in the annex section at the end of this thesis.

2.18. Extended X-ray Absorption Fine Structure (EXAFS) spectroscopy

The EXAFS spectrum was treated with ATHENA, ARTEMIS and FEFF 7.0. The calculations using FEFF 7.0 were performed with the parameters that can be observed below in the input file. The calculations were set to consider only single scattering (2 legs paths) and multiple scattering of 3 legs paths. Scattering paths were calculated until 6 Å farther apart from the Co photoabsorber.

The EXAFS amplitude was given by equation 2-1 [147]

$$\chi(k) = S_0^2 \sum_R N \frac{|f_{eff}(k)|}{kR^2} \sin(2kR + \phi_k) \exp(-2kR/\lambda_k) \exp(-2\sigma^2 k^2) \qquad (2\text{-}1)$$

Where $\chi(k)$ denotes the EXAFS amplitude; k is the wave-vector $k =$

$\sqrt{(2m_e(E-E_0))/\hbar^2}$, where m_e is the mass of the electron, E_0 the energy of the edge and E the energy of the X-ray; S_0^2 stands for the amplitude factor, the summation Σ_R extends over all scattering paths, N is the degeneracy of a given scattering path, $|f_{eff}(k)|$ denotes the effective scattering amplitude, R is the distance between the absorber atom and the back-scatterer neighbor, σ^2 is for the Debye-Wäller (DW) factor, λ_k is the mean free path of the photoelectron, ϕ_k is the total phase shift.

This equation is identical to the one presented during the EXAFS presentation in the Bilbiographic Overview. Nevertheless, it is repeated here to facilitate the reading.

During the fitting, the XRD structure and DFT optimized geometry (B3LYP/LANL2DZ) were used. The following variables were allowed to refine: R, DW factors, E_0 and S_0^2. The degeneracy for each scattering path was not allowed to refine because in this analysis the structure of the molecule was known. Different DW factors were grouped according to chemical sense, with the purpose to limit the number of parameters. This is extensively treated during the discussion of EXAFS results.

The fitting was accomplished in R-space (k range from 3.000 to 11.886 $Å^{-1}$, R range from 1.000 to 4.627 Å). During the analysis, whenever not specified, k^2-weighting was used, and a Hanning window function was employed throughout.

The fitting was performed to minimize the statistical variable chi-squared, given by the equation 2-2 [147]

$$\chi^2 = \frac{\sum_1^{No.of\ points}\left(\frac{1}{s_i}\right)(\chi^{exp}(k_i)-\chi^{calc}(k_i))^2}{No.of\ points - No.of\ variables} \qquad (2\text{-}2)$$

Where $\chi^{exp}(k_i)$ denotes the measured amplitude of EXAFS in point "i", and $\chi^{calc}(k_i)$ represents the calculated EXAFS amplitude at point "i", calculated by FEFF 7.0.

The normalization factor s_i is given by the following equation 2-3 [147]

$$s_i = \frac{\sum_j^{No.of\ points} k_j^3 |\chi^{exp}(k_i)|}{k_i^3} \qquad (2\text{-}3)$$

A typical input file for FEFF (as implemented in ARTEMIS) is presented just below.

```
 TITLE

 HOLE       1    1.0    * FYI: (Co K edge second number is
S0^2)

 *         mphase,mpath,mfeff,mchi
 CONTROL   1      1     1     1
 PRINT     1      0     0     0

 RMAX      6
 NLEG      3

EXCHANGE 0 3 0

 POTENTIALS
 *    ipot   Z  element
     0     27    Co
     1      7    N
     2     17    Cl
     3      5    B
     4      8    O
     5      6    C
     6      1    H

 ATOMS
 *   x          y          z      ipot
      3.093553    3.204397    5.988473 0 Co
      1.743851    4.373741    3.449369 3 B
      4.052862    1.976615    8.669939 3 B
      4.553331    1.177573    7.487361 4 O
      2.591623    5.415120    4.145917 4 O
      2.587760    3.153711    3.141774 4 O
      4.489596    3.415368    8.513384 4 O
      2.552947    1.901958    8.738518 4 O
      0.593250    3.977560    4.328581 4 O
      1.022761    3.499088    5.519708 1 N
      3.987241    4.054601    7.442776 1 N
      3.141727    5.005342    5.310845 1 N
```

```
 4.143392    1.631000    6.287777 1 N
 1.966896    2.387585    7.615787 1 N
 3.152880    2.557411    4.206682 1 N
-1.535186    3.124970    6.082131 2 Cl
-0.325300    2.153669    8.915023 2 Cl
 4.129012    0.805005    2.481906 2 Cl
 5.306808   -0.516801    5.264604 2 Cl
 3.603176    7.559653    5.812962 2 Cl
 4.996130    6.272671    8.479278 2 Cl
 4.424897    0.927127    5.225994 5 C
 0.144897    3.088834    6.362699 5 C
 0.689740    2.533321    7.609260 5 C
 3.869042    1.483594    4.008391 5 C
 3.624000    5.902416    6.117799 5 C
 4.170606    5.336885    7.339263 5 C
 1.196166    4.979821    2.094700 5 C
 4.665577    1.414662   10.012014 5 C
 4.345693    1.934397   10.752045 6 H
 5.623662    1.466898    9.973404 6 H
 4.399973    0.498507   10.126007 6 H
 0.698550    5.779340    2.279845 6 H
 0.624241    4.338679    1.665758 6 H
 1.933796    5.187810    1.515913 6 H
```

CHAPTER 3. Catalytic tuning of Rhodium doped Strontium Titanate photoelectrodes

3.1. Structural, chemical and optical characterization of Rh:$SrTiO_3$

The first step in the characterization of the material was achieved by the crystallographic confirmation of Rh:$SrTiO_3$ by X-ray diffraction (XRD). Non-doped $SrTiO_3$ is known to possess a typical cubic perovskite structure (space group P m -3 m; a = b = c = 3.905 Å; α = β = γ = 90°, cell volume = 59.547 $Å^3$).[101] The XRD determination should permit to establish if the doping process would be a source of appreciable distortion in the crystal lattice or not. Fig. 3-1 shows the comparison between the experimental XRD pattern of Rh:$SrTiO_3$ and a prediction of the $SrTiO_3$ pattern. There is an excellent match between experimental and predicted data. This is the indication that the incorporation of Rh at 1% in Ti(IV) sites does not disturb substantially the hosting crystal structure, which is essentially the same as for non-doped $SrTiO_3$. Fig. 3-1 further confirms that the procedure described in this work is appropriate to obtain a single phase of Rh:$SrTiO_3$ that was not contaminated by excess of precursors such as TiO_2, Rh_2O_3 or $SrCO_3$. Though, XRD analysis was not able to put into evidence the presence of Rh in the sample due to its low content.

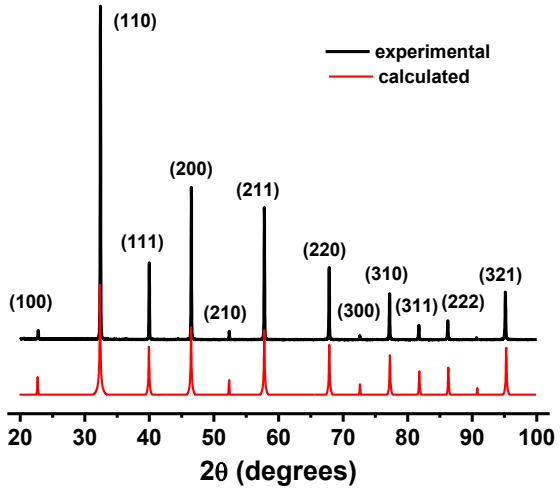

Fig. 3-1. Comparison between experimental XRD pattern for Rh:$SrTiO_3$ and calculated for $SrTiO_3$

In order to assess the presence of Rh as a dopant, XPS spectra were obtained. In addition to the typical Ti and Sr profiles, the presence of Rh in

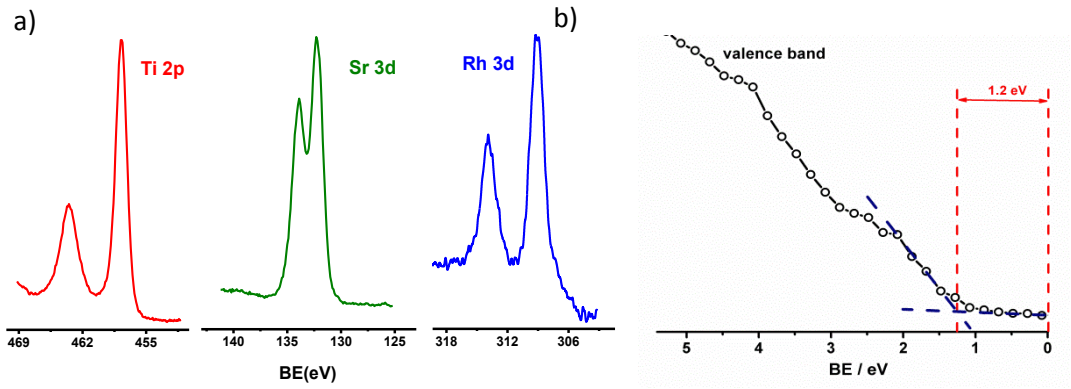

Fig. 3-2 a) XPS spectra of Ti 2p, Sr 3d and Rh 3d and b) Valence band XPS spectrum for the Rh:$SrTiO_3$ material.

the compound was undoubtedly determined (Fig. 3-2 a). XPS was further employed to obtain information on the energetics of the valence band with respect to the Fermi level (E_F). In XPS, the zero in the binding energy (BE) scale corresponds to the energy of the E_F.[25] Consequently, the energy difference between E_F and the maximum of the valence band can be directly estimated by this technique. A value of 1.2 eV was obtained for Rh:$SrTiO_3$.

With the purpose to obtain deeper insights into the band energetics of the photoelectrode, diffuse reflectance spectroscopy was also employed. In Fig. 3-3 we observed a strong absorption in the UV region, which is associated to inter-band transitions of $SrTiO_3$ consistent with the reported band gap of 3.2 eV for this material.[102–104] Fig. 3-3 shows that Rh doping produced in-gap states, observed in the diffuse reflectance spectra with an absorption band with a maximum at 560 nm, lying well in the visible region. Such absorption suggests that the energy difference between Rh in-gap states and the conduction band is approximately 2.7 eV, as observed before using soft X-ray spectroscopy.[103]

There is a weak absorption beyond 1000 nm that may be attributed to d-d transitions in the material. Fig. 3-3 b additionally depicts the emission spectrum of the LED employed

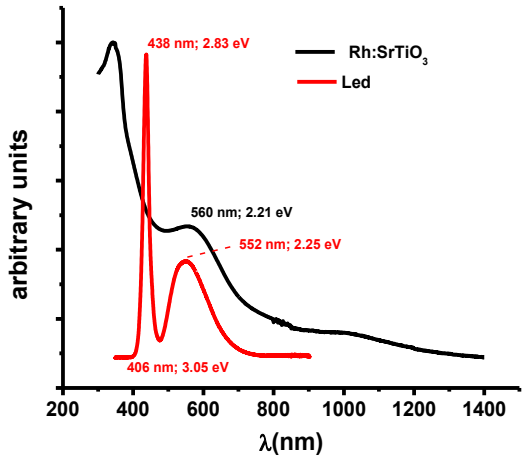

Fig. 3-3. Ddiffuse reflectance spectra for the Rh:$SrTiO_3$ material (black line). Red lines in a) and b) depict the emission spectrum of the LED employed in this work.

in this work which presented two emission bands with maximums at 438 nm and 552 nm. Therefore, the light of the LED possessed enough energy to excite electrons from the in-gap Rh states to the valence band but not from the valence band into the conduction band. It may be appreciated from Fig. 3-3 b that the inter-band transitions characteristic of non-doped $SrTiO_3$ (also present in Rh:$SrTiO_3$) lying in the UV region are completely outside the wavelengths emitted by the LED, thus ensuring that all the results reported herein are due to the sole response of the photoelectrode to visible light irradiation. The UV-Vis spectra also permitted to assess that Rh has a +4 oxidation state in the material.[103,112]

3.1.1. Surface analysis by Scanning Electron Microscopy and Energy Dispersive Spectroscopy

A further step in the characterization of the Rh:$SrTiO_3$ semiconducting material was accomplished by means of Scanning Electron Microscopy (SEM) and Energy Dispersive Spectroscopy (EDS). Fig. 3-4 a shows a SEM micrograph of the bare ITO surface. The surface is notably flat, and the polycrystalline structure of ITO was only

appreciated at the nanometer scale. Fig. 3-4 b shows an image of the ITO-coated glass substrate of the photoelectrode after surface modification by addition of Rh:$SrTiO_3$ and Nafion. In Fig. 3-4 b, the Nafion film cannot be seen, suggesting that it forms a very thin layer on top of the semiconducting powder. Additionally, the polycrystalline nature of the Rh:$SrTiO_3$ surface may be appreciated, as has been reported before,[9] with a very important roughness observed at the micrometer scale. It is worth to note that SEM images were taken before and after the photoelectrode was wet by aqueous Na_2SO_4 electrolyte, and before and after electrochemical testing both in anodic and cathodic polarizations, and the images obtained were essentially the same as the one presented in Fig. 3-4 b, indicating that none of these procedures caused morphological alterations of the surface of the semiconductor.

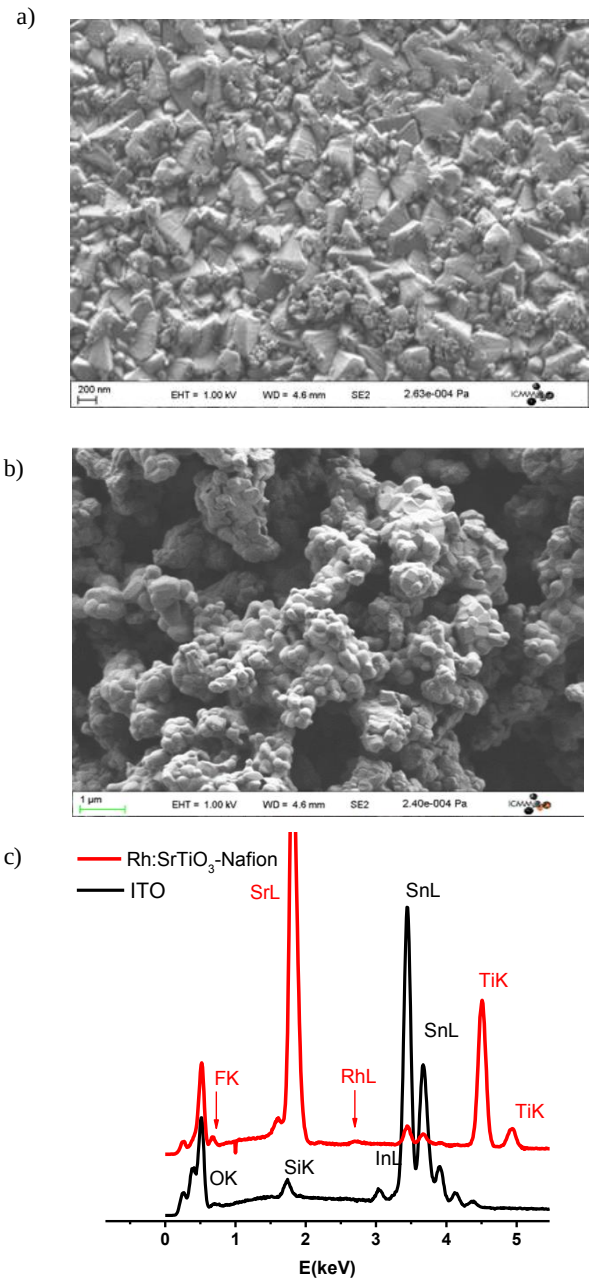

Fig. 3-4 a) SEM image of bare ITO surface; b) SEM image of the electrode surface corresponding to Rh:$SrTiO_3$; b) EDS spectra of surface.

Fig. 3-4 c shows the EDS spectra of the ITO support compared to the semiconductor photoelectrode. The signals of the L-shells of In and Sn coming from ITO are well

defined, and the Si K-shell is observed as well, which originates from the glass substrate on top of which ITO is deposited. In the case of the photoelectrode assembly, EDS revealed the presence of F at the surface, from the Nafion film. Additionally, the Sr and Rh L-shells, and Ti K-shell were consistent with the identity of the semiconducting material. The presence of Rh is indicated in Fig. 3-4 c, but with a notably weak intensity, related to the small loading of such atom whose role is the doping of $SrTiO_3$.

3.1.2. Photoelectrochemical characteristics of Rh:$SrTiO_3$ at open circuit conditions

Once the chemical characterization of the photoelectrode was accomplished, we proceeded to perform the first photoelectrochemical experiments. The evolution of the open-circuit electrode potential with increasing light intensities is shown in Fig. 3-5 a. The trend observed in such photopotential experiments indicates, as expected, that the Rh:$SrTiO_3$ photoelectrodes have a p-type conductivity.[9,13,103,112] On the other hand, Fig. 3-5 b shows the charge transfer and recombination rate constants, calculated by open-circuit photovoltage decay (OCPD) as explained in the Bibliographic Overview (chapter 1 of this thesis) and in appropriate literature.[73,74] For this measurement, dioxygen was extensively purged with Ar gas, and the cell was kept closed in Ar atmosphere during the measurements.

The charge transfer with the electrolyte is expected to occur with the solvent, since it is highly unlikely that an electrochemical reaction with either sodium or sulfate ions can take place in these experimental conditions. Thus, the charge transfer and recombination rate constants displayed in Fig. 3-5 b should correspond to the HER, which is notably slow. Both rate constants proved to be independent of light intensity, even at high levels of illumination (≈ 500 mW/cm^2). Overall, the rate of charge transfer was larger (k_t =

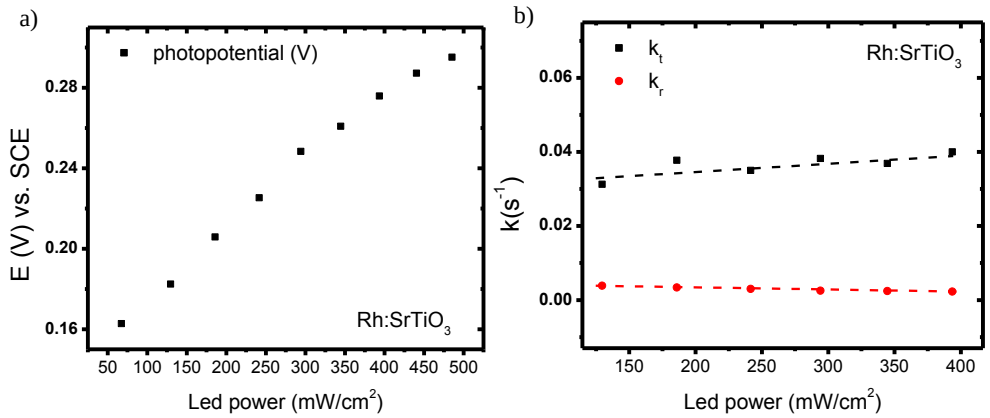

Fig. 3-5. a) Open circuit potential vs. led power for the Rh:$SrTiO_3$ material; b) charge transfer and recombination rate constants, determined by open circuit photovoltage decay.

0.035 s^{-1}) than the rate of recombination (k_r = 0.003 s^{-1}).

It is worth to comment here that there is a possible accumulation of sodium ions within the Nafion film and at the interfaces, and that this could modify the Helmholtz capacitance. However, since all experiments were made using similar Nafion layers, such possible effects are assumed to be constant and do not change the interpretation of the ensemble of results herein presented and the associated conclusions.[201]

3.1.3. Current-potential characteristics of Rh:$SrTiO_3$ photoelectrodes

Before discussing the voltammetric results of either the HER or the OER, it is useful to establish which is the thermodynamic potential for these reactions in the experimental conditions of this work. It is well-known that the thermodynamic potential for the HER and OER are E° = 0.00 V and E° = 1.23 V (vs. NHE) at pH = 0, respectively. However, polarization curves were measured here in Na_2SO_4 0.1 M, pH = 7 and employing the SCE (saturated in KCl) as the reference. Therefore, in the experimental conditions, the thermodynamic potential for the HER is E°'(HER)/V = 0.00 V – 0.059·pH – E_{SCE}, where E_{SCE} stands for the electrode potential of the saturated calomel electrode vs the

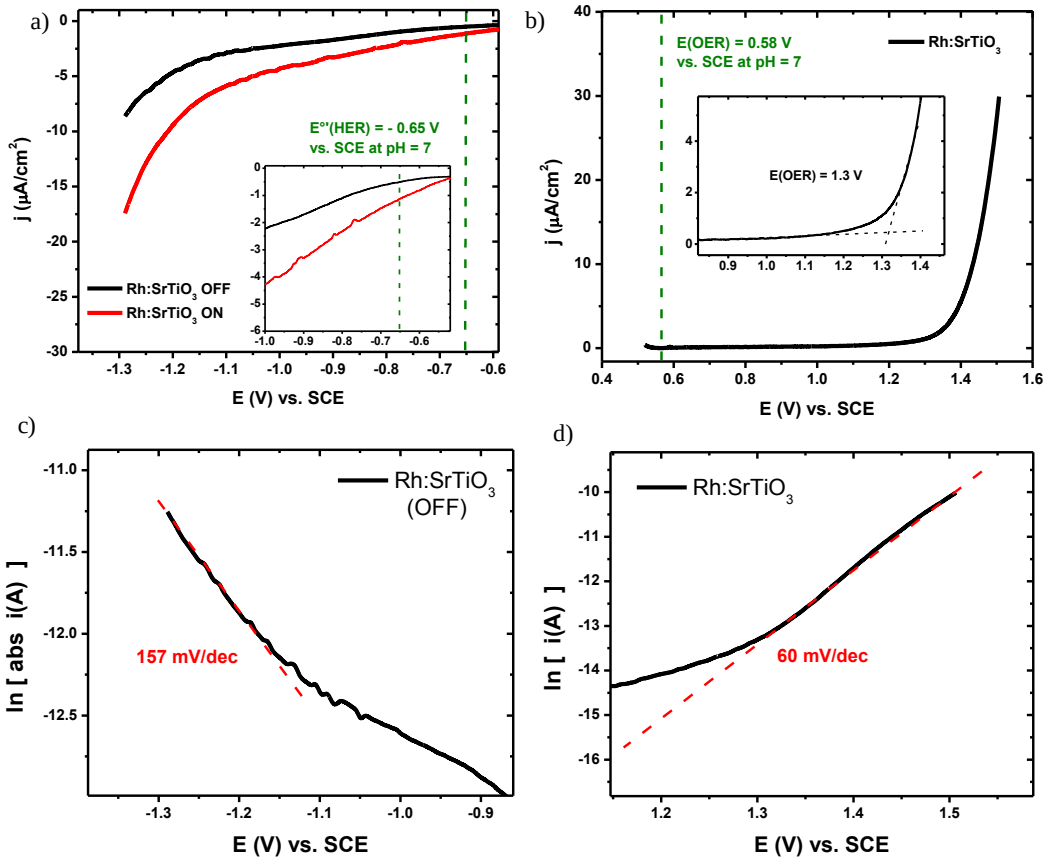

Fig. 3-6. Polarization curve of $Rh:SrTiO_3$ photoelectrodes for a) the hydrogen evolution reaction without and with (529.03 mW/cm^2) illumination b) the oxygen evolution reaction, no photocurrents were observed. Electrode area = 1.5 cm^2. Scan rate = 1 mV/s; c) Tafel plot for the HER; d) Tafel plot for the OER.

NHE, which has a value of +0.24 V.[202] Consequently, E°'(HER) = -0.65 V. Likewise, for the OER we can write E°'(OER)/V = 1.23 V – 0.059·pH – E_{SCE}, resulting in E°'(OER) = +0.58 V. These two reference values shall be represented in all subsequent Figures regarding the voltammetry for both the HER and the OER.

Typical linear sweep voltammograms recorded on $Rh:SrTiO_3$ photoelectrodes are shown in Fig. 3-6. Under cathodic polarization (Fig. 3-6 a), it was observed that dark currents were relatively small until an electrode potential of -1.1 V (vs. SCE) was reached. However, when the electrode was illuminated, an increase in cathodic currents clearly indicated that the photoelectrode acted as a photocathode, which was expected for a p-type semiconductor polarized at negative potentials. The photocurrent for this

material was modest (10 $\mu A/cm^2$), which is not a record but is consistent with previous reports on Rh:$SrTiO_3$ photoelectrodes.[9] It is worth noting that such photocurrent values are better than those obtained with other recent photoelectrode assemblies.[203]

Fig. 3-6 a inset shows that, under illumination, the reduction current starts before the thermodynamic potential of the HER. Indeed, without illumination, the only driving force available to carry out the HER is the applied potential and no HER can occur at potentials more positive than its thermodynamic potential. When the photoelectrode is illuminated, a part of the necessary driving force is supplied by photons, therefore the needed driving force for the HER can be attained at an electrode potential that is more positive than the thermodynamic potential for the HER.[8]

In order to gain insights into the mechanism of the HER, the Tafel slope was extracted (Fig. 3-6 c), and a value of 157 mV/dec was obtained. Such value of the Tafel slope rules out the possibility of both the Tafel and Heyrovsky (in the low surface coverage region of H atoms) reactions as possible rds.[81,204] Nevertheless, 157 mV/dec is slightly larger than the 120 mV/dec predicted for either the Volmer step or the Heyrovsky step (high coverage of H atoms); but the similarity between these values allows to suggest that any of the Volmer step or the Heyrovsky step (high coverage of H atoms) might be the rds at the surface of Rh:$SrTiO_3$.

On the other hand, the linear sweep voltammogram under anodic polarization is presented in Fig. 3-6 b. In this case, no photocurrents were detected (i.e., dark and illuminated currents were the same), which is normal for p-type semiconductors under positive bias. In such conditions, there is an upwards band bending that forces the photoexcited electrons towards the bulk of the semiconductor. Hence, the anodic reaction (OER) occurs by transfer of majority carriers (holes). Indeed, the photoexcitation process does not change much the amount of majority carriers at the

interface and the current density is therefore unperturbed by illumination. Additionally, it may be appreciated that this system displays notoriously low performance for the OER, since appreciable anodic currents start to flow only at +1.3 V (vs. SCE), showing an enormous overpotential of 720 mV.

The Tafel slope of the OER for the Rh:$SrTiO_3$ material was determined to be 60 mV/dec (Fig. 3-6 d). Currently, the mechanism of the OER is much more controversial than that of the HER. Indeed, a recent microkinetic analysis[81] predicts a Tafel slope of 60 mV/dec only under very specific conditions of intermediates' surface concentrations within a multi-slope curve, when eq. 1-21 is rds (see Figure 4 d in reference 81). The fact that Fig. 3-6 d exhibits a single Tafel slope over a relatively wide potential window (in open contrast to Figure 4 d in reference 81) made us reject the equations 1-18 to 1-22 with the rds given by equation 1-21 as a plausible mechanism in this case. On the other hand, it has been shown that avoiding the quasi-equilibrium assumption for the OER within the Bockris' oxide mechanism, such Tafel slope can be accounted for.[87] Certainly, a Tafel slope of 60 mV/dec is obtained when the rds is the reaction $M - O = M + 1/2O_2$ (eq. 1-25) and $\theta_O \approx 0$ and $\theta_{OH} \approx 1$. Henceforward, the mechanism of the OER shall be interpreted in terms of the contemporary revision of Bockris' oxide mechanism (eq. 1-23 to 1-25).[87]

3.1.4. Photoelectrochemical kinetics of the HER at the surface of Rh:$SrTiO_3$ photoelectrodes

PEIS is a powerful technique since it provides information not only on the charge transfer and recombination rate constants but also on interfacial capacitances associated to the system.[17,66,67,71,72,115] Previous optical characterization of Rh:$SrTiO_3$ revealed that Rh existed in the form of Rh^{4+} (dark grey solid).[103] However, it has been shown that

Rh^{4+} may be reduced to Rh^{3+} (yellow solid), which is more active towards the HER.[102,103] During all photoelectrochemical experiments, the photoelectrode was observed to turn yellow, indicating that the active material actually being measured was Rh^{3+}:$SrTiO_3$. The yellow color disappeared from the surface of the electrodes after one minute of contact with air, indicating that Rh^{3+} was easily oxidized to Rh^{4+} by dioxygen when in contact with the photoelectrode. In any case, all kinetic analysis presented henceforward correspond to the stable PEIS response of the photoelectrode, associated to the Rh^{3+} oxidation state.

Fig. 3-7 shows typical PEIS results in the Nyquist plot for Rh:$SrTiO_3$; dots are experimental points and straight lines are the least-squares fit to the photoelectrochemical model developed by Peter and discussed in the Bibliographic Overview of Chapter 1, eq. 1-2.[71,115] In the PEIS response of this system, two relaxations are observed. It was found that the high frequency (HF) relaxation shrank as light was made more intense, while the effect in the LF relaxation was not clearly defined. A more convenient way to compare PEIS for a kinetic interpretation is through the Bode plot of the imaginary component of the impedance because it shows explicitly the frequency where each relaxation occurs. In particular, the maximum of the low frequency (LF) relaxation is a good estimate of the charge transfer rate constant. Bode plots obtained at different light intensities and electrode potentials are represented in Fig. 3-7 b and c.

The effect of light intensity on PEIS spectra (Fig. 3-7 b) was more marked when the potential was more negative. In fact, the effect of light power was evidenced only at -1.30 and -1.25 V (vs. SCE) while at less negative potentials a change in light intensity did not change the shape of PEIS spectra.

Interestingly, the frequency at which the maximum of the LF relaxation occurred did not change, neither with the electrode potential (Fig. 3-7 b) nor with the light intensity (Fig. 3-7 c), indicating that k_t was independent of these experimental parameters. Such behavior is consistent with an ideal semiconductor|electrolyte interface, where most of the potential drops inside the space charge and not in the Helmholtz layer, causing k_t to have a fixed value at any applied potential.[205] However, the behavior of the recombination rate constant was non-ideal, since its value is expected to decrease with increased band bending. The independence of the recombination rate constant on the electrode potential has been reported before, for example in Figure 7 of reference 66.

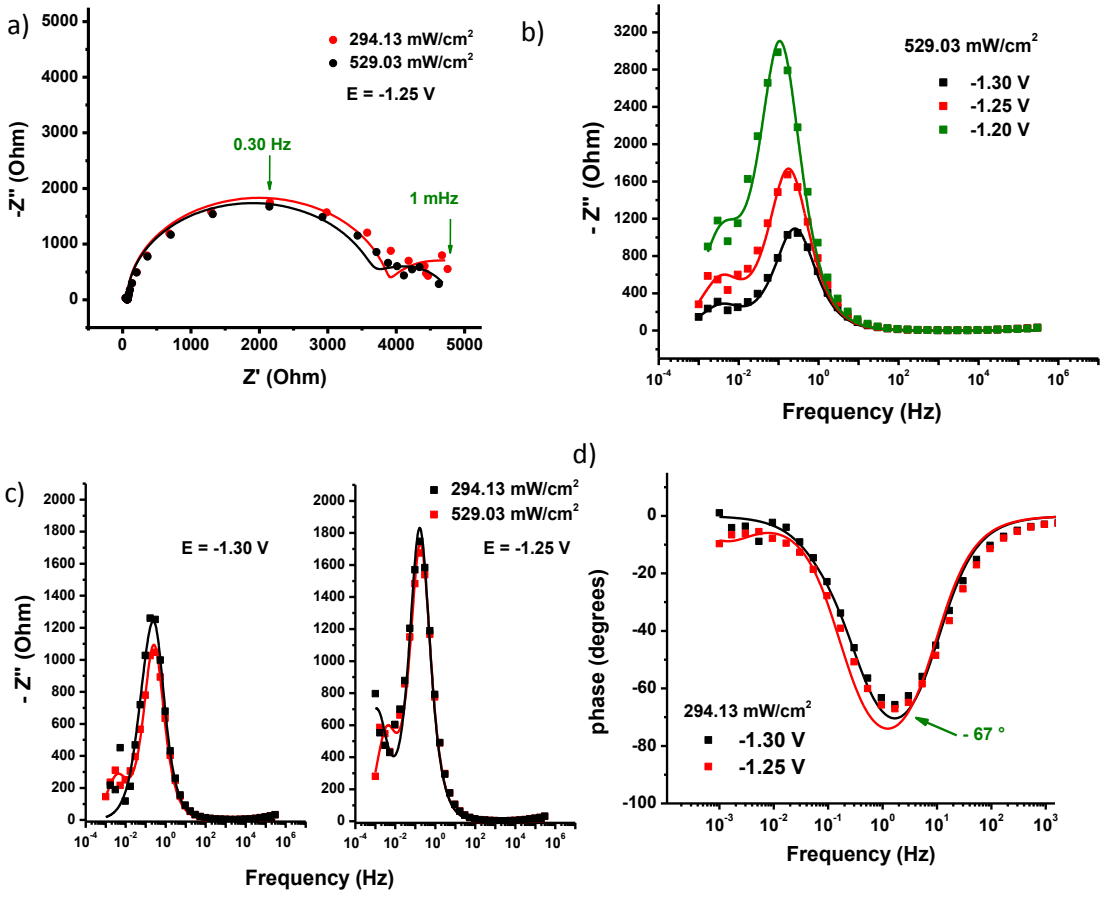

Fig. 3-7. Typical PEIS spectra for Rh:$SrTiO_3$; dots represent experimental values and straight lines are the best fit to equation 1; a) Nyquist representation; b) Bode representation of –Z"; effect of light intensity; c) Bode representation of –Z"; effect of electrode potential; d) Bode representation of the phase angle.

Such behavior has been attributed to the presence of surface states. Overall, charge transfer and recombination kinetic constants had nearly the same value at open-circuit and under cathodic polarization. Therefore, the HER in this material is notably slow over a wide potential window.

Since over the -1.30 V to -1.20 V range the kinetic parameters did not change, the mean value was calculated, providing numeric results of $k_t = (0.020 \pm 0.007)\ s^{-1}$, $k_r = (0.004 \pm 0.002)\ s^{-1}$. The percentage of photogenerated electrons (calculated according to $\eta = k_t/(k_r + k_t)$, eq. 1-7) being transferred to the Helmholtz layer was estimated to be $\eta = (78 \pm 2)$ %.

Furthermore, the increase (towards more positive) of the electrode potential caused PEIS spectra to expand. Such fact may be explained through a widening of the space charge region related to an increase in band bending. This would allow higher light absorption with the concomitant increase in the photogenerated flux of minority carriers (I_0, Table within the annex section at the end of this thesis).[66]

It is worth to comment here on the dependence of the space charge capacitance (derived from the HF relaxation) upon the electrode potential. However, it is necessary to be aware that the phase angle for the HF relaxation was at most -67°, a value which is quite farther apart from the ideal (-90°) value to consider the capacitance associated to the HF relaxation as a pure capacitance. Instead, the HF relaxation may contain contributions from surface roughness, surface states and the Nafion film that covers the photoelectrode.

Under depletion conditions, the space charge capacitance usually follows the Mott-Schottky equation[206]

$$C_{sc}^{-2} = \frac{2}{q\varepsilon\varepsilon_0 N A^2}\left(E - E_{FB} - \frac{k_B T}{q}\right) \qquad (3\text{-}1)$$

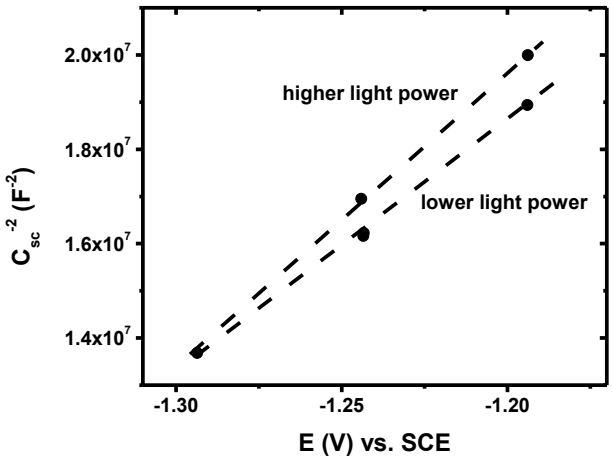

Fig. 3-8. Mott-Schottky plot for the Rh:$SrTiO_3$ photoelectrode.

Where C_{sc} stands for the space charge capacitance, E_{FB} is the flat-band potential, E is the applied potential, ε stands for the relative permittivity of the semiconducting material, ε_0 represents the permittivity of free space, N is the doping density of the semiconductor, A stands for the area of the electrode, k_B represents the Boltzmann constant, q is the elemental charge, and T is the absolute temperature.

Consequently, a plot of C_{sc}^{-2} vs E would give a straight line and extrapolation towards the potential axis would give the flat band potential and the slope allows estimating the doping density of the semiconductor. However, Mott-Schottky analysis can be misleading in some cases because the theory has been developed for flat semiconductors, without surface states[207] and most real photoelectrodes do not comply with these requisites. Despite these simplifying assumptions, the Mott-Schottky plot for Rh:$SrTiO_3$ presents a linear shape that is slightly dependent on light intensity (Fig. 3-8). Interestingly, the positive slope of this graph contrasts not only with the well-established p-type nature of the photoelectrode[9,13] but also with the photopotential measurements presented in Fig. 3-5 a. Indeed, such figure indicates two things: (i) the flat band potential for this semiconductor is located at electrode potentials greater than 0.28 V (vs. SCE), and (ii) the semiconductor is p-type. However, the positive slope in Fig. 3-8 is characteristic of an n-type semiconductor.

Fig. 3-8 suggests that the high (negative) overpotential applied to the photoelectrode

caused strong depletion conditions so that the inversion conditions were achieved.[64,65,206,208] In the inversion region, the space charge is so heavily depleted from majority carriers, that minority carriers (electrons for a p-type semiconductor) themselves can promote electron transfer reactions. Under these conditions, the bulk behaves like a p-type semiconductor, while the surface displays n-type conductivity,[65] which explains the observed positive slope in the Mott-Schottky plot within the potential window from -1.3 to -1.2 V (vs. SCE).

3.1.5. Photoelectrochemical kinetics of the OER at the surface of Rh:$SrTiO_3$ photoelectrodes

The photoelectrochemical study of p-type semiconductors under forward bias is seldom performed and reported in the literature because most p-type semiconductors suffer from corrosion at positive potentials.[115] Nevertheless, Rüdiger Memming recently presented various interesting reports on measuring dark currents in semiconductor-electrolyte interfaces.[64] Considering the stability of Rh:$SrTiO_3$ photoelectrodes under anodic polarization, we undertook the study of this p-type material under forward bias.

PEIS spectra recorded on Rh:$SrTiO_3$ at positive potentials presented two relaxations. The LF relaxation was found at notably low frequencies; with the need to go down to 0.282 mHz to truly observe such relaxation. Clearly, the kinetics of this system towards the OER was very slow, as suspected from the high overpotential of 720 mV determined during the analysis of LSV (Fig. 3-6). Fig. 3-9 a indicates that, when the electrode potential is made less positive, the Nyquist representation expands, preserving the ratios between the two relaxations, suggesting that rate constants do not vary with the electrode potential.

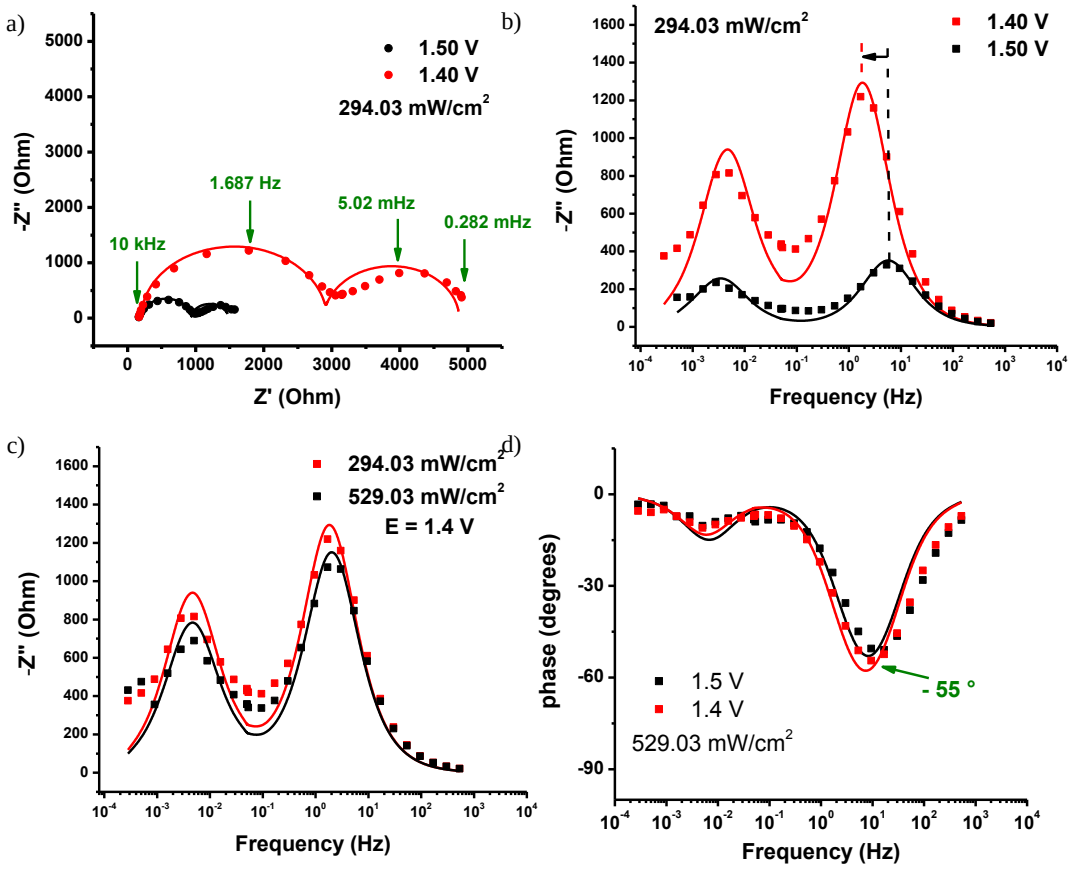

Fig. 3-9. Typical PEIS spectra for Rh:$SrTiO_3$; dots represent experimental values and straight lines are the best fit to equation 1; a) Effect of light in the Nyquist representation; b) effect of electrode potential in the Bode plot of –Z''; c) effect of light intensity in the Bode representation of –Z''; d) Bode representation of the phase angle.

A confirmation of this conclusion was obtained by analyzing the imaginary component of the impedance in the Bode plot (Fig. 3-9 b). It may be observed that the maximum of the LF relaxation occurred at the same frequency, indicating that the rate of charge transfer was independent of the applied potential, which is the behavior of an ideal semiconductor|electrolyte junction without Fermi level pinning.[205] Contrariwise, the HF relaxation did change with applied potential, suggesting that there is a change in the C_{sc} capacitance. Though, the inspection of phase angles indicate that its values are far too low (-55 °) to consider the fitted capacitance associated to this relaxation as a pure capacitance.

3.2. Structural, chemical and spectroscopic characterization of $SrTiO_3$ photoelectrodes modified with the hexachlorine containing cobalt(II) tris-dioximate ($Co(Cl_2Gm)_3(B\text{-}CH_3)_2$)

Results reported in the previous section are related to pristine $Rh:SrTiO_3$ photoelectrodes. In this section, we report on our attempts to improve the performance of the semiconducting material by surface sorption of a model organometallic compound selected from a well-known family of electrocatalysts of the HER in the homogeneous phase. Indeed, the hexachlorine containing cobalt(II) tris-dioximate clathrochelate $Co(Cl_2Gm)_3(B\text{-}CH_3)_2$, (Fig. 3-10 a) was impregnated at the surface of $Rh:SrTiO_3$ photoelectrodes by drop-casting. From now on, this system shall be referred to as $Rh:SrTiO_3$ – Ch.

In the first characterization step, the X-ray photoelectron spectrum of the organometallic compound was recorded on the powder. Fig. 3-10 b shows the spectrum at the Co2p binding energy level. The spectrum is dominated by the prominent Co2p peak in the 780–805 eV binding energy region.[130] The spin-orbit splitting (SOS) was around 15 eV,

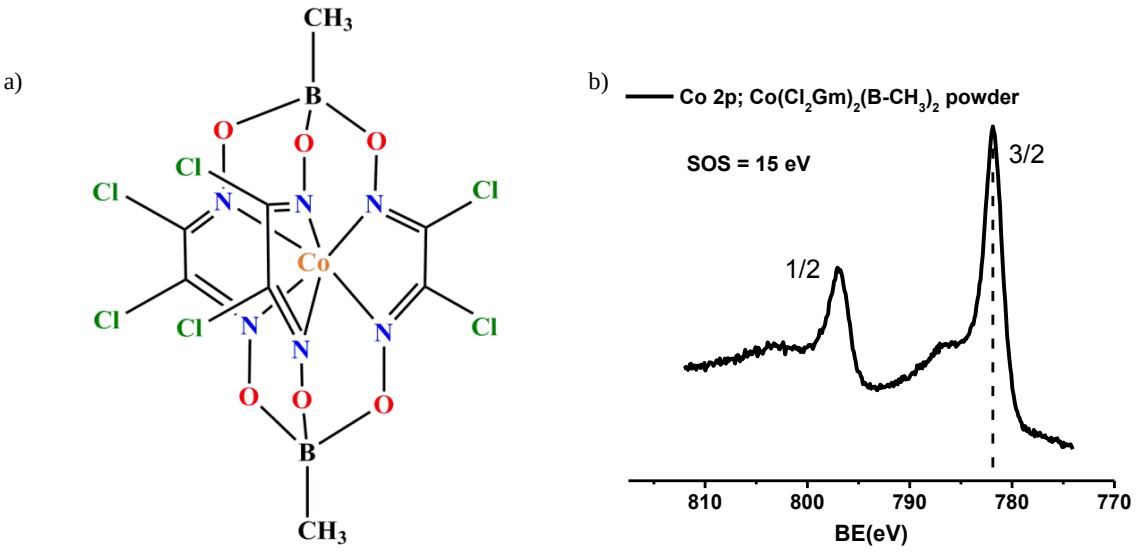

Fig. 3-10 a) Chemical structure of the model clathrochelate studied in this work. b) XPS spectrum of the Co 2p core level for the $Co(Cl_2Gm)_3(B\text{-}CH_3)_2$ molecule in powder form.

which is in agreement for Co^{II} complexes reported earlier [130,140–143]. It should be noted here that SOS values depend on the oxidation state of the encapsulated Co ion centre in the ligand cage.[130] Furthermore, the XPS spectra of this clathrochelate contained weak additional peaks assigned to the shake-up satellites associated with molecular paramagnetism.[144] These results suggest that the clathrochelate contains a Co^{II} ion as the central atom. However, XPS satellites do not allow to differentiate between low spin (S = 1/2) and high spin (S = 3/2) electronic configuration of Co. Such differentiation between low spin and high spin configuration was accomplished experimentally using X-Band EPR spectroscopy (Fig. 3-11 a).

Indeed, the molecule possessed a Co^{II} d^7 low spin configuration with the single occupied molecular orbital (SOMO) being located essentially on Co (Fig. 3-11 b). The Single Occupied Molecular Orbital (SOMO) of the clathrochelate, predicted by DFT, suggested a small probability of existence for the unpaired electron to be located also in N. In order to analyze qualitatively the EPR spectrum of the Co clathrochelate it should be considered that the Co nucleus presents a nuclear spin $I = 7/2$. The splitting pattern

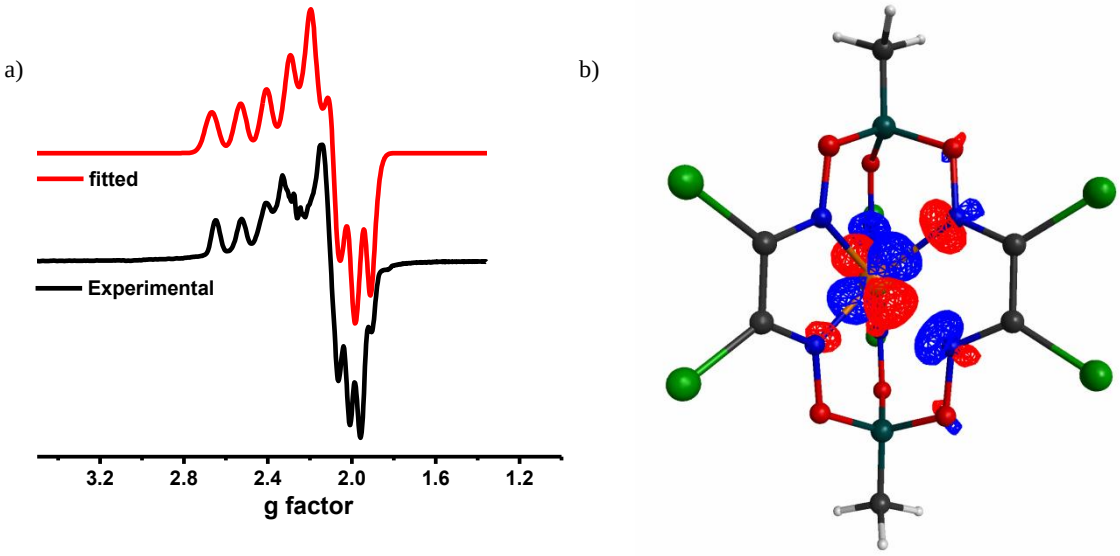

Fig. 3-11. a) EPR spectrum of the $Co(Cl_2Gm)_3(B\text{-}CH_3)_2$ molecule (black), recorded in frozen DMF solution at 20 K; best fit obtained with *easyspin* free software; b) SOMO of the $Co(Cl_2Gm)_3(B\text{-}CH_3)_2$ molecule, calculated with the B3LYP functional and the cc-pVTZ basis for Co and cc-pVDZ for all other atoms.

thus observed in EPR has its origin in the hyperfine interaction of the unpaired electron with the Co nucleus, thus exhibiting $2nI + 1 = 8$ lines, with I representing the nuclear spin of the nucleus, and n the amount of interacting nuclei with the unpaired electron. In the low field region (high g value), only four transitions of the parallel resonance are clearly observed since the other four are merged within the perpendicular signal. The super-hyperfine interaction with N would be observed in EPR as a further signal splitting as a triplet (nuclear spin for N; $I = 1$).[139] However, such super-hyperfine interaction is not resolved in the experimental spectrum, indicating that the unpaired electron is localized essentially on the metallic center. As will be described in Chapter 4, DFT calculations were performed on the low spin and high spin configurations for the Co(II) oxidation state of the clathrochelate, and the low spin doublet was calculated to be 154 kJ/mol more stable than the high spin quartet state, which is in agreement with the EPR results.

For the quantitative description of the EPR spectrum, a fitting procedure was undertaken using the free software *easyspin*, which is based on Matlab.[209] The shape of the EPR spectrum, caused by the anisotropic structure of the molecule, suggested the use of **g** and **A** tensors with three contributions, i.e., $\mathbf{g} = [g_x\ g_y\ g_z]$ and $\mathbf{A} = [A_x\ A_y\ A_z]$. Previous EPR fitting of other clathrochelates has been performed with *easyspin* (see, for example, Figure 1 of the supporting information in reference 127). A look at the EPR spectrum obtained in this work (Fig. 3-11 a) reveals that there is no small splitting due to the super-hyperfine interaction with N. Therefore, the effect of unresolved super-hyperfine interactions, as well as any other contributions to line broadening caused by relaxation, or distributions in **g** and **A** tensors was considered by the inclusion of an anisotropic strain tensor (**H**) as implemented in *easyspin*, so that $\mathbf{H} = [H_x\ H_y\ H_z]$. The fit parameters of the EPR spectrum are shown in Table 3-1, and the comparison between

experimental and fitted EPR spectra is depicted in Fig. 3-11 a.

Table 3-**1**. Magnetic parameters for the $Co(Cl_2Gm)_3(B\text{-}CH_3)_2$ clathrochelate, as obtained by fitting in easyspin.

	z	y	x
g	2.33	2.03	2.01
A (MHz)	272	57	186
H (MHz)	60.0	204.7	180.3

Another step in the characterization of the $Co(Cl_2Gm)_3(B\text{-}CH_3)_2$ complex was accomplished by XANES and EXAFS spectroscopies. A detailed discussion of the XANES and the fit of EXAFS for this complex in the solid state shall be reported in Chapter 4, in the framework of the analysis of DFT calculations of the mechanism of the HER catalyzed by $Co(Cl_2Gm)_3(B\text{-}CH_3)_2$ in the homogeneous phase.

Once the clathrochelate complex was characterized, it was subsequently coated onto the surface of $Rh:SrTiO_3$ photoelectrodes and a thin layer of Nafion was put atop the interface, as described in the Experimental Section of chapter 2. The interaction between the semiconducting substrate and the clathrochelate was assessed by XPS. Unlike other modified photoelectrodes that shall be shown in next sections, in this case

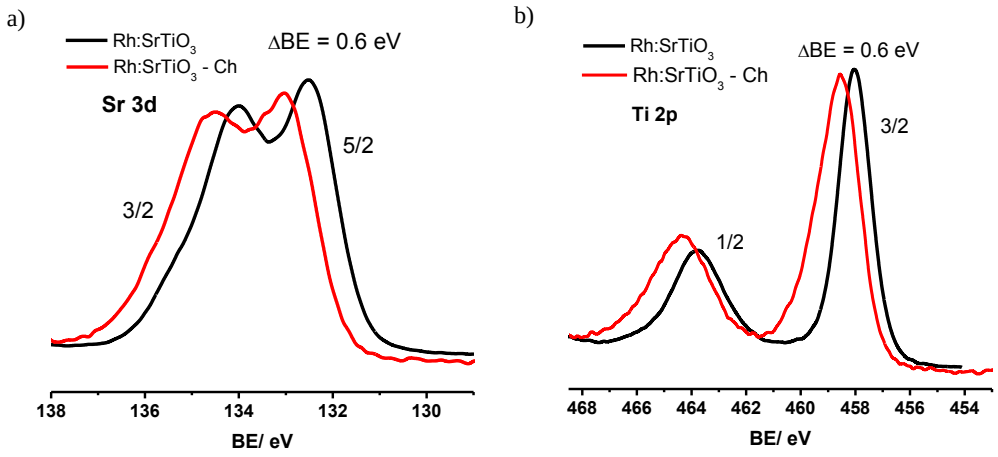

Fig. 3-12. Comparison of XPS spectra of unmodified $Rh:SrTiO_3$ and $Rh:SrTiO_3$ – Ch photoelectrodes for a) Sr 3d and Ti 2p levels.

the surface modification of the semiconductor with the clathrochelate shifted the Ti 2p and Sr 3d peaks 0.6 eV to higher binding energies (Fig. 3-12 a and b). This is an indication that the surface of $Rh:SrTiO_3$ was oxidized by the presence of the molecular catalyst.[201]

3.2.1. Photoelectrochemical characteristics of $Rh:SrTiO_3$ – Ch photoelectrodes at open circuit

The variation of the open circuit potential as a function of light intensity is presented in Fig. 3-13 a. Like for all other photoelectrodes containing $Rh:SrTiO_3$ as photoabsorbing semiconductor, the electrode potential increases as light power increases. This indicates that surface functionalization with the Co containing clathrochelate did not perturb the extrinsic p-type characteristics of the device. Fig. 3-13 a also shows that, at very strong illumination intensities (529.03 mW/cm^2) flat-band conditions have not been attained. Certainly, at electrode potentials more negative than those depicted in Fig. 3-13 a the $Rh:SrTiO_3$ – Ch photoelectrode should behave like a photocathode.

Panel b of Fig. 3-13 shows the kinetic parameters derived from open circuit photovoltage decay measurements. At the illumination levels tested in this work under

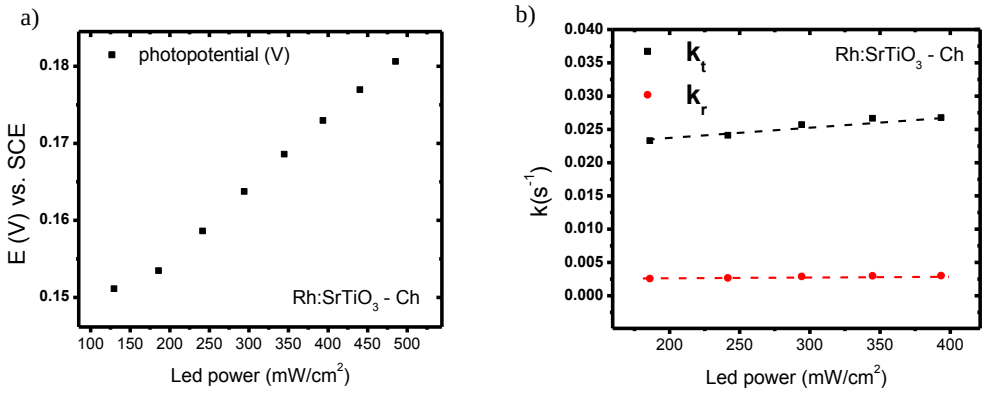

Fig. 3-13. a) Photopotential vs. led power for the system $Rh:SrTiO_3$ – Ch; b) Kinetic parameters for $Rh:SrTiO_3$ - Ch in open-circuit conditions.

open-circuit conditions, charge transfer and recombination rate constants were found quite small and proved to be independent of light intensity. Furthermore, the presence of the clathrochelate at the surface did not change appreciably the rate of charge transfer and recombination at open circuit, when compared to bare Rh:$SrTiO_3$ (Fig. 3-5 b).

3.2.2. Current potential characteristics of Rh:$SrTiO_3$ – Ch photoelectrodes

Fig. 3-14 a and b show the polarization curve under cathodic and anodic bias, respectively, for Rh:$SrTiO_3$ photoelectrodes modified with the hexachlorine containing cobalt(II) tris-dioximate ($Co(Cl_2Gm)_3(B\text{-}CH_3)_2$). Clathrochelates themselves are active towards the HER in the homogeneous phase.[126–128,139] Moreover, previous electrochemical studies on various clathrochelates evidenced that these molecules may act as precatalysts for the deposition of cobalt-based nanoparticles, which are also active towards the HER.[129] Nevertheless, the authors of such report recognized that the chemical nature of the cobalt particles formed after electrolysis was unknown, but EDX analysis showed the presence mainly of Co and O.[129]

In the Rh:$SrTiO_3$ – Ch system studied here, we observed that the electrochemical response under cathodic polarization evolved upon cycling, so that the performance towards the HER increased (increase of the current densities and decrease of the overpotential, Fig. 3-14 a). We speculate that such electrochemical evolution during testing under cathodic polarization might be due either to a better coating of the complex at the surface of the semiconductor or to the transformation of the clathrochelate into another cobalt containing species which is a more active electrocatalyst, by analogy to a previous report.[129] When the photoelectrode was illuminated, the inherent evolution of CV did not allow to clearly determine whether the current density increase was due to incoming light or to the chemical transformation of

the clathrochelate. The effect of light was better observed by PEIS, as shall be discussed below.

At this point, it is worth to note that electrode activation by tiny deposition of Pt and Au coming from the counter electrode has been reported.[210] In order to avoid such interfering effect, a graphite plaque was always employed in this work as the counter electrode. Thus, any evolution in electrochemical responses was due to chemical transformations of the working electrode and not to modifications originated from the counter electrode.

Further insights into the HER mechanism in this system was gained by the determination of Tafel slopes (Figure Fig. 3-14 c). The Tafel slope was determined from

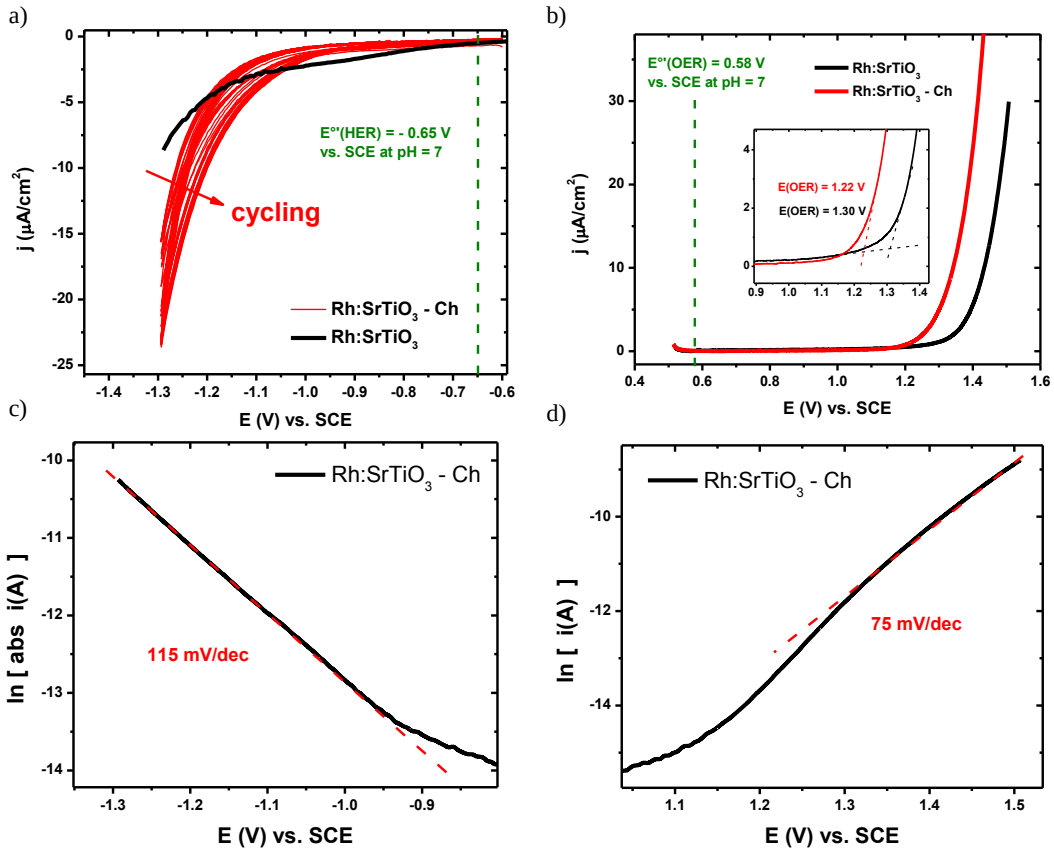

Fig. 3-14. Polarization curve of $Rh:SrTiO_3$ – Ch photoelectrodes for a) the hydrogen evolution reaction without and with (529.03 mW/cm^2) illumination b) the oxygen evolution reaction, no photocurrents were observed. Scan rate = 1 mV/s; c) Tafel plot for the HER; d) Tafel plot for the OER.

the last stable CV depicted in Fig. 3-14 a. A value of 115 mV/dec was obtained, which may originate from either the Volmer step or the Heyrovsky step (in the region of high surface density of H atoms) as possible rds.[81]

On the other hand, the response under anodic polarization was somewhat similar to that previously commented here. No photocurrents were observed, as it is usual for semiconductors under accumulation conditions. The presence of the clathrochelate in the surface caused a decrease in overpotential of 80 mV for the OER (Fig. 3-14 b). The Tafel slope for the OER on this modified electrode was 75 mV/dec (Fig. 3-14 d), which is close to the slope of 60 mV/dec predicted when the reaction $M - O = M + 1/2O_2$ (eq. 1-25) is the rds and $\theta_O \approx 0$ and $\theta_{OH} \approx 1$.[87] Considering the notable overpotential that still remains for the OER, and the absence of photocurrent, the effect of electrochemical cycling upon the anodic response of this photoelectrode under forward bias was not further investigated.

3.2.3. Photoelectrochemical kinetics of the HER at the surface of Rh:$SrTiO_3$ – Ch photoelectrodes

In the previous section it was observed that the electrochemical response was varying upon electrode cycling. In order to have an insight into the effect that such potential cycling had on the kinetic parameters, CV and PEIS were measured alternatively at the same time, i.e., one PEIS after each CV cycle. The trend in CV was already shown in Fig. 3-15 a, while the trend in PEIS is depicted in Fig. 3-15 a and b, for the first and last (70^{th}) cycles, respectively.

Overall, the Nyquist representations of PEIS spectra showed a tendency to shrink upon cycling, a fact which is consistent with the increasing slope of current-potential curves obtained by LSV (Fig. 3-14 b) given that the total resistance of the photoelectrode

measured in PEIS equals $R_{total} = Z(\omega \to 0) = (dj/dV)^{-1}$.[17]

In both the first and last cycles of PEIS analysis, it was found that under high illumination conditions, instead of the two characteristic relaxations in PEIS,[66,71,115] only one relaxation was observed (Fig. 3-15 a and b). Indeed, the two relaxations may appear close in frequency and are consequently merged, or any of both relaxations might lie outside the range of experimentally explored frequencies, or any of both relaxations could present very small impedance and could be a small shoulder at either HF or LF.

However, at lower illumination levels (129.57 mW/cm^2) the two typical relaxations of

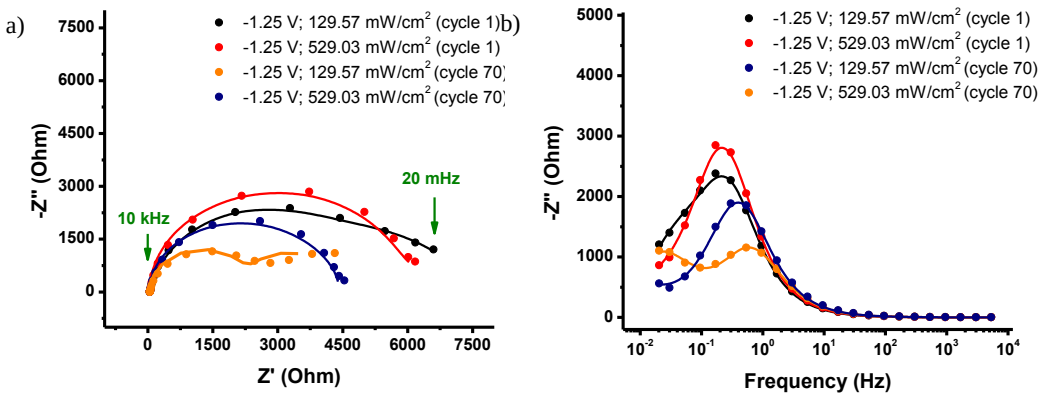

Fig. 3-15. a) Effect of cycling on PEIS in the Nyquist for the Rh:$SrTiO_3$ – Ch photoelectrode a) Nyquist representation b) Bode representation.

semiconducting photoelectrodes were observed (Fig. 3-15 a and b). It was thus possible to unambiguously determine the charge transfer and the recombination rate constants.

Considering the evolution of LSV and PEIS data, the full kinetic analysis was performed when the electrochemical signal became stable, after 70 cycles. Hence, typical PEIS response of such stable response of the Rh:$SrTiO_3$ – Ch photoelectrode is plotted in Fig. 3-16 a to d.

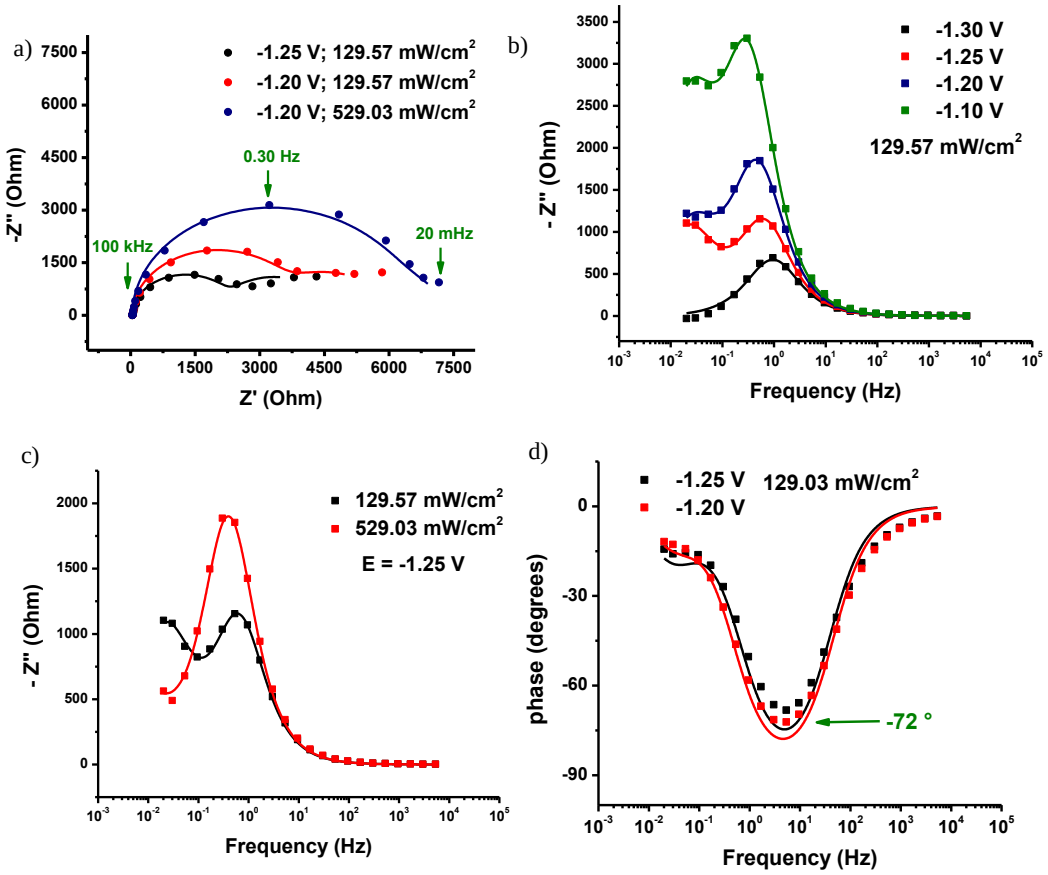

Fig. 3-16 . Typical PEIS spectra for Rh:$SrTiO_3$-Ch a) Effect of light in the Nyquist representation; b) effect of electrode potential in the Bode plot of –Z"; c) effect of light intensity in the Bode representation of –Z"; d) Bode representation of the phase angle.

To determine the kinetic parameters for all PEIS spectra (including those for which the two relaxations were not resolved i.e. those obtained at high illumination), kinetic parameters determined at the lower illumination intensity were used as initial guess for the fitting. The fact that PEIS obtained at 129.57 mW/cm^2 and at potentials of -1.25 and -1.10 V (vs. SCE) displayed the same maximum of the LF relaxation in the Bode plot of –Z", indicated that charge transfer rate was not altered in this potential range.

The results of the fitting of experimental PEIS spectra obtained for the Rh:$SrTiO_3$ – Ch photoelectrode are shown in Table (within the annex section at the end of this thesis). The charge transfer kinetics measured on the clathrochelate-modified semiconductor was found to be 10 times larger than the kinetics measured on the pristine

semiconductor, thus showing evidence of the electrocatalytic effect that was observed also in CV under cathodic bias. However, the recombination rate was also found to be faster on the Rh:$SrTiO_3$ – Ch photoelectrode. Therefore, the fraction of photoexcited electrons transferred to the electrolyte is almost the same, with and without the modification of the semiconductor with the clathrochelate (compare the values of η in Table with those in Table , within the annex section at the end of this thesis).

The effect of the electrode potential on the PEIS spectra follows the usual trend reported in the systems discussed so far, *i.e.*, the Nyquist representations of PEIS spectra expand as the potential is made less negative. Such fact is attributed to a decreasing value of the photogenerated flux of minority carriers (I_0) associated to the shrinking of the space charge region and the decreasing band bending when the potential goes less negative (see Table within the annex section at the end of this thesis).[66]

Finally, it is worth to comment on the behavior of the space charge capacitance. The analysis of the phase angle has shown values of at most -72° (Fig. 3-16 d), which is far from a pure capacitance behavior (-90°) in the HF relaxation and therefore, the capacitance derived from the HF relaxation is not strictly the capacitance of the space charge region. Instead, this is the combination of effects of surface roughness, the presence of Nafion polymer at the surface, and the presence of surface states. Nevertheless, at least theoretically, under depletion conditions, the space charge capacitance usually follows the Mott-Schottky equation (a plot of

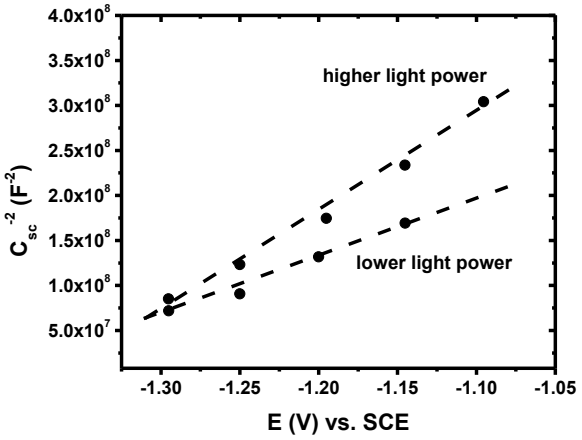

Fig. 3-17. Mott-Schottky representation for the Rh:$SrTiO_3$ – Ch photoelectrode under cathodic bias.

C^{-2} vs E should give a straight line). As discussed before, Mott-Schottky analysis can be misleading because the theory has been developed for flat semiconductors, without surface states, and most real photoelectrodes do not account for these conditions. Nevertheless, the Mott-Schottky analysis performed to Rh:$SrTiO_3$ –Ch photoelectrodes revealed a straight line with a positive slope (Fig. 3-17). Such slope was also encountered in pristine Rh:$SrTiO_3$ photoelectrodes (Fig. 3-8), and was attributed to the strong negative bias applied to the system, causing such strong depletion that inversion conditions were attained,[64,65,206,208] and therefore the surface of a p-type semiconductor behaved with n-type conductivity.[65] Indeed, the presence of the clathrochelate does not modify the potential range where inversion occurs in this semiconductor (compare Fig. 3-8 with Fig. 3-17).

3.2.4. Photoelectrochemical kinetics of the OER at the surface of Rh:$SrTiO_3$ – Ch photoelectrodes

The cobalt clathrochelates were found sufficiently stable from an electrochemical viewpoint to investigate their electrocatalytic activity towards the OER. The kinetics of the OER was studied following the same methodology described so far. The LSV curve of Fig. 3-14 b shows a notable overpotential for the OER, which is similar to what has been observed so far for Rh:$SrTiO_3$ based photoelectrodes under anodic polarization, whatever the surface modification. This fact permitted to draw the early conclusion that the surface of this semiconductor displays poor activity for the OER. The large

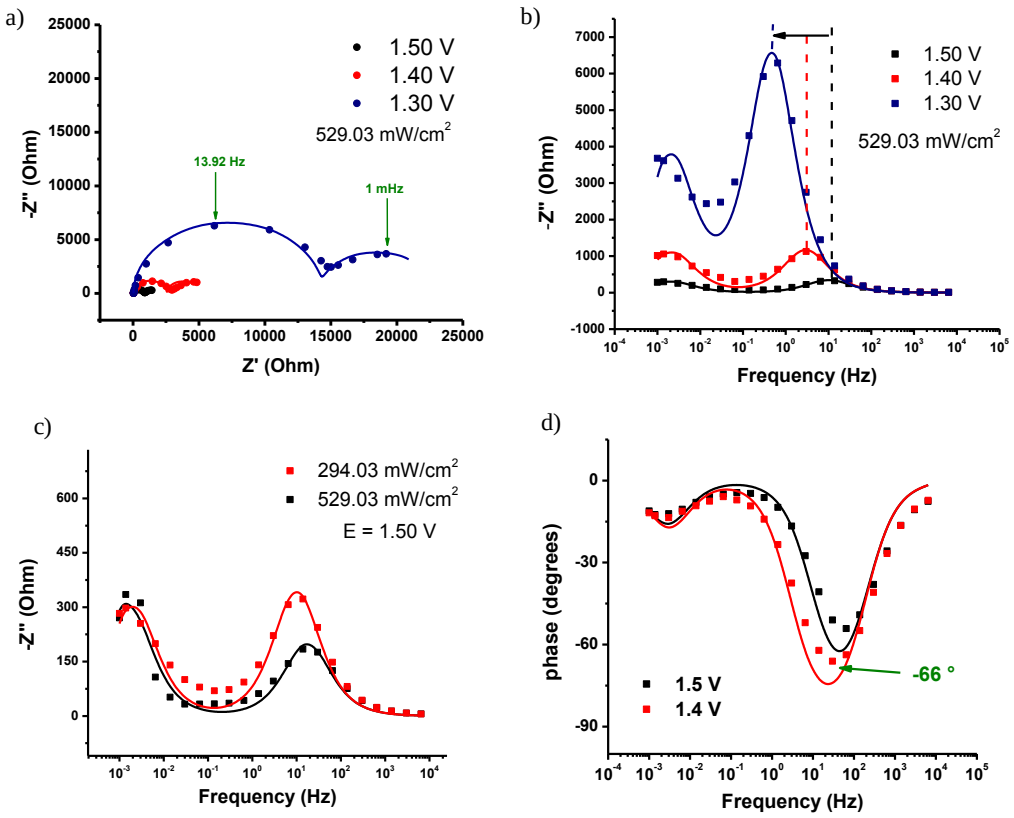

Fig. 3-18. Typical PEIS spectra for Rh:$SrTiO_3$-Ch under anodic polarization; a) Effect of light in the Nyquist representation; b) effect of electrode potential in the Bode plot of –Z"; c) effect of light intensity in the Bode representation of –Z".

overpotential indicates severe kinetic limitations for such reaction with this photoelectrode. Such presumption was confirmed by PEIS analysis, since the LF relaxation was found in the mHz frequency range, where the OER presented significant current densities (from +1.50 to +1.30 V vs. SCE, Fig. 3-18).

The effect of the electrode potential on PEIS spectra is better appreciated in the Bode representation of –Z''. Fig. 3-18 b shows that the frequency position of the LF relaxation does not change with applied bias, suggesting a constant value of k_t no matter the electrode potential. However, the electrode potential shifted the HF relaxation down to lower frequencies, an indication that the space charge capacitance is changing (Table within the annex section at the end of this thesis). Regarding the effect of light power on PEIS spectra, we found that the charge transfer and recombination rate constants were not affected by light intensity, as observed in the LF relaxation (Fig. 3-18 c). This may be due to the fact that, under accumulation conditions, the concentration of majority carriers, responsible for the charge transfer reactions, is not considerably affected by photoexcitation.

3.2.5. Surface characterization after photoelectrochemical testing

The observation that the electrochemical response was varying with the number of cycles under cathodic polarization was not surprising, because of the previous report mentioned above showing that, under strong cathodic polarization, clathrochelates can be decomposed into another active form of Co at the surface of the electrodes. In principle the evolution observed here under cathodic polarization could be due to the same fact. This observation confirms clathrochelates as versatile molecules that can act themselves as electrocatalysts,[126–128,139] or can be transformed into other active compounds under electrolysis conditions.[129] In the previous report on the

electrodeposition of Co clathrochelates, the authors did not determine the exact chemical nature of the electrodeposited active compound, but provided a clue by EDX analysis that the surface of their glassy carbon electrode, after electrodeposition, was containing Co, O and C.[129] We also performed some specific experiments to characterize the decomposition product of the clathrochelate. An XPS spectrum was recorded at the Co 2p core level before and after electrochemical testing (Fig. 3-19).

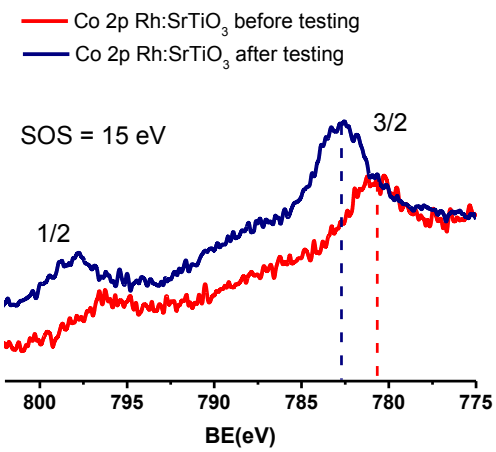

Fig. 3-19. XPS of the Co 2p core level of the photoelectrode Rh:$SrTiO_3$ – Ch, before (red) and after (blue) electrochemical testing.

First of all, the fact we were able to observe Co through the Nafion film at the surface indicates that this film was very thin, with a thickness of at most 10 nm. The intensity of the XPS spectra was found to be quite low, due to the blocking effect of Nafion and to the low loading of the catalyst. After electrochemical testing, it was found that the Co 2p signals shifted to higher binding energies, suggesting that Co was now present with a higher oxidation state, in agreement to a recent report.[211] Additionally, the shake-up satellites were still observed after electrochemical testing, suggesting that the Co species was still paramagnetic. We note that the electrodeposited species reported previously is not necessarily the same as the one we have encountered here.

3.3. Structural, chemical and morphological characterization of Rh:$SrTiO_3$ – Cu photoelectrodes

During this thesis, we also tried to improve the charge transfer kinetics by deposition of Cu and Pt at the surface of Rh:$SrTiO_3$. The same methodology was used to characterize the photoelectrode after the electrodeposition of Cu. A previous report on $SrTiO_3$ – Cu system revealed that the XRD pattern showed only reflections coming from the predominating semiconducting substrate which is due to the small catalyst loading.[212] Likewise, the SEM micrograph (Fig. 3-20) presented the same characteristics as all other micrographs presented so far, *i.e.*, the presence of important surface roughness, and the inability to reveal the presence of neither Nafion nor the Cu catalyst. For this material, SEM images before and after electrochemical testing were indistinguishable. Therefore, we decided that XPS would more likely be the appropriate technique to provide not only convincing proofs for the existence of Cu at the surface, but also to assess its chemical nature. Indeed, the presence of Cu at the surface of Rh:$SrTiO_3$ was undoubtedly put in evidence by XPS, since the Cu 2p signal was easily observed. XPS also provided a means to identify the chemical nature of copper at the surface, which was present in metallic form (Fig. 3-21). Certainly, a characteristic SOS of 19.9 eV, and

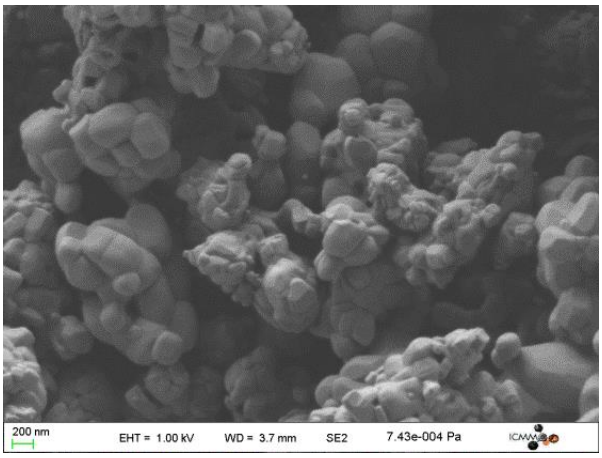

Fig. 3-20. SEM micrograph of the surface of a Rh:$SrTiO_3$ – Cu photoelectrode.

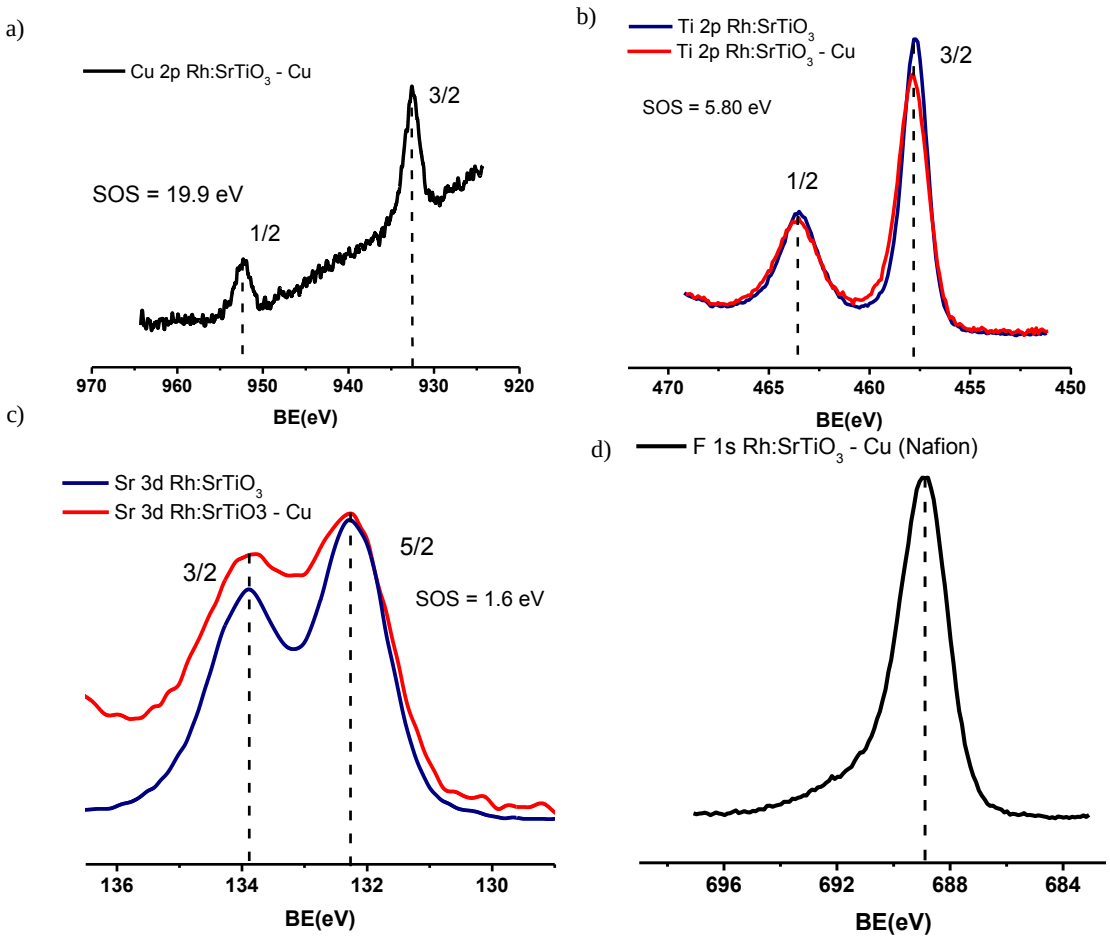

Fig. 3-21. a) XPS spectrum of Cu 2p in Rh:$SrTiO_3$ – Cu; b) comparison of the XPS spectrum of Ti 2p for Rh:$SrTiO_3$ and Rh:$SrTiO_3$ – Cu materials.

the position of Cu 2p 3/2 band at 932.7 eV were consistent with this. Another interesting feature revealed by XPS is that the Ti and Sr 3d signals did not vary much in the presence of the metallic catalyst, indicating that the electronic properties of the surface were essentially the same with and without the Cu catalyst. XPS allowed to make a semi-quantitative evaluation of catalyst loading at the surface, resulting in an atomic ratio Sr:Cu 87:13 at the surface. Additionally, the F 1s signal originating from the Nafion polymer at the surface is shown in Fig. 3-21 d. All photoelectrodes studied here presented this F 1s signal.

3.3.1. Photoelectrochemical characterization of Rh:$SrTiO_3$ – Cu photoelectrodes at open-circuit conditions

A plot of the photopotential vs. light intensity is provided in Fig. 3-22 a. The fact that the electrode potential increases as the light is made more intense indicates that surface modification with Cu does not change the p-type conductivity of this system. As was mentioned before, the fact that the photopotential does not appear to reach a plateau even at the highest LED intensities (529.03 mW/cm^2) indicates that flat-band conditions have not been attained. Nevertheless, it is possible to affirm that the flat-band potential for this system is somewhere above 0.28 V (vs. SCE).

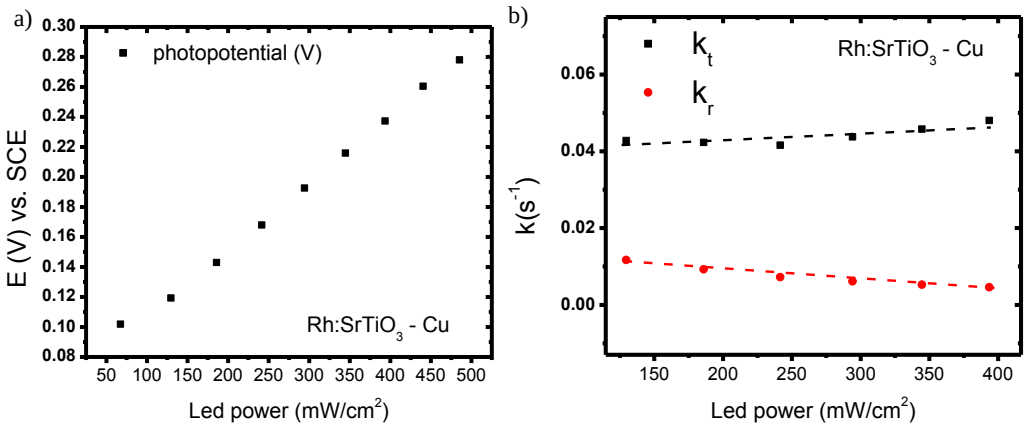

Fig. 3-22. a) Photopotential vs. LED power for the $SrTiO_3$ – Cu system; b) Kinetic parameters at open-circuit for the Rh:$SrTiO_3$ – Cu system.

Additionally, OCPD measurements gave access to the kinetics of charge transfer under open-circuit conditions.[73,74] The behavior is similar to those of other systems discussed so far: charge transfer and recombination rate constants are notably small and nearly independent of light power. For Rh:$SrTiO_3$ – Cu, k_t is around 0.04 s^{-1} and k_r is around 0.01 s^{-1}.

3.3.2. Current-potential characteristics of Rh:$SrTiO_3$ – Cu photoelectrodes

The LSV curve recorded on the Rh:$SrTiO_3$ – Cu photoelectrodes during the HER is shown in Fig. 3-23 a. The response obtained in the dark with pristine Rh:$SrTiO_3$ is also plotted for comparison purposes. As shall be observed in the next section for Rh:$SrTiO_3$ – Pt photoelectrodes, the dark current of Rh:$SrTiO_3$ – Cu differed from dark currents of pristine Rh:$SrTiO_3$, while the photocurrents displayed a similar value. The onset of cathodic currents under illumination occurs before the thermodynamic potential. As discussed before, this fact is due to the additional driving force supplied by photons, causing that the needed driving force for the HER is delivered at a lower electrode potential.[8]

The Rh:$SrTiO_3$ – Cu photoelectrode exhibited an unusually high value of Tafel Slope (202 mV/dec) for the HER (Fig. 3-23 c). Such value is not consistent with current theoretical models, and therefore we do not propose a rds for the HER in this case.

The electrochemical behavior of Rh:$SrTiO_3$ – Cu photoelectrodes at positive potentials is shown in Fig. 3-23 b. The electrocatalytic effect of 100 mV brought by the presence of Cu at the surface of the photoelectrode is observed. Nevertheless, the OER still requires a high overpotential on this system. This is the indication of a slow charge transfer kinetics despite the electrocatalytic effect of Cu. Using this photoelectrode, no photocurrent was detected in the potential ranging from 0.0 V to +1.5 V (vs. SCE). Such behavior can be considered as normal for a p-type semiconductor under forward bias.

The Tafel slope for Rh:$SrTiO_3$ – Cu photoelectrodes towards the OER was determined to be 73 mV/dec (Fig. 3-23 d), which is close to the value determined for the Rh:$SrTiO_3$ – Ch system, and could be due to a rds represented by the reaction $M - O = M + 1/2O_2$ (eq. 1-25) when and $\theta_O \approx 0$ and $\theta_{OH} \approx 1$.[87]

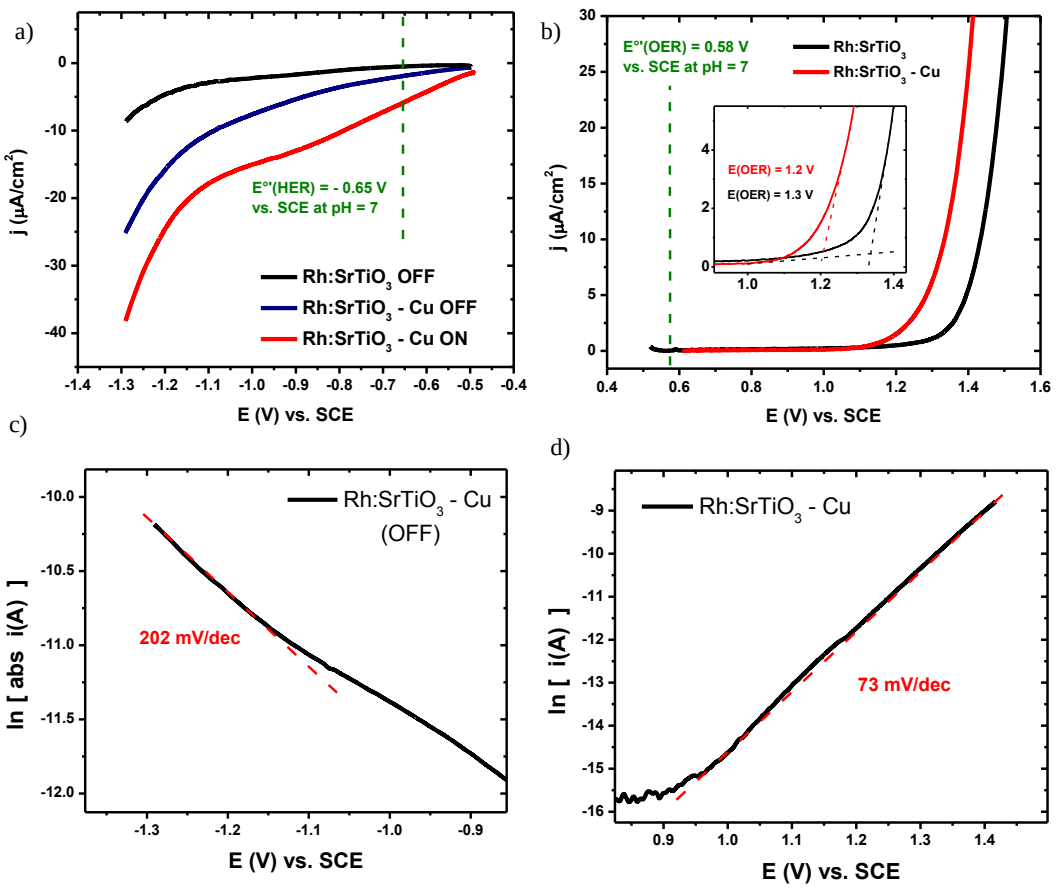

Fig. 3-23. Polarization curve of Rh:$SrTiO_3$ – Cu photoelectrodes for a) the hydrogen evolution reaction without and with (529.03 mW/cm^2) illumination b) the oxygen evolution reaction, no photocurrents were observed. Scan rate = 1 mV/s; c) Tafel plot for the HER; d) Tafel plot for the OER.

3.3.3. Photoelectrochemical kinetics of the HER at the surface of Rh:$SrTiO_3$ – Cu photoelectrodes

Following the same methodology, the evaluation of the heterogeneous kinetics of the HER using Rh:$SrTiO_3$-Cu was performed by PEIS analysis [66,71,72,115] at different light intensities and electrode potentials.

Fig. 3-24 a shows that the HF relaxation constant shrinks upon light power increase. However, the LF relaxation constant clearly expands as light is made more intense, indicating that the recombination rate constant k_r shows a slight tendency to increase under stronger illumination. Such trend is consistent with the increase of the electron

concentration at the surface according to eq. 3-2. As a result, an important amount of the potential drop probably appears in the Helmholtz layer (Fermi level pinning).[66,67,71]

$$k_r = k_r^0 \exp\left(\frac{-\beta q \phi_{sc}}{kT}\right) \qquad (3\text{-}2)$$

Where k represents Boltzman's constant, T is the absolute temperature, q is the elemental charge, ϕ_{sc} is the potential drop in the space charge, and β is an empirical parameter related to surface non-ideality caused by Fermi level pinning. In this context, k_r is treated as a pseudo first order rate constant.

The potential dependence of the recombination rate constant depends on the non-ideality factor (referred here to as β), while the potential dependence of the charge transfer rate constant depends on the transfer coefficient (herein referred to as α). This nomenclature is usual in published research.[115,213,214] It should be noted here that there is a dispersion of the parameter's nomenclature in published literature; hence, the electrochemical literature can be confusing, because these two letters (α and β) have been sometimes exchanged to refer to the opposite parameter.[67,71]

Returning to the qualitative analysis of PEIS spectra, Fig. 3-25 c clearly shows that k_t increased as the potential was made more negative because the maximum of the LF semicircle increased. This can be attributed to a direct consequence of Fermi level pinning due to the presence of surface states. Conversely, Fig. 3-24 c demonstrates that k_t was independent of light intensity.

The kinetics of Rh:$SrTiO_3$-Cu photoelectrodes is much richer than that of either Rh:$SrTiO_3$ or Rh:$SrTiO_3$ – Ch. Therefore, a detailed analysis of the dependence of each kinetic parameter upon electrode potential and light intensity is represented better by the three-dimensional plots of Fig. 3-25. Fig. 3-25 a shows the variation of the space charge capacitance as a function of applied potential and light intensity. Though, the phase angle for the HF relaxation constant is considerably low (-54°), and therefore the capacitance values derived here ought to contain contributions form surface states, surface roughness, and from the Nafion film on top of the photoelectrode. Nevertheless, a qualitative discussion can be undertaken. Fig. 3-25 a depicts that increasing light power caused a decrease in the space charge capacitance C_{sc}. Indeed, as light increases,

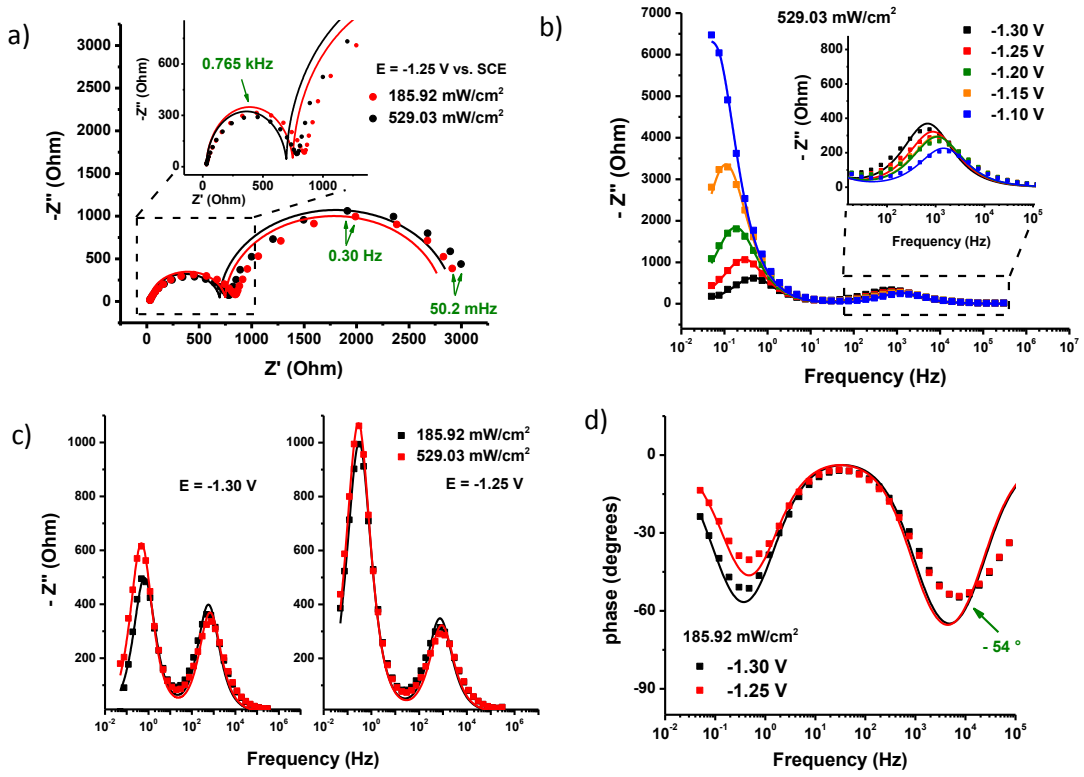

Fig. 3-24. Typical PEIS spectra for Rh:$SrTiO_3$-Cu a) Effect of light in the Nyquist representation; b) effect of electrode potential in the Bode plot of –Z"; c) effect of light intensity in the Bode representation of –Z"; d) Bode representation of the phase angle.

more electrons go to the surface while the holes remaining inside the material create an opposing electric field that continually reduces the band bending (ϕ_{sc}). According to eq. 3-3, such fact would increase C_{sc}

$$C_{sc} = \frac{dQ_{sc}}{d\phi_{sc}} \qquad (3\text{-}3)$$

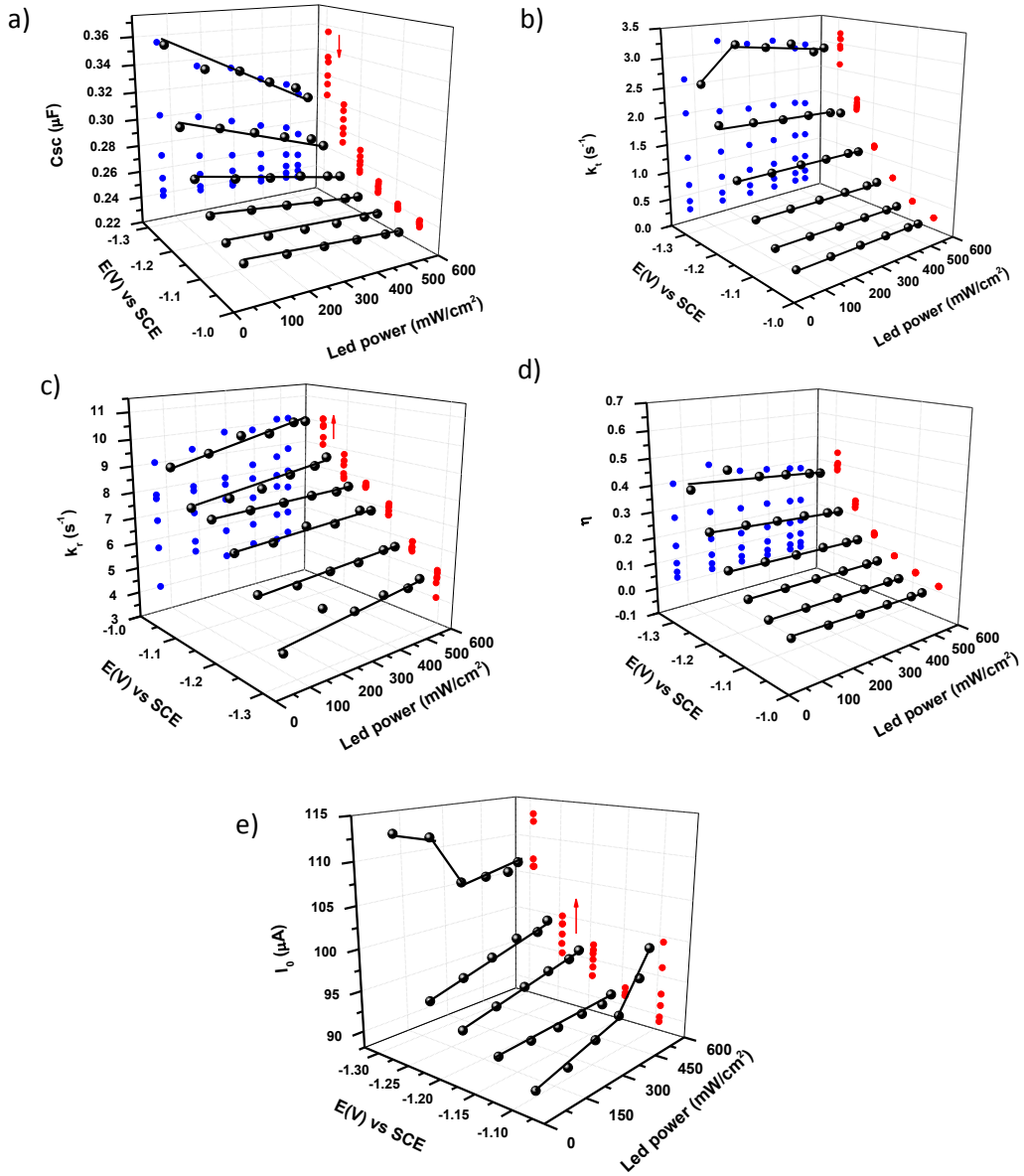

Fig. 3-25. Relevant kinetic parameters of Rh:$SrTiO_3$-Cu towards the HER, at various electrode potentials and light intensities; a) space-charge capacitance C_{sc}; b) charge transfer rate constant k_t; c) recombination rate constant k_r; d) efficiency of minority carrier transfer at the photoelectrode.

Though, as light intensity increases, the electrons to migrate towards the surface and the holes move towards the bulk (where no electric field exists), the net charge in the space charge region (Q_{sc}) diminishes as well, which appears to be the dominating factor to explain the observed trend in C_{sc} with increasing light intensity.

Further analysis of the behavior of the space charge capacitance can be obtained from a Mott-Schottky plot. As it was commented before, a plot of C_{sc}^{-2} vs. E should give a straight line with negative slope (for a p-type semiconductor) under depletion conditions. Such a prediction contrasts with the experimental Mott-Schottky plot (Fig. 3-26 a). As already discussed above, the p-nature of Rh:$SrTiO_3$ – Cu was confirmed by OCPD measurements, in addition to the observed photocurrents under negative bias, and the absence of measured photocurrent under positive polarization. The origin of such a positive slope in the Mott-Schottky plot, in the potential range between -1.30 V to -1.10 V (vs. SCE) is attributed to the strong polarization applied to the electrode, that allowed to reach inversion conditions,[64,65,206,208] where the bulk of the material behaves as a p-type semiconductor while the surface as a n-type character.[65]

As mentioned before, for an ideal semiconductor-electrolyte junction, the whole of the applied potential drops in the space charge and there is almost no potential drop in the Helmholtz layer, therefore, k_t is independent of the electrode potential.[205] However, in this case, we observed a decrease of k_t as the electrode potential was made more positive, indicating that the photoelectrode did not behave ideally and that there is a potential drop in the Helmholtz layer that influences the rate of charge transfer. Assuming that the Tafel equation describes the HER reaction (eq. 3-4)[67]

$$k_t = k_t^0 \exp(\frac{\alpha q \phi_H}{kT}) \qquad (3\text{-}4)$$

Where α is the transfer coefficient and ϕ_H is the potential drop in the Hemholtz layer, and considering that the applied potential is the sum of the drops in the space charge and the Helmhotz layer (eq. 3-5)

$$V = \phi_H + \phi_{sc} \qquad (3\text{-}5)$$

a plot of the logarithm of k_t and k_r vs. applied bias should give a straight line, which is in excellent agreement with our experimental results (Fig. 3-26 b). From a mechanistic perspective, the slope of the plot of $\ln k_t$ vs V gives the charge transfer coefficient for the HER as determined to be $\alpha = 0.28$ in this material.

On the other hand, the slope of the plot of the logarithm of k_r vs. E gives a measure of β. For an ideal semiconductor|electrolyte junction β = 1, and departure of this ideal value is related to the presence of surface states, and their influence in the potential distribution across the interface. In some recent literature, such non-ideality factor was just ignored and PEIS spectra were fitted and analyzed without considering this effect, even though the presence of surface states is established through the dependence of rate constants upon the applied potential.[66,215] However, there are some other publications where this parameter is effectively determined.[115,214] Values of β have been determined for TiO_2 plane (011) and plane (100) to be 0.11 and 0.21,[214] and for CdS values ranging from 0.43 to 0.67 have been determined,[115] with a clear dependence on the nature of the semiconductor|electrolyte interface. It is interesting indeed to see how the same authors can neglect this non-ideality factor [66,215] after having considered and determined it more than a decade before.[115] Perhaps the origin of this was expressed by the authors, who established that their publication[66] was devoted to a phenomenological analysis only.

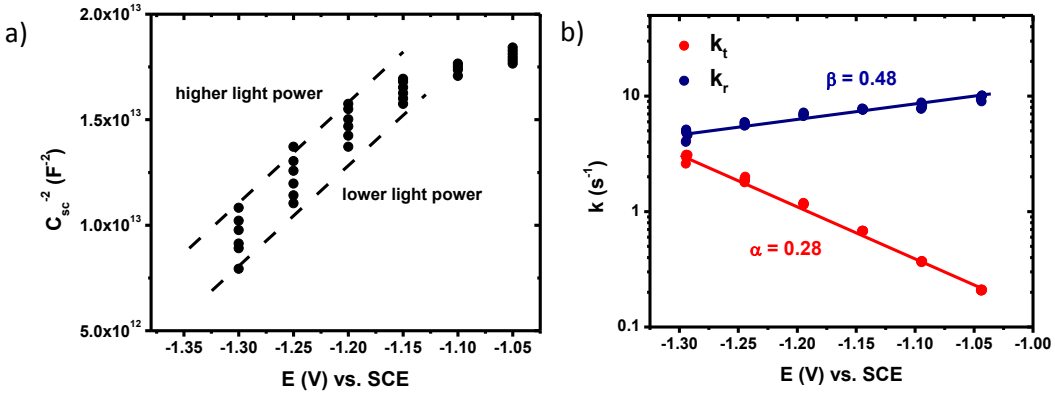

Fig. 3-26. a) Mott-Schottky plot for the Rh:$SrTiO_3$ – Cu photoelectrode; b) Tafel plot for charge transfer (red) and recombination rate constants (blue) for Rh:$SrTiO_3$ – Cu photoelectrodes.

In the case of Rh:$SrTiO_3$ – Cu photoelectrodes, we found that $\beta = 0.48$, indicating that this junction behaved non-ideally.

Fig. 3-25 d shows the dependence of the efficiency in the transfer of photoexcited electrons through the interface upon light intensity and electrode potential. We observed the loss in efficiency as the electrode potential became more positive, due to an increase in the rate of recombination and the decrease in the rate of charge transfer. Such behavior is consistent with previous determinations in other photoelectrocatalytic systems.[71] The fitted results of PEIS spectra, used to construct Fig. 3-25 a to e are reported in Table (within the annex section at the end of this thesis).

3.3.4. Photoelectrochemical kinetics of the OER at the surface of Rh:$SrTiO_3$ – Cu photoelectrodes

The kinetic parameters and interfacial capacitances of Rh:$SrTiO_3$ – Cu photoelectrodes during the OER were determined by PEIS analysis.[66,67,71] Typical PEIS spectra are reported in Fig. 3-27. The Rh.$SrTiO_3$ – Cu system displays the two characteristic relaxation constants that have already been discussed for Rh:$SrTiO_3$ and Rh:$SrTiO_3$ –

Ch. The qualitative effect of electrode potential on the OER kinetics is better appreciated by considering the –Z imaginary part of the spectra in the Bode representation (Fig. 3-27 b). It can be seen that the charge transfer rate constant is potential independent and has the same value as determined before for pristine Rh:$SrTiO_3$ and Rh:$SrTiO_3$ – Ch. The kinetics of water oxidation at the surface of any of these photoelectrodes is significantly slow: the characteristic frequency of the LF semicircle is found in the mHz range and the necessary overpotential that was observed by LSV analysis for this system is large (Fig. 3-23 b).

The effect of light intensity on PEIS spectra is shown in Fig. 3-27: there is a contraction of the HF semicircle while the LF semicircle remains virtually unaffected (Fig. 3-27).

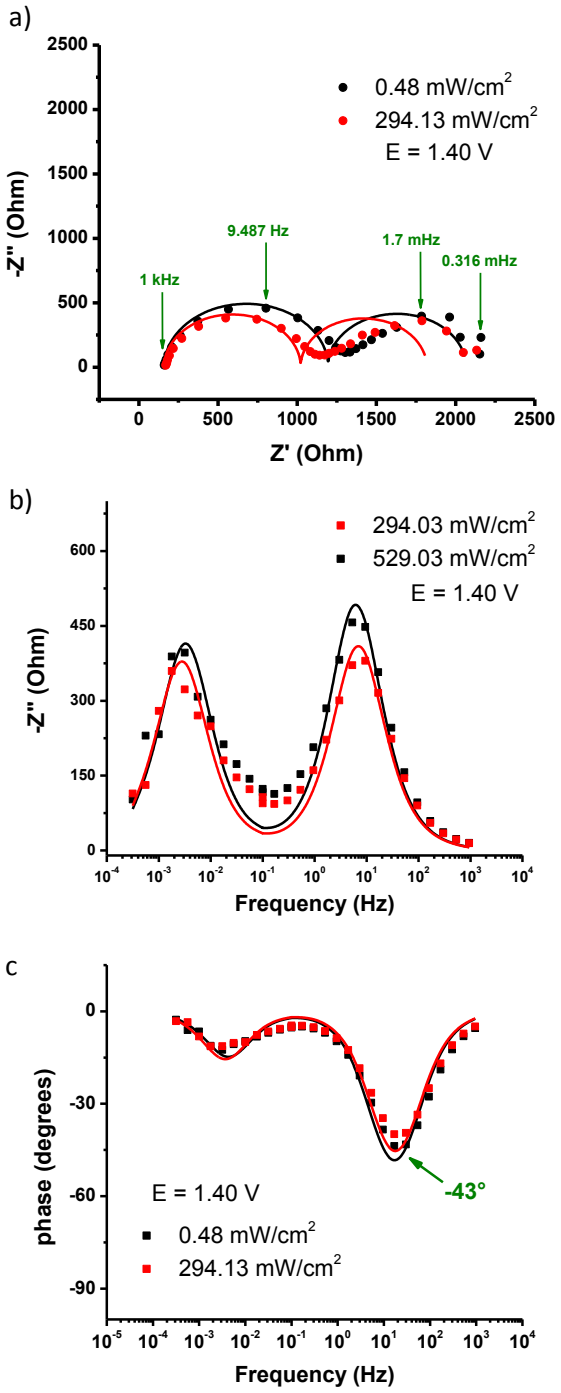

Fig. 3-27. Typical PEIS spectra for Rh:$SrTiO_3$-Cu a) Effect of light in the Nyquist representation; b) effect of electrode potential in the Bode plot of –Z"; c) effect of light intensity in the Bode representation of –Z".

Fitting results of PEIS spectra are compiled in Table (within the annex section at the end of this thesis).

The kinetic information was determined by fitting PEIS spectra. Results (Fig. 3-27 a to c) show the effect of applied potential and illumination level. Fig. 3-27 a shows the the capacitance associated to the HF semi-circle for two different light power values at constant electrode potential. The physical meaning of the capacitance associated to the HF relaxation must be discussed carefully because the phase angle (-43°) is far away from the (-90°) value expected for a pure capacitance (Fig. 3-27 c). The capacitance of the HF relaxation can be considered as a true interfacial capacitance for phase angles between -90° and -80°. This is obviously not the case for this system. As discussed above, the capacitances experimentally determined contain contributions from surface roughness, surface states and the Nafion polymer.

3.4. Structural, chemical and morphological characterization of the Rh:$SrTiO_3$ – Pt photoelectrodes

Measurements on the HER and OER at Rh:$SrTiO_3$ – Pt photoelectrodes have also been made. Following the same characterization methodology employed so far, we have obtained the XRD pattern of the material. The XRD pattern of the Rh:$SrTiO_3$ – Pt powder was found indistinguishable from pristine Rh:$SrTiO_3$. Fig. 3-28 shows that main diffraction peaks correspond to reflections coming from the typical perovskite structure of $SrTiO_3$ that was already discussed. The most likely explanation for not observing any diffraction peak from Pt is the relatively low loading of the surface co-catalyst.

Likewise, the SEM image revealed no differences with that of pristine Rh:$SrTiO_3$, indicating that surface loading of platinum does not change the morphology of the semiconductor (Fig. 3-4 b) which was not a surprise. These two observations have been reported before in similar photoelectrocatalytic systems.[212]

XPS analysis has proven to be sensitive enough to put in evidence relatively small amounts of catalysts. For the Rh:$SrTiO_3$ – Pt solid, the XPS spectrum of Pt 4f is shown in Fig. 3-29 c, displaying an asymmetric shape which is characteristic of metallic Pt.[216]

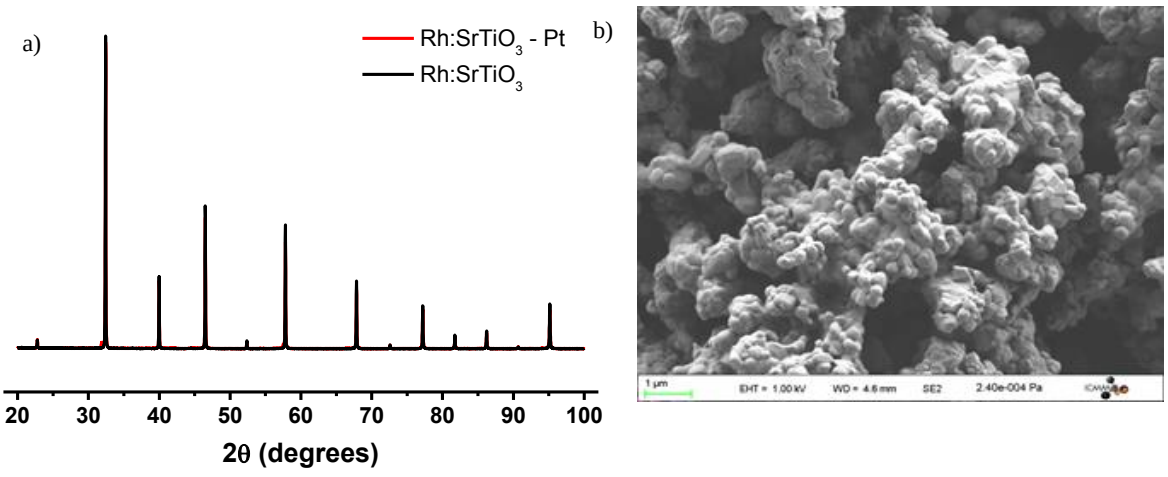

Fig. 3-28. a) Comparison of the XRD pattern for Rh:$SrTiO_3$ and Rh:$SrTiO_3$ – Pt materials; b) SEM micrograph of the surface of a Rh:$SrTiO_3$ – Pt photoelectrode.

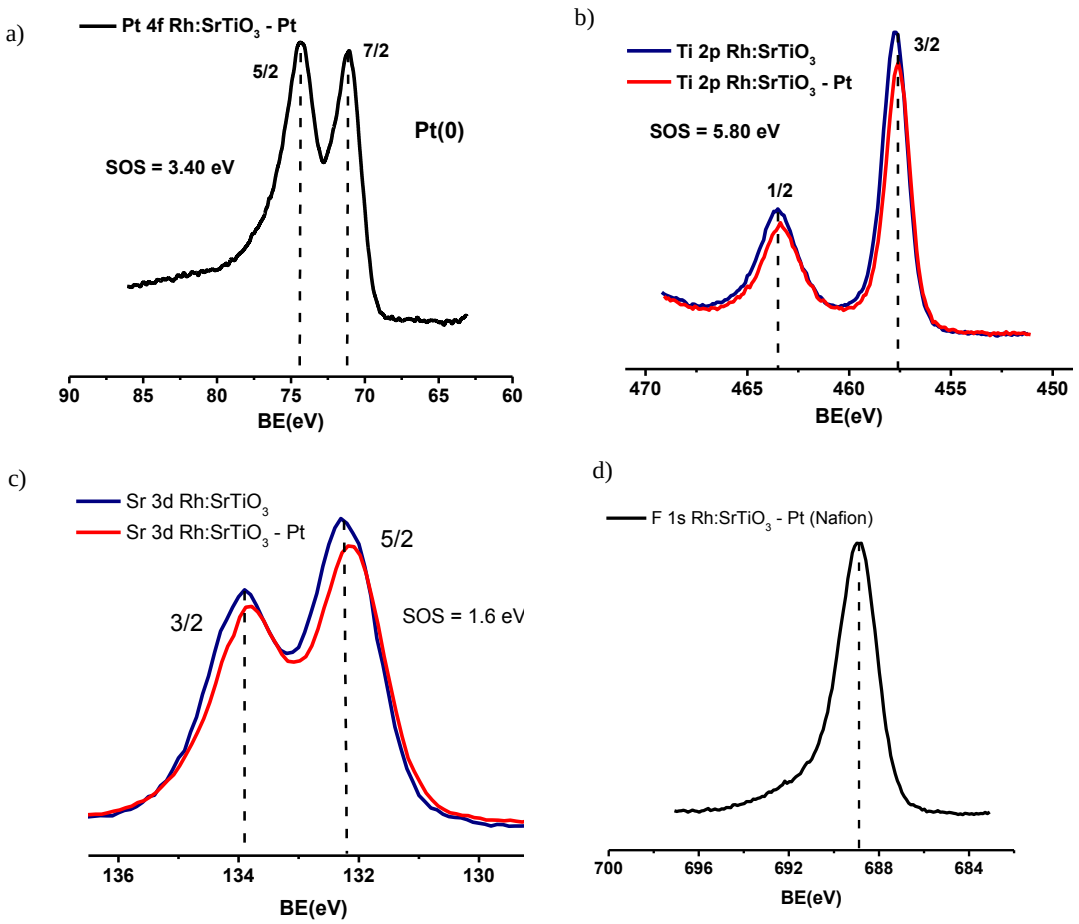

Fig. 3-29. a) XPS spectrum of Pt 4f in Rh:$SrTiO_3$ – Pt; b) comparison of the XPS spectrum of Ti 2p for Rh:$SrTiO_3$ and Rh:$SrTiO_3$ – Pt materials.

Moreover, the binding energy of the Pt 4f 7/2, found at 71 eV, and the spin-orbit splitting (SOS) of 3.4 eV undoubtedly confirm that Pt was present at the surface in metallic form.[216] Fig. 3-28 b and c show the Ti 2p and Sr 3d doublets, with and without the presence of Pt. The spectrum of the semiconducting support was almost the same in both cases, indicating that the presence of the Pt catalyst did not change appreciably the chemical nature of the semiconducting surface. Moreover, semiquantitative evaluation of the surface composition revealed a Sr:Pt ratio around 90:10.

3.4.1. Photoelectrochemical characteristics of Rh:$SrTiO_3$ – Pt photoelectrodes at open-circuit

The first photoelectrochemical experiment performed on the Rh:$SrTiO_3$ – Pt photoelectrodes was to illuminate and to observe the increase of the electrode potential (Fig. 3-30 a). The trend observed with Rh:$SrTiO_3$ – Pt is similar to what was observed for the different photoelectrodes tested so far. This is the indication that the material kept its p-type conductivity with the presence of Pt at the surface. The photopotential was around 1 V, which was the largest value obtained for all the materials studied in this work.

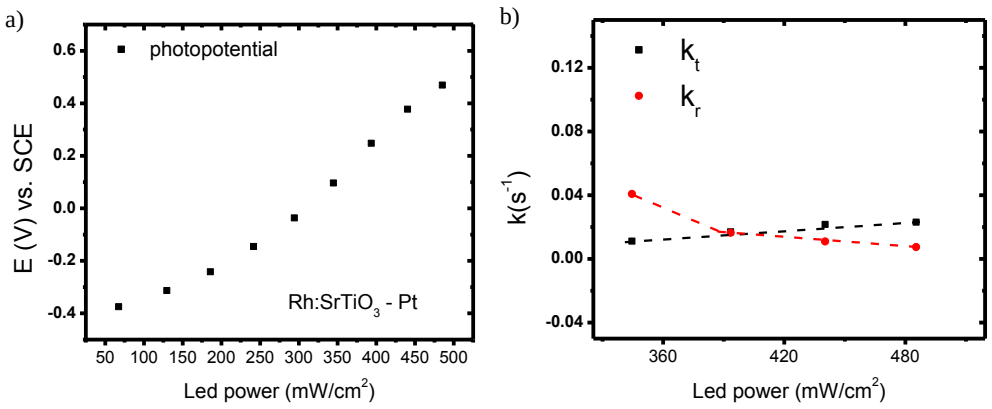

Fig. 3-30. a) Photopotential vs. led power for the system Rh:$SrTiO_3$ – Pt b) Kinetic parameters for Rh:$SrTiO_3$ – Pt in open-circuit conditions. Dashed lines have been put as a guide to the eye.

Photoelectrochemical kinetic studies performed under open circuit conditions[73,74] revealed that the charge transfer and recombination rate constants displayed similar values and were nearly independent of light intensity. Fig. 3-30 b might induce the thought that k_t increases linearly with light power, while k_r decreases. However, the variations are so small that it is not possible to affirm the existence of a true dependence of kinetic parameters upon illumination intensity.

3.4.2. Current potential characteristics of Rh:$SrTiO_3$ – Pt photoelectrodes

The current-potential curves were then recorded on the Rh:$SrTiO_3$ – Pt photoelectrodes (Fig. 3-31 a and b). The responses obtained for Rh:$SrTiO_3$ in the dark is given as well for comparison. Under cathodic polarization, an enormous electrocatalytic effect is brought to the photoelectrode by small amounts of Pt. The cathodic current is overwhelmingly dominated by the dark contribution, while the photocurrent displayed the same modest value as for the Rh:$SrTiO_3$ photoelectrode (Fig. 3-6 a). This observation suggests that Pt at the surface of the photoelectrode acts as an electrocatalyst but does not contribute to light-induced processes. Indeed, it is likely that under illumination there are probably two coexisting HER mechanisms, one caused by

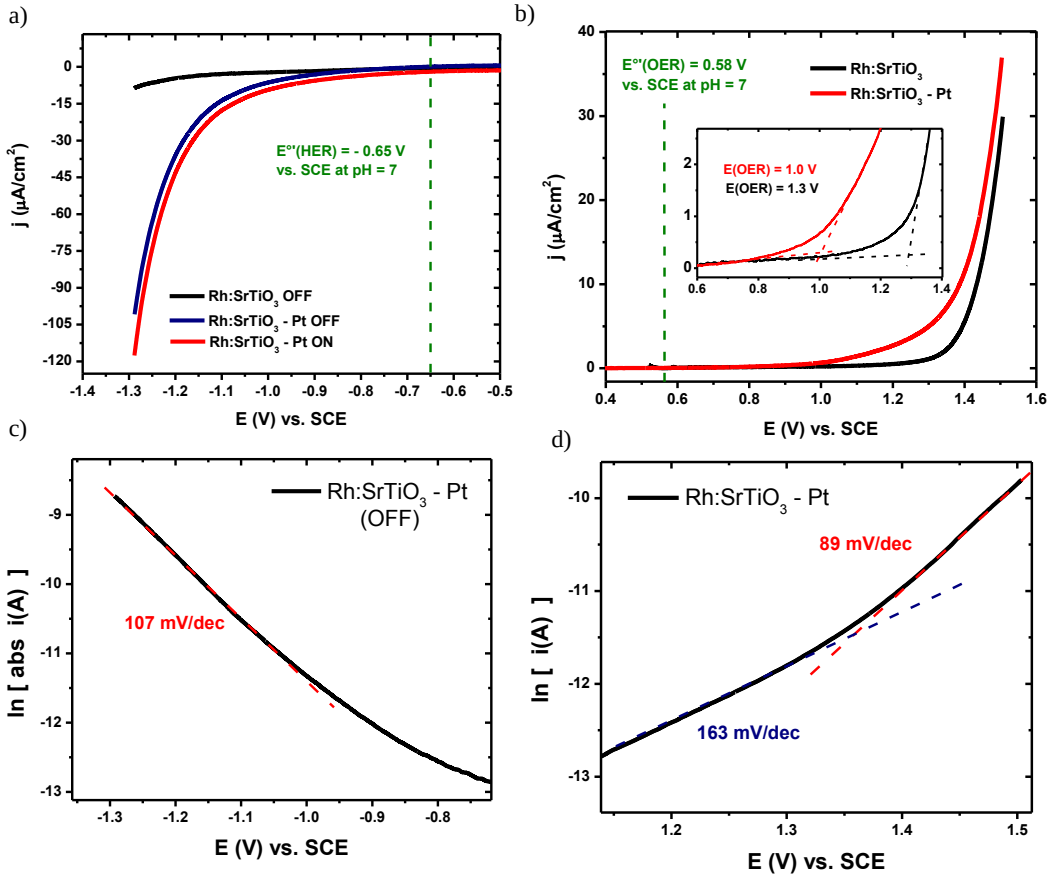

Fig. 3-31. Polarization curves measured on Rh:$SrTiO_3$ – Pt photoelectrodes for a) the hydrogen evolution reaction without and with (529.03 mW/cm^2) illumination b) the oxygen evolution reaction (no photocurrents were observed). Scan rate = 1 mV/s; c) Tafel plot for the HER; d) Tafel plot for the OER.

the Pt particles operating even in the dark, and another one caused by photon absorption by the semiconductor.

The Tafel plot of the HER on the Rh:$SrTiO_3$ – Pt system is shown in Fig. 3-31 c. The Tafel slope of 107 mV/dec is close to 120 mV/dec, again suggesting that either the Volmer step, or the Heyrovsky step (in the region of high surface density of adsorbed H) are possible rds in the multistep mechanism.[81]

Conversely, the LSV curve in the anodic region is depicted in Fig. 3-31 b. As it was observed for Rh:$SrTiO_3$, dark and illuminated contributions were identical, which is the usual behavior of p-type semiconductors under anodic bias. Fig. 3-31 b allows appreciating that the presence of Pt at the surface also catalyzes the OER, since the onset of the OER decreases from +1.3 V on pristine Rh:$SrTiO_3$ down to +1.0 V on Rh:$SrTiO_3$ – Pt. However, even with Pt, the OER overpotential is still important, indicating a sluggish electron transfer rate.

The Tafel plot of the OER clearly presents two different slopes (Fig. 3-31 d): a slope of 89 mV/dec beyond +1.4 V (vs. SCE) and a slope of 163 mV/dec before +1.3 V (vs. SCE). Such dual behavior indicates that the mechanism of the OER switches from low to high applied overpotentials. However, published models concerning the OER do not predict Tafel slopes greater than 120 mV/dec.[81,87,88] Considering this, the Tafel analysis for current-potential curves obtained for Rh:$SrTiO_3$ – Pt photoelectrodes towards the OER shall not be further performed. Suffice it to say that a dual Tafel slope suggests the coexistence of two mechanisms running in parallel, as supposed for the HER. Evidently, nowadays models for the OER are still limited and require further improvements. The cause behind the discrepancies between observed and predicted Tafel slopes might be that the surface is likely to present different sites with distinct reactivity, in contrast to model assumptions.[81,87,88] In the case of semiconducting photoelectrodes, another cause

could be that a fraction of the applied potential falls in the space charge region[66] thereby justifying a weaker potential dependence of the current density.

3.4.3. Photoelectrochemical kinetics of the HER at Rh:$SrTiO_3$ – Pt photoelectrodes

The electrochemical HER kinetics on Rh:$SrTiO_3$ – Pt was also studied by PEIS analysis and interpreted with the same kinetic model used so far.[66,67,71,115] Typical Nyquist plots recorded between -1.30 V and -1.10 V (vs. SCE) are shown in Fig. 3-32 a. For this system, the two characteristic semi-circles were clearly resolved. Fig. 3-32 a and b show that the HF time constant was nearly independent of the electrode potential, which is typical of photoelectrodes presenting Fermi level pinning.[12] Fermi level pinning can be qualitatively assessed by the fact that the maximum of the LF relaxation depended on the applied potential (Fig. 3-32 b, highlighted with dashed lines). It was also found that the recombination rate constant increased as the applied potential was made less negative, because the LF relaxation tends to expand.

For this system, light had virtually no effect on any of the kinetic parameters, as observed in Fig. 3-32 c. This is perhaps due to the strong contribution of dark currents to the overall response. As a final comment for the qualitative interpretation of PEIS spectra, it may be seen that the phase of the HF relaxation is never larger than -55°. Again, this is the indication that the fitted capacitance associated to this relaxation should not be considered as a pure capacitance, where the phase angle should be preferably – 80 ° (or even closer to the ideal – 90°).[202]

As a consequence, the discussion of the space charge capacitance that follows should be considered carefully, because, as expressed before, the HF relaxation should contain contributions not only from the space charge capacitance, but also from surface

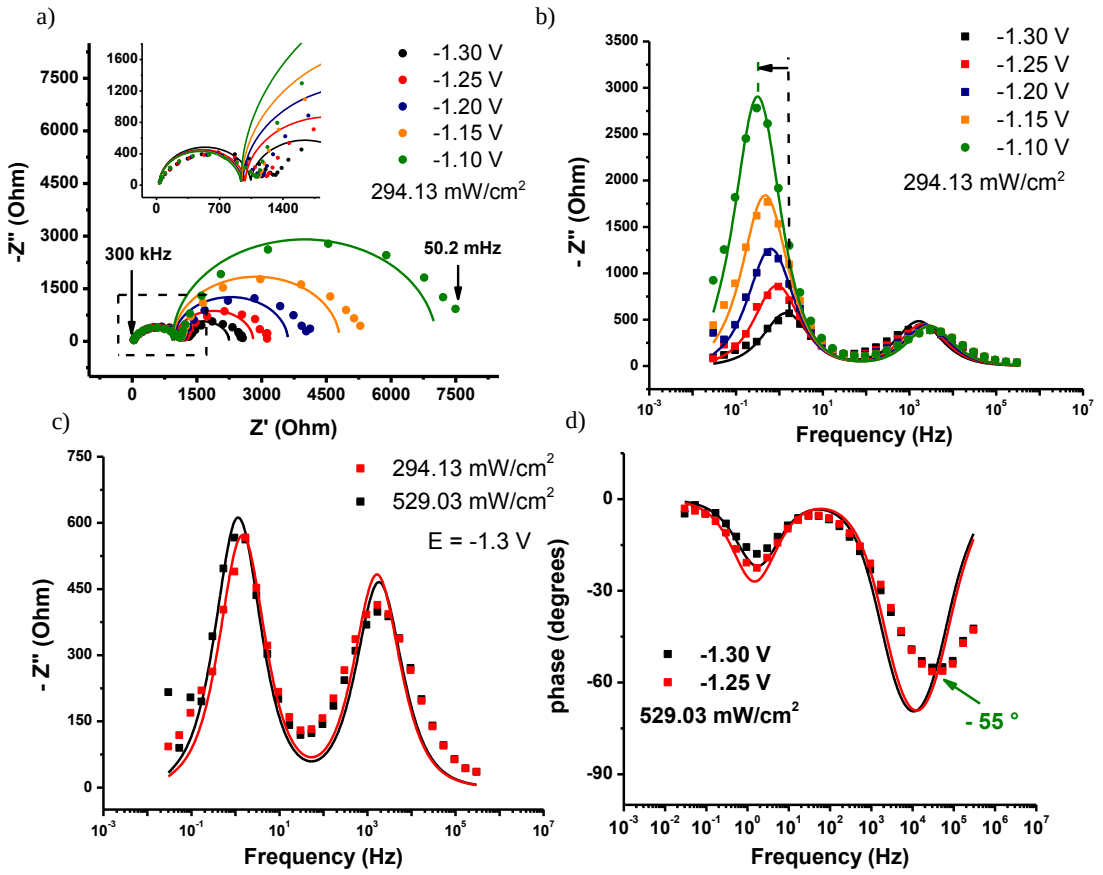

Fig. 3-32. Photoelectrochemical impedance spectroscopy for Rh:$SrTiO_3$ – Pt under cathodic polarization a) Effect of electrode potential on Nyquist representation) b) effect of the electrode potential on the Bode representation of –Z"; c) effect of light intensity on the Bode representation of –Z";d) Bode representation of the phase angle.

roughness and the polymeric Nafion as well.

Fig. 3-33 a to d show the kinetic parameters obtained for this system by fitting experimental PEIS spectra. The evolution of the space charge capacitance, despite the issues discussed in the previous paragraph, presents a linear tendency when plotted in Mott-Schottky manner (Fig. 3-34 a). Again, the positive slope of this graph is in contrast with the p nature of the semiconductor. The origin of this fact has already been discussed in this Chapter for Rh:$SrTiO_3$, Rh:$SrTiO_3$ – Ch and Rh:$SrTiO_3$ – Cu photoelectrodes, and is attributed again to the inversion of the semiconductor due to the high applied driving force,[64,65,208] that makes that the semiconductor behaves as a p-type in the bulk and as a n-type at the surface.[65]

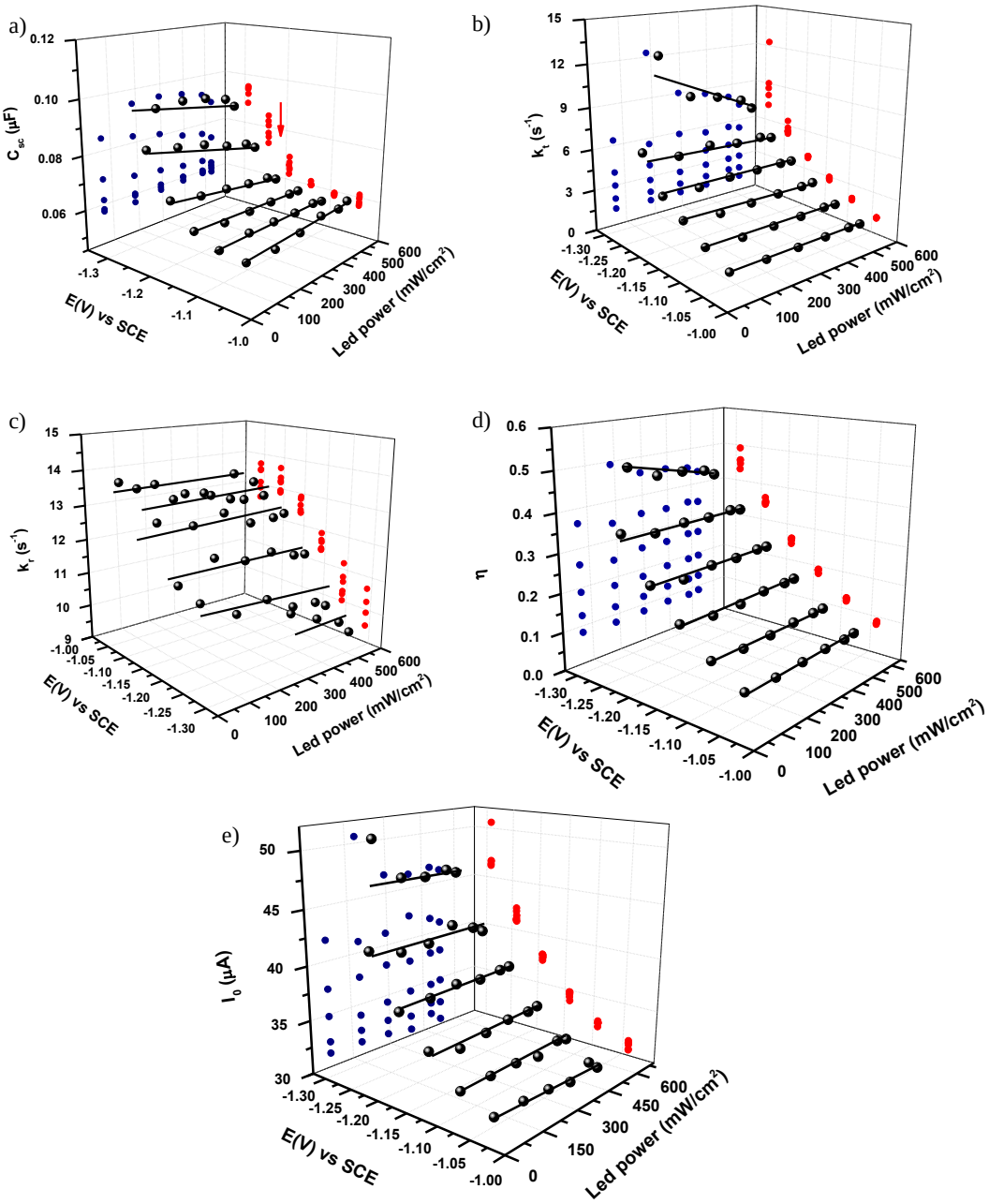

Fig. 3-33. Kinetic parameters for Rh:$SrTiO_3$ – Pt a) Space charge capacitance b) charge transfer rate constant c) recombination rate constant d) fraction of transferred electrons across the interface; d) photogenerated flux of minority carriers.

Fig. 3-34 b shows the evolution of the charge transfer rate constant vs. applied potential and LED power. The recombination rate constant (k_r) increases monotonically as the electrode potential is made more negative. The origin of this behavior was already discussed for Rh:$SrTiO_3$ – Cu photoelectrodes and is consistent with eq. 3-4. This is due

to the presence of surface states which pin the Fermi level. On the other hand, Fig. 3-33 c shows the evolution of the recombination rate constant, which decreases slightly as the electrode potential is made more negative (observe that the potential axis in Fig. 3-33 c has been inversed for the sake of clarity): this is consistent with eq. 3-2. The effect of electrode potential on rate parameters is opposed, *i.e.*, k_t increases when k_r decreases, which is a usual behavior for photoelectrodes displaying Fermi level pinning. The increasing value of k_t when the applied potential is made more negative is related to the increasing driving force in the Helmholtz layer, while the decreasing value of k_r with more negative potential is associated to a decrease of the surface concentration of majority carriers. Therefore, the efficiency of the transfer of photoexcited electrons in this photoelectrode increased with band bending, and attained a value close to 50% at -1.30 V (vs. SCE).

Both k_r and k_t are shown in a Tafel plot in Fig. 3-34 b. As already discussed, the linear relationship observed on this Tafel plot is expected from theory,[67] but the mechanistic complexity of multistep charge transfer during the HER and the presence of surface states can cause the potential dependence of kinetic constants to be quite odd in frequent cases.[66,215]

For the Rh:$SrTiO_3$ – Pt photoelectrode, the slope of $\ln(k_t)$ vs. E provided a Butler-Volmer transfer coefficient of $\alpha = 0.21$, in reasonable agreement with the Rh:$SrTiO_3$ – Cu material. On the other hand, the slope of the $\ln(k_r)$ vs. E plot gave a very low value for the ideality factor ($\beta = 0.04$). This value indicates that the presence of Pt at the surface makes the photoelectrode highly non-ideal, suggesting a very high density of surface states with the concomitant Fermi level pinning. Apparently, the highly non-ideal behavior of the interface can be a consequence of the important dark current baseline of the LSV (Fig. 3-31 a), which dominates the current-potential characteristics

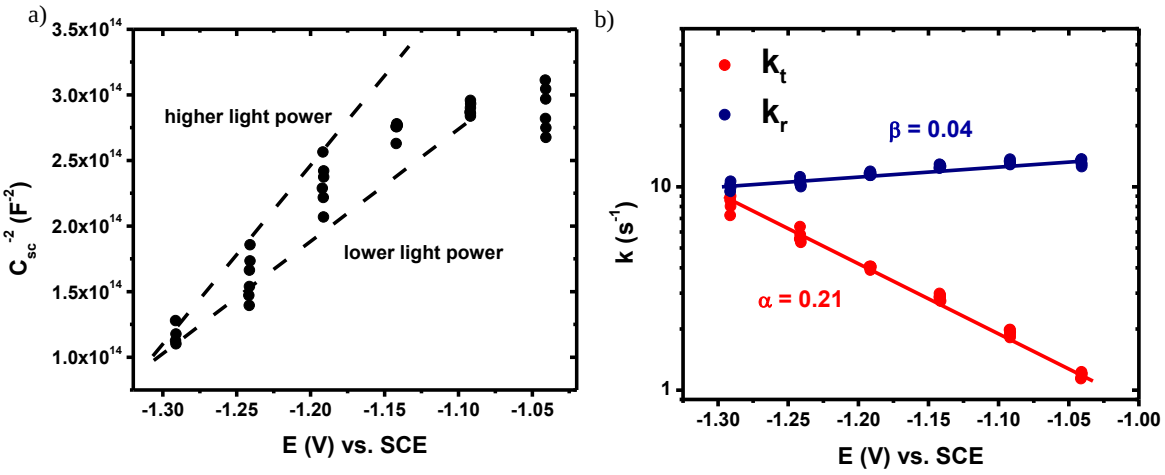

Fig. 3-34. a) Mott-Schottky plot for Rh:$SrTiO_3$ – Pt; .b) Tafel plot of k_t and k_r for the Rh:$SrTiO_3$ – Pt photoelectrode.

of the photoelectrode, while the photocurrent is quite small compared to such background current in the dark, and hence the negligible effect of light on PEIS spectra (Fig. 3-32).

The kinetic parameters obtained after the fitting of PEIS spectra for Rh:$SrTiO_3$ – Pt under cathodic polarization are compiled in Table , within the annex section at the end of this thesis.

3.4.4. Photoelectrochemical kinetics of the OER at Rh:$SrTiO_3$ – Pt photoelectrodes

In the next step, the kinetic characterization of Rh:$SrTiO_3$ – Pt photoelectrodes was performed under anodic polarization. The same methodology employed so far is used again because semiconductor electrodes, no matter whether they are either under depletion conditions (positive potentials for n-type and negative potentials for p-type) or accumulation conditions (negative potentials for n-type and positive potentials for p-type) possess a space-charge region and, consequently, PEIS spectra of p-type semiconductors at positive potentials display two relaxations as well.

PEIS spectra measured on Rh:$SrTiO_3$ – Pt photoelectrodes at different positive electrode potentials and light levels are plotted in Fig. 3-35. The first issue to note is that two relaxations were observed. The LF relaxation, which is associated with the interplay between charge transfer and recombination, appeared again at very low frequencies.

The fact that the OER is a multistep heterogeneous process involving the exchange of four electrons makes not surprising the observed slow kinetics. These values follow the trend observed so far for all other photoelectrodes. Interestingly, the presence of Pt at the surface of Rh:$SrTiO_3$ did not improve the kinetics of charge transfer towards the OER, in contrast with the notable increase in the rate for the HER.

There is another interesting difference in the behavior of this material under positive and negative potentials. Indeed, when we studied the HER, the HF relaxation (which should possess an important contribution from C_{sc}) did not depend much upon applied potential, suggesting an almost constant interfacial capacitance, which is a cause of Fermi level pinning. Such Fermi level pinning causes an important drop of potential in the Helmholtz layer and therefore the maximum of the LF semicircle (k_t) depended on the applied potential. In contrast, Fig. 3-35 b clearly shows that the HF relaxation was

significantly affected by electrode potential, while the LF relaxation looks nearly the same, no matter the applied potential was. This indicated that the charge transfer rate was constant and independent of applied potential (which again is normal for an ideal semiconductor|electrolyte junction) and the absence of Fermi level pinning, hence the stronger influence of the applied potential upon the HF relaxation (i.e., upon C_{sc}).

The limited effect of light intensity upon PEIS spectra can be appreciated on Fig. 3-35 c and d. No significant effect was observed on the LF relaxation, indicating that rate constants were unaffected by light intensity. On the other hand, the HF relaxation shrank with increased light power in the same manner as occurred under cathodic

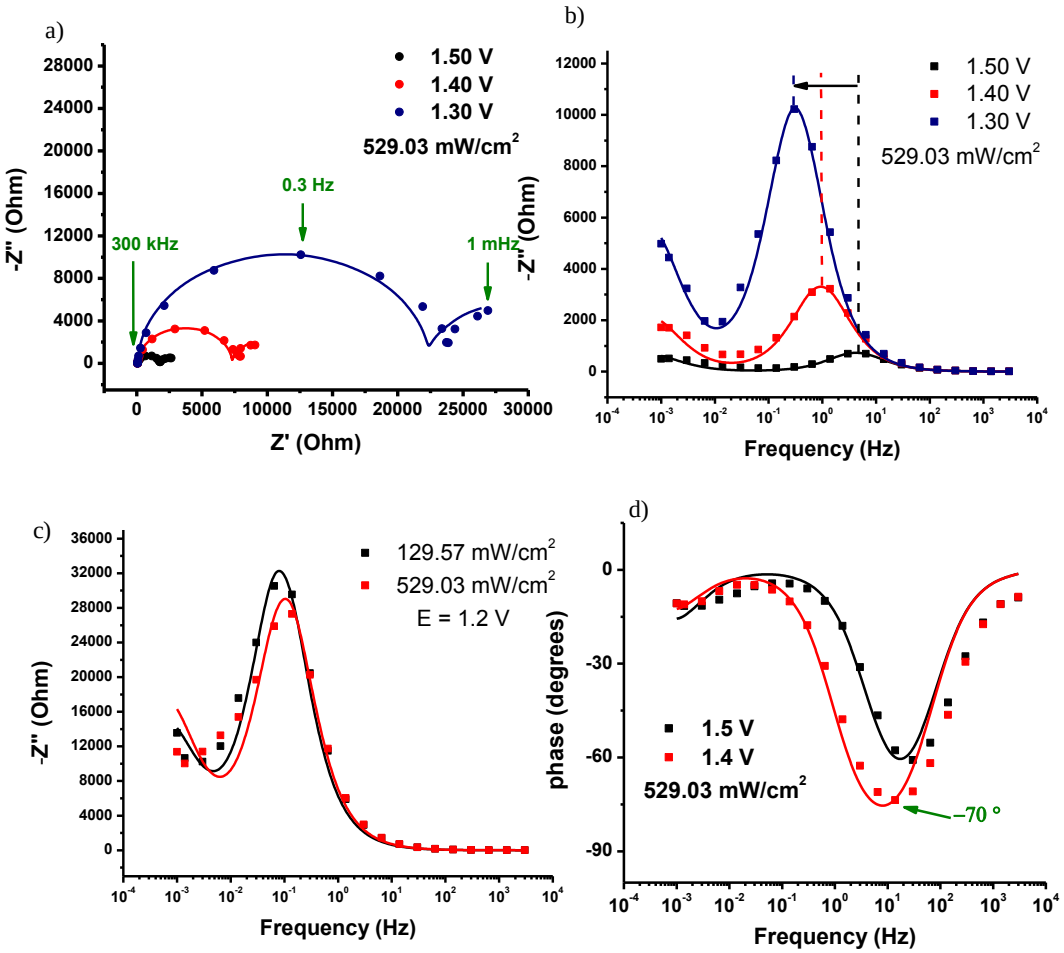

Fig. 3-35. Photoelectrochemical impedance spectroscopy for Rh:$SrTiO_3$ – Pt under anodic polarization a) Effect of electrode potential on Nyquist representation) b) effect of the electrode potential on the Bode representation of –Z"; c) effect of light intensity on the Bode representation of –Z";d) Bode representation of the phase angle.

polarization. Fitting results of PEIS spectra obtained on Rh:$SrTiO_3$ – Pt photoelectrodes under anodic polarization are summarized in Table (within the annex section at the end of this thesis).

3.5. Kinetic comparison of the different photoelectrodes studied in Chapter 3

The first kinetic determinations reported in this chapter were performed under open-circuit conditions. The four photoelectrodes did not present significant differences among them. In general, the charge transfer rate constant possessed values of approximately 0.04 s^{-1} and was larger than the recombination rate constant, which displayed values of approximately 0.01 s^{-1}, excepting the case of Rh:$SrTiO_3$ – Pt photoelectrodes, where both k_t and k_r presented similar values. Overall, the kinetics of charge transfer at open-circuit was notably slow without applied bias.

Mechanistic insights into both the HER and OER were discussed in terms of a Tafel analysis. Table 3-2 summarizes the Tafel slopes obtained for each photoelectrode, towards the HER and the OER.

Table 3-2. Tafel slopes determined for each photoelectrode towards the HER and the OER, based on LSV measurements. Tafel slopes reported for the HER were determined in the dark.

	$\partial V/\partial \log(i)$ (mV/dec)	
	HER	OER
Rh:$SrTiO_3$	157	60
Rh: $SrTiO_3$ – Ch	115	75
Rh: $SrTiO_3$ – Cu	202	73
Rh: $SrTiO_3$ – Pt	107	89[a]
		163[b]

[a] determined in the potential range from 1.5 to 1.4 V (vs. SCE); [b] determined in the potential range between 1.3 and 1.2 V (vs. SCE).

For the HER, the systems Rh:$SrTiO_3$, Rh: $SrTiO_3$ – Ch and Rh: $SrTiO_3$ – Pt displayed Tafel slopes fairly close to 120 mV/dec, suggesting that either the Volmer step[81,217] or

the Heyrovsky step (in the region of high surface density of adsorbed H)[81] are possible rds in the multistep mechanism. Conversely, the OER at Rh:$SrTiO_3$, Rh: $SrTiO_3$ – Ch and Rh: $SrTiO_3$ – Cu exhibited Tafel slopes fairly close to 60 mV/dec, suggesting that the reaction $M - O = M + 1/2O_2$ is the rds, with $\theta_O \approx 0$ and $\theta_{OH} \approx 1$.[87] Additionally we observed Tafel slopes of 202 mV/dec for the $SrTiO_3$ – Cu system towards the HER, and a dual Tafel behavior for $SrTiO_3$ – Pt for the OER. It is worth mentioning that current mechanistic models do not account for these observations.[81,87,88]

The dynamics of both the HER and the OER of the four different illuminated photoelectrodes was then studied under polarization by PEIS analysis. An adequate way to qualitatively analyze the charge transfer rate constant is provided by the Bode plot of the imaginary component, since differences in HF (related to the space charge capacitance) and LF (related to the kinetics of charge transfer and recombination) relaxations are easily appreciated.

At positive potentials (Fig. 3-36 a), the OER required a very high overpotential for the four photoelectrodes. The absence of photocurrents in this region indicated that the measurements were performed under accumulation conditions of majority carriers (i.e.,

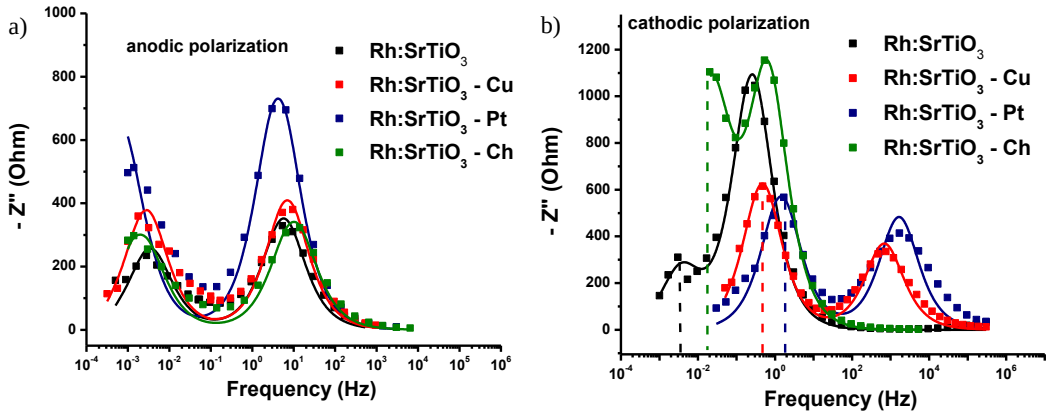

Fig. 3-36.. a) Bode representation of –Z" under anodic polarization, electrode potentials are 1.50 V (vs. SCE) for all spectra excepting Rh:$SrTiO_3$ – Pt which is 1.40 V; b) Bode representation of –Z" under anodic polarization, electrode potential is -1.30 V for metal-modified electrodes, and -1.25 for the other systems.

holes) in the p-type semiconductor. Moreover, the kinetics of charge transfer in these systems was extremely low and showed no difference from one system to the other, as observed in the LF relaxation in Fig. 3-36 a.

Much more interesting was the study of the HER. Both the charge transfer and the recombination rate constants can be ordered in the following increasing way: $Rh:SrTiO_3$ < $Rh:SrTiO_3$ – Ch < $Rh:SrTiO_3$ – Cu < $Rh:SrTiO_3$ – Pt, which is highlighted in Fig. 3-36 b by the Bode plot of –Z" with dashed lines. Additionally, the four photoelectrodes studied here can be classified into two groups according to their behavior. One group is composed by $Rh:SrTiO_3$ modified with metals (Pt and Cu) and the other group is formed by unmodified $Rh:SrTiO_3$ and by $Rh:SrTiO_3$ modified with the hexachlorine containing Co clathrochelate.

In the case of photoelectrodes modified with either Pt or Cu as the catalysts, the HF relaxation occurred at a higher frequency when compared to the other two photoelectrodes, and therefore, $Rh:SrTiO_3$ – Pt and $RhSrTiO_3$ – Cu photoelectrodes had a lower space charge capacitance.

Another striking difference encountered was the dependence of the rate constant upon applied potential (Fig. 3-37). Indeed, for metal modified semiconductors, k_t exhibited an exponential dependence on the electrode potential, indicating the presence of surface states and therefore, Fermi level pinning. Such dependence is depicted in a Tafel plot in Fig. 3-37, which allowed to calculate a transfer coefficient for the HER at the surface of $Rh:SrTiO_3$ – Cu and $Rh:SrTiO_3$ – Pt, displaying values of 0.28 and 0.21, respectively.

Conversely, for Rh:$SrTiO_3$ and Rh:$SrTiO_3$ – Ch photoelectrodes,[201] the charge transfer rate constant did not change with the applied potential (Fig. 3-37), a behavior that is consistent with an ideal semiconductor|electrolyte junction. Though, the surface of Rh:$SrTiO_3$ and Rh:$SrTiO_3$ – Ch was far from being ideal, because the recombination rate constant should decrease with increasing (*i.e.*, more negative) bias. However, for these two electrodes, the recombination rate constant kept a constant value. We speculate that such behavior is related to the presence of surface states but with a lower surface density when compared to the metal-modified photoelectrodes. Indeed, a lower density of surface states should not significantly modify the potential drop across the Helmholtz layer, so that the charge transfer rate constant would not be affected, but the presence of surface states could explain surface non-ideality in the behavior of k_r.

On the other hand, the recombination rate constant of the metal-modified photoelectrodes varied exponentially with the applied potential. Such dependence (Fig. 3-37) allowed us to calculate the non-ideality factor β, which is related to Fermi level pinning by surface states. The non-ideality factor exhibited values of 0.48 and 0.04 for Rh:$SrTiO_3$ – Cu and Rh:$SrTiO_3$ – Pt, respectively, confirming the important role of

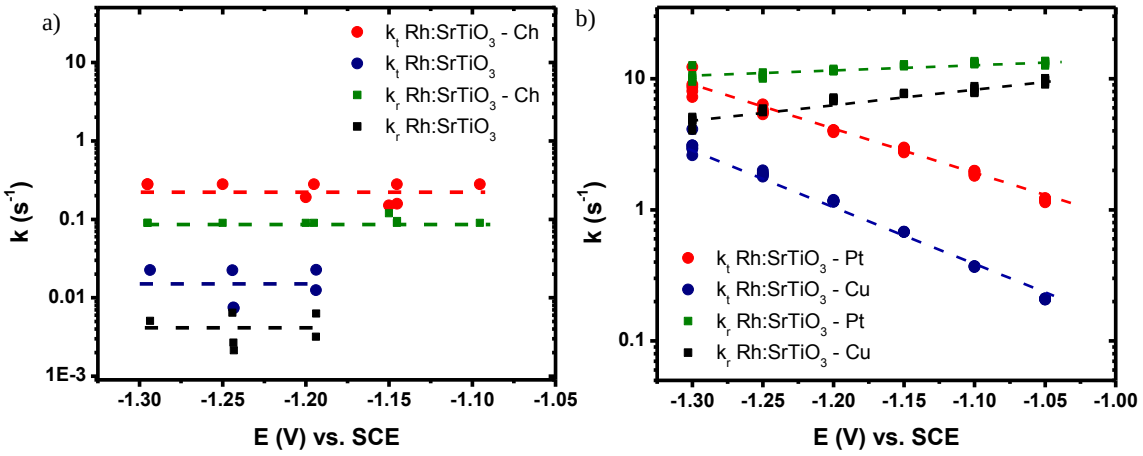

Fig. 3-37. a) Charge transfer and recombination rate constants for Rh:$SrTiO_3$ and Rh:$SrTiO_3$ – Ch photoelectrodes; b) Comparison of the Tafel plot for Rh:$SrTiO_3$ – Cu and Rh:$SrTiO_3$ – Pt photoelectrodes.

surface states in the performance of these photoelectrodes, and further demonstrating that the modification of the semiconductor with Pt lead to the most non-ideal surface, where the recombination rate constant was only slightly dependent on the electrode potential.

The potential dependence of C_{sc} deserves a special comment. Indeed, the p-nature of this material is beyond doubts, not only because of multiple previous reports,[9,13,103] but also due to the determinations of open-circuit potential vs. light power, and the photocurrents under cathodic bias reported in this Thesis. Despite this, Mott-Schottky analysis showed a positive slope throughout this work, in open contrast with the nature of the semiconductor (*i.e.*, p-type semiconductors exhibit negative Mott-Schottky slopes). This fact was explained in terms of an inverted region in the semiconductor-electrolyte interface.[64,65,206,208] The behavior of the space charge capacitance in the inverted region has been poorly investigated in semiconductor electrochemistry. Indeed, references to this can be found mostly in books[64,202] or in relatively old papers.[65,208] Only recently, B. Fabre described it in a Chemical Reviews paper.[206] The quantitative behavior of semiconducting electrodes under inversion conditions has been described in specialized books,[64] though. The literature presents contradictory explanations regarding its qualitative behavior. Some authors express that under inverted conditions, the photoelectrode behaves metal-like,[208] while others note that p-type semiconductors in inverted conditions behave as n-type at the surface and as p-type in the bulk.[65] The experimental results obtained in this thesis support the early opinion of Hagfeldt and Grätzel,[65] because at sufficiently negative potentials, the positive slope in Mott-Schottky plots indicates that the surface of the p-type photoelectrodes behaves as n-type.

3.6. Conclusions for Chapter 3

In this Chapter we have reported thorough photoelectrochemical determinations of four photoelectrodes employing visible light irradiation. The photoelectrodes are Rh:$SrTiO_3$, Rh:$SrTiO_3$ modified with the hexachlorine cobalt(II) tris-dioximate ($Co(Cl_2Gm)_3(B\text{-}CH_3)_2$) (referred to as Rh:$SrTiO_3$ – Ch), and Rh:$SrTiO_3$ modified with metallic Cu and Pt.

All photoelectrodes and materials were characterized by different techniques including XRD, XPS, SEM, EDS, DRS, EPR. This allowed us to verify that the crystallographic structure of $SrTiO_3$ was not appreciably distorted by the inclusion of Rh as a dopant. The presence of Rh was confirmed by Diffuse Reflectance Spectroscopy and by X-ray Photoelectron Spectroscopy (XPS). XPS was the technique of choice for the characterization of the interface, since it provided conclusive proof for the presence of metallic copper (atomic ratio Sr:Cu at the surface 87:13) and metallic platinum (atomic ratio Sr:Pt at the surface 90:10) at the surface of Rh:$SrTiO_3$.

The morphology analysis of all these systems was carried out by Scanning Electron Microscopy (SEM), revealing the polycrystalline nature of the semiconducting material. On the other hand, the presence of surface catalysts could not be appreciated by SEM, probably because of the low loading.

Photoelectrochemical determinations under open-circuit conditions confirmed the p-type conductivity of these photoelectrodes because the open circuit potential was found to rise as light was made more intense. Additionally, kinetic determinations performed by open-circuit photovoltage decay indicated that there were no significant differences in these systems at open-circuit conditions.

Initial insights into the mechanisms of both the HER and the OER was gained by Tafel analysis. In general, the rds for the OER was presumed to be the reaction $M - O =$

$M + 1/2O_2$, with $\theta_O \approx 0$ and $\theta_{OH} \approx 1$, while for the HER the observed Tafel slopes did not allow us to differentiate between the Volmer step or the Heyrovsky step as rds in the potential region of high surface density of adsorbed H atoms. In particular, there were two Tafel behaviors (the system Rh:$SrTiO_3$ – Cu towards the HER and the system Rh:$SrTiO_3$ – Pt towards the OER) that could not be explained with current kinetic models.

Subsequently, photoelectrochemical kinetic determinations under anodic and cathodic polarizations were performed by Photoelectrochemical Impedance Spectroscopy (PEIS) analysis. In most cases (excepting Rh:$SrTiO_3$ – Ch photoelectrodes at strong illumination of 529.03 mW/cm^2), the experimental PEIS spectra displayed the two characteristic relaxations associated to the space charge capacitance (at HF) and to the interplay between charge transfer and recombination kinetics (at LF).

At positive overpotentials, no photocurrents were detected, indicating that the measurements were performed beyond the flat-band potential and under accumulation of majority carriers at the interface (holes for p-type semiconductors), thus, minority carriers (electrons) originated from visible-light photoexcitation moved towards the bulk of the semiconductor, hence the independence of current density on light intensity. All photoelectrodes displayed very slow charge transfer kinetics with k_t in the order of 10^{-2} s^{-1} which were independent of the electrode potential (in the range of +1.5 V to +1.3 V vs. SCE) and light intensity (in the range of 0.4 to 529.03 mW/cm^2), as determined by PEIS analysis. Likewise, all photoelectrodes displayed huge overpotentials in LSV, which is due to the slow charge transfer kinetics. Nevertheless, the overpotentials observed in LSV were not the same for all photoelectrodes, and we speculate that this could be due to differences in proton affinities at the surfaces.

Conversely, the behavior of the four photoelectrodes under cathodic bias can be

classified into two groups: (i) pristine Rh:$SrTiO_3$ and Rh:$SrTiO_3$ – Ch, characterized by the independence of kinetic rate constants upon applied potential and light intensity; and (ii) Rh:$SrTiO_3$ – Cu and Rh:$SrTiO_3$ – Pt, characterized by an exponential dependence of the rate constants on the applied potential, characteristic of electrodes presenting important Fermi level pinning due to the presence of surface states. Such potential dependence allowed us to determine transfer coefficients of 0.28 (Rh:$SrTiO_3$ - Cu) and 0.21 (Rh:$SrTiO_3$ - Cu). Additionally, the non-ideality factor was calculated for these photoelectrodes (0.48 for Rh:$SrTiO_3$ – Cu and 0.04 for Rh:$SrTiO_3$ – Pt), indicating that the photoelectrode Rh:$SrTiO_3$ – Pt presented the most marked non-ideal interface.

Overall, kinetic parameters did not significantly depend on light intensity, since only a slight increase in the recombination rate constant k_r upon light power increase could be clearly observed in the case of Rh:$SrTiO_3$-Cu. Such phenomenon was associated to the increase in the surface concentration of electrons. On the other hand, the electrode potential significantly influenced the width of the space charge in the four photoelectrodes, by increasing its value as the electrode potential was made more negative, and thus incrementing the absorption of light and the flux of photogenerated minority carriers (I_0 in the PEIS model).

The rate of charge transfer on Rh:$SrTiO_3$ photoelectrodes during the HER is slower than on several other materials.[71,73,205] However, surface modification with a Co(II) containing clathrochelate, metallic Cu and Pt, systematically increased the charge transfer rate constant. Consequently, this work identifies ($Co(Cl_2Gm)_3(B\text{-}CH_3)_2$) and copper as possible heterogeneous catalysts to improve the performance of Rh:$SrTiO_3$ photoelectrodes for the HER.

It should be noted that the External Quantum Efficiency (EQE) of all these photoelectrodes could be estimated considering the LED power of the incident light, its

energy, related to the measured photocurrent density. Overall, a value of EQE below 0.01 % was estimated, which was not ameliorated by any of the catalysts tested. Therefore, the model clathrochelate, and Cu and Pt were electrocatalysts that improved the dark current in all cases, but did not contribute to increase the photocurrent. Hence, the photon to current efficiency was not increased by the presence of the surface catalysts studied in this thesis.

CHAPTER 4. The Hydrogen Evolution Reaction Catalyzed by a Model Clathrochelate: Insights from Density Functional Theory analysis

4.1. Introduction

Molecular hydrogen of electrolytic grade (obtained by water electro-, photo- or photo-electro- dissociation) is considered as a promising energy carrier. In terms of technology, engineers tend to prefer acidic electrolytes of larger ionic conductivity. In acidic media, iridium dioxide nanoparticles are used for the oxyen evolution reaction (OER) and platinum nanoparticles (usually supported by carbon black) are used for the hydrogen evolution reaction (HER). Platinum is the most efficient catalyst of the HER but as a result of its scarcity and high sensitivity to trace amounts of pollutants, catalysts based on abundant and cheap transition metals are required. Several candidates have been investigated from experimental and theoretical points of view.[125,152,155,156,159,162,163,166,169]

The ultimate goal is to incorporate such materials in electrolysis or PEC cells to transform visible light into useful chemical fuels, as discussed in Chapter 3. Regarding electrocatalysis engineering (*i.e.* the design of customized catalytic sites from both the energetic and geometrical viewpoints), there is still a deficit of theoretical developments, in order to go beyond mere empirical approaches. Theoretical investigations reported so far in the literature on the HER catalyzed by transition metal complexes have been directed to identify stable pathways in the catalytic cycle.[125,155,156,160,162,163,166,168,169]

Tris-dioximate metal clathrochelates such as the cobalt species shown in Fig. 4-1 are a family of cage-type metal complexes that have been shown to be efficient catalysts for the HER.[126–128] Clathrochelates are basically polymacrocyclic cage compounds which are able to stabilize the low oxidation states of transition metals (e.g. Fe, Co or Ni),

thereby offering interesting possibilities to act as hydrogen-producing catalysts with an appealing potential as molecular electrocatalysts.[126,127] Even though DFT studies of the geometric and electronic structures of these molecules have already been reported in the literature,[129,137] a thorough exploration of the HER mechanism has received scarce attention from a theoretical perspective. The only attempt to rationalize HER catalyzed by cobalt clathrochelates was presented a few years ago.[129] In such study, DFT calculations on the reduced form of a model complex was reported, considering single protonation either on Co or on the iminic C, while neglecting other possible protonation sites or double protonation.

Concerning the experimental cyclic voltammogram of clathrochelates, qualitative prove of electrocatalysis regarding the HER in protic media is well established.[126–128] Some previous experimental work however has been performed with inorganic acids dissolved in water,[126,128] and consequently, any mechanistic analysis is made difficult due to the two sources of proton present in the system. Future experimental mechanistic studies on clathrochelates should be performed with defined organic acids of varying strength, in order to provide experimental support for the mechanistic possibilities discussed below.

Recently, we have reported on the qualitative correlation between the electronegativity of substituents in the organic cage and the overpotential for the HER, employing a combined electrochemical, spectroscopic and DFT analysis.[139] Nevertheless, some issues on the nature of the intermediates participating to

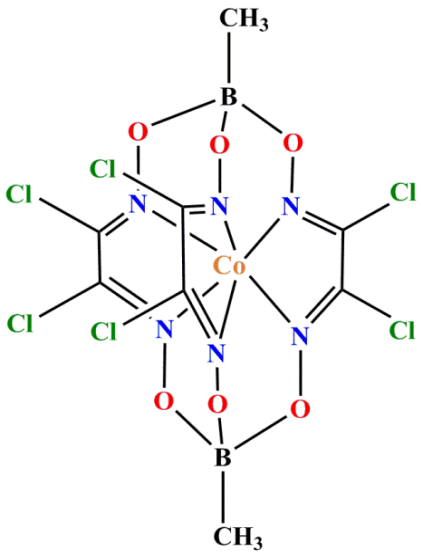

Fig. 4-1. Chemical structure of the model clathrochelate studied in this work.

the hydrogen evolution electrocatalysis are still underexplored. The increasing practical interest in clathrochelates as catalysts in PEM water electrolysis cells,[134,135] joined to the lack of full theoretical insights into the mechanistic pathways justifying the catalytic potential of clathrochelates, prompted us to make a thorough DFT study of HER catalyzed by clathrochelates. To carry out this study, we have selected a model clathrochelate hexachlorine containing an encapsulated cobalt(II) ion, ($Co(Cl_2Gm)_2(B\text{-}CH_3)_2$). Its structure is presented in Fig. 4-1.

4.2. Selection of DFT functional and basis set for geometry optimizations

Current literature regarding DFT calculations on clathrochelates, reveals that most calculations have been performed with the B3LYP exchange correlation functional.[129,132,137,139,218] Though, it has been recognized that transition metal complexes can be described by several other functionals.[169] Therefore, the first step in our theoretical study was to use different functionals in the calculations. In order to accomplish this, geometry optimizations were undertaken with B3LYP, M06-L, TPSS, BP86, PBE and PBE0 functionals. The highly challenging problem caused by the DFT analysis of clathrochelates was put into evidence when the only functional that permitted an adequate optimization of the Co clathrochelate shown in Fig. 4-1 was found to be B3LYP. Indeed, M06-L, TPSS and BP86 were unconverged after 21, 26 and 27 iterations, respectively; while PBE and PBE0 yielded chemically unreasonable structures after 100 iterations. It is worth noting that the number of iterations performed for (un)convergence does not give physical information. Instead, it may suggest that the numeric approach (or the DFT functional) used to solve the problem is (in)adequate.

This is perhaps the cause behind the fact that B3LYP functional has been the most popular choice in published literature concerning DFT calculations in clathrochelates.

Subsequently, two basis sets were employed to perform geometry optimizations in the framework of the B3LYP functional. First, the LANL2DZ with effective core potentials for Co and Cl (basis 1) was employed. Second, a mixture of basis sets comprising the all-electron basis cc-p-VTZ for Co and cc-p-VDZ for all other atoms (basis 2) was utilized. Table 4-1 displays a comparison of crystallographic Co-N distances, and metric data calculated with these two basis sets. The structural comparison was performed in terms of (i) the Co-N bound distances; (ii) the Bailar twist angle θ taken as the dihedral between BNN'B' atoms (from here on, the apostrophe differentiates between the two apical extremes of the molecule) and (iii) the angle φ taken between BCoB'. The angle θ expresses the rotation around the pseudo-C_3 axis between the N···N···N and N'···N'···N' triangles, while the φ angle provides a measure of the displacement of the central Co atom inside the organic cage. Equal bond distances and θ = 0° with φ = 180° are characteristic of D_{3h} symmetry, while of θ = 60° and φ = 180° correspond to D_3 symmetry.

Table 4-1. Comparison between calculated and experimental metric data for the organic cage of the model clathrochelate studied in this work ($[^2Co]^0$). Theoretical calculations were performed with the B3LYP exchange correlation functional. Basis 1 corresponds to the LANL2DZ with effective core potentials for Co and Cl. Basis 2 was cc-pVTZ for Co and cc-p-VDZ for all other atoms. Atomic distances are given in Angstroms. Bond angles are given in degrees. The Bailar twist angle was measured through the N atoms lying farther apart from Co.

	XRD	basis 1	basis 2
Bond distances			
Co-N1	1.91	1.89	1.90
Co-N2	1.90	1.93	1.96
Co-N3	1.92	1.94	1.96
Co-N4	1.92	1.96	1.92
Co-N5	2.14	2.12	2.16
Co-N6	2.14	2.15	2.23
Angles			
θ (BNN'B')	12	20	38
φ (BCoB')	172	174	171

A comparison of the results of this work and previously published data[137,139] indicate that the B3LYP functional slightly overestimates bond distances. Even though it should be kept in mind that geometry in the solid state is not necessarily the same as in an organic solution. The Jahn-Teller effect leading to a 4 + 2 coordination scheme is adequately reproduced by the B3LYP functional and each of the bases employed (φ angle), while the Bailar twist angle is in reasonable agreement with experiment, in particular for the LANL2DZ (basis 1). In general both basis sets reproduce well the geometry of the clathrochelate. Even though the LANL2DZ basis with ECP for Co and Cl is less elaborated (and less expensive from a computational perspective), it provides a good geometric description of the complex. Therefore, for the present study, we selected the B3LYP functional and the basis 1 to run the geometry optimizations and hessian calculations, and we selected basis 2 to refine the calculated energy through single point calculations. The choice of B3LYP functional and LANL2DZ basis set as an adequate choice is further supported by several publications describing the behavior of various organometallic compounds[157,219,220] including a phthalo-cyanino-clathrochelate.[218]

Another important effect considered in these calculations is the presence of solvent. In order to describe the contribution of solvent molecules, we have utilized the PCM-SMD model. To provide an evaluation of the impact of different solvents on the theoretical results, we performed optimization and energy calculations of some significant intermediates in acetonitrile and dimethylformamide. Table 4-2 indicates that, at least from a computational perspective, the trend regarding the stability of different intermediates was not affected by the choice of the solvent. According to this, the full computational study of the mechanism was performed considering DMF as the solvent.

Table 4-2. Total energies in Hartrees of the three different redox states (high and low spin) in acetonitrile (AN) and dimethyl-formamide (DMF). Level of theory B3LYP cc-pVTZ for Co cc-p-VDZ for all other atoms.

	$[^1Co]^{-1}$	$[^3Co]^{-1}$	$[^2Co]^0$	$[^4Co]^0$
AN	-5281.2472991695	-5281.2453638159	-5281.1698643585	-5281.1111792086
DMF	-5281.2472991695	-5281.2453638160	-5281.1698643585	-5281.1111792086
	$[^1Co]^1$	$[^5Co]^1$		
AN	-5280.9312627981	-5280.8849278885		
DMF	-5280.9312627980	-5280.8849278885		

4.3. X-ray Near Edge (XANES) and Extended X-ray Absorption Fine Structure (EXAFS) analysis of the Co K-edge in the $Co(Cl_2Gm)_3(B\text{-}CH_3)_2$ clathrochelate

X-ray absorption spectroscopy is a very precise technique to determine molecular structures. Indeed, it is interesting to investigate XANES and EXAFS for this complex, and to establish whether the known XRD geometry and the optimized DFT geometry could reproduce adequately the spectroscopic observations.

The process of extracting the EXAFS signal is depicted in Fig. 4-2. After the absorption coefficient is obtained (Fig. 4-2 a), a smooth pre-edge is subtracted in order to eliminate instrumental background or absorption from other edges (Fig. 4-2 b).

The similarities between optical UV-Vis and X-ray absorption spectroscopy (XAS) explained in Chapter 1 devoted to the Bibliographic Overview indicates that the selection rules for the transitions are the same in both spectroscopies governed by Fermi's golden rule.[146] Indeed, transitions are allowed between sates whose variation in the magnetic quantum number is $\Delta m = \pm 1$. Therefore, transitions between s and p orbitals are allowed, likewise transitions between p and d orbitals. Conversely, electronic transitions between s and d orbitals are forbidden. In a molecule, there is always a mixture of atomic orbitals to form molecular orbitals. That is why, when there

is some extent of mixing (hybridization) between p and d orbitals, the forbidden $s \rightarrow d$ transition can be weakly observed because the d orbital have a partial p character.

Such analysis allows to interpret the XANES part of the XAS for the $Co(Cl_2Gm)_3(B\text{-}CH_3)_2$ clathrochelate (Fig. 4-3). Fig. 4-3 shows that the spectrum is dominated by the $1s \rightarrow 4p$ transition, which constitutes the edge-step. Rigorously speaking, the edge step should be regarded as a combination of $1s \rightarrow 4p$ transition, with the emission of the photoelectron wave. Moreover, a magnification of the pre-edge region of the spectrum, between 7.68 and 7.72 keV shows a weak pre-edge absorption attributable to a forbidden $1s \rightarrow 3d$ transition.[130] The apparition of such transition with such a low intensity indicates a certain degree of mix between p and d electronic levels in the clathrochelate molecule.[201]

In the energy range that begins at approximately 0.1 keV beyond the edge step, the Extended X-ray Absorption Fine Structure (EXAFS) can be observed. EXAFS spectroscopy has been notoriously employed for precise structural determinations in the framework of material science and electrocatalysis.[10,54,130,162,221–225]

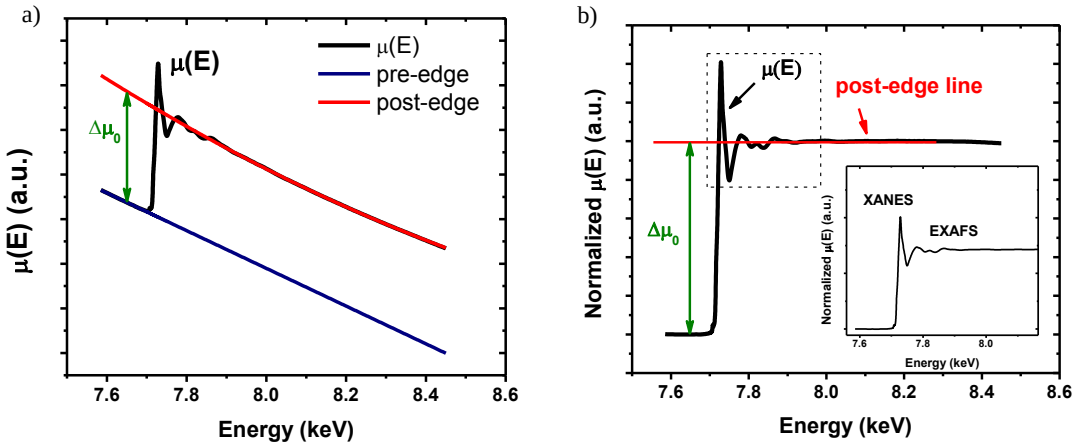

Fig. 4-2. a) Absorption coefficient μ(E) vs. X-ray energy of the Co K-edge; b) background-corrected absorption coefficient μ(E) vs. X-ray energy.

The oscillating EXAFS signal in k-space can be appreciated in Fig. 4-4 a, while Fig. 4-4 b shows the corresponding EXAFS shown in the R-space. Fig. 4-4 b allows identifying at least three main different contributions to the FT-EXAFS, which could correspond to three scattering shells in the molecule. A look at the structure of the clathrochelate studied here (Fig. 4-5 a) indicates that the first shell should be dominated by the single scattering Co-N.

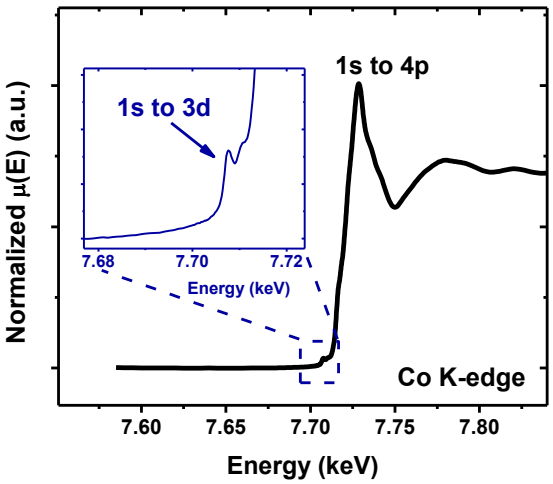

Fig. 4-3. Normalized XANES spectrum of the Co K-edge for $Co(Cl_2Gm)_3(B\text{-}CH_3)_2$ clathrochelate, whose main contribution is the allowed transition from the 1s core level to the 4p level. The inset shows a magnification of a pre-edge forbidden transition from the 1s core level to the 3d level.

However, the second shell appears more complicated because several light atoms (O Csp_2 and B) lie at similar distances from the Co absorber; therefore, the second shell is likely to be composed by contributions from each of these light atoms. Farther apart in a

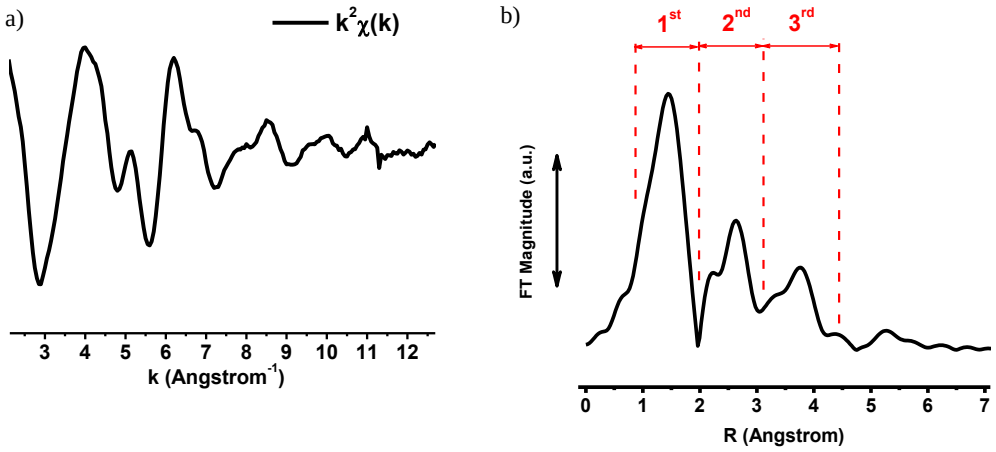

Fig. 4-4. a) Co K-edge k^2-EXAFS signal ($\chi(k)$) in k space; d) Co K-edge k^2-EXAFS signal in R space. The 1st, 2nd and 3rd shell labels are put only as a guide to the eye.

third shell there are Cl and C sp_3 atoms. Given the fact that scattering amplitudes are more intense when the atomic number (Z) of the back-scatterer is larger, it is presumed that this third shell shall be predominantly due to Co-Cl single scattering rather than Co-C(sp_3). A way to support such presumption is to plot the normalized FT of the spectrum with different k-weights, so that the FT of the first neighbor has the same intensity (Fig. 4-5 b). The FT-EXAFS signal scattered from different atoms has different dependencies on k-weight; shells that decrease with increasing k-weight may contain atoms with lower Z. Conversely, shells that grow with increasing k-weight may be composed by atoms with larger Z.[54,146]

Consequently, Fig. 4-5 suggests that the EXAFS signal appearing at approximately 2 Å could be due to light atoms (corresponding to the second shell of O C sp_2 and B), while the EXAFS signal beyond 3 Å could belong to atoms with larger Z (probably Cl from the third shell).

Once such qualitative interpretation of the experimental EXAFS was performed, the EXAFS signal was fitted by using the XRD geometry as a first approach. It is convenient to recall here that the spectrum is fitted according to the EXAFS equation[147]

$$\chi(k) = S_0^2 \sum_R N \frac{|f_{eff}(k)|}{kR^2} \sin(2kR + \phi_k) \exp(-2kR/\lambda_k) \exp(-2\sigma^2 k^2) \quad (4\text{-}1)$$

Where $\chi(k)$ is the EXAFS amplitude, S_0^2 represents the amplitude factor, the summation Σ_R extends over all scattering paths, N stands for the number of scatterers for a given scattering path, $|f_{eff}(k)|$ represents the effective scattering amplitude, R is the distance between the absorber atom and the back-scatterer neighbour, k is the wave-vector which is directly related to the energy of the X-rays through the expression $k = \sqrt{(2m_e(E - E_0))/\hbar^2}$, with m_e being the mass of the electron, E_0 the energy of the edge

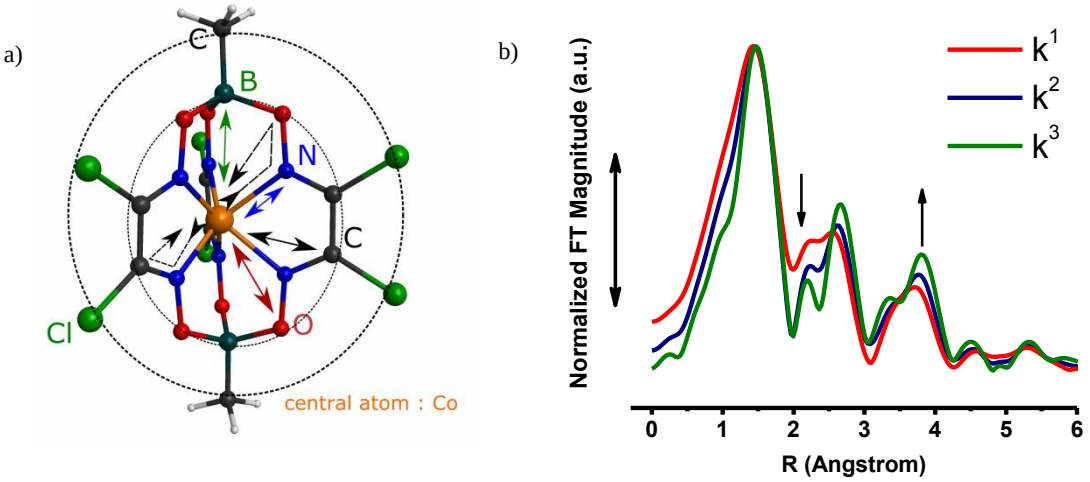

Fig. 4-5. a) Structure of the clathrochelate. Some single scattering (solid arrows) and multiple scattering (dashed arrows) paths are illustrated. Not all possibilities were depicted with arrows to avoid figure overcrowding. The 2nd and 3rd scattering shells are represented by dashed circles; b) Fourier transform of the EXAFS signal with different k-weights. The spectra were normalized at the intensity of the first neighbor.

and E the energy of the X-ray, σ^2 stands for the Debye-Wäller (DW) factor, λ_k is the mean free path of the photoelectron, ϕ_k is the total phase shift, whose origin resides in the interaction of the photoelectron wave with the absorber and the scatterer.

Initially, the first and second shells were fitted together (Fig. 4-6 a and b) in the R space from R = 1.0 to 3.1 Å. For such fit, all single scattering and multiple scattering paths below 3.1 Å were included. It may be appreciated that these two shells reproduce acceptably the shape of the EXAFS spectrum. Fig. 4-6 a permits to conclude that the EXAFS signals coming from the second shell do overlap with the signals from the first shell. Consequently, the EXAFS of the third shell might mix with the EXAFS of the second shell as well.

Fig. 4-6 b further shows that there is a rapid oscillation around k = 5.15 $Å^{-1}$ and k = 6.85 $Å^{-1}$ (corresponding to a long scattering path) that is not well reproduced (highlighted with small arrows in Fig. 4-6 b), indicating that the fit of the two first shells neglects important structural information of the system, which is associated to the scattering of

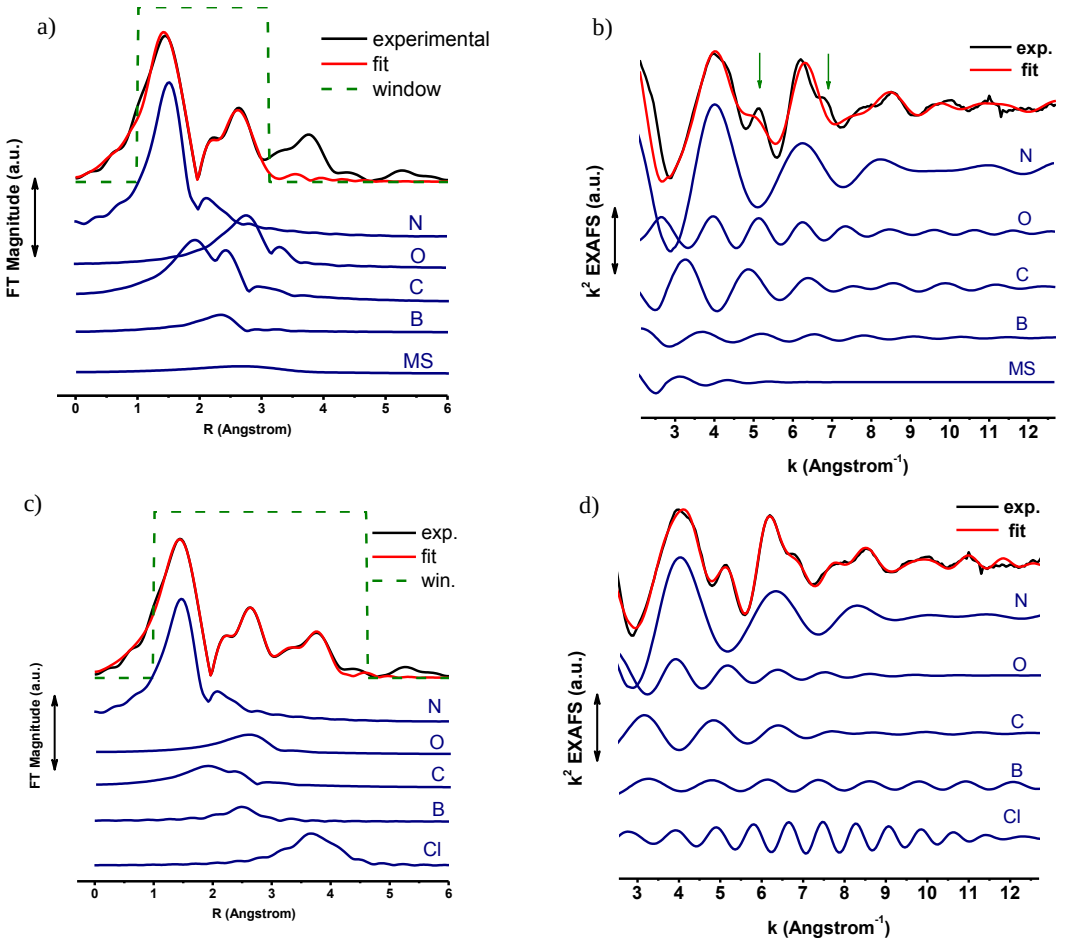

Fig. 4-6. a) FT-EXAFS and b) $k^2\chi(k)$ spectrum of the clathrochelate. Fit from R = 1 to 3.1 Å. Main scattering paths are depicted below the spectrum. MS stands for multiple-scattering; c) FT-EXAFS and d) $k^2\chi(k)$ spectrum of the clathrochelate. Fit from R = 1.000 to 4.627 Å. Main scattering paths are depicted below each spectra. The contribution of MS paths was negligible and is not represented, even though it was considered in the fit.

the third shell. Therefore, fitting parameters of the first and second shells were used as initial guess to perform a more complete fit comprising the whole spectrum.

Consequently, the fit was performed from R = 1.000 to 4.627 Å, thus comprising all relevant EXAFS signals in the spectrum. Likewise, all single scattering and multiple scattering paths shorter than 4.627 Å were considered in the fit. All parameters were permitted to refine without any constraint, excepting the amplitude reduction term S_0^2, which was restrained to 1.00.[201]

The fit was chosen so as to minimize the reduced χ^2 statistical parameter. As a final

result, there is an excellent match between experimental and fitted spectrum both in R and k spaces (Fig. 4-6 c and d), with logical values for the fitting parameters (Table 4-3). The rapid oscillations that could not be reproduced with the fit of the first and second shells only, are now nicely reproduced by the inclusion of the third shell. Fig. 4-6 c confirms that the signals of the second and third shells do overlap.

Table 4-3. DW factors and path distances for the hexachlorine containing cobalt(II) tris-dioximate clathrochelate ($Co(Cl_2Gm)_2(B\text{-}CH_3)_2$). Fit performed with the XRD geometry.*

Shell	Path	Degeneracy	σ^2(Å^2)	Error σ^2(Å^2)	R (Å)	ΔR (Å)
1	Co-N	4	0.007	0.002	1.92	0.01
	Co-N	2	0.003	0.002	2.06	-0.08
2	Co-O	4	0.018	0.003	3.35	0.45
	Co-O	2			3.30	0.20
	Co-C(sp_2)	4	0.011	0.004	2.40	-0.58
	Co-C(sp_2)	2			2.95	0.21
	Co-B (r)	2	0.0003	-	3.04	-0.07
3	Co-Cl	4	0.003	0.0003	4.32	-0.06
	Co-Cl	2			4.70	0.07

*E_0 = (-8.8 ± 1.4 eV); S_0^2 = 1.00 (restrained variable); R-factor = 0.0054; reduced-χ^2 = 279; MS = Multiple-Scattering; r = restrained variable.

The fit of EXAFS with the XRD structure was successful;[201] DW factors were grouped by shell and atom type. For the first neighbors, two different DW factors were introduced to distinguish between the different environments in the 4 + 2 coordination scheme around the Co central atom. For the second and third shells, a single DW for each type of atom was enough to reproduce the spectrum.

In a second step, the EXAFS spectrum was fitted using the DFT optimized geometry. Initially, the strategy was to follow the same procedure employed with the XRD

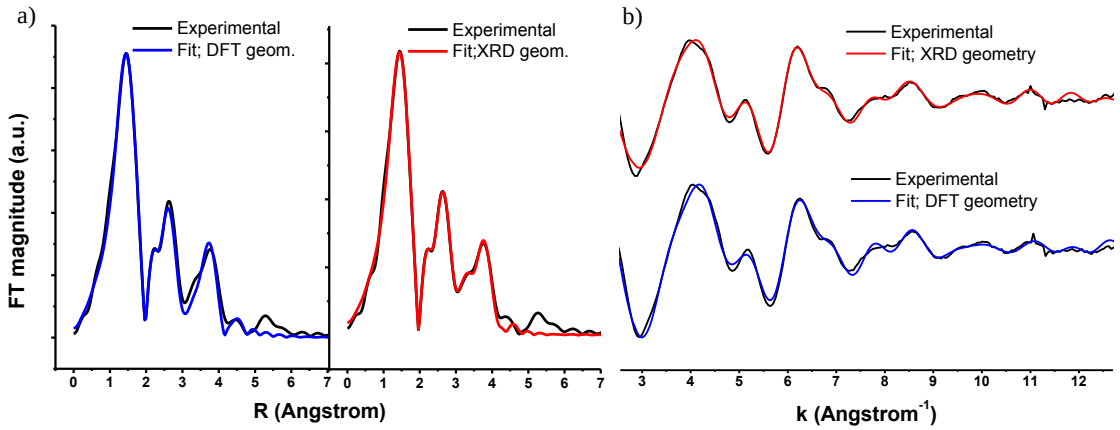

Fig. 4-7. a) Comparison of the FT-EXAFS spectra and fit of the clathrochelate using DFT geometry (left) and XRD geometry (right); b) the same fits shown in a), but in $k^2\chi(k)$ form; using the XRD geometry (up) and the DFT geometry (down).

geometry (as shown in Table 4-3), i.e., to use a 4 + 2 coordination scheme and two different DW factors for the first shell while for the second and third shells, to group the DW factors per atom type. Unfortunately, such procedure led to poor quality fits, probably due to the fact that the DFT geometry is slightly different than the XRD geometry. To face this issue, the amounts of variables were incremented, by fitting the second shell similarly to the first, i.e., by employing two DW factors for each atom type, in order to differentiate the 4 + 2 coordination around Co. The fitting results may be observed in Table 4-4. For reasonable EXAFS fit values of organometallic complexes see reference 147.

This strategy led to an acceptable fit of the EXAFS spectrum, as shown in Fig. 4-7. As might be expected, the statistical parameters (reduced-χ^2 and R-factor) indicated a better fit when the XRD geometry was employed. Nevertheless, the possibility to reproduce the EXAFS shape with the DFT geometry indicates that the computational procedure allows the finding of structures that are close to the experiment ones.

Table 4-4. DW factors and path distances for the hexachlorine containing cobalt(II) tris-dioximate clathrochelate ($Co(Cl_2Gm)_2(B\text{-}CH_3)_2$). Fit performed with the DFT optimized geometry at B3LYP/LANL2DZ level.

Shell	Path	Degeneracy	$\sigma^2(Å^2)$	Error $\sigma^2(Å^2)$	R (Å)	ΔR (Å)
1	Co-N (r)	4	0.007	-	1.9	-0.04
	Co-N (r)	2	0.003	-	2.13	-0.1
2	Co-O	4	0.015	0.006	2.76	-0.19
	Co-O	2	0.003	0.008	3.32	0.21
	Co-C (sp_2)	4	0.014	0.008	2.54	-0.23
	Co-C (sp_2)	2	0.009	0.005	2.39	-0.58
	Co-B (r)	2	0.0003	-	3	-0.17
3	Co-Cl	4	0.002	0.001	4.51	0.08
	Co-Cl	2			4.65	-0.05
	MS		0.023	0.01		

*E_0 = (-10 ± 5 eV); S_0^2 = 1.00 (restrained variable); R-factor = 0.015; reduced-χ^2 = 1020; MS = Multiple-Scattering; r = restrained variable.

Numeric results of the fits compiled in Tables 2 and 3 have a common trend. The structural determination of the first and third shells is excellent with both XRD and DFT geometries, with ΔR no larger than 0.1 Å and DW factors in the order of 10^{-3} $Å^2$. For example, Table 4-5 shows that the shortest Co-N neighbors are at 1.91 Å according to XRD, while the prediction from the EXAFS fit is at 1.92 Å, showing that the EXAFS fit overestimated the distance by only 0.01 Å, which is exactly the value of ΔR. Likewise, for the farthest Co-Cl distance, it was determined to be 4.63 Å by XRD and predicted to be 4.70 Å by the EXAFS fit, corresponding to a ΔR = 0.07 Å. As expected, all R values of the model (either XRD or DFT) equal the (R + ΔR) of the EXAFS fit.

Table 4-5. Comparison between metric data derived from XRD, DFT, and their corresponding EXAFS fits. The distances reported here from the 4 + 2 coordination motif, are mean values of the 4 and 2 neighbors, respectively.

Path	Degeneracy	EXAFS (Solid geom.)		XRD		EXAFS (DFT geom.)		DFT
		R (Å)	ΔR (Å)	R (Å)		R (Å)	ΔR (Å)	R (Å)
Co-N	4	1.92	0.01	1.91		1.90	-0.04	1.93
Co-N	2	2.06	-0.08	2.14		2.13	-0.10	2.14
Co-O	4	3.35	0.45	2.90		2.76	-0.19	2.95
Co-O	2	3.30	0.20	3.10		3.32	0.21	3.11
Co-C (sp_2)	4	2.40	-0.58	2.74		2.39	-0.23	2.78
Co-C (sp_2)	2	2.95	0.21	2.98		2.54	-0.58	2.97
Co-B	2	3.04	-0.07	3.10		3.00	-0.17	3.17
Co-Cl	4	4.32	-0.06	4.38		4.51	0.08	4.49
Co-Cl	2	4.70	0.07	4.63		4.65	-0.05	4.70

Regarding the second shell, the position of the B atoms was adequately determined. However, the positions of O and iminic C appear in the fit with a rather large ΔR value of up to -0.58 Å (see Tables 2 3 and 4). The meaning of such values is that both the XRD and the DFT models employed to fit the EXAFS spectrum had a difference with the actual position of O and C iminic atoms in the second shell of the clathrochelate. In order to provide an explanation for these high values in ΔR for these two atoms in the second shell, a thorough inspection of the cif (crystallographic information file, containing XRD information) corresponding to the clathrochelate was performed. It was observed that the cif contained nine different files, each one comprising a slightly different structure for the molecule. Metric distances corresponding to Co-O and Co-C(sp_2) distances, obtained with two of these cif files are shown in Table 4-6.

Table 4-6. Comparison between Co-O and Co-C(sp_2) distances for two different XRD structures of the clathrochelate.

Distance (Å)	cif 1	cif 9		Distance (Å)	cif 1	cif 9
Co-O1	2.87	2.92		Co-C1	2.72	2.79
Co-O2	2.89	2.92		Co-C2	2.73	2.79
Co-O3	2.91	2.97		Co-C3	2.77	2.84
Co-O4	2.95	2.97		Co-C4	2.76	2.84
Co-O5	3.05	3.01		Co-C5	2.95	2.86
Co-O6	3.11	3.01		Co-C6	2.97	2.86

It should be noted that even XRD data display a spreading in the positions of O and C(sp_2) in the second shell of the clathrochelate. Apparently, Co-O and Co-C(sp_2) distances are not entirely homogeneous in the solid state, which should be the cause for the slightly elevated values of ΔR obtained in the fit of these two atoms in the second shell of the clathrochelate.

4.4. Analyses of the three redox states with two spin multiplicities

After the structural characterization by XAS spectroscopy, we proceeded to study the model clathrochelate in different oxidation states. A previous theoretical study on clathrochelates was devoted to the detailed description of a molecule having fluorine and methyl as the apical and ribbed substituents, respectively.[137] The molecule studied here (Fig. 4-1) possesses a methyl and Cl atoms as the apical and ribbed substituents, respectively. Such structural differences imply that all theoretical results between these two works are not directly comparable. Nevertheless, a comparison between the geometric and electronic characteristics obtained for these two systems shall be undertaken, highlighting the differences and similarities between the two complexes. From the perspective of the computational procedure, both works have employed the same functional (B3LYP), but the previous work used the Aldrich's group all-electron

triple-ζ basis set (TZVP) for Co and the double-ζ split valence (SV) for all other atoms. In the previous work, high-spin and low-spin configurations were considered for the $[Co]^{-1}$ species only, while only the low-spin case was considered for $[Co]^{0}$ and $[Co]^{+1}$ redox states. In this work, we have calculated high-spin and low-spin configuration for all (three) redox states (Table 4-7).

It may be appreciated in Table 4-7 that both spin configurations of $[Co]^{0}$ display Jahn-Teller distortion (structure of $[^{2}Co]^{0}$ shown in the center of Fig. 4-8), clearly observed in a 4 + 2 coordination where four N atoms are nearly equidistant to Co, while two other lie farther apart, and the φ angle departs from 180°. The mean value of the Co-N distance is 2.00 and 2.02 Å for $[^{2}Co]^{0}$ and $[^{4}Co]^{0}$, respectively (2.01 in reference 137).

Table 4-7. Calculated metric data for the three redox states and two spin multiplicities of the model clathrochelate studied in this work. Theory level B3LYP/ LANL2DZ with ECP for Co and Cl.

	$[^{1}Co]^{-1}$	$[^{3}Co]^{-1}$	$[^{2}Co]^{0}$	$[^{4}Co]^{0}$	$[^{1}Co]^{+1}$	$[^{5}Co]^{+1}$
Bond distances in Å						
Co N1	1.87	1.89	1.89	1.89	1.93	2.07
Co N2	1.87	1.90	1.93	1.93	1.94	2.07
Co N3	1.90	1.92	1.94	1.97	1.94	2.07
Co N4	1.91	1.93	1.96	2.03	1.94	2.08
Co N5	1.96	2.42	2.12	2.14	1.95	2.09
Co N6	2.62	2.80	2.15	2.18	1.95	2.09
Angles in degrees						
θ (BNB'N')	20	44	5	23	71	4
φ (BCoB')	174	173	171	157	179	179

After the one-electron reduction, the characteristic 4 + 2 coordination scheme of the clathrochelate is predicted to be reinforced, as expressed by the departure of the two N atoms that lie farther apart, from 2.12-2.15 Å in $[^{2}Co]^{0}$ to 2.42-2.80 Å in $[^{3}Co]^{-1}$ or 1.96-2.62 in $[^{1}Co]^{-1}$. Such a one-electron reduction provoked a movement of 0.7 Å of Co within the organic cage, so that the central atom is nearly in a square-planar

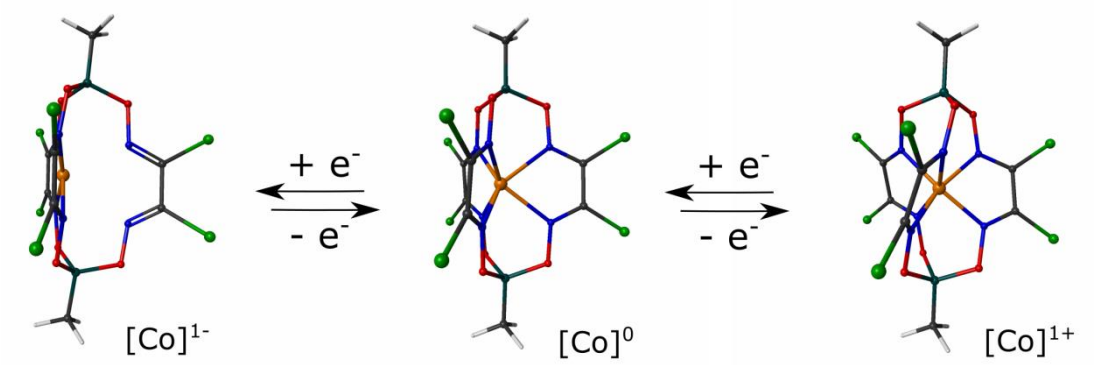

Fig. 4-8. View of Co clathrochelate studied in this work. This figure highlights the position of Co inside the organic cage for $[Co]^{-1}$ (left), $[Co]^{0}$ (center) and $[Co]^{1}$ (right).

coordination (structure of $[^{1}Co]^{-1}$ shown in the left of Fig. 4-8). The structures of the $[Co]^{-1}$ species that we obtained is different to that of the previous work,[137] where low-spin reduced complex had this quasi-square planar structure, with two N considered as decoordinated, but the high-spin counterpart presented a highly symmetric structure. In the context of HER electrocatalysis, the structure of the $[Co]^{-1}$ obtained in this work is interpreted as favorable because the exposition of the Co should make the coordination of H^{+} more sterically favorable, while the decoordination of two N leaves vacant coordination sites for H^{+} binding to form a reactive intermediate. These facts shall be discussed later in the text.

Finally, the oxidation of the initial $[Co]^{0}$ leads to $[Co]^{1}$. Both spin states in the $[Co]^{1}$ complex display a highly symmetric structure, with Co-N mean values of 1.94 Å for $[^{1}Co]^{1}$ and 2.08 for $[^{5}Co]^{1}$, which is in agreement with the reported value of 1.92 Å for the low-spin oxidized analogue. The φ and θ angles suggest that the $[^{1}Co]^{1}$ and $[^{5}Co]^{1}$ clathrochelate are very close to the D_3 and D_{3h} symmetry groups, respectively.

Overall, our calculations suggest that there are marked geometric differences between each oxidation state in this clathrochelate. However, the structures of the low and high spin species within the same oxidation state resemble quite closely, in contrast with the conclusions of the previous study where the low and high spin configurations of the

reduced clathrochelate were predicted to have a very different structure.

4.5. Computation of the equilibrium redox potentials for the $Co(Cl_2Gm)_3(B\text{-}CH_3)_2$ clathrochelate

The relevant observable under consideration in this Chapter is the equilibrium redox potential. As was mentioned before, clathrochelates possess two well defined redox waves in cyclic voltammetry, associated to the $Co^{III}|Co^{II}$ and $Co^{II}|Co^{I}$ redox couples.[127,128,139] There are several alternatives described in the literature aiming to estimate the redox potential from ab-initio quantum chemistry.[163,169,174–177] A first possibility is through the calculation of Born-Haber cycles: this is done by optimizing the relevant redox states in gas phase and in a certain solvent. In another manner, the relevant redox states may be directly optimized in the solvent,[169] and the absolute free energy difference between oxidized and reduced states can be referred to an absolute electrode potential according to equation 4-2.

$$E^0_{abs} = -(\Delta G^0_{abs}/nF) \qquad (4\text{-}2)$$

Where ΔG^0_{abs} is the free energy change of the reaction $Ox + e^- = Red$, where Ox and Red stand for relevant redox states of the clathrochelate. E^0_{abs} obtained in such a way should be referred to an appropriate reference. We selected the redox couple $Fc^+|Fc$ (i.e., Ferrocenium|Ferrocene) as a reference reaction, which was optimized at the same level of theory of the clathrochelate. In equation 4-2, F and n stand for Faraday's constant and the number of exchanged electrons, respectively.

The experimental results used to compare our theory were found vs. $Ag|AgCl_{(s)}|KCl_{(aq)}$, and can be appreciated in the right-most column of Table 1 in reference 128. Recently,

in order to compare theoretically-estimated equilibrium redox potentials as calculated above, with equilibrium potentials found experimentally with the above-mentioned reference electrode, we employed an experimentally determined value for the $Fc^+|Fc$ couple,[139] which is in close agreement to the 0.5 V shift that has been applied before.[152] Nevertheless, we note that the use of usual aqueous references in organic electrochemistry is biased by the liquid junction potential (LJP)[226] which depends on electrolyte composition. Therefore, differences between theory and experiment can have their origin not only in the inherent simplifications of theoretical model (e.g. harmonic approximation or continuum solvation etc.), but also on variations in LJP that are difficult to systematize in different experimental conditions.

Table 4-8. Comparison of calculated and experimental redox potential of the clathrochelate vs. the $Fc^+|Fc$ couple. B3LYP/ LANL2DZ.

	$Fc^+|Fc$	$Co^{II}|Co^{I}$	$Co^{III}|Co^{II}$
Experimental $E°\ vs.\ Ag|AgCl|Cl^-$	0.46[139]	-0.24[128]	1.125[128]
Experimental $E°\ vs.\ Fc^+|Fc$	0	***-0.70***	***0.665***
Calculated ΔG^0_{abs} (kJ/mol)	-424.56	-369.29	-485.24
Calculated E^0_{abs} (V)	4.40	3.83	5.03
Calculated $E°\ vs.\ Fc^+|Fc$	0	***-0.57***	***0.63***

We found a difference of 130 mV for the cathodic wave, and of 30 mV for the anodic response, which is in reasonable agreement with experiment. Strictly speaking, the actual prediction of redox potentials is currently a challenge, with error values ranging from 150 to 170 mV in calculations of small organic molecules or metallocenes[174,176] or up to 200 mV[227] for organometallic complexes relevant to electrocatalysis. Consequently, it has been recognized that quantum chemistry should be regarded as a powerful tool to assess trends due to the systematic cancellation of computational errors[124] since the accuracy of absolute values is still challenging. Considering these

facts, the calculation of equilibrium potentials using the methodology described in this work was found acceptable.

The reliability of theoretical calculations comes from the predictions these can make. So far, the DFT methodology employed has been tested against (i) the structural information from XRD (Table 4-8), (ii) EXAFS spectroscopy and (iii) the prediction of the equilibrium potentials. These facts provide a degree of confidence regarding the theoretical results that shall be presented in the following sections.

4.6. Explored pathway for the electrocatalytic HER

The experimental cyclic voltammogram of the clathrochelate of Fig. 4-1[128] indicates that the catalytically active species is a $[Co]^{-1}$. This fact that had been recognized before [127,128,130,136,139] and the monomolecular catalytic mechanism depicted in Fig. 4-9 has been explicitly proposed elsewhere,[127,130] in agreement with experimental results. We note that the clathrochelate studied experimentally possessed n-butyl moieties as the apical substituents.[128] Nevertheless, for computational rationality, the molecule calculated here possessed methyl groups as the apical substituents, as depicted in Fig. 4-1.

The monomolecular catalytic pathway comprises the one-electron reduction of $[Co]^{0}$ to form the catalytically active $[Co]^{-1}$, and then the formation of various protonated intermediates, usually termed in the literature as a "hydride complex". Previous theoretical work on clathrochelates has considered protonation on the iminic C.[129] Thus, we have extended this approach by calculating three possible protonation sites, namely, Co, N and C. In order to clarify the nomenclature herein employed, it may be defined that the formula $[^{1}Co(C)H]^{0}$ represents the model clathrochelate of Fig. 4-1, in the singlet state with a proton bound to an iminic C of the ligand, with an overall zero

charge of the complex. In the same way, the formula $[^1Co(Co)H]^0$ means that the proton is coordinated directly to Co, with multiplicities and charges being the same as in the first example. Whenever the spin multiplicity is not specified, as in $[Co]^{-1}$, we are referring to the redox state only, without distinction between spin states.

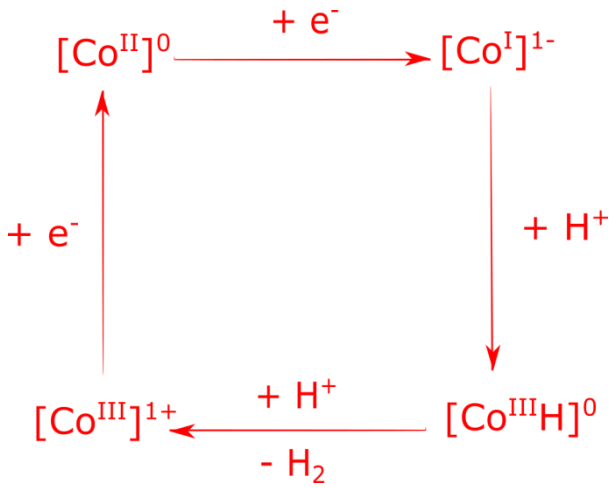

Fig. 4-9. Monomolecular catalytic mechanism usually proposed for Co containing clathrochelates.

The structure of clathrochelates suggests that a second proton could be then incorporated to the structure to form a H-H complex. Four distinct possibilities were investigated for such a second protonation: they are represented as (NCo), (NN), (NC) or (CC). Likewise, the formula $[^1Co(NN)HH]^1$ stands for a complex species in the singlet state, with two H attached to two adjacent N atoms of the organic ligand, with the overall charge of the complex being +1. Dihydrogen could evolve from such doubly protonated species giving rise to $[Co]^1$ which is then reduced at the electrode to complete the catalytic monomolecular path.

4.7. Analysis of main protonated intermediates

As discussed above, the structure of clathrochelates (Fig. 4-1) is such that various protonation sites can be considered for further dihydrogen evolution. We have hence considered single protonation in Co, N and C, and further second protonation. For each case, we have calculated high spin and low spin states. Table 4-9 displays selected

metric data for the most relevant protonated intermediates.

A detailed discussion of the structure of each particular single-protonated intermediate is not necessary, since it may be appreciated that the 4 + 2 coordination scheme holds approximately for all of them with the particularity that, of the two N atoms lying farther apart, there is always one that is more elongated than the other. The quasi square planar geometry for the clathrochelate persists in these intermediates, with ϕ angles below 170°. Additionally, the X-H distance (X stands for the protonated site in the clathrochelate cage) indicates that H is bound to the clathrochelate by a single bond. The larger X-H bond distance in the case of $[Co(Co)H]^0$ suggests that H could be more loosely bound in this species and it might be a reactive intermediate in the catalytic cycle.

Table 4-9. Calculated metric data for the relevant protonated intermediates in the HER mechanism. Theory level B3LYP/ LANL2DZ with ECP for Co and Cl.

	$[^1Co(Co)H]^0$	$[^3Co(Co)H]^0$	$[^1Co(N)H]^0$	$[^3Co(N)H]^0$	$[^1Co(C)H]^0$	$[^3Co(C)H]^0$	$[^1Co(NN)HH]^1$	$[^1TS]^1$
Bond distances in Å								
Co N1	1.91	1.88	1.82	1.90	1.78	1.87	1.92	1.93
Co N2	1.91	1.88	1.91	1.90	1.92	1.92	1.94	1.93
Co N3	1.92	1.90	1.95	1.94	1.94	1.94	1.94	1.94
Co N4	1.93	1.92	1.98	2.00	1.98	1.94	1.98	1.94
Co N5	2.37	2.41	2.09	2.32	2.06	2.37	1.98	2.48
Co N6	2.65	2.75	2.69	2.82	2.59	2.65	2.06	2.50
XH *	1.44	1.44	1.04	1.04	1.10	1.09	1.03	1.78
H---H							2.69	0.785
Angles in degrees								
θ (BNB'N')	5	18	12	26	6	12	70	3
ϕ (BCoB')	159	156	164	157	167	159	177	179
δ (HNN'H')							1	

*In the entry X-H, the X stands for the protonation site in the ligand of the clathrochelate.

In the case of doubly protonated complexes, any attempt to optimize η^2-$[Co(CoCo)HH]^1$ (i.e., direct double protonation in Co) lead to H_2 dissociation. However,

H-H complexes with H in separate positions of the ligand could be optimized. Double protonation in adjacent iminic carbons lead to unreasonable (and unconverging) structures, probably due to heavy structural changes in C due to a hybridization modification from sp_2 to sp_3. The simultaneous protonation of N and C, written here as (NC), or double protonation of N and Co, termed as (NCo), resulted in highly distorted molecular structures as well. Interestingly, the $[^3Co(NN)HH]^1$ species converged to $[^3Co(CoN)HH]^1$. All these species were found to possess notably high energies and were no further considered as plausible intermediates for the mechanism. The only doubly protonated structure with chemical sense was found to be $[^1Co(NN)HH]^1$. This structure with double protonation in adjacent N was not as distorted as all other doubly protonated intermediates. A look at bond distances and angles in Table 4-9, indicates that the organic cage in this molecule was quite close to a D_3 symmetry, and the N-H bond distance is essentially the same as in $[Co(N)H]^1$. Therefore, despite the favorable periplanar HNN'H' dihedral, the H-H distance is far too large (2.69 Å) to envision a direct dihydrogen evolution form $[^1Co(NN)HH]^1$.

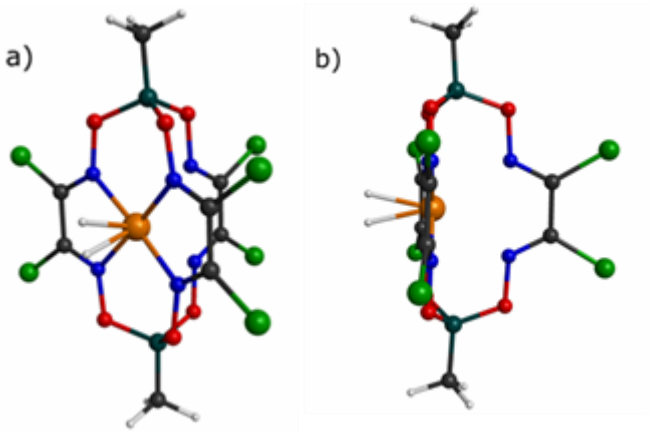

Fig. 4-10. Structure of the transition state leading to dihydrogen evolution from the model clathrochelate; a) perspective view, b) side view.

Subsequently, a saddle point search was undertaken, leading to a transition state (TS) consistent with a η^2-$[^1Co(CoCo)HH]^1$ low spin species (Fig. 4-10 a and b). The Co-H distance in the TS was calculated to be slightly larger than in $[^1Co(Co)H]^0$ while the H-H distance was 0.79 Å which is very close to the 0.76 Å in H_2. The structure of the TS

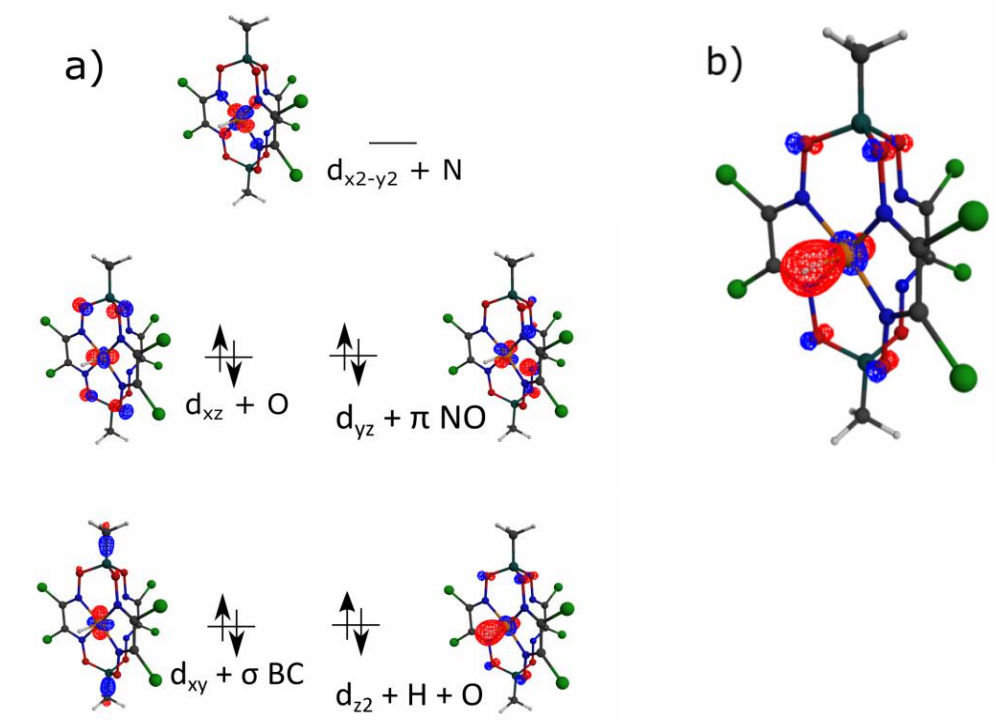

Fig. 4-11 a) Orbital d manifold in $[^1Co(Co)H]^0$; we note that these orbitals are not degenerate b) Magnification of the cage of $[^1Co(Co)H]^0$ showing the dz^2 orbital. The dz^2 orbital of Co is crucial in the binding of H^+, by forming a σ bond with its empty 1s orbital

suggests that the Co central atom has a relevant role in the electrocatalytic performance of the model clathrochelate. Any attempt to locate a TS with a high-spin electronic configuration failed.

An overall structural analysis of the various protonated intermediates calculated here, suggests that a putative sequence such as $[^1Co(Co)H]^0 + H^+ \rightarrow [^1Co(NN)HH]^1 \rightarrow [^1Co(CoCo)HH]^1$ (TS) $\rightarrow [^1Co]^1 + H_2$ should not be much favored because of the notable structural rearrangements involved in passing from $[^1Co(Co)H]^0$ to $[^1Co(NN)HH]^1$ and then from $[^1Co(NN)HH]^1$ to $[^1Co(CoCo)HH]^1$ (TS).

Among all intermediates, the $[^1CoH]^0$ species appears as the most relevant protonated intermediate and will be given special attention regarding its electronic structure. Molecular orbital analysis (Fig. 4-11 a) shows the d^8 manifold typical of a Co^I, with four filled d orbitals and one empty. The only d orbital contributing to the binding of H^+

is the filled dz^2 combined with the empty 1s of H^+ (magnification in Fig. 4-11 b). Such, interaction can be viewed as metal-to-ligand charge transfer to achieve a partial reduction of H^+ in this intermediate.

4.8. Energetic analysis of the HER mechanism

After the geometric description of main species in the proposed mechanism, an energetic analysis is presented, in order to support the partial conclusions obtained so far. The full energetic description presented in the main text, was undertaken with B3LYP functional and cc-p-VTZ for Co and cc-p-VDZ for all other atoms. The energy calculations on some relevant intermediates were also calculated with BP86 and PBE0 functionals (Table 4-10 Table 4-13), displaying the same trend as the B3LYP functional. Total energies for all species calculated in this work are presented in Table and Table (within the annex section at the end of this thesis).

Table 4-10. Comparison of the energies obtained with various functionals for the process $[^1Co]^{-1} + HA = [^1Co(Co)H]^0 + A^-$. Calculated with the basis set cc-pVTZ for Co and cc-pVDZ for all other atoms, where HA stands for trifluoroacetic acid, and A^- is the trifluoroacetate anion.

Functional	E(kJ/mol)
B3LYP	117.85
PBE0	125.18
BP86	150.58

Table 4-11. Comparison of the total energy (in Hartrees) between some species of the HER mechanism studied here, calculated with different DFT functionals and the basis set cc-pVTZ for Co and cc-pVDZ for all other atoms.

	$[^1Co]^{-1}$	$[^1Co(Co)H]^0$	$[^1Co(NN)HH]^1$	TS
B3LYP	-5281.247299	-5281.746202	-5282.069582	-5282.026552
BP86	-5282.823112	-5283.309549	-5283.666282	-5283.634031
PBE0	-5279.831869	-5280.327978	-5280.656901	-5280.605563

Table 4-12. Comparison of the total energy (in kJ/mol) between some species of the HER mechanism studied here, calculated with different DFT functionals and the basis set cc-pVTZ for Co and cc-pVDZ for all other atoms.

	$[^1Co]^{-1}$	$[^1Co(Co)H]^0$	$[^1Co(NN)HH]^1$	TS
B3LYP	-13865914.78	-13867224.65	-13868073.69	-13867960.71
BP86	-13870052.08	-13871329.22	-13872265.82	-13872181.15
PBE0	-13862198.57	-13863501.11	-13864364.69	-13864229.90

Table 4-13. Relative energies (in kJ/mol) between some species of the HER mechanism studied here, calculated with different DFT functionals and the basis set cc-pVTZ for Co and cc-pVDZ for all other atoms.

	$[^1Co]^{-1}$	$[^1Co(Co)H]^0$	$[^1Co(NN)HH]^1$	TS
B3LYP	1310	0	-849	-736
BP86	1277	0	-937	-852
PBE0	1303	0	-864	-729

Fig. 4-12 shows an energetic diagram of the electrocatalytic HER mechanism. Our results show that after the $1e^-$ reduction of $[Co]^0$ (Fig. 4-12, panel a, black), the first protonation step is likely to occur preferentially in Co, with $[^1Co(Co)H]^0$ being more stable than $[^3Co(C)H]^0$ and $[^3Co(N)H]^0$ by 8 and 74 kJ/mol, respectively (Fig. 4-12, panel b). As might be expected from chemical intuition, direct protonation on Co differentiates the energies of both spin configurations more markedly than protonation in the ligand, with the proton increasing the strength of the ligand field reflected as a stabilization of 157.55 kJ/mol of the low spin configuration in comparison to the high spin complex. The second protonation step is even more energetically expensive, with

the [^{1}Co(NN)HH]^{1} species being the most energetically favored (Fig. 4-12, panel c). The energies of other doubly protonated species were far above the presented scale (See tables Table A9 and Table A10 within the annex section at the end of this thesis, for the numeric values), possibly as a consequence of structural distortions mentioned in the previous sections.

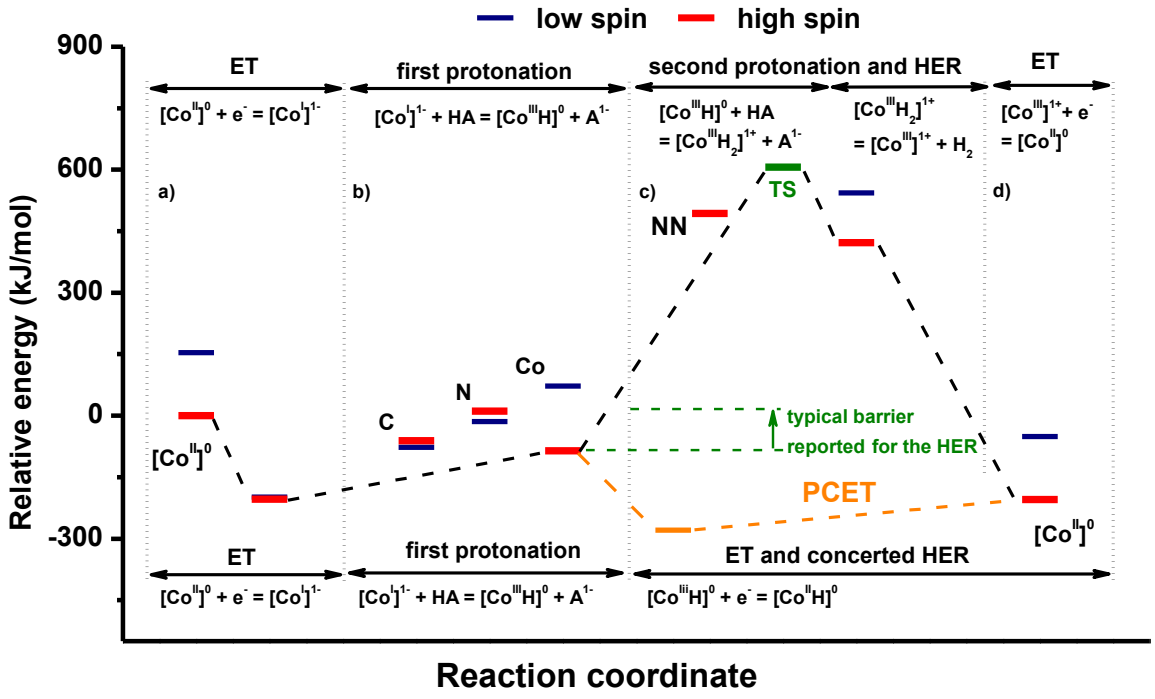

Fig. 4-12. Energy profile for the hydrogen evolution reaction catalyzed by the model clathrochelate investigated in this work. Blue thin lines represent high spin species, red thick lines stand for the low spin species. Dashed lines connecting different states have been put as a guide to the eye. The figure is composed of four panels. Panel (a) represents the energy evolved upon the one electron reduction of the catalyst, high and low spin energies for the $[Co]^{-1}$ species are close enough that cannot be appreciated separately in the figure. Panel (b) represents the energy change associated to the first protonation of the catalyst, distinct protonation sites are written near each line. Each state in panel (b) corresponds to an equivalent coordinate of reaction. Panel (c) up, conveys the energy change evolved upon the second protonation and further hydrogen evolution through a transition state (represented in green). Panel (c) down, depicts the one-electron reduction of the clathrochelate with the proton in Co, and the further Proton Coupled Electron Transfer. Panel (d) deals with the reduction of $[Co]^{+}$ to $[Co]^{0}$ to regenerate the initial state of the catalyst. It should be kept in mind that panels (a) and (d) depict only the relevant cobalt species; however, the initial state in panel (a) truly corresponds to $2[Co]^{0}$ + 2HA and the final state in panel (d) is $2[Co]^{0}$ + H_2 + $2A^{-}$, with HA being trifluoroacetic acid.

An inspection of Fig. 4-12 could suggest that $[^1Co(NN)HH]^1$ is an intermediate species before reaching the TS. However, heavy structural rearrangement discussed above makes it appear more logic that, after the first protonation yielding $[^1Co(Co)H]^0$, the second proton could be incorporated to form directly the transient TS and thereby evolve H_2. Nevertheless, the doubly protonated $[^1Co(NN)HH]^1$ species could exist in acidic solutions, but probably with no relevant role in homogeneous electrocatalysis. Finally, after dihydrogen evolution, the catalytic cycle is closed by the one-electron reduction from $[Co]^1 + 1e^- = [Co]^0$.

However, the energetic barrier calculated for the HER is far too high, since typical barriers for the HER catalyzed by organometallic complexes are around 90 kJ/mol,[162] which is in open contrast with the calculated barrier of 691.65 kJ/mol. A revision of the literature indicates that the mechanism in Fig. 4-9 is the only one proposed for clathrochelates,[127,130] therefore it is tacitly assumed that this is the actual operating mechanism. Though, our results suggest that, at least for the $Co(Cl_2Gm)_3(B\text{-}CH_3)_2$ complex, the mechanism depicted in Fig. 4-9 is not much favored.

Accordingly, instead of the ECCE mechanism discussed so far, we have investigated the possibility of an ECEC pathway (Fig. 4-13), i.e., the one-electron reduction of the most promising $[^1Co(Co)H]^0$ intermediate to yield the species $[^2Co(Co)H]^{-1}$ presenting a d^9 electronic configuration. Consequently, all further computational efforts were

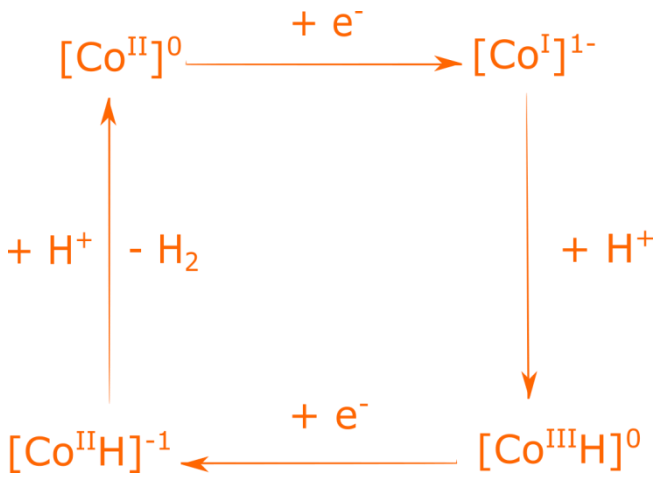

Fig. 4-13. Alternative ECEC monomolecular catalytic mechanism proposed for the $Co(Cl_2Gm)_3(B\text{-}CH_3)_2$ clathrochelate.

devoted to the investigation of such a putative species and the possibility to find another transition state that would be more energetically favorable than the one depicted in Fig. 4-9.

The $[^2Co(Co)H]^{-1}$ species could be optimized. Structurally it was similar to $[^1Co(Co)H]^0$, with Co-N distances and bond angles presenting close values (Table 4-14).

Table 4-14. Comparison of the calculated metric data for the intermediates protonated directly in Co. Theory level B3LYP/ LANL2DZ with ECP for Co and Cl.

	$[^1Co(Co)H]^0$	$[^3Co(Co)H]^0$	$[^2Co(Co)H]^{-1}$
Bond distances in Å			
Co N1	1.91	1.88	1.88
Co N2	1.91	1.88	1.89
Co N3	1.92	1.90	1.88
Co N4	1.93	1.92	1.89
Co N5	2.37	2.41	2.71
Co N6	2.65	2.75	2.82
Co-H	1.44	1.44	1.47
Angles in degree			
θ (BNB'N')	5	18	26
ϕ (BCoB')	159	156	151

The orbital d manifold for this species is characteristic of a d^9 transition metal (Fig. 4-14): the Single Occupied Molecular Orbital (SOMO) is essentially composed by the combination of the d_{z2} orbital of Co with the π* orbital of the glyoxime moieties that lie closer to the metal (Fig. 4-14 a). Additionally, the d_{z2} orbital of Co combines with the empty 1s orbital of H^+ to form the σ bonding orbital that justifies the binding between these two species in a similar manner as in the $[^1Co(Co)H]^0$ species (Fig. 4-11 b).

Furthermore, there is an energetic gain of 194.08 kJ/mol upon such a one-electron reduction (Fig. 4-12, orange). Nevertheless, all attempts to optimize doubly protonated intermediates failed, including the possibility of an H_2 complex with a Co(0) species. Likewise, no transition state of the type shown in Fig. 4-10 could be found. It is worth

mentioning that a thorough computational study was performed, and numerous initial guesses of possible structures were tested.

These facts analyzed together made us propose that the last step in the HER catalyzed by the $Co(Cl_2Gm)_3(B\text{-}CH_3)_2$ clathrochelate should be concerted. Concerted steps are not bizarre and have been reported several times in the literature regarding computational chemistry. In the words of Sharon Hammes-Schiffer et al. "The concerted PCET mechanism is thought to lower the overpotential required for catalysis by avoiding high-energy intermediates".[169] For more details about this issue the interested reader may revise an interesting perspective article from the journal Inorganic Chemistry.[169]

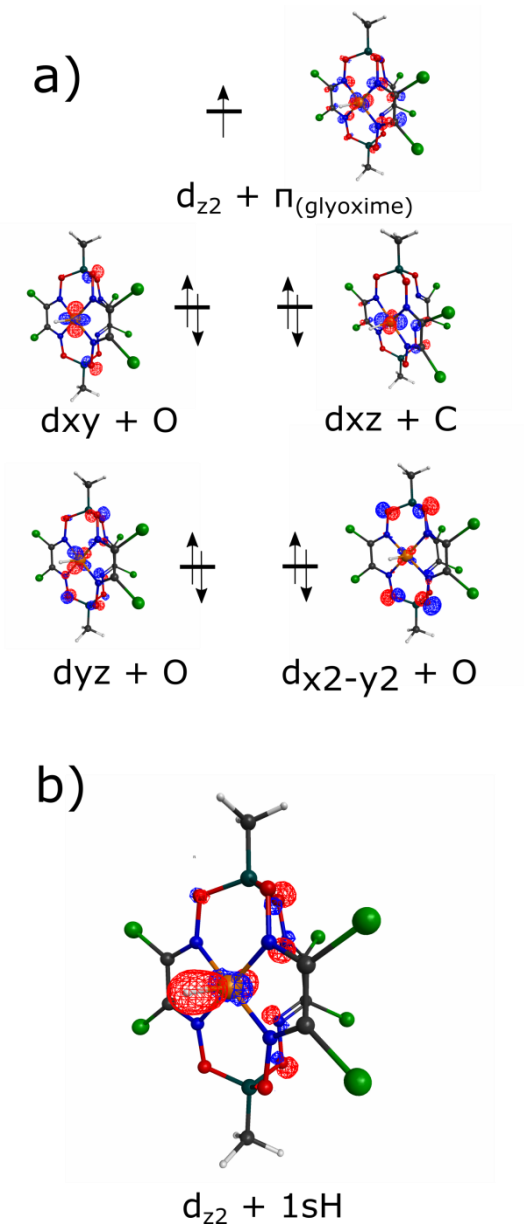

Fig. 4-14. Orbital d manifold in $[^2Co(Co)H]^{-1}$; we note that these orbitals are not degenerate b) Magnification showing the dz^2 orbital of Co forming a σ bond with the empty 1s orbital of H^+.

The basic idea of a concerted reaction of this kind (also known in the literature as Proton Coupled Electron Transfer, PCET or Electron Proton Transfer, EPT)[169] is that the second proton and the ET from Co to form H_2 does not occur sequentially (as in

ECEC or ECCE) but simultaneously, i.e., the proton and the electron are transferred at the same time. Another recent example of a concerted PCET reaction is given by Frank Neese and coworkers in order to explain the up-hill electrochemical reduction of carbon dioxide by Ni cyclam.[227] Considering the possibility of PCET for the last step, the ECEC mechanism appears to be a reasonable option for the HER electrocatalytic mechanism of the $Co(Cl_2Gm)_3(B\text{-}CH_3)_2$ clathrochelate.

4.9. Conclusions for Chapter 4

In this Chapter we fully addressed the homogeneous reduction of protons by a model cobalt clathrochelate in the homogeneous phase. To the best of our knowledge, such work was done for the first time. First, geometry optimizations were carried out with several functionals and basis sets. An analysis of published literature and the results obtained in this work suggest that B3LYP is the most appropriate functional to perform DFT calculations on clathrochelates. The geometry optimization did not show appreciable differences when the LANL2DZ basis set with effective core potentials for Co and Cl was employed, or when the mixture of the all-electron cc-pVTZ for Co and cc-pVDZ for all other atoms was utilized. Considering that the former basis set being the less expensive from a computational perspective, it was selected for geometry optimizations and Hessian calculations, while the latter was used for refining electronic energies and molecular orbitals.

Second, the DFT and the XRD geometries were employed to fit the experimental EXAFS spectrum of the clathrochelate. Despite the slight differences between both geometries, EXAFS proved to be sensitive to such minor differences, and therefore the adequate fitting of the observed EXAFS using the DFT geometry was possible with more variables than in the case of the XRD geometry. Nevertheless, the DFT optimized

geometry was good enough to allow the fitting of the EXAFS spectrum. Besides, another experimental quantity used to test our theory was the DFT calculation of the equilibrium potential for the model clathrochelate, with an error of 170 mV, which can be considered a good result given the inherent simplifications of the methodology employed, for example, the DFT functional which is not the true functional (the true functional is unknown, as explained in the section devoted to DFT in Chapter 1), the incomplete basis set (the use of a complete basis set is impossible, because a complete basis set would have infinite mathematical functions), the continuum treatment of solvation, and the harmonic oscillator approximation to estimate thermodynamic quantities. It is worth to mention that the methodology employed here is the one that is most widely used in nowadays research.

Subsequently, the three redox states of the clathrochelate and their high and low spin configurations were explored. The HER mechanism calculated here was based on a proposition made in previous publications.[127,130] The explored ECCE mechanism consisted in the activation of a $[Co]^0$ clathrochelate by one-electron reduction to yield the catalytically active $[Co]^{-1}$. In such a species, the Co central atom was found to move 0.7 Å within the organic cage, to be more accessible for direct protonation. In the process, two N atoms of the organic cage decoordinated, thus allowing H^+ binding through a σ bond between the filled dz^2 orbital of Co and the empty 1s orbital of H^+. Doubly protonated species could be optimized, nevertheless, further HER starting from a doubly protonated species, and then involving a transition state with η^2-$[^1Co(CoCo)HH]^1$ character was considered unlikely, not only because of important structural rearrangements involved, but also because of the high energy of the transition state. Alternatively, we have studied an ECEC mechanism on the basis of the reduction of the singly protonated $[^1Co(Co)H]^0$. In the case of this mechanism, the $[^2Co(Co)H]^{-1}$

species could be optimized and its structure was rather similar to $[^1Co(Co)H]^0$. However, neither doubly protonated species, nor an H_2 complex directly bound to Co, nor a transition state were found. These facts prompted us to propose that the last step in the HER catalyzed by the $Co(Cl_2Gm)_3(B\text{-}CH_3)_2$ clathrochelate should not occur by sequential steps, but as a proton coupled electron transfer.

CHAPTER 5. Non-steady state response observed through IMVS in Rhodium doped Strontium Titanate based photoelectrodes

5.1. Introduction

Different experimental techniques and mathematical models have been developed and reported in the literature to account for heterogeneous photoelectrochemical kinetics. Among these techniques, Intensity Modulated Photovoltage Spectroscopy (IMVS) has been mostly used for the characterization of dye-sensitized solar cells.[27,32,75–77] In addition to PEIS analysis; which we have been using so far to analyze the kinetics of both the HER and the OER at the surface of Rh:$SrTiO_3$ photoelectrodes, surface-modified by addition of co-catalysts of diverse nature (see previous chapters), we have also characterized our Rh:$SrTiO_3$-based photoelectrodes by means of IMVS. In order to facilitate the discussion, we will first recall the fundamental aspects of IMVS analysis and will briefly compare IMVS with PEIS in order to outline main differences, despite the fact that the topic was already addressed in the Bibliographic Overview (Chapter 1). As already shown, the purpose of PEIS is to record a usual EIS spectrum at a constant level of illumination. EIS spectra are obtained by applying a small ac current $\tilde{I}$ (or voltage $\tilde{U}$) perturbation to the stationary system, and by recording the sinusoidal voltage $\tilde{U}$ (or current $\tilde{I}$) response. EIS data are analyzed through a transfer function known as impedance (Z) which is defined according to eq. 5-1, where the ~ symbol on top of the variables indicates the periodic (harmonic) modulation.

$$Z = \frac{\tilde{U}}{\tilde{I}} \qquad (5\text{-}1)$$

In the case of IMVS, the photoelectrode is held at open circuit conditions and a constant level of illumination is applied to the photoelectrode, joined to a small ac perturbation of the illumination level $\widetilde{\Phi}$. This causes the development of an oscillating photopotential ($\widetilde{U}$). IMVS is analyzed through a transfer function as well as EIS, defined in eq. 5-2

$$H = \frac{\widetilde{U}}{\widetilde{\Phi}} \qquad (5\text{-}2)$$

Where H stands for the transfer function for IMVS, $\widetilde{U}$ is the modulated photovoltage, and $\widetilde{\Phi} = led_0\left(1 + e^{-i\omega t}\right)$ is the modulation of light, while led_0 represents the LED power.

At this stage, it is necessary to discuss the physical meaning of the IMVS transfer function. When an increasing illumination intensity is applied to a photoelectrode, usually a greater photovoltage is measured. This would increase the numerator ($\widetilde{U}$) in the fraction written in eq. 5-2, causing an increase in the absolute value of H. Conversely, an increased level of illumination will certainly increase the denominator of eq. 5-2 causing a contraction in the absolute value of H. Which of these two effects predominates will determine whether the IMVS spectrum will shrink or expand upon increased light power.

Experimentally, it is observed that an increasing light power causes a contraction of IMVS, which permits to conclude that the increase in the incident light power dominates the behavior of the absolute value of H.

The analogy between PEIS and IMVS if even more evident when the transfer function H is depicted in the Nyquist and Bode representations (Fig. 5-1, a c e).

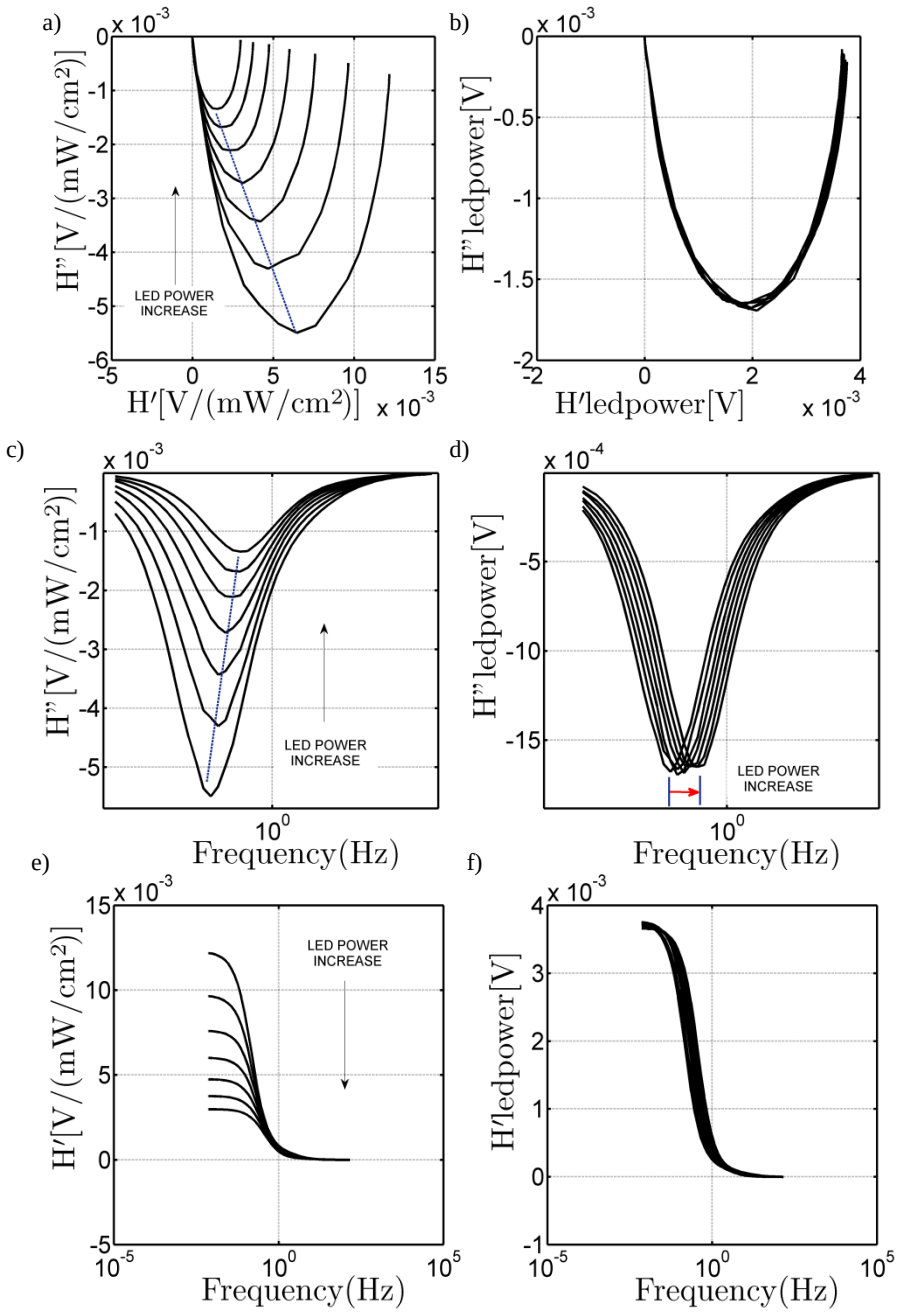

Fig. 5-1. Experimental IMVS response for the test cell provided by the company solaronix, effect of light intensity; a) Nyquist c) Bode of the imaginary component e) Bode of the real component; b) d) and e) similar to a) c) and e) but normalized against the led power.

Fig. 5-1 a c and e show the experimental IMVS response of a dye-sensitized solar cell[78–80] supplied by the Swiss company *Solaronix* as a complement in the training for using the optical bench coupled to the Modulab potentiostat that allowed performing all

photoelectrochemical experiments reported in this thesis. In current literature, PEIS and EIS spectra are usually represented as (-Z", Z') plots in Nyquist coordinates; therefore, the information appear in the first quadrant of the complex plane. However, it is also possible to find photoelectrochemical literature (e.g. in the middle of the 90s) where the Nyquist representation was (Z", Z').

In the case of IMVS, apparently there is no current agreement regarding the Nyquist representation[76] as it is for EIS, where the imaginary component of the impedance is plotted with the reversed sign. Therefore, in this work the axis of the imaginary component of H shall be depicted as is.

A recent publication clearly indicated that the units of H, which follow directly from its definition (eq. 5-2), is $[V/sun]$,[76] where 1 sun = 100 mW/cm^2. For the sake of consistency with the units of light power employed in this thesis, the units of IMVS that shall appear henceforward are $[V/\ (mWcm^{-2})\ ]$.

The parameter calculated from IMVS spectra when the technique is applied to dye-sensitized solar cells is the electron lifetime (τ), which is directly derived from the maximum of $H^{"}$. Indeed, Fig. 5-1 a, c and e show the evolution of IMVS spectra for a *Solaronix* test cell in the Nyquist and Bode representations at different levels of illumination, while Fig. 5-1 b, d and f stand for the same plots but H has been multiplied by the absolute light power. It may be observed that the absolute value of H is independent of light intensity, and that the shrinking of H in the Nyquist plot was due to the increase of the denominator of the transfer function. Though, the frequency of the maximum of $H^{"}$ does move with increased light power (highlighted with a red arrow in Fig. 5-1 d), indicating that the electron lifetime decreases with increasing illumination power.

Nonetheless, the interest of this thesis is not devoted to the kinetic analysis of dye-

sensitized solar cells, but to kinetic determinations of water splitting in photoelectrochemical cells (PEC), as shall be presented now.

5.2. Comments on the existing analytical models of IMVS

Even though DSSC and PEC systems are characterized using the same photoelectrochemical techniques, the processes taking place in DSSC and PEC are so fundamentally different that the interpretation of the experimental results using either IMVS or PEIS is totally different. More details on these differences were given in Chapter 1 devoted to the Bibliographic Overview.

The photomodulated electrochemical spectroscopy was created by Laurie M. Peter and co-workers in the middle of the 80s.[228] The seminal theoretical foundations to describe mathematically these techniques were developed by the same author and co-workers between 1995 and 1997.[71,72,213,229] It is interesting to note that in the case of PEC systems, the development of PEIS and IMPS was carried out in parallel, with several publications aiming to give a comparison between these two techniques. However, it is striking to note the absence of any mention to IMVS for the characterization of PEC systems 30 years after its invention. In contrast, IMVS characterization of DSSC has been widely developed and applied to multiple cells. To the best of our knowledge, there is only one article published in 2016 presenting the analysis of IMVS of a PEC cell which photoelectrode was n-type hematite.[55] The authors of this publication explicitly recognized that, to the best of their knowledge, their paper was the first to present a discussion of IMVS analysis of a PEC used for water splitting. The approach of the authors was empirical, and they did not analyze the photoinduced processes with the help of kinetic models.

A thorough revision of the literature revealed only one mention to a possible analysis by

IMVS of a PEC cell. The mathematical description employed consisted in the same kinetic model used in this thesis to address the kinetics by PEIS.[58,71,72,115,213,229]

In particular, Ponomarev and Peter described the possibility to measure very fast reactions under coulostatic conditions at low illumination levels, so that the photopotential was no larger than a few millivolts.[229] Under these conditions the complex plane plot of $\omega U(\omega)$ should give a semicircle which low frequency intercept should occur at $\omega U(\omega)_{\omega\to 0} = (\mathrm{I}_0/C)(k_t/(k_t + k_r))$, which high frequency limit should be $\omega U(\omega)_{\omega\to\infty} = (\mathrm{I}_0/C_{SC})$ and the maximum of which should be located at $\omega_{max} = (k_t + k_r)$. However, such assertion has not been taken into consideration in the following publications, not by the authors or by other researchers. Indeed, in the framework of this thesis, the first analysis of IMVS responses was performed by plotting a Nyquist representation of the product $\omega U(\omega)$, as suggested by Ponomarev and Peter, but such graph did not display any tendency, and certainly not the one predicted (or suggested) by the authors in their original publication.

5.3. Experimental IMVS response of Rh:$SrTiO_3$ – Pt photoelectrodes

The experimentally measured IMVS responses of Rh:$SrTiO_3$ – Pt photoelectrodes obtained in this thesis are presented in Fig. 5-2 a to d. The shape of the IMVS response is strikingly different to any previous report obtained with this technique.[27,32,55,75–77] The frequency sweep was performed from high to low frequencies, and a spiral shape was repeatably observed in the Nyquist representation (Fig. 5-2 a). The real and imaginary components of H begin with zero absolute value: this is consistent with the initial zero photopotential, that further develops as the experiments runs. Then, as the frequency decreases, the real and imaginary components of H oscillate while the absolute value of the transfer function increases.

It is worth to note that these spirals can be observed only when the points-per-decade being measured is relatively large. In this work, the number of points per decade being measured was increased form the default value (10) up to 60. IMVS determinations with 10 points per decade gave poorly resolved spirals.

When light is made more intense, the spirals show a tendency to contract. This could be due either to the increase in the denominator (Φ) of the transfer function (H), or due to other factors that will be discussed in detail in the next sections. Apparently, the change in LED power also causes an important phase shift in the IMVS response, as may be observed in the Bode representations of H'', H' and the phase angle (Fig. 5-2 b to d). The

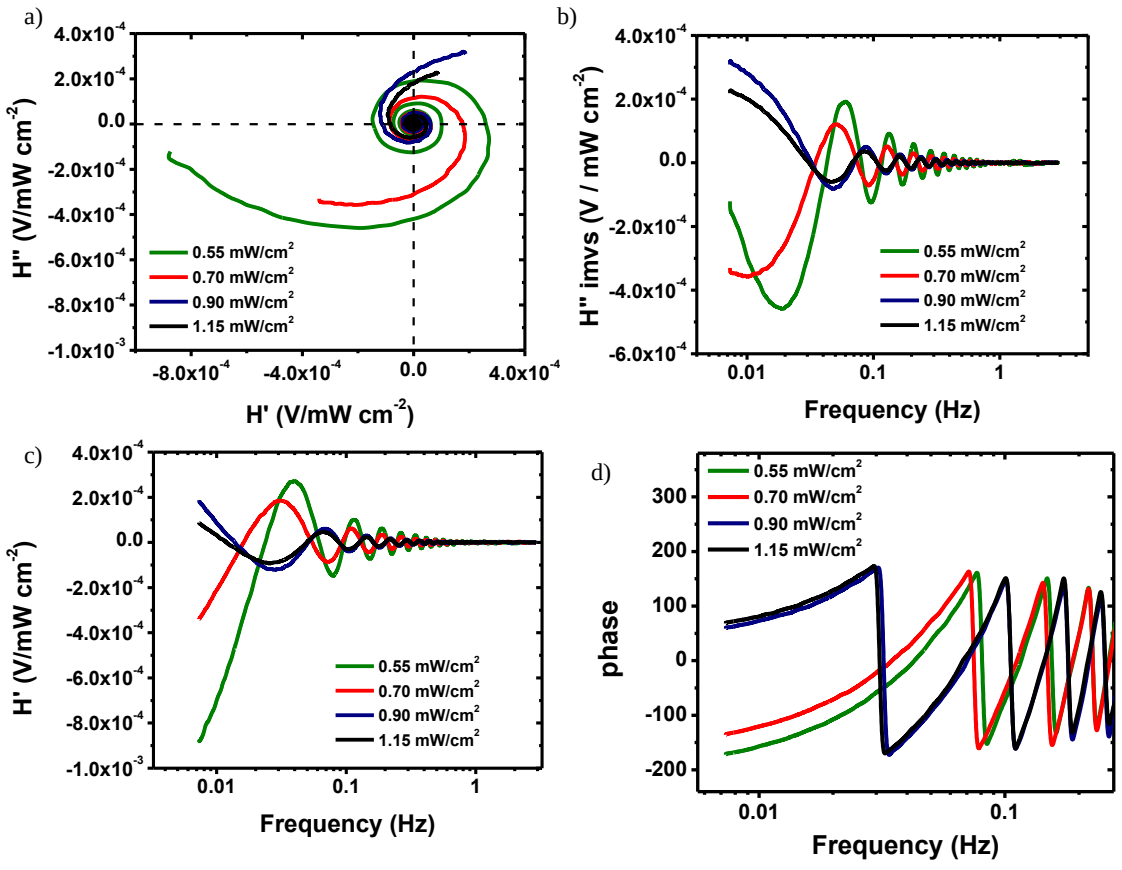

Fig. 5-2. Experimental IMVS response for a Rh:$SrTiO_3$ –Pt photoelectrode, effect of light intensity; a) Nyquist representation; b) Bode representation of the imaginary component of H;) Bode representation of the real component of H; d) Bode plot of the phase angle.

alternating sign of the phase angle (Fig. 5-2 d) is consistent with the shape of the Nyquist representation of H, thus describing the alternative pass through the different quadrants of the complex plane plot.

Another experimental observation to note is the clock-wise rotation of the spirals in the Nyquist plot of Fig. 5-2 a, when the frequency sweep is from high to low value.

From a mathematical viewpoint, the first step is to develop a model that adequately reproduces the oscillating modulation of the perturbing light. Such light modulation is measured in a silicon-based photodetector providing a potential difference that is proportional to the LED power. The photodetector is located outside the PEC and receives the same light as the photoelectrode. From now on, the photovoltage measured by the silicon photodetector shall be represented with the letter A. Of course, the inherent periodic modulation of A gives rise to a real and imaginary component, hereto represented as A' and A'', respectively. The experimental Nyquist representation of the photodetector voltage is depicted in Fig. 5-3 a. As expected, the figure describes concentric circles with increasing radius, the radius being proportional to the LED power.

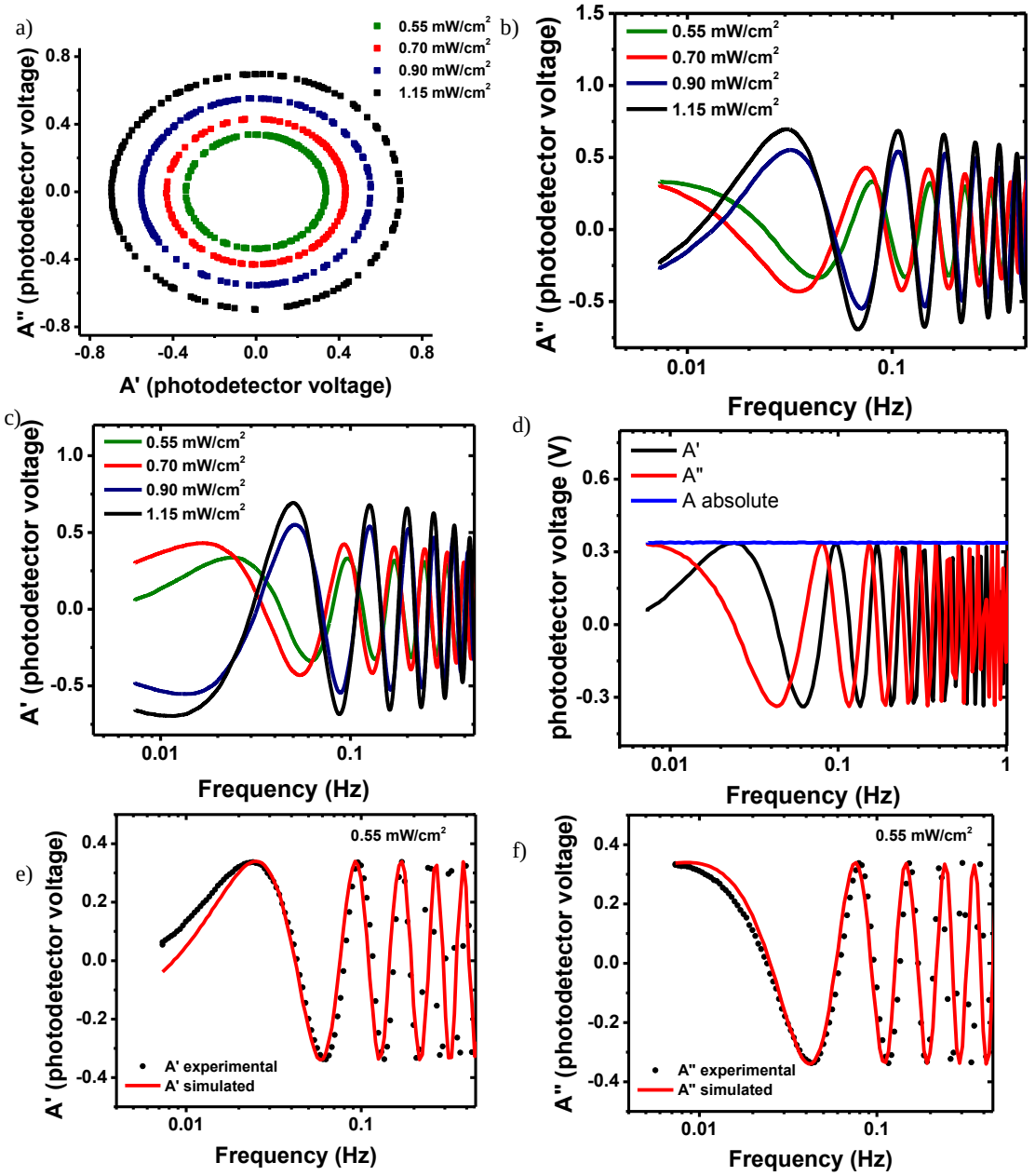

Fig. 5-3. Experimental data obtained from the photodetector that provides a measure of the intensity of light in IMVS measurements; a) Nyquist representation; b) Bode representation of the imaginary component of A; c) Bode representation of the real component of A; d) Bode plot of A'' and A' and the absolute value of A e) Experimental and simulated real part of the light modulation. f) Experimental and simulated imaginary part of the light modulation.

Fig. 5-3 b and c show the Bode plots of the real and imaginary components of A. The IMVS experiments reported in this thesis obtained at different light intensities, were recorded using the same photoelectrode one after the other. Indeed, the four measurements reported in Fig. 5-3 at LED powers of 0.55, 0.70, 0.90 and 1.15 mW/cm^2 were performed between the same initial and final frequencies, and the change in light intensity was performed automatically by the software of the Modulab potentiostat.

Interestingly, Fig. 5-3 b and c depict the same trend in phase shift as Fig. 5-2 b and c. Therefore, the phase shifts observed in the experimental Bode plots of H" and H' reported in Fig. 5-2 b to d, are not due to changes in the photoelectrode surface associated to increased illumination levels, but due to inherent instrumental uncertainty of the ac controller of the LED.

Fig. 5-3 d illustrates an interesting feature of the light modulation employed in IMVS. A'' and A' are represented on the same plot, along with the absolute value of A_{abs}, where the following condition holds: $A_{abs} = (A''^2 + A'^2)^{1/2}$. Fig. 5-3 d clearly exemplifies how the light intensity can be modulated periodically while keeping a constant absolute value, corresponding to an established level of illumination.

Fig. 5-3 e and f show A'' and A' in Bode coordinates. The solid red line stands for a fit of light modulation according to equation $\Phi = led_0\left(1 + e^{-i\omega t}\right)$ where led_0 stands for the constant bias illumination, and the factor $\left(1 + e^{-i\omega t}\right)$ accounts for the periodic oscillation of light, with i being the imaginary number, ω the angular frequency of the modulation, and t the time. At this point it is worth to recall Euler's trigonometric identity $e^{i\theta} = cos\theta + i\, sin\theta$ and $e^{-i\theta} = cos\theta - i\, sin\theta$, that clearly shows the periodic nature of Φ. In most of the photoelectrochemical literature, light modulation is treated by using the imaginary function;[213,229] yet, to the best of our knowledge there is one report where the trigonometric functions are directly employed.[32] In any case, both

treatments are entirely analogous.

The frequency sweep rate is controlled automatically by the potentiostat. For frequencies below 1 Hz, the measurement of one IMVS point takes more than 1s, for example, and the measurement of one point at 0.1 Hz takes at least 10 s. Therefore, it was experimentally observed that the time elapsed between two measured points was inversely proportional to the corresponding frequency, i.e., $t \propto \omega^{-1}$ at frequencies below 1 Hz.

5.4. Mathematical model of the IMVS response

The origin of the unusual shape of the IMVS spectra reported in this thesis was initially puzzling. In order to provide an explanation for the observed (spiral) behavior, it was hypothesized that the classic model for heterogeneous electrochemical kinetics at illuminated semiconducting electrodes was still valid in our experimental conditions.

The simplest (and the first) kinetic model that we used coincides with the one presented by Ponomarev and Peter.[229] It is described by the following system of differential equations:

$$\frac{dQ_{sc}}{dt} = I_0\left(1 + e^{-i\omega t}\right) - k_r(Q_{sc} - Q_H) \qquad (5\text{-}3)$$

$$\frac{dQ_H}{dt} = k_t(Q_{sc} - Q_H) \qquad (5\text{-}4)$$

$$U = \frac{Q_{sc}}{C_{sc}} + \frac{Q_H}{C_H} \qquad (5\text{-}5)$$

Where Q_{sc} and Q_H are the charge located in the space charge and the Helmholtz layer, respectively; k_t and k_r are the charge transfer and recombination rate constants; i is the imaginary number.

The first differential equation represents the time variation of the electric charge in the space charge ($\frac{dQ_{sc}}{dt}$). The time evolution of Q_{sc} is due to the interplay between (i) the modulated photoexcitation process $I_0\left(1 + e^{-i\omega t}\right)$, which is a positive term because illumination promotes minority carriers (electrons for a p-type semiconductor) to the conduction band; and (ii) the rate of recombination $k_r(Q_{sc} - Q_H)$, which is negative because recombination removes photoexcited electrons from the space charge. Note that the recombination rate is $k_r(Q_{sc} - Q_H)$. Indeed, the difference $(Q_{sc} - Q_H)$ equals the amount of charge accumulated at the surface (the physical meaning has already been discussed during the analysis of PEIS data), since the recombination rate is proportional to the surface concentration of electrons.

The second differential equation describes the time evolution of Q_H. Indeed, the charge in the Helmholtz layer increases with the electron transfer; this is taken into account by the term $k_t(Q_{sc} - Q_H)$, where such electron transfer is also proportional to the charge accumulated at the surface.

The last equation accounts for the sum of potential drops across the system, i.e., the overall measured potential (U) should equal the sum of the potential drop inside the space charge (Q_{sc}/C_{sc}) plus the potential drop in the Helmholtz layer (Q_H/C_H).

Additionally, the dynamic model was extended in order to include the presence of surface states, as described by Ponomarev and Peter, using the following system of differential equations.

$$\frac{dQ_{sc}}{dt} = I_0\left(1 + e^{-i\omega t}\right) - j_{ss} - k_r(Q_{sc} - Q_H) \qquad (5\text{-}6)$$

$$\frac{dQ_H}{dt} = k_t(Q_{sc} - Q_H) \qquad (5\text{-}7)$$

$$U = \frac{Q_{sc}}{C_{sc}} + \frac{Q_H}{C_H} \quad (5\text{-}8)$$

$$\frac{dQ_{SS}}{dt} = j_{SS} \quad (5\text{-}9)$$

$$\frac{Q_{SS}}{C_{SS}} + j_{ss}R_{ss} = \frac{Q_{sc}}{C_{sc}} \quad (5\text{-}10)$$

Where j_{ss} is the current associated to the charging of surface states while R_{SS} and C_{SS} are the resistance and the capacitance associated to surface states. All other symbols were already described.

In this extended model, the surface states only contribute to chare accumulation and do not play any role in the electron transfer process. Equations 5-6 to 5-10 are similar to those of the simpler model described by equations 5-3 to 5-5. The differences between the two models are, (i) in equation 5-6, the effect of charging of surface states in removing charge from the space charge is considered by including j_{SS}, which is calculated according to equation 5-9, and (ii) the effect of surface states in the redistribution of charge in the space charge expressed by equation 5-10, means that the

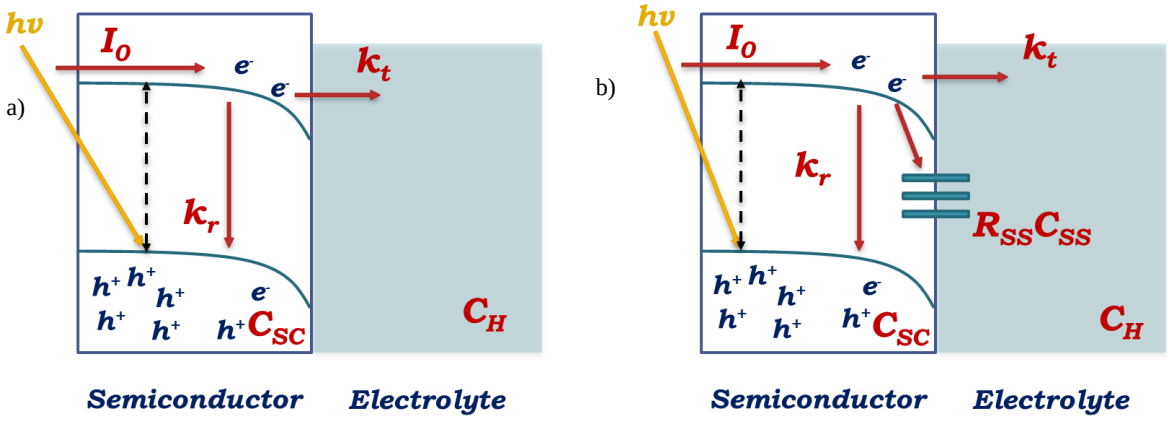

Fig. 5-4. Comparison of kinetic models employed in this work to simulate non-steady-state IMVS responses; a) without the consideration of surface states; b) considering the contribution of surface states

potential drop in the space charge (Q_{sc}/C_{sc}) is equal to the sum of the potential drop caused by charge accumulation in surface states (Q_{ss}/C_{ss}) and the potential drop associated to the charging of surface states ($j_{SS}R_{SS}$). The initial conditions for the two systems of differential equations was set so that $H = 0$ at $t = 0$. A graphical comparison of the physical meaning of both models is presented in Fig. 5-4 a and b.

5.5. Comments on the methods employed for the numerical solution of the system of first order ordinary differential equations

The first set of ordinary differential equations was implemented and solved numerically in Matlab, a very versatile program with a wide library of built-in numerical methods that are available for the most diverse applications. In particular, we are interested in the solution of equations 5-3 to 5-5 and equations 5-6 to 5-10, as discussed in the previous section. The numerical methods available in Matlab to solve ordinary differential equations use the acronym "ode" and a number (with or without letters). Overall, there are seven different methods that are candidates to be used for the solution of the present problem, whose names are ode45; ode23; ode113; ode15s; ode23s; ode23t and ode23tb. The first solver, ode45, is based on the explicit Runge-Kutta (4,5) method. It is a one-step solver in the sense that, for the computation of the solution at $y(t_n)$ it is only required the solution at the previous time $y(t_{n-1})$. Matlab documentation suggests that this should be the first solver to attempt for the majority of the problems.[230] The solver ode23 is based on an explicit Rung-Kutta (2,3) method, and presents similar characteristics to the ode45, but may be more efficient than the latter when applied to problems presenting moderate stiffness.[231] The ode113 is an implementation of a variable order Adams-Bashforth-Moulton solver, which is a multi-step solver that needs the solution at various prior times to predict the solution at $y(t_n)$.[232] These three solvers

are recommended for non-stiff systems of differential equations.

Other solvers are recommended for stiff systems of differential equations. The solver ode15s is based on numerical differentiation formulas that can use backward differentiation formulas, known as Gear's method, and this is a multi-step solver.[233,234] The solver ode23s is based on a modified Rosenbrock formula of order 2 and is a one-step solution.[234]. The solver ode23t consists in an implementation of the trapezoidal rule that performs an interpolation between various points in the solution.[233] Finally, the solver ode23tb is based on an implicit Runge-Kutta formula that consists in a mixed implementation of various methods. In the first stage it comprises a trapezoidal rule step (TR) and in the second stage uses a second order backward differentiation formula (BDF2).[235]

A detailed presentation of the explicit formulation of each of these solvers lies beyond the scope and purposes of this work, which is devoted to utilize the numerical library already built-in in Matlab. Fig. 5-5 presents the numerical solution of equations 5-3 to 5-5 by using each of the seven methods implemented in Matlab. The first issue to note is that the classical differential equations for heterogeneous photoelectrochemical kinetics at the surface of illuminated semiconducting electrodes are able to account for the observed IMVS response obtained experimentally in this work. Indeed, compare the experimental Bode representation shown in Fig. 5-2 b and c, with the simulation presented in Fig. 5-5 a and b.

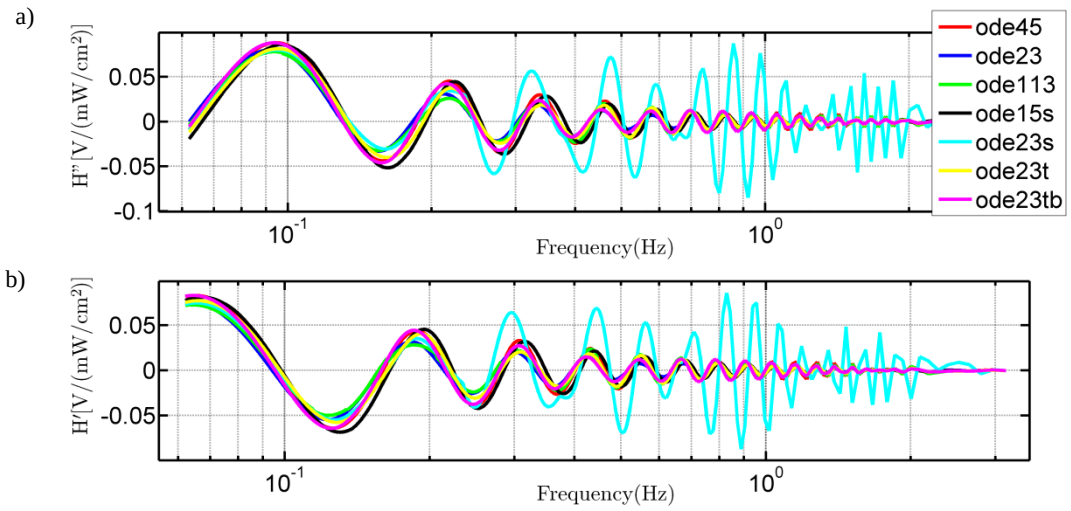

Fig. 5-5. Simulated study of the effect of Matlab built-in solver of ordinary differential equations on the calculated response of IMVS. Calculated data shown in in the Bode representation; a) Imaginary component of H; b) real component of H.

Additionally, it may be appreciated that most solvers perform well. Indeed, only small variations were observed from one method to the other, as depicted in Fig. 5-5 a and b. The only solver that failed completely (mostly at high frequencies) in the reproduction of the IMVS response was the ode23s. Given that all other solvers provide closely similar results, further numerical simulation was carried out by using the ode23t solver, which is an arbitrary choice.

5.6. Numerical exploration of non-steady state IMVS response

The experimental photoelectrochemical response is due to non-steady-state dynamics because the time derivatives cannot be equalized to zero. We note that the spiral pattern described here has never been reported before. Therefore, a numerical exploration of the differential equations 5-3 to 5-5 and 5-6 to 5-10 is necessary in order to shed light onto some questions. For example, (i) which is the cause behind the sense of rotation of the spirals, (ii) what is the effect of charge transfer and recombination rate constants on the

size and shape of the spirals, (iii) what is the effect of interfacial capacitances and (iv) what is the effect of illumination intensity upon the IMVS response. Indeed, the complexity of the differential equations describing the exciton generation (electron-hole pair) and the heterogeneous kinetics of water splitting is not straightforward and cannot be predicted without the rigorous solution of the dynamic model. The numerical exploration described below aims to provide a physical explanation regarding why the spirals shrink when the illumination power increases, i.e., we intend to determine whether the shrinking of the spirals observed experimentally is due to a dependence of the kinetic parameters upon light intensity, or whether this is due only to the increase in the light power that increases the denominator of transfer function H.

A common problem of numerical simulations is that different sets of parameters (k_t, k_r, C_{sc}, C_H, I_0, C_{SS}, R_{SS} for example) can reproduce similarly the observed experimental response. In order to circumvent this fact, some parameters should be determined experimentally by other means. For example, recombination and charge transfer rate constants were already determined by open-circuit photovoltage decay, as discussed in Chapter 3. Such determinations yielded k_t and k_r values of approximately 10^{-2} s^{-1}. Thus, in all our simulations, the rate constants have been set to these constant values.

First, the light modulation was investigated by means of the following two functions: (i) $\Phi = I_0(1 + e^{-i\omega t})$ and (ii) $\Phi = I_0(1 + e^{i\omega t})$. The change in the sign of the imaginary exponent only affects the imaginary component of Φ while maintaining the real component unchanged as can be appreciated from the following equations

$$e^{i\omega t} = cos\omega t + i\, sin\omega t \qquad (5\text{-}11)$$

$$e^{-i\omega t} = cos\omega t - i\, sin\omega t \qquad (5\text{-}12)$$

Thus, in the Nyquist representation, such sign inversion affects the sense of rotation of the light modulation because the real component (plotted in the abscissa) remains unchanged, while the imaginary component (plotted in the ordinates) is reflected through the abscissa axis because of the change in sign. The consequence of the sign of the imaginary exponent is therefore the sense of rotation of the light modulation.

The calculated IMVS response with both positive ($e^{i\omega t}$) and negative ($e^{-i\omega t}$) light modulation are shown in Fig. 5-6 a to d. In addition, the simulated LED modulation is represented in Fig. 5-6 e to h.

Certainly, Fig. 5-6 demonstrates that the sense of rotation of the spirals is the same as the sense of light modulation. Fig. 5-6 shows that, when the sign of the imaginary exponent was changed, the real component of both *H* and *A* was unaffected while the imaginary component of *H* and *A* presented inverted signs. Additionally, the phase angle (Fig. 5-6) has the same shape as the experimental one (Fig. 5-2 d). Such odd shape is a consequence of the alternative pass from one quadrant to the other of the complex plane (Nyquist plot), due to the periodic modulation of light.

In conclusion, the direction of spirals' rotation is not due to inherent kinetic characteristics of the photoelectrochemical system, but caused by the sense of light modulation, which is controlled by the optical bench coupled to the potentiostat.

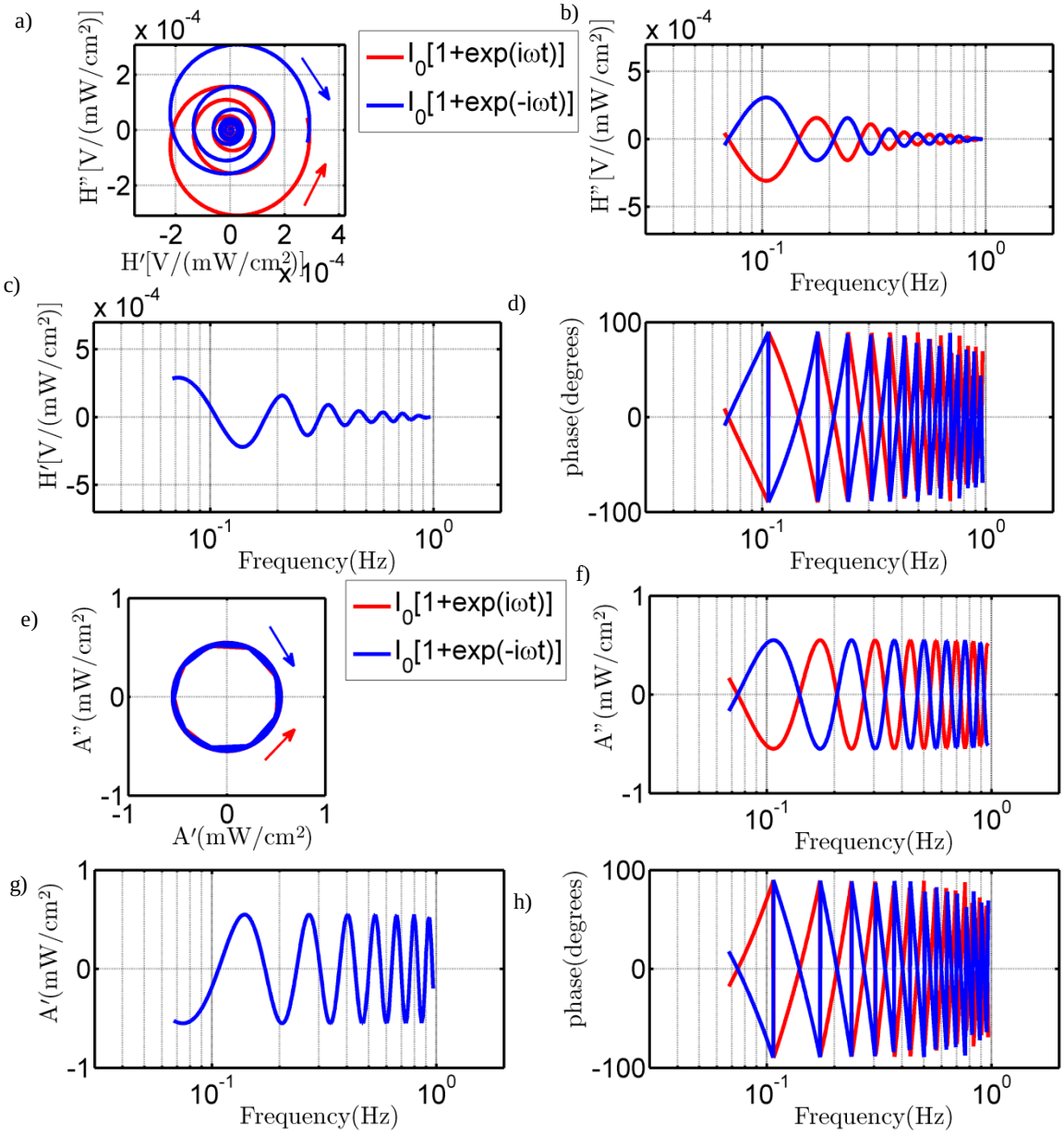

Fig. 5-6. Simulation of the rotation sense of the spirals; a) to d) Nyquist and Bode plots of the simulated IMVS response; e) to h) Nyquist and Bode plots of the simulated light modulation. Blue lines depict a clock-wise rotation, obtained with negative modulation, while red lines show counter-clock-wise rotation, calculated with positive modulation.

All the experimental IMVS spirals reported in this thesis rotate clock-wise, in the sense of decreasing frequency and increasing absolute H value: this is consistent with a negative frequency modulation of the LED ($e^{-i\omega t}$).

In the previous section, two sets of differential equations, describing two different models (with and without surface states) were proposed. The numerical exploration shall be undertaken first with the simplest model (equations 5-3 to 5-5), and then shall be extended to the model comprising surface states (equations 5-6 to 5-10).

First, the influence of the charge transfer and recombination rate constants on the observed IMVS response was determined. Fig. 5-7 show the simulation results at different k_t values (a to d) and different k_r values (e to h) on the IMVS response. The simulations were performed using a logarithmic sweep of the relevant parameters: this is why figure labels indicate the exponent of the parameter. Consequently, from here on, a label of -2 means that the actual value of the parameter is 10^{-2}, likewise, a label of -4.4 indicates that the value of the parameter is $10^{-4.4} = 3.9811 \cdot 10^{-5}$, for example.

Fig. 5-7 shows that the charge transfer and recombination rate constants have an opposite influence on the non-steady-state IMVS response. An increase in k_t causes an increase in the absolute value of H and therefore an expansion of the spirals. Conversely, an increase in k_r provokes a contraction of the spirals. Interestingly, the decrease in the rate constants does not change the frequency of the IMVS oscillations.

It is worth noting that the range of variation of the constants presented in Fig. 5-7 is narrow, and the same observation may be made for all other simulations presented below. However, extensive numerical simulation permitted to extract the conclusions exposed below. The presentation of greatly dissimilar values in a single figure would not allow observing clearly the trends described herein, because of large differences in scales.

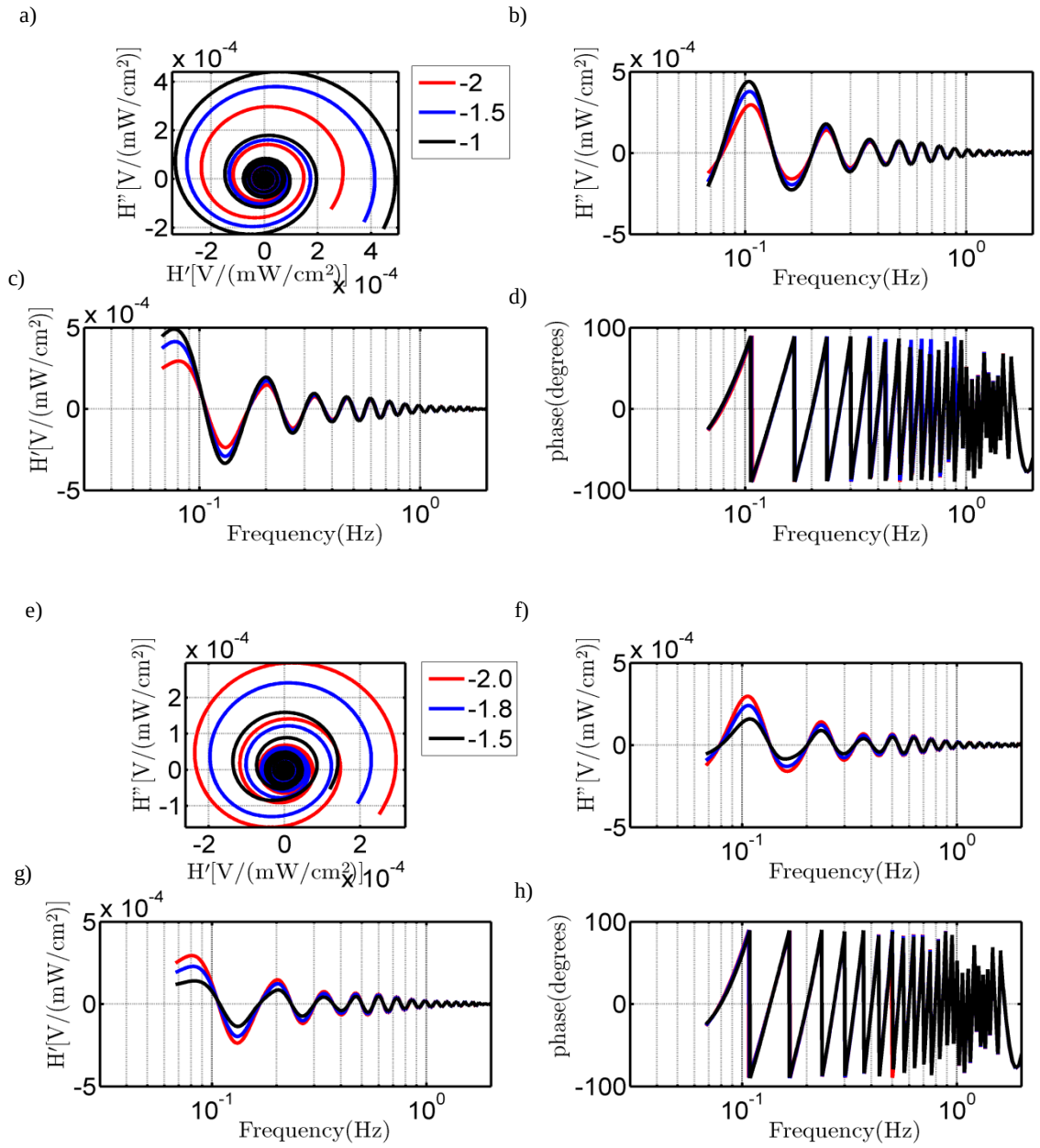

Fig. 5-7. Simulation of the effect of the charge transfer (a to d) and recombination (e to h) rate constant on the non-linear response of IMVS. Calculations were performed through a logarithmic sweep of the relevant parameter (either k_t or k_r), therefore figure labels depict the exponent of the actual parameter value, e.g. -2 in the red line of (a) indicates that $k_t = 0.01\ s^{-1}$. Other parameters: $C_{sc} = 40\ \mu F$; $C_H = 10\ mF$; $I_0 = 10^{-8}\ A$; $R = 44\ \Omega$; from (a) to (d) $k_r = 0.01\ s^{-1}$; from (e) to (h) $k_t = 0.01\ s^{-1}$.

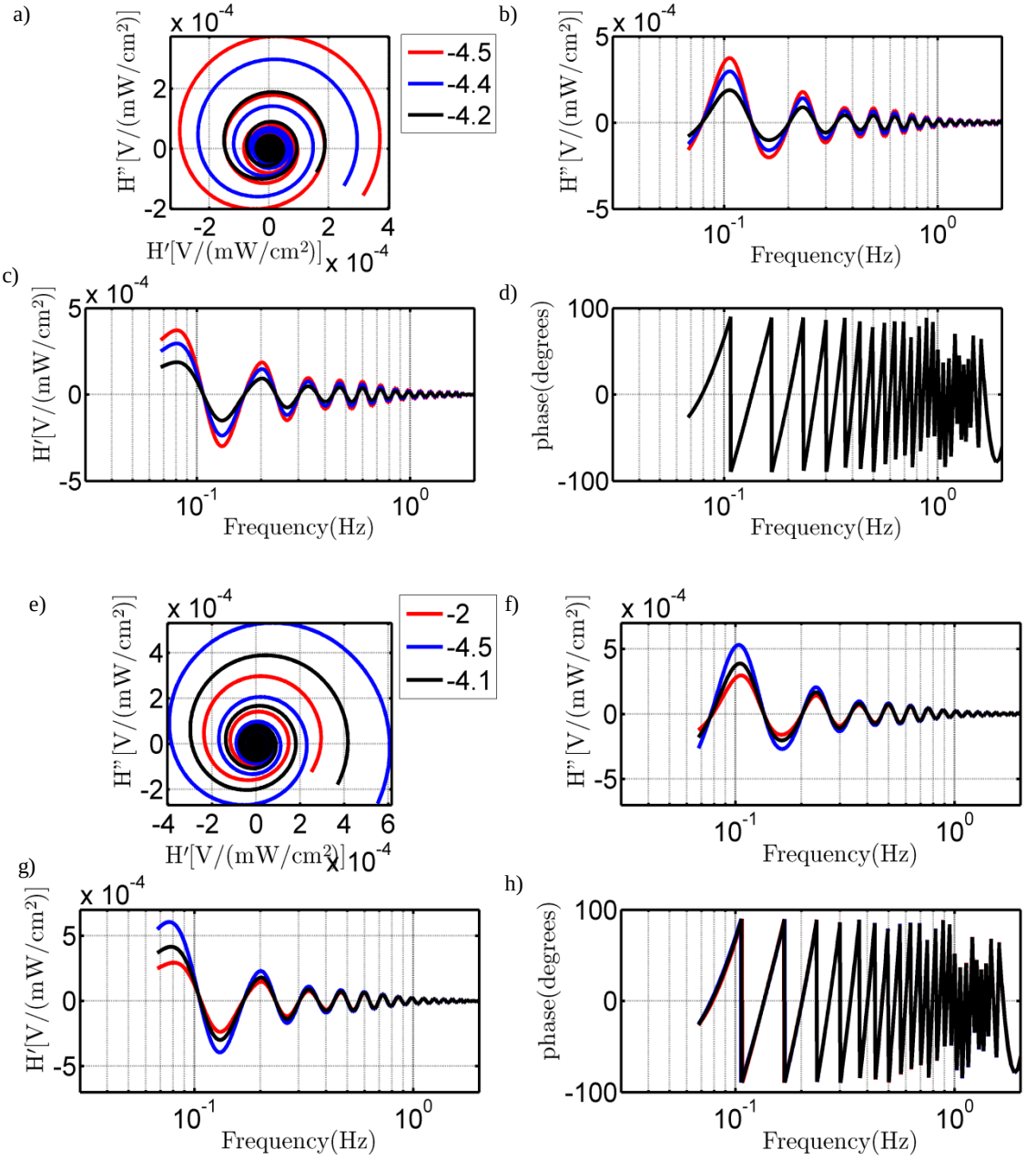

Fig. 5-8. Simulation of the effect of the space charge (a to d) and Helmholtz (e to h) capacitances on the non-linear response of IMVS. Calculations were performed through a logarithmic sweep of the relevant parameter (either C_{SC} or C_H), therefore figure labels depict the exponent of the actual parameter value, e.g. -4.5 in the red line of (a) indicates that C_{SC} = 31.6 µF. Other parameters: $k_t = k_r = 0.01\ s^{-1}$; $I_0 = 10^{-8}$ A; R = 44 Ω; from (a) to (d) C_H = 10 mF; from (e) to (h) C_{SC} =40 µF.

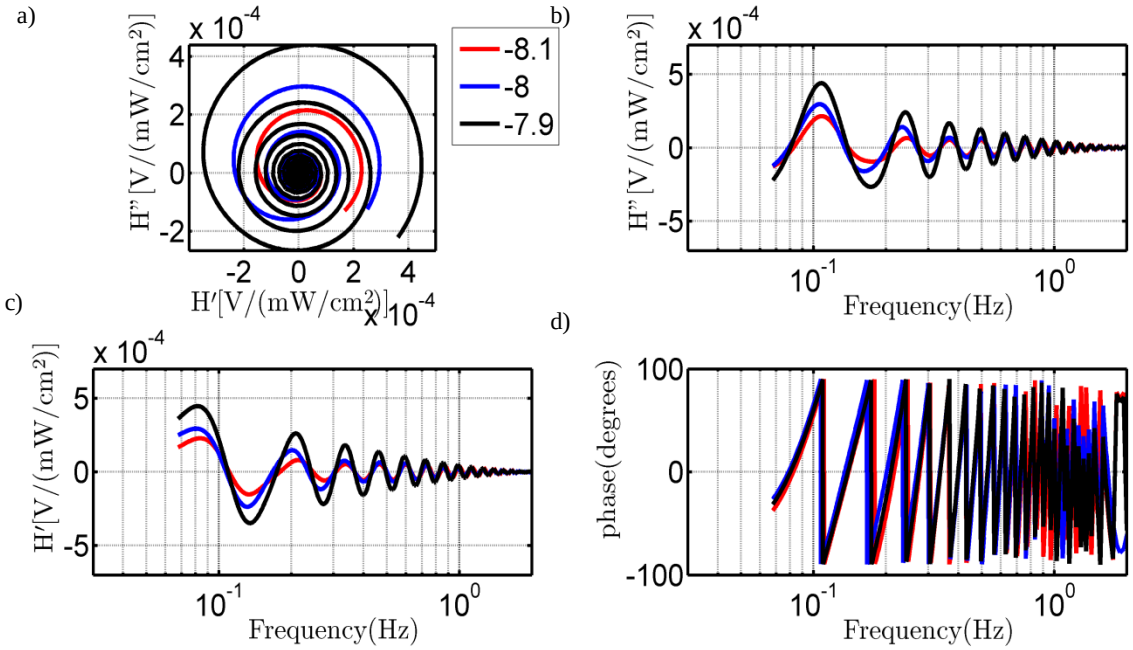

Fig. 5-9. Simulation of the effect of the photogenerated current of minority carriers I_0 (a to d) on the non-steady state response in IMVS. Calculations were performed through a logarithmic sweep of the relevant parameter (either I_0 or R), therefore figure labels depict the exponent of the actual parameter value, e.g. -8 in the blue line of (a) indicates that $I_0 = 10^{-8}$ A. Other parameters: $k_t = k_r = 0.01\ s^{-1}$; C_H = 10 mF; C_{SC} =40 μF; from (a) to (d) R = 44 Ω from.

Subsequently, the effect of interfacial capacitances (C_{sc} and C_H) was explored. The most usual scenario in semiconductor photoelectrodes in contact with an electrolyte solution is that the space charge capacitance is much smaller than the Helmholtz capacitance. This condition does not hold true in heavily doped semiconductors, but this is not the case of the Rh:$SrTiO_3$ material in which the doping level of Rh is 1 %. Nevertheless, we have simulated the shape of non-steady-state IMVS when C_H and C_{sc} have comparable values.

Fig. 5-8 a to d indicates that an increase in the space charge capacitance causes a decrease in the absolute value of the transfer function and therefore a shrinking in the spirals.

On the other hand, the increase in Helmholtz capacitance makes the spirals shrink. The shrinking in the spirals has a limit, when C_H is around 10^2 times larger than $C_{SC,}$ and

therefore the interfacial capacitance (C) is dominated by the space charge capacitance because $C^{-1} = C_{SC}^{-1} + C_H^{-1}$.

The effect of the photogenerated current of minority carriers (I_0) was also explored (Fig. 5-9 a to d). It was observed that I_0 had a very strong effect on the absolute value of *H*. The observed trend was that a decrease in I_0 causes a shrinking in the spirals.

Finally, the effect of the presence of surface states was also evaluated, as depicted in Fig. 5-10. When surface states are present (equations 5-6 to 5-10), the effect in the oscillatory IMVS response of the other parameters is the same as the effect described just above, when the presence of surface states was not considered. For example, the effect of k_t and k_r is opposite. Furthermore, as observed before, an increase in k_t causes and expansion in the spirals and an increase in k_r causes a contraction of the spirals. The effect of interfacial capacitances, and the photogenerated current of minority carriers is the same as the one depicted in Figures Fig. 5-7 to Fig. 5-9.

However, the presence of surface states does have an impact in the IMVS oscillatory response. We found that the presence of surface states did not change appreciably the absolute value of the transfer function *H*. But we observed that surface states make the non-steady-state IMVS oscillations shift to lower frequencies, as observed in the Bode plots *H* and the phase angle (Fig. 5-10 b to d).

Among all kinetic parameters tested so far, the only one that caused a phase shift in the IMVS oscillatory response was the presence of surface states. The other parameters caused either a decrease (shrinking) or increase (expansion) of the transfer function *H* (of the spirals in the Nyquist representation), but did not cause a phase shift.

These simulations put in evidence that more than one kinetic parameter (interfacial capacitance rate constants, or light intensity) may have the same effect in the observed IMVS. At the beginning of this Chapter, it was experimentally demonstrated that an

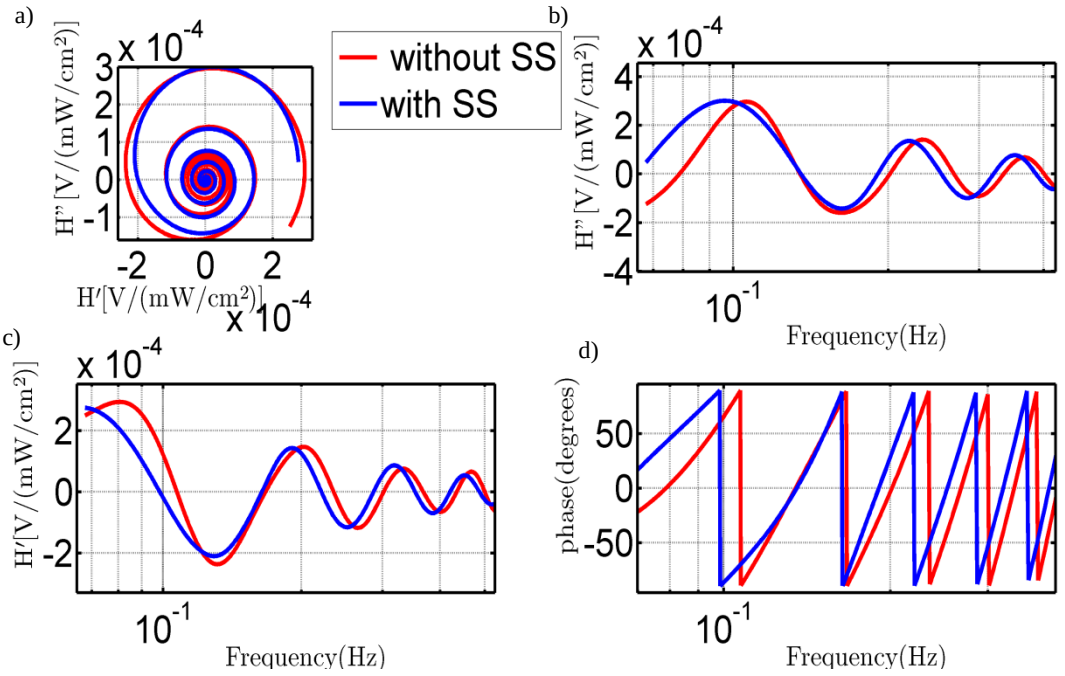

Fig. 5-10. Simulation of the effect of surface states on the non-linear response of IMVS. The letters SS in the label of this figure stand for "surface states". Common simulation parameters: $k_t = k_r = 0.01\ s^{-1}$; $C_H = 10$ mF; $C_{SC} = 40$ μF; $R = 44\ \Omega$; $I_0 = 10^{-8}$ A. Additional simulation parameters to account for the presence of surface states: $Rss = 10^4\ \Omega$; $C_{SS} = 10$ mF, giving rise to $\tau_{SS} = 10^2$ s.

increase in the light power causes a decrease in the absolute value of IMVS transfer function *H* (Fig. 5-1), by increasing the denominator of its definition (eq. 5-2).

However, it is not clear if the shrinking of IMVS when light power increase as observed in this thesis (Fig. 5-2) was due only to the increase in the denominator of the transfer function, or it was also caused to a change in rate constants, interfacial capacitances, surface states charging or changes in photogenerated flux of minority carriers.

In order to separate the effect of putative variations in kinetic parameters with light power from the inherent tendency of IMVS to shrink due to light power increase, IMVS must be analyzed by normalizing *H* against light power.

Of course, if the light-normalized IMVS response is found to be dependent on light intensity, this will mean that there are kinetic parameters which depend on light power. The simulations just described have indicated that IMVS alone cannot provide a certain

diagnosis indicating which parameter varied with light. The safest manner to proceed is thus to use complementary techniques to determine the role of some parameters independently. For example, rate constants can be estimated with open-circuit photovoltage decay (as explained in Chapter 1 and presented in Chapter 3), and the space charge capacitance can be determined by electrochemical impedance spectroscopy. Once these parameters are known and set to a constant value, a confident simulation of the oscillatory IMVS response can be undertaken.

5.7. Experimental vs. simulated non-steady-state IMVS oscillatory response

Fig. 5-11 presents the comparison between simulated and experimental IMS spectra in Nyquist coordinates. It may be appreciated that the sense of rotation of the spirals is adequately reproduced.

The dynamic models employed so far can be considered as successful because they are able to reproduce the main features of the experimental observations. For example, not only the oscillatory nature of IMVS and sense of rotation of the spirals, but also the absolute value of the transfer function, and the behavior of the real and imaginary components of H in the Bode representation, which rise from zero when the frequency is swept decreasingly.

The differences that can be noted in Fig. 5-11 show however that the differential equations are not a perfect model to describe the experimental observations. For example, at small values of the transfer function H (high frequency) the shape is adequately reproduced. Though, at larger values of H (low frequencies) the experimental IMVS response presented a higher absolute value when compared to the simulation. Likewise, in the Bode representation of H'', it may be seen that peaks and valleys of the experimental non-steady-state IMVS do not coincide precisely with the

simulation. Probably, this is due to the heterogeneous nature of the photoelectrode surface, which brings as consequence a distribution of kinetic parameters[71] which, given the sluggish nature of charge transfer in these photoelectrodes at open circuit conditions, should be more significant at low frequencies.

Despite this, the initial hypothesis that the classical equations describing heterogeneous charge transfer and recombination in semiconducting electrodes could reproduce the

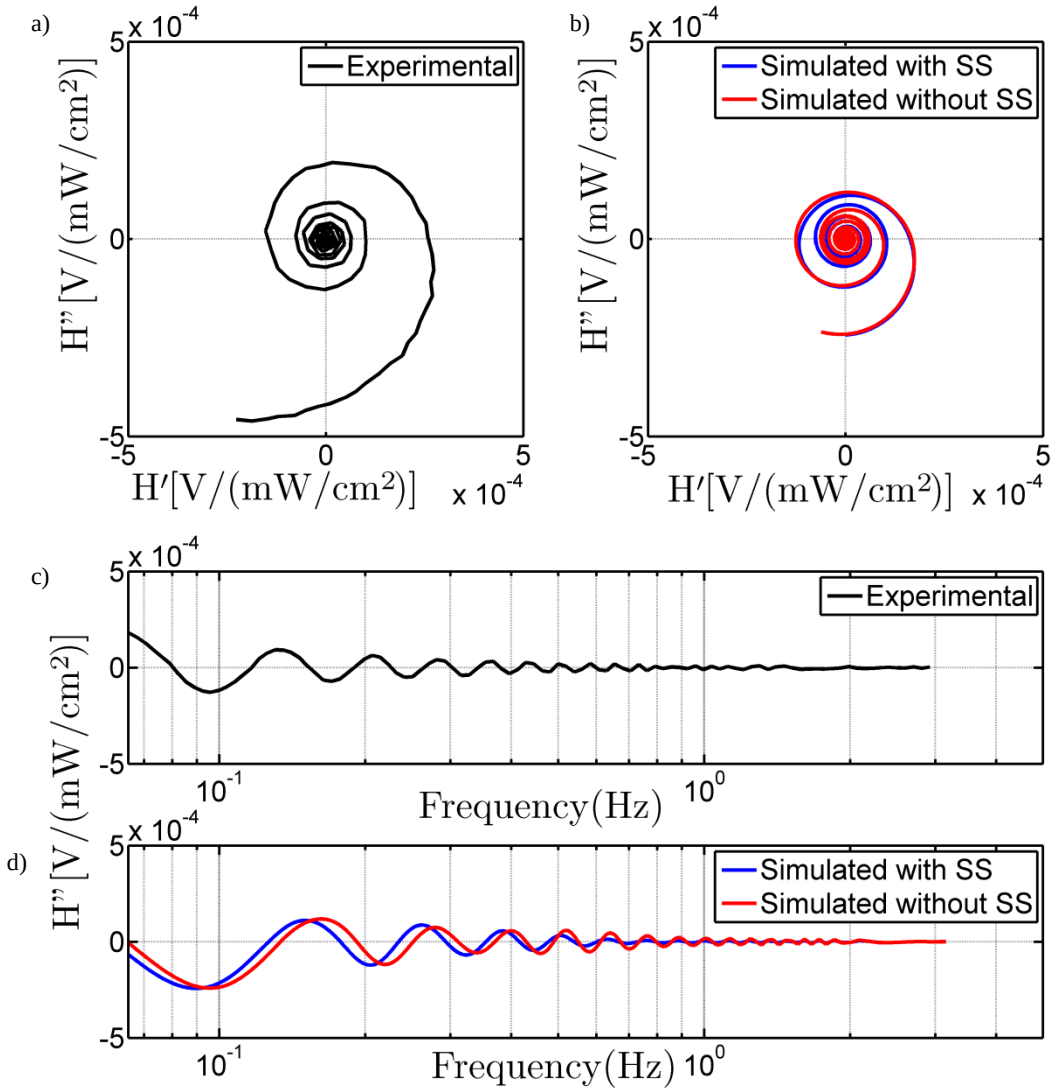

Fig. 5-11. Comparison of the experimental and simulated non-steady-state IMVS response for the Rh:$SrTiO_3$ – Pt. Parameters employed for the simulation without surface states: $k_t = k_r = 0.01\ s^{-1}$; C_H = 10 mF; C_{SC} =40 μF; R = 44 Ω; $I_0 = 10^{-8}$ A. Simulation parameters to account for the presence of surface states: Rss = 10^4 Ω; C_{SS} = 10 mF, giving rise to $\tau_{SS} = 10^2$ s.

unusual oscillatory IMVS obtained experimentally was correct (Fig. 5-11).

Once the physical origin behind the IMVS spirals has been understood, we proceeded to compare the experimental behavior of $Rh:SrTiO_3$ and $Rh:SrTiO_3$ – Pt photoelectrodes under these experimental conditions.

5.8. Experimental non-steady-state IMVS response of $Rh:SrTiO_3$ – Pt photoelectrodes

Fig. 5-12 a and c show the experimental non-steady-state IMVS response of $Rh:SrTiO_3$ – Pt photoelectrodes. The first issue to note is that the absolute value of IMVS varies appreciably with small variations in illumination. Additionally, different light power apparently causes a phase shift in the data.

With the purpose to analyze whether these changes are due to light-dependent kinetic parameters, the IMVS response is presented normalized against light power in Fig. 5-12 b and d. The comparison between Fig. 5-12 a with Fig. 5-12 b is interesting in the sense that the differences between the absolute value of the transfer function *H* (Fig. 5-12 a) have virtually vanished when the IMVS signal is normalized against light (Fig. 5-12 b).

The interpretation of this observation is that, for $Rh:SrTiO_3$ – Pt photoelectrodes at the light power tested, the shrinking in IMVS spirals is essentially due to the increase in photon flux (Φ) that determines an increase in the denominator of *H* (eq. 5-2). This further suggests that none of the kinetic parameters of the system has changed appreciably with the experimental variation of light.

This observation is also supported by the Bode representation of *H"*, when it is compared without light normalization (Fig. 5-12 c) and with light normalization (Fig. 5-12 d). Yet, there is an important phase shift between the four experiments presented here that must be explained. Indeed, the phase shift can be suspicioned in the Nyquist representation since the IMVS measurements performed at 0.90 and 1.15 mW/cm^2 finish in the positive part of *H"* while the determinations at 0.55 and 0.70 mW/cm^2 end

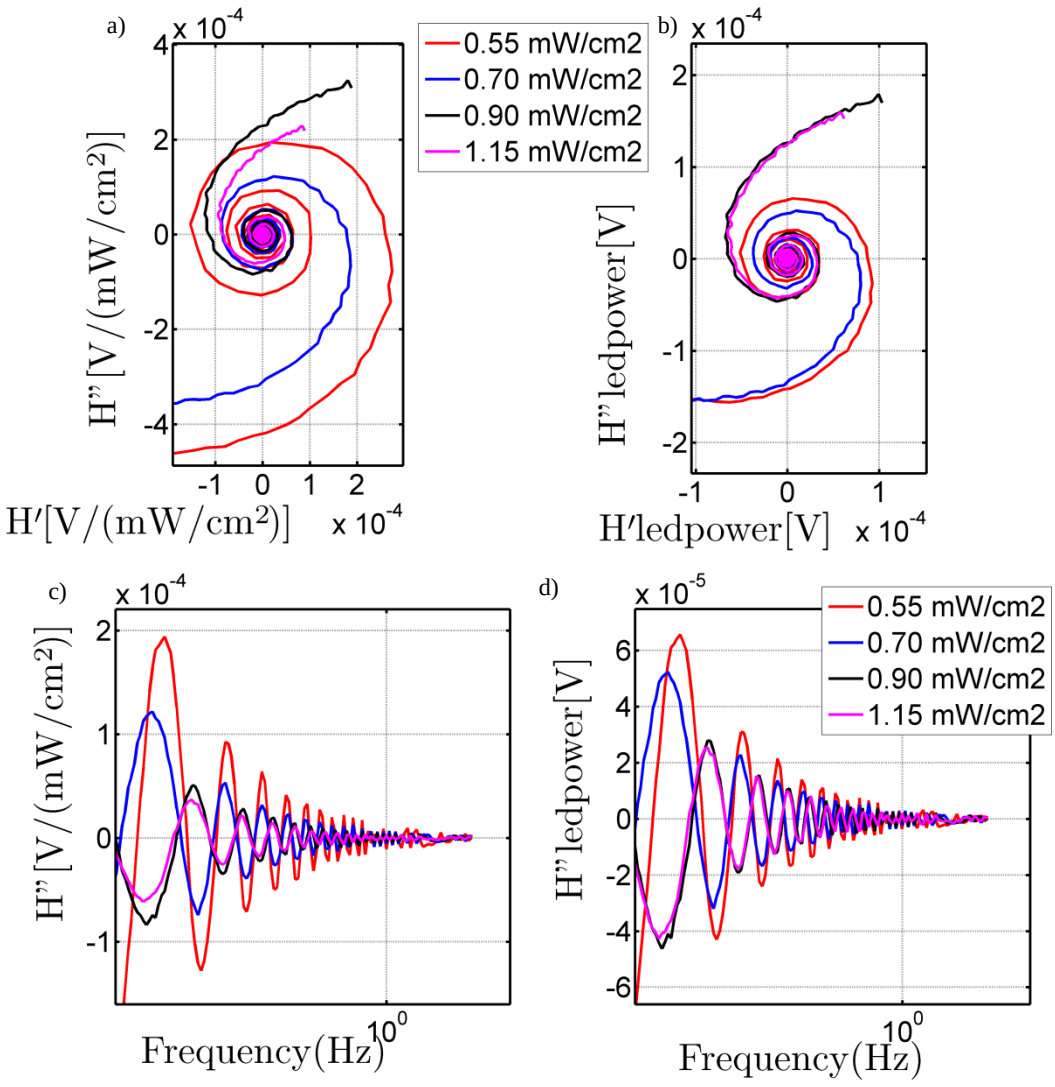

Fig. 5-12. Effect of light intensity on the experimental IMVS response for the Rh:$SrTiO_3$ – Pt photoelectrodes; a) Nyquist representation; b) Nyquist representation normalized for the incident led power; c) Bode representation of the imaginary component of H; d) Bode representation of the imaginary component of H normalized for the incident led power.

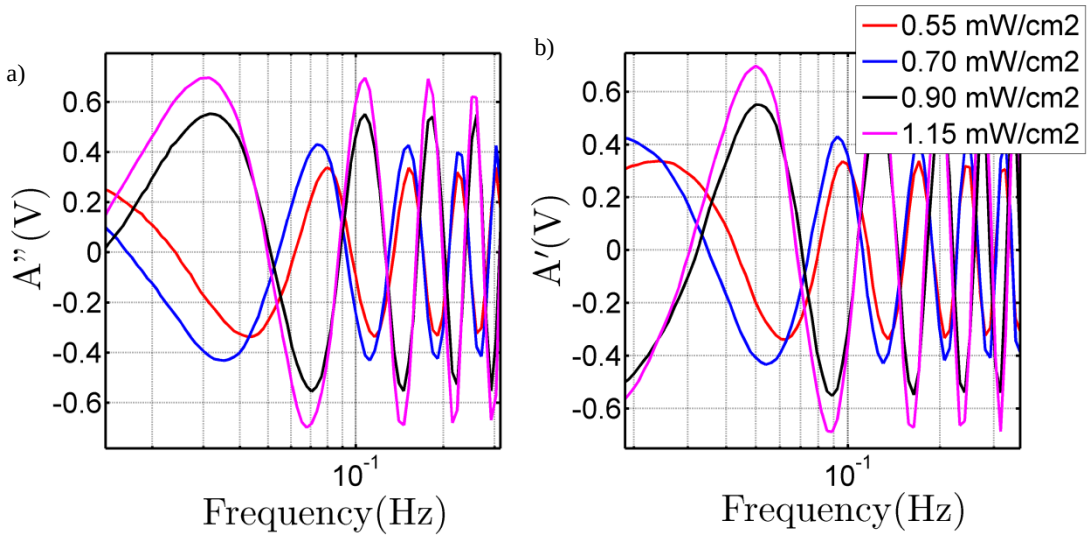

Fig. 5-13. Comparison of the experimental photodetector voltage for the IMVS experiments of Rh:$SrTiO_3$ – Pt photoelectrodes at different light intensities. a) Imaginary component; b) real component. The phase shift observed between both measurements is due to instrumental uncertainties.

in the negative part of *H"*. This is clearly seen in the Bode representation of H", where these two pairs of determinations are completely out of phase (Fig. 5-12 c and d).

Previously, we demonstrated that from one IMVS measurement to another, the photodetector voltage (which is outside the PEC cell and is only responsible for the measurement of light modulation) exhibited a phase shift (Fig. 5-3 b and c). Therefore, such effect was verified, as can be appreciated in Fig. 5-13 a and b, where the real (*A'*) and imaginary (*A"*) components of the light modulation, as measured by the photodetector, are displayed. Fig. 5-13 shows that the observed phase shift in the IMVS spectra is the same as the one measured in the photodetector, which indicates that the phase shift observed in IMVS has an instrumental origin, and is not due to differences in light-induced interfacial effects.

These IMVS determinations performed on the Rh:$SrTiO_3$ – Pt system recall the PEIS determinations performed on the same system. In both cases, a small dependence of the photoelectrochemical response upon light intensity was evidenced (Fig. 3-33).

5.9. Experimental non-steady-state IMVS response of Rh:$SrTiO_3$ photoelectrodes

Following the same methodology described so far, we proceeded to evaluate the non-steady-state IMVS response of Rh:$SrTiO_3$ photoelectrodes, without (Fig. 5-14 a and c) and with (Fig. 5-14 b and d) light normalization.

The light dependence for Rh:$SrTiO_3$ is different to that presented for Rh:$SrTiO_3$ – Pt. Certainly, the Nyquist representation reveals that, at light intensities of 2.23 and 2.86 mW/cm^2, the representation of the response is hardly observed due to the difference in the absolute value of *H* with the experiments performed at the lower LED powers of 1.37 and 1.74 mW/cm^2. In the Rh:$SrTiO_3$ system, the absolute value of *H* does depend upon light power, as observed in Fig. 5-14 b and d.

Again, a phase shift is observed for these experiments when light power is changed, but the verification of the oscillating photodetector voltage (outside the PEC cell) confirmed the instrumental origin of the phase shift observed in IMVS (Fig. 5-15 a and b).

Thus, the decrease in the absolute value of *H* does have its origin in variations of any of the kinetic parameters. The numeric exploration of the IMVS spirals discussed earlier indicated that the shrinking in the spirals may be due to one or more of the following reasons: (i) to a decrease in charge transfer rate, (ii) to an increase in recombination rate, (iii) to an increase in the space charge capacitance, or (iv) to a decrease in the photogenerated flux of minority carriers.

Taking into consideration that the estimation of rate constants at open circuit conditions, obtained from photovoltage decay measurements (Fig. 3-5 b), revealed that these constants were independent of light intensity, it is probable that the decrease in the absolute value of *H* when light increases is an increase in the space charge capacitance, for the case of Rh:$SrTiO_3$ photoelectrodes.

However, variations in the flux of photogenerated minority carriers (I_0) should also play a role, but its qualitative description is far less evident because, in one hand it may be

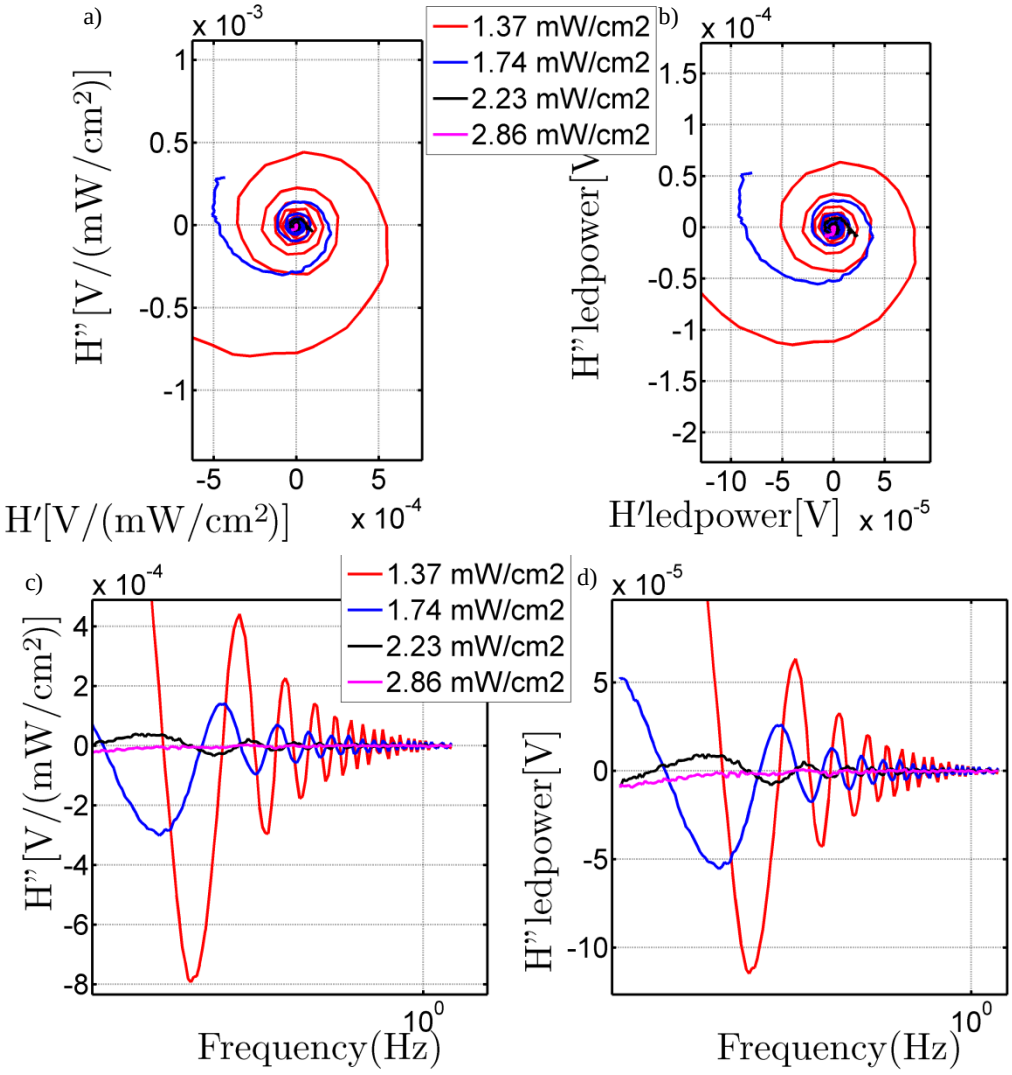

Fig. 5-14. Effect of light intensity on the experimental IMVS response for the Rh:$SrTiO_3$ photoelectrodes; a) Nyquist representation; b) Nyquist representation normalized for the incident led power; c) Bode representation of the imaginary component of H; d) Bode representation of the imaginary component of H normalized for the incident led power.

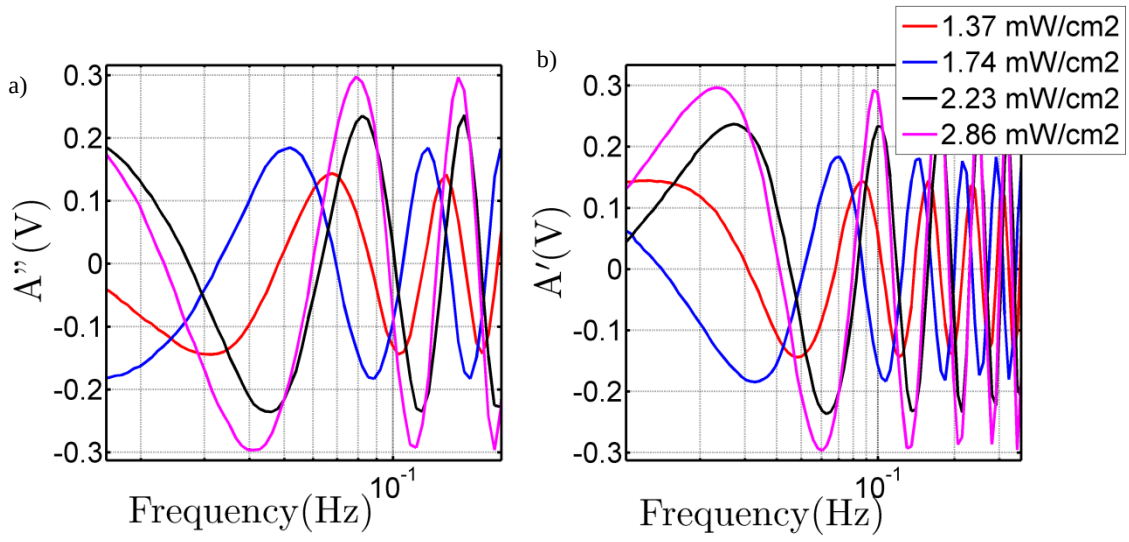

Fig. 5-15 Comparison of the experimental photodetector voltage for the IMVS experiments of Rh:$SrTiO_3$ photoelectrodes at different light intensities. a) Imaginary component; b) real component. The phase shift observed between both measurements is due to instrumental uncertainties.

argued that increased light power should directly increase I_0, but, on the other hand, it is known that if light power is strong enough to diminish appreciably band bending (i.e., the width of the space charge region), I_0 could decrease at strong illumination.

Nonetheless, and inspection of the light power employed in these experiments (up to 2.86 mW/cm^2) suggests that the low intensity employed makes unlikely any decrease in band bending. Thus, we speculate that, in this low intensity limit of light power, an increase in light power would increase the photogenerated current of minority carriers, that would contribute to an increase in the absolute value of *H* (which is not observed experimentally as depicted in Fig. 5-14).

These considerations reinforce the interpretation that the observed decrease in the absolute value of *H* is due to an increase in the space charge capacitance.

5.10. Comparison of non-steady-state IMVS response for Rh:SrTiO$_3$ and Rh:SrTiO$_3$ – Pt photoelectrodes

A comparison between experimental IMVS response obtained for Rh:SrTiO$_3$ and Rh:SrTiO$_3$ – Pt is presented in Fig. 5-16 a and c. The IMVS experiments performed in Rh:SrTiO$_3$ and Rh:SrTiO$_3$ – Pt were carried out with slightly different light intensities. Thus, for a meaningful comparison, the IMVS response should be normalized against light intensity, as illustrated in Fig. 5-16 b and d.

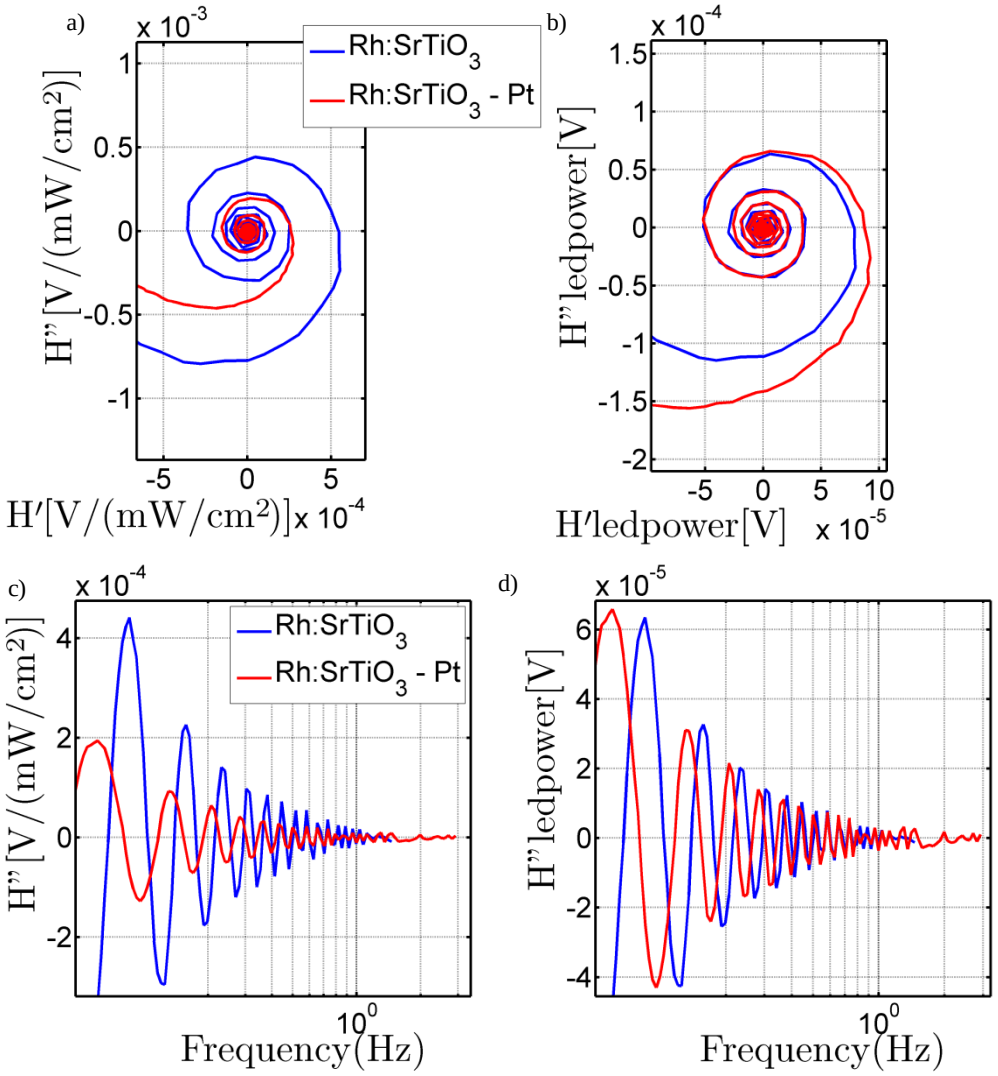

Fig. 5-16. Comparison of the experimental IMVS response for the Rh:SrTiO$_3$ and Rh:SrTiO$_3$ – Pt photoelectrodes; a) Nyquist representation; b) Nyquist representation normalized for the incident led power; c) Bode representation of the imaginary component of H; d) Bode representation of the imaginary component of *H* normalized for the incident led power.

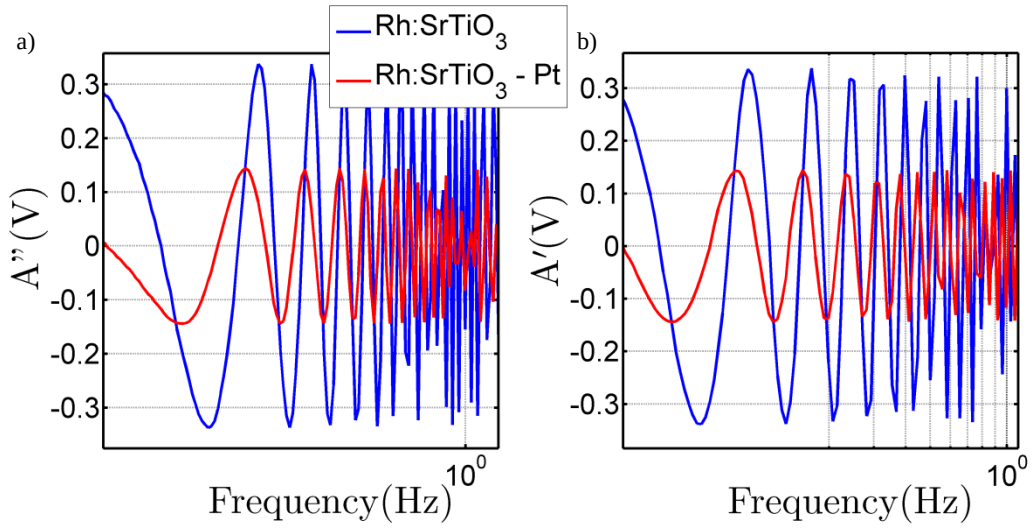

Fig. 5-17. Comparison of the experimental photodetector voltage for the IMVS experiments described above. a) Imaginary component; b) real component. The phase shift observed between both measurements is due to instrumental uncertainties and not to differences in surface kinetics between $Rh:SrTiO_3$ and $Rh:SrTiO_3$ – Pt.

A phase shift is observed between these two measurements. It was confirmed above that the phase shift was due to the ac light generator, because the phase shift observed in the light modulation was the same observed in the IMVS measurements (compare the Bode plots of Fig. 5-16 c and d with those of Fig. 5-17 a and b).

Additionally, after light normalization, it may be observed that both $Rh:SrTiO_3$ – Pt and $Rh:SrTiO_3$ IMVS spirals are essentially the same (Fig. 5-16 b and d), excepting a small phase shift (Fig. 5-16 d) whose origin is instrumental and is not related to the interfacial photoelectrochemistry, as demonstrated in Fig. 5-17. This indicates that both systems do not present significant differences in their photoelectrochemical characteristics at open circuit conditions, as had already been established before through open-circuit photovoltage decay (Fig. 3-5 and Fig. 3-13).

5.11. Conclusions for Chapter 5

In this chapter, experimental results related to the non-steady-state dynamics of the photoelectrodes of interest observed by the IMVS technique have been presented. Such behavior was observed as an oscillating pattern in the Bode representation, and a spiral pattern in the Nyquist plot. It was demonstrated that such behavior can be satisfactorily explained and modeled by a set of classical differential equations developed to describe the heterogeneous processes at illuminated semiconductor|electrolyte interfaces.

Two mathematical models have been numerically implemented and solved in Matlab. The simplest model comprised charge transfer and recombination rate constants, with the usual interfacial capacitances originating from the space charge and the Helmholtz layers, and the presence of a current due to photoexcitation of minority carriers. The more elaborated mathematical model also included contributions from surface states capacitance. A detailed and thorough parametric analysis was performed to determine the role of kinetic parameters upon the IMVS response. The results provided guidelines to interpret the variation of IMVS when various parameters were changed.

Experimental results showed that the inclusion of surface states was not necessary to reproduce the experimental observations in $Rh:SrTiO_3$ and $Rh:SrTiO_3$ – Pt photoelectrodes.

Additionally, a phase shift of instrumental origin was put into evidence through the analysis of the ac photovoltage measurements of the photodetector which is related to the optical bench.

It is worth to comment why most IMVS responses reported in the literature do have a shape that resemble a typical EIS response, while in this work we have reported on the highly unusual spiral shape that has never been reported before.

One of the most important studies describing a mathematical model for heterogeneous

charge transfer and recombination at illuminated semiconducting electrodes was presented by Peter in 1995.[229] Such study was devoted to the theory of IMPS, but we have employed it here for modeling IMVS. In this paper[229] Peter arrives to analytical solutions for IMPS but does not describe under which conditions these solutions hold. However, two years after, in 1997, the same authors presented another paper[213] (also devoted to IMPS) where it is clear that they employed the steady-state approximation to find the analytical expressions (in reference [213], it may be appreciated that equations 9, 10 and 11 are the steady-state solution of the differential equations 6 and 7).

Regarding IMVS, other authors have presented theoretical treatments of this light-modulated technique. In the context of this discussion, it is necessary to highlight two publications that also use the steady state approximation to find analytical expressions for IMVS in the case of DSSC.[32,76] The authors obtain expressions that describe an EIS-like shape of IMVS. There are other models that employ Fick-type partial differential equations to treat the diffusion of photoexcited electrons, aiming at predicting IMVS.[27] Such models are appropriate for nano-structured photoelectrochemical systems where band-bending does not develop because of the reduced size of the semiconducting particles, and also yield EIS-like shape of IMVS.

The numerical approach used during our thesis has not considered the steady-state approximation and therefore, none of the relevant time derivatives was equated to zero.

This allows concluding that the most widely presented and discussed IMVS response (displaying an EIS-like shape) is observed when the system behaves following the steady-state approximation where all time derivatives are zero. Conversely, when the steady-state approach does not hold, a complex spiral-like shape is obtained, as reported in this thesis.

Both observations (EIS-like versus spiral-like) appear strikingly different. However,

these are certainly not so different because they originate form a common root obeying to the classical dynamic model for heterogeneous reactions occurring at illuminated semiconducting electrodes, that unifies the description of this beautiful photoelectrochemical technique.

OVERALL CONCLUSIONS

The main findings and conclusions that can be extracted from the results reported in this thesis shall be presented in coherence with the specific objectives expressed at the beginning of this manuscript. For the sake of clarity, the overall conclusions shall be written in concise items.

- The Rh:$SrTiO_3$ semiconducting material was characterized by means of XPS, EDS, XRD and SEM techniques. XPS and EDS techniques permitted to assess the chemical composition of the material. Furthermore, XRD undoubtedly permitted to identify the characteristic perovskite structure in Rh:$SrTiO_3$. SEM images put into evidence the rough and irregular nature of the surface of the Rh:$SrTiO_3$ material.

- The $Co(Cl_2Gm)_3(B\text{-}CH_3)_2$ clathrochelate was characterized by means of XPS and EPR spectroscopies. XPS revealed the presence of a Co^{II} metallocenter with paramagnetic characteristics, as observed by characteristic shake-up satellites. This fact did not allow discerning whether the complex possessed either high-spin or low-spin configuration. Such differentiation was achieved by EPR spectroscopy, where the low-spin configuration was observed and fitted to yield the relevant magnetic parameters of the complex.

- Photoelectrodes based on the Rh:$SrTiO_3$ semiconducting material were modified with metallic Pt and Cu, and with the molecular $Co(Cl_2Gm)_3(B\text{-}CH_3)_2$ clathrochelate. These systems were characterized by XPS, XRD and SEM techniques. XPS permitted to confirm the modification process in each case through the determination of the surface chemical composition. Conversely,

XRD was unable to put into evidence the modification of Rh:$SrTiO_3$ due to the small loading of surface catalysts. SEM revealed that the rough nature of the surface was not modified by the presence of different surface co-catalysts.

- The polarization curves with and without illumination, under anodic applied electrode potentials were measured on unmodified Rh:$SrTiO_3$ photoelectrodes, and on modified (with metallic Pt and Cu, and with the molecular $Co(Cl_2Gm)_3(B\text{-}CH_3)_2$ clathrochelate) photoelectrodes. In all cases no photocurrents were observed, indicating that the photoelectrodes were working under accumulation conditions, which is characteristic of p-type materials polarized at positive potentials.

- Measurements of open-circuit potentials with increasing light intensity showed an increase in photovoltage. This confirmed the p-type conductivity in all photoelectrodes tested in this work, based on unmodified Rh:$SrTiO_3$ and its modification with metallic Pt and Cu, and with the molecular $Co(Cl_2Gm)_3(B\text{-}CH_3)_2$ clathrochelate.

- Charge transfer and recombination kinetic parameters in Rh:$SrTiO_3$ photoelectrodes modified with metallic Pt and Cu, and with the molecular $Co(Cl_2Gm)_3(B\text{-}CH_3)_2$ clathrochelate were obtained by means of Open Circuit Photovoltage Decay. No significant differences were found in the kinetics at open circuit conditions; in general, the charge transfer rate constant was found larger than the recombination rate constant.

- The polarization curves with and without illumination, under cathodic applied electrode potentials were determined for photoelectrodes based on pristine Rh:$SrTiO_3$ semiconducting material, and photoelectrodes modified with metallic Pt (atomic ratio at the surface Sr:Pt, 90:10) and Cu (atomic ratio at the surface Sr:Cu 87:13), and with the molecular $Co(Cl_2Gm)_3(B\text{-}CH_3)_2$ clathrochelate (10^{-2} μmol at the surface). In all cases, photocurrents around 15 $\mu A/cm^2$ were observed. The observation of cathodic photocurrents is characteristic of p-type semiconducting photoelectrodes working under cathodic polarization.

- The estimated incident photon to current efficiency of all photoelectrodes was notably small (below 0.01 %). Hence, all catalysts were electrocatalysts which did not contribute to light harvesting and to increase the absolute photocurrent. Instead, metallic Cu, Pt and the molecular $Co(Cl_2Gm)_3(B\text{-}CH_3)_2$ clathrochelate increased the dark currents and decreased the overpotential of the HER.

- Tafel slopes obtained from polarization curves were analyzed for both the hydrogen evolution reaction (HER) and the oxygen evolution reaction (OER) in the four photoelectrodes tested. For the HER, a Tafel slope of approximately 120 mV/dec was obtained, which did not permit to distinguish between the Volmer reaction $H_2O + e^- + M = M - H + OH^-$ or the Heyrovsky step $M - H + H_2O + e^- = H_2 + OH^- + M$ (in the limit of high surface density of adsorbed H atoms, $\theta_H > 0.6$) as rds. For the OER, Tafel slopes close to 60 mV/dec were obtained; this was interpreted in terms of Bockris' oxide mechanism, with reaction $M - O = M + 1/2O_2$ under the conditions $\theta_O \approx 0$ and $\theta_{OH} \approx 1$ as a possible rds. Additionally, Tafel slopes deviating from

mathematical models were obtained for the Rh:$SrTiO_3$ – Cu towards the HER and for Rh:$SrTiO_3$ – Pt towards the OER.

- The kinetic parameters of the hydrogen evolution reaction (HER) at different cathodic applied electrode potentials and illumination levels was determined by means of Photoelectrochemical Impedance Spectroscopy (PEIS), for unmodified Rh:$SrTiO_3$ photoelectrodes, and for photoelectrodes modified with metallic Pt and Cu, and with the molecular $Co(Cl_2Gm)_3(B\text{-}CH_3)_2$ clathrochelate.

  Regarding the HER, the photoelectrodes can be classified into two groups: a first group comprising pristine Rh:$SrTiO_3$, and Rh:$SrTiO_3$ modified with $Co(Cl_2Gm)_3(B\text{-}CH_3)_2$, and a second group composed by Rh:$SrTiO_3$ modified with Pt and Cu. In pristine Rh:$SrTiO_3$, and Rh:$SrTiO_3$ modified with $Co(Cl_2Gm)_3(B\text{-}CH_3)_2$ photoelectrodes, recombination and charge transfer rate constants were found to be independent of applied potential and light intensity. Conversely, on Rh:$SrTiO_3$ photoelectrodes modified with Pt and Cu, recombination and charge transfer rate constants displayed an exponential dependence with applied electrode potential. These observations can be attributed to the presence of surface states at the surface, which is the origin of such non-ideal behaviors.

- Under cathodic polarization, the Mott-Schottky plots of the space charge capacitance for all photoelectrodes displayed a positive slope, which indicates that at electrode potentials more negative than -1.1 V (vs. SCE), the semiconductor was forced to inversion conditions, where the Fermi level approaches the conduction band (for p-type semiconductors). Under these

conditions, p-type semiconductors behave like n-type semiconductors at the surface and p-type in the bulk.

- Concerning the kinetics of the OER, all photoelectrodes displayed slow electron transfer kinetics, indicating that the surface of Rh:$SrTiO_3$, modified or not by the addition of metallic Pt and Cu, or by the molecular $Co(Cl_2Gm)_3(B\text{-}CH_3)_2$ clathrochelate, is not suitable for dioxygen evolution.

- The electrocatalytic mechanism of the molecular $Co(Cl_2Gm)_3(B\text{-}CH_3)_2$ for the hydrogen evolution reaction (HER) in the homogeneous phase was computed by means of Density Functional Theory (DFT). Several possible protonation sites were identified in the organic ligand cage, according to our calculations. Additionally, double protonation in two adjacent N atoms was also found possible, but a structural analysis of the involved intermediates suggested that such double protonated species should not participate in the actual HER electrocatalysis. Additionally, the calculated transition state for an ECCE mechanism presented a very high energy. Therefore we considered an alternative ECEC mechanism. In this case, neither a doubly protonated species nor a transition state could be found, which lead us to propose that the last HER step could be a Proton Coupled Electron Transfer.

- The structural elucidation of the clathrochelate $Co(Cl_2Gm)_3(B\text{-}CH_3)_2$ by means of EXAFS spectroscopy was treated in detail, by using the known XRD geometry and the DFT optimized geometry as well. Both geometries accounted for a satisfactory reproduction of the EXAFS spectrum. Nonetheless, the DFT

geometry was slightly different to the geometry found by XRD. Despite the small difference, the adequate fitting of EXAFS with the DFT geometry required more variables in the second scattering shell. This confirms the sensitivity and accuracy of EXAFS in structural determinations.

- Intensity Modulated Photovoltage Spectroscopy was used to characterize photoelectrodes made of pristine Rh:$SrTiO_3$ and Rh:$SrTiO_3$ – Pt. The IMVS response observed at open circuit conditions presented a spiral-like shape in the Nyquist representation. To the best of our knowledge, this is the first report of such behavior in semiconducting photoelectrodes studied by IMVS.

- By means of numerical simulations, it was established that the spiral-like shape observed by IMVS analysis was determined by a non-steady state dynamic response. Such non-steady state dynamics was adequately simulated using the classical system of differential equations that describes charge transfer and recombination at the surface of illuminated photoelectrodes.

- The numerical simulations permitted to determine the influence of charge transfer and recombination kinetic parameters, interfacial capacitances, and surface states, upon the non-steady state dynamic behavior of the photoelectrodes in IMVS conditions. An increase in charge transfer rate constant causes increase in the absolute value of the IMVS transfer function (H) and therefore an expansion of the spirals. Contrariwise, an increase in k_r causes a contraction of the spirals. An increase in the space charge capacitance causes a decrease in the absolute value of the transfer function and consequently a shrinking in the spirals. In the same manner, a decrease in I_0 causes a shrinking

in the spirals. The sole simulation condition that caused a phase shift in the IMVS response was the presence of surface states. All other parameters caused either a decrease (shrinking) or increase (expansion) of the transfer function *H* (i.e., the spirals in the Nyquist representation), but did not cause phase shift.

REFERENCES

1. Zhang, W. *et al.* Unravelling Photocarrier Dynamics beyond the Space Charge Region for Photoelectrochemical Water Splitting. *Chem. Mater.* **29,** 4036–4043 (2017).
2. Kafizas, A. *et al.* Optimizing the Activity of Nanoneedle Structured WO3 Photoanodes for Solar Water Splitting: Direct Synthesis via Chemical Vapor Deposition. *J. Phys. Chem. C* **121,** 5983–5993 (2017).
3. Sheridan, M. V. *et al.* All-in-One Derivatized Tandem p+n-Silicon–SnO2/TiO2 Water Splitting Photoelectrochemical Cell. *Nano Lett.* **17,** 2440–2446 (2017).
4. Yengantiwar, A. *et al.* Direct Liquid Injection Chemical Vapor Deposition of Molybdenum-Doped Bismuth Vanadate Photoelectrodes for Efficient Solar Water Splitting. *J. Phys. Chem. C* **121,** 5914–5924 (2017).
5. Pham, T. A., Ping, Y. & Galli, G. Modelling heterogeneous interfaces for solar water splitting. *Nat. Mater.* **16,** 401–408 (2017).
6. Schreier, M. *et al.* Coordinative immobilization of a molecular catalyst on Cu2O photocathodes for CO2 reduction. *J. Am. Chem. Soc.* **138,** 1938–1946 (2016).
7. Huang, Z.-F. *et al.* Hollow Cobalt-Based Bimetallic Sulfide Polyhedra for Efficient All-pH-Value Electrochemical and Photocatalytic Hydrogen Evolution. *J. Am. Chem. Soc.* **138,** 1359–1365 (2016).
8. Thorne, J. E., Li, S., Du, C., Qin, G. & Wang, D. Energetics at the surface of photoelectrodes and its influence on the photoelectrochemical properties. *J. Phys. Chem. Lett.* **6,** 4083−4088 (2015).
9. Iwashina, K. & Kudo, A. Rh-Doped SrTiO3 Photocatalyst Electrode Showing Cathodic Photocurrent for Water Splitting under Visible-Light Irradiation. *J. Am. Chem. Soc.* **133,** 13272–13275 (2011).
10. Subbaraman, R. *et al.* Enhancing Hydrogen Evolution Activity in Water Splitting

by Tailoring Li+-Ni(OH)2-Pt Interfaces. *Science (80-.).* **334,** 1256–1260 (2011).

11. Saioa Cobo, J. H. *et al.* A Janus cobalt-based catalytic material for electro-splitting of water. *Nat. Mater.* **11,** 802–807 (2012).
12. Lewerenz, H.-J. & Peter, L. *Photoelectrochemical Water Splitting Materials, Processes and Architectures*. (RSC Publishing, 2013).
13. Jia, Q., Iwase, A. & Kudo, A. BiVO4-Ru/SrTiO3:Rh composite Z-scheme photocatalyst for solar water splitting. *Chem. Sci.* **5,** 1513–1519 (2014).
14. Qian Wang, T. H. *et al.* Scalable water splitting on particulate photocatalyst sheets with a solar-to-hydrogen energy conversion efficiency exceeding 1%. *Nat. Mater.* just accepted (2016).
15. Zhang, B., Zhang, X., Xiao, X. & Shen, Y. Photoelectrochemical Water Splitting System-A Study of Interfacial Charge Transfer with Scanning Electrochemical Microscopy. *ACS Appl. Mater. Interfaces* acsami.5b07180 (2015). doi:10.1021/acsami.5b07180
16. Chen, H.-C., Huang, C.-W., Wu, J. C. S. & Lin, S.-T. Theoretical Investigation of the Metal-Doped $SrTiO_3$ Photocatalysts for Water Splitting. *J. Phys. Chem. C* **116,** 7897–7903 (2012).
17. Klahr, B., Gimenez, S., Fabregat-Santiago, F., Hamann, T. & Bisquert, J. Water oxidation at hematite photoelectrodes: The role of surface states. *J. Am. Chem. Soc.* **134,** 4294–4302 (2012).
18. Morales-Guio, C. G. *et al.* An Optically Transparent Iron Nickel Oxide Catalyst for Solar Water Splitting. *J. Am. Chem. Soc.* **137,** 9927–9936 (2015).
19. Lin, F., Bachman, B. F. & Boettcher, S. W. Impact of Electrocatalyst Activity and Ion Permeability on Water- Splitting Photoanodes. (2015). doi:10.1021/acs.jpclett.5b00904

20. Rausch, B., Symes, M. D., Chisholm, G. & Cronin, L. Decoupled catalytic hydrogen evolution from a molecular metal oxide redox mediator in water splitting. *Science (80-.).* **345,** 1326–1330 (2014).

21. Fabian, D. M. *et al.* Particle Suspension Reactors and Materials for Solar-Driven Water Splitting. *Energy Environ. Sci.* **8,** 2825–2850 (2015).

22. Hisatomi, T., Kubota, J. & Domen, K. Recent advances in semiconductors for photocatalytic and photoelectrochemical water splitting. *Chem. Soc. Rev.* **43,** 7520–7535 (2014).

23. Ran, J., Zhang, J., Yu, J., Jaroniec, M. & Qiao, S. Z. Earth-abundant cocatalysts for semiconductor-based photocatalytic water splitting. *Chem. Soc. Rev.* **43,** 7787–7812 (2014).

24. Swierk, J. R. & Mallouk, T. E. Design and development of photoanodes for water-splitting dye-sensitized photoelectrochemical cells. *Chem. Soc. Rev.* **42,** 2357–87 (2013).

25. Izaki, M. *et al.* Hybrid ZnO/phthalocyanine photovoltaic device with highly resistive ZnO intermediate layer. *ACS Appl. Mater. Interfaces* **5,** 9386–9395 (2013).

26. Zhang, Y., Zhang, W., Xie, T., Wang, D. & Song, X. A novel research approach on the dynamic properties of photogenerated charge carriers at Ag2S quantum-dots-sensitized TiO2 films by a frequency-modulated surface photovoltage technology. *Mater. Res. Bull.* **48,** 3242–3246 (2013).

27. Krüger, J., Plass, R., Grätzel, M., Cameron, P. J. & Peter, L. M. Charge Transport and Back Reaction in Solid-State Dye-Sensitized Solar Cells : A Study Using Intensity-Modulated Photovoltage and Photocurrent Spectroscopy. *J. Phys. Chem. B* **107,** 7536–7539 (2003).

28. Liu, Q. Analysis on dye-sensitized solar cells based on Fe-doped TiO 2 by intensity-modulated photocurrent spectroscopy and Mott – Schottky. *Chinese Chem. Lett.* **25,** 953–956 (2014).

29. Du, J. *et al.* Zn-Cu-In-Se Quantum Dot Solar Cells with a Certified Power Conversion Efficiency of 11.6%. (2016). doi:10.1021/jacs.6b00615

30. Okhay, O., Krishna, R., Titus, E., Andreeva, K. & Savkina, R. Photovoltage Study of Graphene Oxide with Ni Nanoparticles. *Mater. Today Proc.* **2,** 431–435 (2015).

31. Petrozza, A., Groves, C. & Snaith, H. J. Electron Transport and Recombination in Dye-Sensitized Mesoporous TiO2 Probed by Photoinduced Charge-Conductivity Modulation Spectroscopy with Monte Carlo Modeling. *JACS* **130,** 12912–12920 (2008).

32. Schlichthörl, G., Huang, S. Y., Sprague, J. & Frank, A. J. Band Edge Movement and Recombination Kinetics in Dye-Sensitized Nanocrystalline TiO2 Solar Cells : A Study by Intensity Modulated Photovoltage Spectroscopy. *J. Phys. Chem. B* **101,** 8141–8155 (1997).

33. Osterloh, F. E., Holmes, M. A., Chang, L., Moule, A. J. & Zhao, J. Photochemical Charge Separation in Poly(3-hexylthiophene) (P3HT) Films Observed with Surface Photovoltage Spectroscopy. *J. Phys. Chem. C* **117,** 26905−26913 (2013).

34. Roelofs, K. E., Herron, S. M. & Bent, S. F. Increased Quantum Dot Loading by pH Control Reduces Interfacial Recombination in Quantum-Dot- Sensitized Solar Cells. *ACS Nano* **9,** 8321–8334 (2015).

35. Bisquert, J. & Mora-Seró, I. Simulation of Steady-State Characteristics of Dye-Sensitized Solar Cells and the Interpretation of the Diffusion Length. *J. Phys.*

Chem. Lett. **1,** 450–456 (2010).

36. Bisquert, J. On Voltage, Photovoltage, and Photocurrent in Bulk Heterojunction Organic Solar Cells. *J. Phys. Chem. Lett.* **2,** 1950–1964 (2011).

37. Parkinson, B. & Turner, J. in *Photoelectrochemical Water Splitting Materials, Processes and Architectures* (eds. Lewerenz, H.-J. & Peter, L.) 1–18 (RSC Publishing, 2013).

38. Hossain, M. K. *et al.* Solution Combustion Synthesis, Characterization, and Photocatalytic Activity of CuBi2O4 and Its Nanocomposites with CuO and α-Bi2O3. *J. Phys. Chem. C* **121,** 8252–8261 (2017).

39. Zhou, X., Liu, N. & Schmuki, P. Photocatalysis with TiO2 Nanotubes: 'Colorful' Reactivity and Designing Site-Specific Photocatalytic Centers into TiO2 Nanotubes. *ACS Catal.* **7,** 3210–3235 (2017).

40. Li, M. *et al.* Graphene with Atomic-Level In-Plane Decoration of h-BN Domains for Efficient Photocatalysis. *Chem. Mater.* **29,** 2769–2776 (2017).

41. Kuang, P.-Y. *et al.* Facile Construction of Dual p–n Junctions in CdS/Cu2O/ZnO Photoanode with Enhanced Charge Carrier Separation and Transfer Ability. *ACS Omega* **2,** 852–863 (2017).

42. Chen, Y. *et al.* Enhanced photogenerated carrier separation in CdS quantum dot sensitized ZnFe2O4/ZnIn2S4 nanosheet stereoscopic films for exceptional visible light photocatalytic H2 evolution performance. *Nanoscale* **9,** 5912–5921 (2017).

43. Zachäus, C., Abdi, F. F., Peter, L. M. & Krol, R. van de. Photocurrent of BiVO4 is limited by surface recombination, not surface catalysis. *Chem. Sci.* **8,** 3712–3719 (2017).

44. McKone, J. R., DiSalvo, F. J. & Abruña, H. D. Solar energy conversion, storage, and release using an integrated solar-driven redox flow battery. *J. Mater. Chem.*

A **5,** 5362–5372 (2017).

45. Lin, Z., Li, L., Yu, L., Li, W. & Yang, G. Modifying photocatalysts for solar hydrogen evolution based on the electron behavior. *J. Mater. Chem. A* **5,** 5235–5259 (2017).

46. Wu, A. *et al.* Band-gap tailoring and visible-light-driven photocatalytic performance of porous (GaN)1−x(ZnO)x solid solution. *Dalt. Trans.* **46,** 2643–2652 (2017).

47. Wei, W.-D., Liu, X.-Y., Cui, S.-C. & Liu, J.-G. Loading of Co3O4 onto Pt-modified nitrogen-doped TiO2 nanocomposites promotes photocatalytic hydrogen production. *RSC Adv.* **7,** 25650–25656 (2017).

48. Robinson, M. T., Simons, C. E., Cliffel, D. E. & Jennings, G. K. Photocatalytic photosystem I/PEDOT composite films prepared by vapor-phase polymerization. *Nanoscale* **9,** 6158–6166 (2017).

49. Gao, J., Wang, Y., Zhou, S., Lin, W. & Kong, Y. A Facile One-Step Synthesis of Fe-Doped g-C3N4 Nanosheets and Their Improved Visible-Light Photocatalytic Performance. *ChemCatChem* **9,** 1708–1715 (2017).

50. Hu, X., Tian, J., Xue, Y., Li, Y. & Cui, H. Bi2WO6 Nanosheets Decorated with Au Nanorods for Enhanced Near-Infrared Photocatalytic Properties Based on Surface Plasmon Resonance Effects and Wide-Range Near-Infrared Light Harvesting. *ChemCatChem* **9,** 1511–1516 (2017).

51. Sivula, K. & Grätzel, M. in *Photoelectrochemical Water Splitting Materials, Processes and Architectures* (eds. Lewerenz, H.-J. & Peter, L.) 83–108 (2013).

52. Barea, E. M. & Bisquert, J. Properties of Chromophores Determining Recombination at the TiO2 − Dye − Electrolyte Interface. *Langmuir* 8773−8781 (2013).

53. Wang, H. *et al.* Enhanced Carrier Transport Distance in Colloidal PbS Quantum-Dot-Based Solar Cells Using ZnO Nanowires. *J. Phys. Chem. C* **119,** 27265−27274 (2015).

54. Shinde, P. S., Choi, S. H., Kim, Y., Ryu, J. & Jang, J. S. Onset potential behavior in α-Fe2O3 photoanodes: the influence of surface and diffusion Sn doping on the surface states. *Phys. Chem. Chem. Phys.* **18,** 2495–509 (2016).

55. Klotz, D., Ellis, D. S., Dotan, H. & Rothschild, A. Empirical in operando analysis of the charge carrier dynamics in hematite photoanodes by PEIS, IMPS and IMVS. *Phys. Chem. Chem. Phys.* **18,** 23438–23457 (2016).

56. Click, K. A., Beauchamp, D. R., Huang, Z., Chen, W. & Wu, Y. Membrane-Inspired Acidically Stable Dye-Sensitized Photocathode for Solar Fuel Production. *J. Am. Chem. Soc.* **138,** 1174−1179 (2016).

57. Krawicz, A. *et al.* Photofunctional Construct That Interfaces Molecular Cobalt-Based Catalysts for H2 Production to a Visible-Light-Absorbing Semiconductor. *J. Am. Chem. Soc.* **135,** 11861−11868 (2013).

58. Dunn, H. K. *et al.* Tin doping speeds up hole transfer during light-driven water oxidation at hematite photoanodes. *Phys. Chem. Chem. Phys.* **16,** 24610–24620 (2014).

59. Liang, Y. & Messinger, J. Improving BiVO4 photoanodes for solar water splitting through surface passivation. *Phys. Chem. Chem. Phys.* **16,** 12014–12020 (2014).

60. Trzesniewski, B. J. & Smith, W. A. Photocharged BiVO4 photoanodes for improved solar water splitting. *J. Mater. Chem. A* **4,** 2919–2926 (2016).

61. Ma, Y., Pendlebury, S. R., Reynal, A., Formal, F. Le & Durrant, J. R. Dynamics of photogenerated holes in undoped BiVO4 photoanodes for solar water

oxidation. *Chem. Sci.* **5,** 2964–2973 (2014).

62. Xiao, B., Lin, L., Hong, J., Lin, H. & Song, Y. Synthesis of a monoclinic BiVO4 nanorod array as the photocatalyst for efficient photoelectrochemical water oxidation. *RSC Adv.* **7,** 7547–7554 (2017).

63. Hamann, T. W., Gstrein, F., Brunschwig, B. S. & Lewis, N. S. Measurement of the driving force dependence of interfacial charge-transfer rate constants in response to pH changes at n-ZnO/H2O interfaces. *Chem. Phys.* **326,** 15–23 (2006).

64. Memming, R. *Semiconductor Electrochemistry*. (Wiley-VCH Verlag GmbH and Co. KGaA, 2015).

65. Hagfeldt, A. & Grätzel, M. Light-Induced Redox Reactions in Nanocrystalline Systems. *Chem. Rev.* **95,** 49–68 (1995).

66. Upul Wijayantha, K. G., Saremi-Yarahmadi, S. & Peter, L. M. Kinetics of oxygen evolution at α-Fe2O3 photoanodes: a study by photoelectrochemical impedance spectroscopy. *Phys. Chem. Chem. Phys.* **13,** 5264 (2011).

67. Leng, W. H., Zhang, Z., Zhang, J. Q. & Cao, C. N. Investigation of the Kinetics of a TiO2 Photoelectrocatalytic Reaction Involving Charge Transfer and Recombination through Surface States by Electrochemical Impedance Spectroscopy. *J. Phys. Chem. B* **109,** 15008–15023 (2005).

68. Cachet, H. & Sutter, E. M. M. Kinetics of Water Oxidation at TiO2 Nanotube Arrays at Different pH Domains Investigated by Electrochemical and Light-Modulated Impedance Spectroscopy. *J. Phys. Chem. C* **119,** 25548−25558 (2015).

69. Bertoluzzi, L., Lopez-varo, P., Jim, A. & Bisquert, J. Charge transfer processes at the semiconductor / electrolyte interface for solar fuel production: insight from impedance spectroscopy. *J. Mater. Chem. A* **4,** 2873–2879 (2016).

70. Bertoluzzi, L. & Bisquert, J. Equivalent Circuit of Electrons and Holes in Thin Semiconductor Films for Photoelectrochemical Water Splitting Applications. *J. Phys. Chem. Lett.* **3,** 2517–2522 (2012).

71. Ponomarev, E. a. & Peter, L. M. A comparison of intensity modulated photocurrent spectroscopy and photoelectrochemical impedance spectroscopy in a study of photoelectrochemical hydrogen evolution at p-InP. *J. Electroanal. Chem.* **397,** 45–52 (1995).

72. Schefold, J. Impedance and intensity modulated photocurrent spectroscopy as complementary differential methods in photoelectrochemistry. *J. Electroanal. Chem.* **341,** 111–136 (1992).

73. Babenko, S. D., Balakai, A. a., Lavrushko, A. G., Ponomarev, E. a. & Simbirtseva, G. V. Kinetics of the photoelectrochemical evolution of hydrogen at p-type Si. *J. Electroanal. Chem.* **382,** 175–177 (1995).

74. Ponomarev, E. A. & Babenko, S. D. Theoretical analysis of the laser-induced phototransient response of semiconductor | electrolyte circuits with 'current-doubling' reactions. *J. Electroanal. Chem.* **371,** 27–35 (1994).

75. Bisquert, J., Zaban, A., Greenshtein, M. & Mora-Seró, I. Determination of Rate Constants for Charge Transfer and the Distribution of Semiconductor and Electrolyte Electronic Energy Levels in Dye-Sensitized Solar Cells by Open-Circuit Photovoltage Decay Method. *JACS* **126,** 13550–13559 (2004).

76. Set, Y. T. *et al.* Analytical modeling of intensity-modulated photovoltage spectroscopic responses of organic bulk-heterojunction solar cells. *Appl. Phys. Lett.* **107,** 173301 (2015).

77. Liu, C., Qiu, Z., Yue, W., Zhou, X. & Wang, M. Characterization of Photocurrent Generation Dynamics in Polymer Solar Cells Based on ZnO / CdS-

Core / Shell Nanoarrays by Intensity Modulated Photocurrent Spectroscopy : Theoretical Modeling. *J. Phys. Chem. C* **118,** 28462−28473 (2014).

78. Titanium dioxide. Available at: http://shop.solaronix.com/ti-nanoxide-t-sp.html. (Accessed: 5th December 2017)

79. Ruthenium dye N719. Available at: http://shop.solaronix.com/ruthenizer-535-bistba.html. (Accessed: 5th December 2017)

80. Electrolyte. Available at: http://shop.solaronix.com/mosalyte-tde250. (Accessed: 5th December 2017)

81. Shinagawa, T., Garcia-Esparza, A. T. & Takanabe, K. Insight on Tafel slopes from a microkinetic analysis of aqueous electrocatalysis for energy conversion. *Sci. Rep.* **5,** 13801 (2015).

82. Bockris, J. O. Kinetics of activation controlled consecutive electrochemical reactions: anodic evolution of oxygen,. *J. Chem. Phys.* **24,** 817–827. (1956).

83. Lyons, M. E. G. & Floquet, S. Mechanism of oxygen reactions at porous oxide electrodes. Part 2 —Oxygen evolution at RuO2, IrO2 and IrxRu1−xO2 electrodes in aqueous acid and alkaline solution. *Phys. Chem. Chem. Phys.* **13,** 5314–5335 (2011).

84. DeFaria, L. A., Boodts, J. F. C. & Trasatti, S. Electrocatalytic properties of ternary oxide mixtures of composition Ru0.3Ti(0.7−x)CexO2: oxygen evolution from acidic solution. *J. Appl. Electrochem.* **26,** 1195–1199 (1996).

85. Hu, J.-M., Zhang, J.-Q. & Cao, C.-N. Oxygen evolution reaction on IrO2-based DSA type electrodes: kinetics analysis of Tafel lines and EIS. *Int. J. Hydrog. Energy* **29,** 791–79 (2004).

86. Riddiford, A. Mechanisms for the evolution and ionization of oxygen at platinum electrodes. *Electrochim. Acta* **4,** 170–178 (1961).

87. Marshall, A. T. & Vaisson-Béthune, L. Avoid the quasi-equilibrium assumption when evaluating the electrocatalytic oxygen evolution reaction mechanism by Tafel slope analysis. *Electrochem. commun.* **61,** 23–26 (2015).

88. Bockris, J. O. & Otagawat, T. Mechanism of Oxygen Evolution on Perovskites. *J. Phys. Chem* **87,** 2960–2971 (1983).

89. Conway, B. E. & Bai, L. Determination of adsorption of OPD H species in the cathodic hydrogen evolution reaction at Pt in relation to electrocatalysis. *J. Electroanal. Chem.* **198,** 149 (1986).

90. Markovic, N. M., Sarraf, S. T., Gasteiger, H. A. & Ross, P. N. Hydrogen electrochemistry on platinum lower-index single-crystal surfaces in alkaline solution. *J. Chem. Soc.* **92,** 3719 (1996).

91. Popczun, E. J. et al. Highly active electrocatalysis of the hydrogen evolution reaction by cobalt phosphide nanoparticles. *Angew. Chem. Int. Ed.* **53,** 5427 (2014).

92. Moon, J.-S. et al. The nature of active sites of Ni2P electrocatalysts for hydrogen evolution reaction. *J. Catal.* **326,** 92 (2015).

93. Jaksic, J. M., Vojnovic, M. V. & Krstajic, N. V. Kinetic analysis of hydrogen evolution at Ni-Mo alloy electrodes. *Electrochim. Acta* **45,** 4151 (2000).

94. Conway, B. E. & Bai, L. H2 evolution kinetics at high activity Ni-Mo-Cd electrocoated cathodes and its relation to potential dependence of sorption of H*. *Int. J. Hydrog. Energy* **11,** 533 (1986).

95. Zheng, Y. et al. Toward design of synergistically active carbon-based catalysts for electrocatalytic hydrogen evolution. *ACS Nano* **8,** 5290 (2014).

96. Damjanovic, A., Deyt, A. & Bockris, J. O. Kinetics of oxygen evolution and dissolution on platinum electrodes. *Electrochim. Acta* **11,** 791 (1966).

97. Miles, M. H. et al. The oxygen evolution reaction on platinum, iridium, ruthenium and their alloys at 80 °C in acid solutions. *Electrochim. Acta* **23,** 521 (1978).

98. Lu, Z. et al. Three-dimensional NiFe layered double hydroxide film for high-efficiency oxygen evolution reaction. *Chem. Commun.* **50,** 6479 (2014).

99. Grimaud, A. et al. Double perovskites as a family of highly active catalysts for oxygen evolution in alkaline solution. *Nat. Comm.* **4,** 4239 (2013).

100. Shi, H. & Zhao, G. Water oxidation on spinel NiCo2O4 nanoneedles anode: microstructures, specific surface character, and the enhanced electrocatalytic performance. *J. Phys. Chem. C* **118,** 25939 (2014).

101. Longo, M. *et al.* On the photoluminescence behavior of samarium-doped strontium titanate nanostructures under UV light . A structural and electronic understanding w. *Phys. Chem. Chem. Phys.* **12,** 7566–7579 (2010).

102. Kawasaki, S. *et al.* Electronic Structure and Photoelectrochemical Properties of an Ir-Doped SrTiO 3 Photocatalyst. *J. Phys. Chem. C* **118,** 20222–20228 (2014).

103. Kawasaki, S. *et al.* Elucidation of Rh-Induced In-Gap States of Rh:SrTiO 3 Visible-Light- Driven Photocatalyst by Soft X‑ray Spectroscopy and First-Principles Calculations. *J. Phys. Chem. C* **116,** 24445–24448 (2012).

104. Modak, B. & Ghosh, S. K. Role of F in improving the photocatalytic activity of Rh doped SrTiO3. *J. Phys. Chem. C* **119,** 7215–7224 (2015).

105. Yamakata, A., Kawaguchi, M., Murachi, R., Okawa, M. & Kamiya, I. Dynamics of Photogenerated Charge Carriers on Ni- and Ta-Doped SrTiO3 Photocatalysts Studied by Time-Resolved Absorption and Emission Spectroscopy. *J. Phys. Chem. C* **120,** 7997–8004 (2016).

106. Wei, W., Dai, Y., Jin, H. & Huang, B. Density functional characterization of the

electronic structure and optical properties of Cr-doped SrTiO $_3$. *J. Phys. D. Appl. Phys.* **42,** 55401 (2009).

107. Tan, H. *et al.* Oxygen Vacancy Enhanced Photocatalytic Activity of Pervoskite SrTiO3. *ACS Appl. Mater. Interfaces* **6,** 19184–19190 (2014).

108. Piskunov, S. *et al.* C-, N-, S-, and Fe-Doped TiO 2 and SrTiO 3 Nanotubes for Visible-Light-Driven Photocatalytic Water Splitting: Prediction from First Principles. *J. Phys. Chem. C* **119,** 18686–18696 (2015).

109. Modak, B. & Ghosh, S. K. Enhancement of Visible Light Photocatalytic Activity of SrTiO3 : A Hybrid Density Functional Study. *J. Phys. Chem. C* **119,** 23503–23514 (2015).

110. Li, W., Liu, S., Wang, S., Guo, Q. & Guo, J. The roles of reduced Ti cations and oxygen vacancies in water adsorption and dissociation on SrTiO3(110). *J. Phys. Chem. C* **118,** 2469–2474 (2014).

111. Gerhold, S. *et al.* Nickel-Oxide-Modified SrTiO(110)-(4 x 1) Surfaces and Their Interaction with Water. *J. Phys. Chem. C. Nanomater. Interfaces* **119,** 20481–20487 (2015).

112. Furuhashi, K., Jia, Q., Kudo, A. & Onishi, H. Time-Resolved Infrared Absorption Study of SrTiO 3 Photocatalysts Codoped with Rhodium and Antimony. *J. Phys. Chem. C* **117,** 19101–19106 (2013).

113. Kumar, S., Tonda, S., Baruah, A., Kumar, B. & Shanker, V. Synthesis of novel and stable g-C3N4/N-doped SrTiO3 hybrid nanocomposites with improved photocurrent and photocatalytic activity under visible light irradiation. *Dalton Trans.* **43,** 16105–14 (2014).

114. Liu, C. *et al.* Enhanced photoelectrochemical and photocatalytic activity by Cu2O/SrTiO3 p–n heterojunction via a facile deposition–precipitation technique.

RSC Adv. **5,** 33938–33945 (2015).

115. Fermín, D. J., Ponomarev, E. A. & Peter, L. M. Kinetic study of CdS photocorrosion by intensity modulated photocurrent and photoelectrochemical impedance spectroscopy. *J. Electroanal. Chem.* **473,** 192–203 (1999).

116. Chu, S. & Majumdar, A. Opportunities and challenges for a sustainable energy future. *Nature* **488,** 294–303 (2012).

117. Liu, Q., Pu, Z., Asiri, A. M. & Sun, X. Nitrogen-doped carbon nanotube supported iron phosphide nanocomposites for highly active electrocatalysis of the hydrogen evolution reaction. *Electrochim. Acta* **149,** 324–329 (2014).

118. Gómez-Marín, A. M. & Ticianelli, E. A. Analysis of the electrocatalytic activity of α-molybdenum carbide thin porous electrodes toward the hydrogen evolution reaction. *Electrochim. Acta* **220,** 363–372 (2016).

119. Devadas, B. & Imae, T. Hydrogen evolution reaction efficiency by low loading of platinum nanoparticles protected by dendrimers on carbon materials. *Electrochem. commun.* **72,** 135–139 (2016).

120. Zhu, L. *et al.* Ru-modified silicon nanowires as electrocatalysts for hydrogen evolution reaction. *Electrochem. commun.* **52,** 29–33 (2015).

121. Gao, S. *et al.* General urea-assisted synthesis of carbon-coated metal phosphide nanoparticles for efficient hydrogen evolution electrocatalysis. *Electrochim. Acta* **199,** 99–107 (2016).

122. Vargas-Uscategui, A., Mosquera, E., Chornik, B. & Cifuentes, L. Electrocatalysis of the hydrogen evolution reaction by rhenium oxides electrodeposited by pulsed-current. *Electrochim. Acta* **178,** 739–747 (2015).

123. Assaud, L. *et al.* Systematic increase of electrocatalytic turnover at nanoporous platinum surfaces prepared by atomic layer deposition. *J. Mater. Chem. A* **3,**

8450–8458 (2015).

124. Raugei, S. *et al.* Experimental and Computational Mechanistic Studies Guiding the Rational Design of Molecular Electrocatalysts for Production and Oxidation of Hydrogen. *Inorg. Chem.* **55,** 445–460 (2016).

125. Zarkadoulas, A. *et al.* Experimental and Theoretical Insight into Electrocatalytic Hydrogen Evolution with Nickel Bis(aryldithiolene) Complexes as Catalysts. *Inorg. Chem.* **55,** 432–444 (2015).

126. Belov, A. S. *et al.* Molecular design of cage iron(ii) and cobalt(ii,iii) complexes with a second fluorine-enriched superhydrophobic shell. *Dalton Trans.* **3,** 3773–3784 (2015).

127. Dolganov, A. V *et al.* Iron vs. cobalt clathrochelate electrocatalysts of HER: the first example on a cage iron complex. *Dalt. Trans.* **42,** 4373–6 (2013).

128. Voloshin, Y. Z., Dolganov, A. V, Varzatskii, A. & Bubnov, Y. N. Efficient electrocatalytic hydrogen production from H+ ions using specially designed boron-capped cobalt clathrochelates. *Chem. Comm.* **47,** 7737–7739 (2011).

129. Ghachtouli, S. El *et al.* Monometallic Cobalt − Trisglyoximato Complexes as Precatalysts for Catalytic H2 Evolution in Water. *J. Phys. Chem. C* **117,** 17073–17077 (2013).

130. Kochubey, D. *et al.* Combined X-ray absorption near-edge structure and X-ray photoelectron study of the electrocatalytically active cobalt(I) cage complexes and the clathrochelate cobalt(II)- and cobalt(III)-containing precursors and analogs. *J. Phys. Chem. C* **117,** 2753–2759 (2013).

131. Novikov, V. V. *et al.* Transition ion strikes back: Large magnetic susceptibility anisotropy in cobalt(II) clathrochelates. *J. Phys. Chem. Lett.* **5,** 3799–3803 (2014).

132. Vologzhanina, A. V. *et al.* Synthesis and Temperature-Induced Structural Phase

and Spin Transitions in Hexadecylboron-Capped Cobalt(II) Hexachloroclathrochelate and Its Diamagnetic Iron(II)-Encapsulating Analogue. *Inorg. Chem.* **54,** 5827–5838 (2015).

133. Jansze, S. M. *et al.* Ligand Aspect Ratio as a Decisive Factor for the Self-Assembly of Coordination Cages. *J. Am. Chem. Soc.* **138,** 2046–2054 (2016).

134. Dinh Nguyen, M. T. *et al.* Implementing molecular catalysts for hydrogen production in proton exchange membrane water electrolysers. *Coord. Chem. Rev.* **256,** 2435–2444 (2012).

135. Millet, P., Rozain, C., Villagra, A., Ragupathy, A. & Guymont, M. Implementation of Cobalt Clathrochelates in Polymer Electrolyte Water Electrolysers for Hydrogen Evolution. *Chem. Eng. Trans.* **41,** 325–330 (2014).

136. Pantani, O. *et al.* Cobalt clathrochelate complexes as hydrogen-producing catalysts. *Angew. Chem. Int. Ed. Engl.* **47,** 9948–50 (2008).

137. Nguyen, M. T. D., Charlot, M. F. & Aukauloo, A. Structural, electronic, and theoretical description of a series of cobalt clathrochelate complexes in the Co(III), Co(II) and Co(I) oxidation states. *J. Phys. Chem. A* **115,** 911–922 (2011).

138. Gupta, V., Ganegoda, H., Engelhard, M. H., Terry, J. & Linford, M. R. Assigning Oxidation States to Organic Compounds via Predictions from X-ray Photoelectron Spectroscopy: A Discussion of Approaches and Recommended Improvements. *J. Chem. Educ.* **91,** 232–238 (2014).

139. Antuch, M. *et al.* Effect of the ligand framework of cobalt clathrochelates on hydrogen evolution electrocatalysis: electrochemical, spectroscopic and Density Functional Theory analyses. *Electrochim. Acta* **245,** 1065–1074 (2017).

140. Kaeffer, N. *et al.* The dark side of molecular catalysis: Diimine-dioxime cobalt complexes are not the actual hydrogen evolution electrocatalyst in acidic aqueous

solutions. *ACS Catal.* **6,** 3727–3737 (2016).

141. Briggs, D. & Gibson, V. A. Direct Observation of Multiplet Splitting in 2p photoelectron peaks of Cobalt Complexes. *Chem. Phys. Lett.* **25,** 493–496 (1974).

142. Tufts, B. J. *et al.* XPS and EXAFS Studies of the Reactions of Co (III) Ammine Complexes with GaAs Surfaces. *J. Am. Chem. Soc.* **112,** 5123–5136 (1990).

143. Krawicz, A. *et al.* Photofunctional Construct that Interfaces Molecular Cobalt-based Catalysts for H Production to a Visible-light Absorbing Semiconductor Photofunctional Construct that Interfaces Molecular Cobalt-based Catalysts for H 2 Production to a Visible-light Absorbi. *J. Am. Chem. Soc.* **135,** 11861−11868 (2013).

144. Borodko, Y. G., Vetchinkin, S. I., Zimont, S. L., Ivleva, I. N. & Shulga, Y. M. Nature of satellites in X-ray photoelectron spectra XPS of paramagnetic Cobalt(II) compounds. *Chem. Phys. Lett.* **42,** 264–267 (1976).

145. Atkins, P. & de Paula, J. *Physical Chemistry: Thermodynamics, Structure, and Change*. (W. H. Freeman, 2014).

146. Bunker, G. *Introduction to XAFS: A Practical Guide to X-ray Absorption Fine Structure Spectroscopy*. (Cambridge University Press, 2010).

147. Beckwith, M. A. *et al.* How Accurately Can Extended X-ray Absorption Spectra Be Predicted from First Principles? Implications for Modeling the Oxygen-Evolving Complex in Photosystem II. *J. Am. Chem. Soc.* **137,** 12815–12834 (2015).

148. S. I. Zabinsky, Rehr, J. J., Ankudinov, A., Albers, R. C. & Eller, M. J. . *Phys. Rev. B* **52,** 2995 (1995).

149. Ankudinov, A. L., Ravel, B., Rehr, J. J. & Conradson, S. D. . *Phys. Rev. B* **58,** 7565 (1998).

150. Jensen, F. *Introduction to Computational Chemistry*. (John Wiley & Sons Inc., 2007).

151. Cramer, C. J. *Essentials of Computational Chemistry*. (John Wiley & Sons Ltd, 2004).

152. Fogeron, T. *et al.* A Cobalt Complex with a bioinspired molybdopterin-like ligand: a Catalyst for Hydrogen Evolution. *Dalt. Trans.* **2,** 14754–14763 (2016).

153. Bertran, J., Gallardo, I., Moreno, M. & Savéant, J.-M. Dissociative Electron Transfer. Ab Initio Study of the Carbon-Halogen Bond Reductive Cleavage in Methyl and Perfluoromethyl Halides. Role of the Solvent. *JACS* **114,** 9576–9583 (1992).

154. Hamad, S., Balestra, S. R. G., Bueno-Perez, R., Calero, S. & Ruiz-Salvador, A. R. Atomic charges for modeling metal-organic frameworks: Why and how. *J. Solid State Chem.* **223,** 144–151 (2015).

155. Panetier, J. A., Letko, C. S., Tilley, T. D. & Head-Gordon, M. Computational Characterization of Redox Non-Innocence in Cobalt-Bis(Diaryldithiolene)-Catalyzed Proton Reduction. *J. Chem. Theory Comput.* **12,** 223–230 (2016).

156. Anjali, B. A., Sayyed, F. B. & Suresh, C. H. Correlation and Prediction of Redox Potentials of Hydrogen Evolution Mononuclear Cobalt Catalysts via Molecular Electrostatic Potential: A DFT Study. *J. Phys. Chem. A* **120,** 1112–1119 (2016).

157. Grelaud, G. *et al.* Redox-active molecular wires derived from dinuclear ferrocenyl/ ruthenium(II) alkynyl complexes: Covalent attachment to hydrogen-terminated silicon surfaces. *J. Phys. Chem. C* **118,** 3680–3695 (2014).

158. Greco, C. *et al.* Electrocatalytic dihydrogen evolution mechanism of [Fe2(CO)4(kappa(2)-Ph2PCH2CH2PPh2)(mu-S(CH2)3S)] and related models of the [FeFe]-hydrogenases active site: a DFT investigation. *Dalton Trans.* **39,**

7320–9 (2010).

159. Liao, R. Z., Wang, M., Sun, L. C. & Siegbahn, P. E. M. The mechanism of hydrogen evolution in Cu(bztpen)-catalysed water reduction: a DFT study. *Dalt. Trans.* **44,** 9736–9739 (2015).

160. Solis, B. H. & Hammes-Schiffer, S. Substituent Effects on Cobalt Diglyoxime Catalysts for Hydrogen Evolution. *JACS* **133,** 19036–19039 (2011).

161. Mondal, B., Neese, F. & Ye, S. Toward Rational Design of 3d Transition Metal Catalysts for CO 2 Hydrogenation Based on Insights into Hydricity-Controlled Rate-Determining Steps. *Inorg. Chem.* acs.inorgchem.6b00471 (2016). doi:10.1021/acs.inorgchem.6b00471

162. Kaeffer, N., Chavarot-Kerlidou, M. & Artero, V. Hydrogen evolution catalyzed by cobalt diimine-dioxime complexes. *Acc. Chem. Res.* **48,** 1286–1295 (2015).

163. Solis, B. H. & Hammes-Schiffer, S. Theoretical analysis of mechanistic pathways for hydrogen evolution catalyzed by cobaloximes. *Inorg. Chem.* **50,** 11252–11262 (2011).

164. Dance, I. Mimicking nitrogenase. *Dalton Trans.* **39,** 2972–2983 (2010).

165. Qi, X., Fu, Y., Liu, L. & Guo, Q. Ab Initio Calculations of Thermodynamic Hydricities of Transition-Metal Hydrides in Acetonitrile. *Organometallics* **26,** 4197–4203 (2007).

166. Harshan, A. K., Solis, B. H., Winkler, J. R., Gray, H. B. & Hammes-Schiffer, S. Computational Study of Fluorinated Diglyoxime-Iron Complexes: Tuning the Electrocatalytic Pathways for Hydrogen Evolution. *Inorg. Chem.* **55,** 2934–2940 (2016).

167. Sieffert, N., Kendrick, T., Tiana, D. & Morrison, C. A. First principles static and dynamic calculations for the transition metal hydride series MH4L3 (M = Fe, Ru

and Os; L = NH3, PH3 and PF3). *Dalton Trans.* **44,** 4259–70 (2015).

168. Solis, B. H. & Hammes-Schiffer, S. Computational Study of Anomalous Reduction Potentials for Hydrogen Evolution Catalyzed by Cobalt Dithiolene Complexes. *JACS* **134,** 15253−15256 (2012).

169. Solis, B. H. & Hammes-Schiffer, S. Proton-Coupled Electron Transfer in Molecular Electrocatalysis : Theoretical Methods and Design Principles. *Inorg. Chem.* **53,** 6427–6443 (2014).

170. Mondal, B., Neese, F. & Ye, S. Control in the Rate-Determining Step Provides a Promising Strategy To Develop New Catalysts for CO<inf>2</inf> Hydrogenation: A Local Pair Natural Orbital Coupled Cluster Theory Study. *Inorg. Chem.* **54,** 7192–7198 (2015).

171. Marcus, R. A. On the Theory of Oxidation Reduction Reactions Involving Electron Transfer. I. *J. Chem. Phys.* **24,** 966–978 (1956).

172. Marcus, R. A. On the Theory of Oxidation Reduction Reactions Involving Electron Transfer. II. Applications to Data on the Rates of Isotopic Exchange Reactions. *J. Chem. Phys.* **26,** 867–871 (1957).

173. Marcus, R. A. Transfer . III . Applications to Data on the Rates of Organic Redox Reactions Involving Electron Transfer. III. Applications to Data on the Rates of Organic Redox Reactions. *J. Chem. Phys.* **26,** 872–877 (1957).

174. Baik, M. & Friesner, R. A. Computing Redox Potentials in Solution : Density Functional Theory as A Tool for Rational Design of Redox Agents. *J. Phys. Chem. A* **106,** 7407–7412 (2002).

175. Benassi, R., Ferrarini, P., Fontanesi, C., Benedetti, L. & Paolucci, F. Calculated electron affinities and redox E0 values of polypyridinic derivatives. *J. Electroanal. Chem.* **564,** 231–237 (2004).

176. Fu, Y., Liu, L., Yu, H., Wang, Y. & Guo, Q. Quantum-Chemical Predictions of Absolute Standard Redox Potentials of Diverse Organic Molecules and Free Radicals in Acetonitrile. *JACS* 7227–7234 (2005).

177. Lewis, A., Bumpus, J. A., Truhlar, D. G. & Cramer, C. J. Molecular Modeling of environmentally important processes: Reduction potentials. *J. Chem. Educ.* **81,** 596–604 (2004).

178. Hu, L. *et al*. Reorganization Energy for Internal Electron Transfer in Multicopper Oxidases. *J. Phys. Chem. B* **115,** 13111–13126 (2011).

179. Ørnsø, K. B., Jónsson, E. O., Jacobsen, K. W. & Thygesen, K. S. Importance of the Reorganization Energy Barrier in Computational Design of Porphyrin-Based Solar Cells with Cobalt-Based Redox Mediators. *J. Phys. Chem. C* **119,** 12792−12800 (2015).

180. Chang, Y. & Chao, I. An Important Key to Design Molecules with Small Internal Reorganization Energy: Strong Nonbonding Character in Frontier Orbitals. *J. Phys. Chem. Lett.* **1,** 116–121 (2010).

181. Ghosh, S. & Hammes-Schiffer, S. Calculation of Electrochemical Reorganization Energies for Redox Molecules at Self-Assembled Monolayer Modi fi ed Electrodes. *J. Phys. Chem. Lett.* **6,** 1–5 (2015).

182. Vaissier, V., Frost, J. M., Barnes, P. R. F. & Nelson, J. Influence of Intermolecular Interactions on the Reorganization Energy of Charge Transfer between Surface-Attached Dye Molecules. *J. Phys. Chem. C* (2015). doi:10.1021/acs.jpcc.5b09739

183. Ghosh, S., Horvath, S., Soudackov, A. V & Hammes-schi, S. Electrochemical Solvent Reorganization Energies in the Framework of the Polarizable Continuum Model. *J. Chem. Theory Comput.* **10,** 2091−2102 (2014).

184. Amashukeli, X., Gruhn, N. E., Lichtenberger, D. L., Winkler, J. R. & Gray, H. B. Inner-Sphere Electron-Transfer Reorganization Energies of Zinc Porphyrins. *JACS* **126,** 15566–15571 (2004).

185. Basu, G., Kitao, A., Kuki, A. & Go, N. Protein Electron Transfer Reorganization Energy Spectrum from Normal Mode Analysis. 1. Theory. *J. Phys. Chem. B* **102,** 2076–2084 (1998).

186. Hamann, T. W., Gstrein, F., Brunschwig, B. S. & Lewis, N. S. Measurement of the Dependence of Interfacial Charge-Transfer Rate Constants on the Reorganization Energy of Redox Species at n-ZnO/H 2 O Interfaces. *JACS* **127,** 13949–13954 (2005).

187. Miyashita, O. & Go, N. Reorganization Energy of Protein Electron Transfer Reaction: Study with Structural and Frequency Signature. *J. Phys. Chem. B* **104,** 7516–7521 (2000).

188. Gupta, S. & Matyushov, D. V. Effects of Solvent and Solute Polarizability on the Reorganization Energy of Electron Transfer. *J. Phys. Chem. A* **108,** 2087–2096 (2004).

189. Mertz, E. L., Tikhomirov, V. A. & Krishtalik, L. I. Stokes Shift as a Tool for Probing the Solvent Reorganization Energy. *J. Phys. Chem. A* **101,** 3433–3442 (1997).

190. Brinkley, D. W. & Roth, J. P. Determination of a Large Reorganization Energy Barrier for Hydride. *JACS* **127,** 15720–15721 (2005).

191. Schmidt, M. W. *et al.* General atomic and molecular electronic structure system. *J. Comput. Chem.* **14,** 1347–1363 (1993).

192. Bode, B. M. & Gordon, M. S. MacMolPlt: A graphical user interface for GAMESS. *J. Mol. Graph. Model.* **16,** 133–138 (1998).

193. Schuchardt, K. L. *et al.* Basis set exchange: A community database for computational sciences. *J. Chem. Inf. Model.* **47,** 1045–1052 (2007).

194. Hay, P. J. & Wadt, W. R. Ab initio effective core potentials for molecular calculations. Potentials for the transition metal atoms Sc to Hg. *J. Chem. Phys.* **82,** 270 (1985).

195. Hay, P. J. & Wadt, W. R. Ab initio effective core potentials for molecular calculations. Potentials for K to Au including the outermost core orbitals. *J. Chem. Phys.* **82,** 299 (1985).

196. Wadt, W. R. & Hay, P. J. Ab initio effective core potentials for molecular calculations. Potentials for main group elements Na to Bi. *J. Chem. Phys.* **82,** 284 (1985).

197. Williams, T. G., DeYonker, N. J. & Wilson, A. K. Hartree-Fock complete basis set limit properties for transition metal diatomics. *J. Chem. Phys.* **128,** 44101 (2008).

198. Balabanov, N. B. & Peterson, K. A. Basis set limit electronic excitation energies, ionization potentials, and electron affinities for the 3d transition metal atoms: Coupled cluster and multireference methods. *J. Chem. Phys.* **125,** 74110 (2006).

199. Marenich, A. V., Cramer, C. J. & Truhlar, D. G. Universal solvation model based on solute electron density and on a continuum model of the solvent defined by the bulk dielectric constant and atomic surface tensions. *J. Phys. Chem. B* **113,** 6378–6396 (2009).

200. GAMESS input description. (2016). Available at: http://www.msg.ameslab.gov/gamess/GAMESS_Manual/input.pdf. (Accessed: 23rd February 2018)

201. Antuch, M. *et al.* Characterization of Rh:SrTiO3 photoelectrodes surface-

modified with a cobalt clathrochelate and their application to the hydrogen evolution reaction. *Electrochim. Acta* **258,** 255–265 (2017).

202. Bard, A. J. & Faulkner, L. R. *Electrochemical Methods Fundamentals and Applications*. (John Wiley & Sons, Inc., 2001).
203. Gong, L. *et al.* Photocurrent Response in Multiwalled Carbon Nanotube Core − Molybdenum Disulfide Shell Heterostructures. *J. Phys. Chem. C* **119,** 24588−24596 (2015).
204. Morales-Guio, C. G., Stern, L.-A. & Hu, X. Nanostructured hydrotreating catalysts for electrochemical hydrogen evolution. *Chem. Soc. Rev.* **43,** 6555–69 (2014).
205. Cass, M. J. *et al.* Microwave Reflectance Studies of Photoelectrochemical Kinetics at Semiconductor Electrodes. 1. Steady-State, Transient, and Periodic Responses. *J. Phys. Chem. B* **107,** 5857–5863 (2003).
206. Fabre, B. Functionalization of Oxide-Free Silicon Surfaces with Redox-Active Assemblies. *Chem. Rev.* **116,** 4808–4849 (2016).
207. Gelderman, K., Lee, L. & Donne, S. W. Flat-Band Potential of a Semiconductor: Using the Mott–Schottky Equation. *J. Chem. Educ.* **84,** 685–688 (2007).
208. Turner, J. A. Energetics of the semiconductor electrolyte interfase.pdf. *J. Chem. Educ.* **60,** 327–329 (1983).
209. Stoll, S. Spectral Simulations in Solid-State Electron Paramagnetic Resonance. (Eidgenössische Technische Hochschule Zürich, 2003).
210. Morozan, A. *et al.* Synergy between molybdemun mitride and gold leading to platinum-like activity for hydrogen evolution. *Phys. Chem. Chem. Phys.* **17,** 4047–4053 (2015).
211. Lassalle-Kaiser, B., Zitolo, A., Fonda, E., Robert, M. & Anxolabéhère-Mallart, E.

In Situ Observation of the Formation and Structure of Hydrogen-Evolving Amorphous Cobalt Electrocatalysts. *ACS Energy Lett.* **2,** 2545–2551 (2017).

212. Bui, D., Mu, J., Wang, L., Kang, S. & Li, X. Preparation of Cu-loaded SrTiO3 nanoparticles and their photocatalytic activity for hydrogen evolution from methanol aqueous solution. *Appl. Surf. Sci.* **274,** 328–333 (2013).
213. Peter, L. M., Ponomarev, E. a. & Fermín, D. J. Intensity-modulated photocurrent spectroscopy: reconciliation of phenomenological analysis with multistep electron transfer mechanisms. *J. Electroanal. Chem.* **427,** 79–96 (1997).
214. Ahmed, A. Y., Oekermann, T., Lindner, P. & Bahnemann, D. Comparison of the photoelectrochemical oxidation of methanol on rutile TiO2 (001) and (100) single crystal faces studied by intensity modulated photocurrent spectroscopy. *Phys. Chem. Chem. Phys.* **14,** 2774–2783 (2012).
215. Cummings, C. Y., Marken, F., Peter, L. M., Tahir, A. a & Wijayantha, K. G. U. Kinetics and mechanism of light-driven oxygen evolution at thin film α-Fe2O3 electrodes. *Chem. Commun.* **48,** 2027–9 (2012).
216. Saveleva, V. A. *et al.* Operando Near Ambient Pressure XPS (NAP-XPS) Study of the Pt Electrochemical Oxidation in H2O and H2O/O2 Ambients. *J. Phys. Chem. C,* **120,** 15930–15940 (2016).
217. Wang, K. *et al.* MoS2 Nanoparticles Grown on Graphene: An Advanced Catalyst for the Hydrogen Evolution Reaction. *J. Am. Chem. Soc.* **133,** 7296–7299 (2011).
218. Sabin, J. R. *et al.* Insight into the electronic structure, optical properties, and redox behavior of the hybrid phthalocyaninoclathrochelates from experimental and density functional theory approaches. *Inorg. Chem.* **51,** 8362–8372 (2012).
219. Zigler, D. F. *et al.* Disentangling the Physical Processes Responsible for the Kinetic Complexity in Interfacial Electron Transfer of Excited Ru(II) Polypyridyl

Dyes on TiO2. *J. Am. Chem. Soc.* jacs.5b12996 (2016). doi:10.1021/jacs.5b12996

220. Pichaandi, K. R., Kabalan, L., Kais, S. & Abu-Omar, M. M. Mechanism of Isomerization and Methyl Migration in Heterobimetallic Rhenium-Iridium Complexes: Experimental and DFT Study. *Organometallics* **35,** 605–611 (2016).

221. Mitra, D. *et al.* Nitrogenase Fe Protein at Three Oxidation Levels via Combined. *J. Am. Chem. Soc.* **135,** 2530–2543 (2013).

222. Wang, H. *et al.* In Operando Identification of Geometrical-Site-Dependent Water Oxidation Activity of Spinel Co3O4. *J. Am. Chem. Soc.* **138,** 36–39 (2016).

223. Mara, M. W. *et al.* Electron Injection from Copper Diimine Sensitizers into TiO $_2$: Structural Effects and Their Implications for Solar Energy Conversion Devices. *J. Am. Chem. Soc.* **137,** 9670–9684 (2015).

224. Sakane, H. *et al.* Second Hydration Shell Single Scattering versus First Hydration Shell Multiple Scattering in M(H 2 O) 6 3+ EXAFS Spectra. *J. Am. Chem. Soc.* **120,** 10397–10401 (1998).

225. Yang, K. R. *et al.* Solution structures of highly active molecular ir water-oxidation catalysts from density functional theory combined with high-energy X-ray scattering and EXAFS spectroscopy. *J. Am. Chem. Soc.* **138,** 5511–5514 (2016).

226. Kolthoff, I. M. & Thomas, G. Electrode Potentials in Acetonitrile. Estimation of the Liquid Junction Potential between Acetonitrile Solutions and the Aqueous Saturated Calomel Electrode. *J. Phys. Chem.* **69,** 3049–3058 (1966).

227. Song, J., Klein, E. L., Neese, F. & Ye, S. The Mechanism of Homogeneous CO2 Reduction by Ni(cyclam): Product Selectivity, Concerted Proton − Electron Transfer and C − O Bond Cleavage. *Inorg. Chem.* **53,** 7500–7507 (2014).

228. Peat, R. & Peter, L. M. Characterization of Semiconductor Electrodes by Intensity Modulated Spectroscopy (IMPS). *J. Electrochem. Soc.* **133,** C334 (1986).

229. Ponomarev, E. a. & Peter, L. M. A generalized theory of intensity modulated photocurrent spectroscopy (IMPS). *J. Electroanal. Chem.* **396,** 219–226 (1995).

230. Dormand, J. R. & Prince, P. J. A family of embedded Runge-Kutta formulae. *J. Comp. Appl. Math.* **6,** 19–26 (1980).

231. Bogacki, P. & Shampine, L. F. A 3(2) pair of Runge-Kutta formulas. *Appl. Math. Lett.* **2,** 1–9 (1989).

232. Shampine, L. F. & Gordon, M. K. *Computer Solution of Ordinary Differential Equations: the Initial Value Problem*. (W. H. Freeman, 1975).

233. Shampine, L. F., M. W. Reichelt, and J. A. K. Solving Index-1 DAEs in MATLAB and Simulink. *SIAM Rev.* **41,** 538–552 (1999).

234. Shampine, L. F. & Reichelt, M. W. The MATLAB ODE Suite. *SIAM J. Sci. Comput.* **18,** 1–22 (1997).

235. Shampine, L. F. & Hosea, M. E. Analysis and Implementation of TR-BDF2. *Appl. Numer. Math.* **20,** 1996

ANNEXES

ANNEX I. Example of Matlab program to treat OCPD measurements

```
clc
clear all
format short

B = importdata('2016-04-26 SrTiO3 Pt OCPD.csv');

color_fit_line = ['r' 'b' 'g' 'k' 'c' 'y' 'm'];
color_line = color_fit_line(2);
linewidth_show_points = 2.5;
linewidth_show_lines = 1.7;
font_size_show = 20;
export_variable = 1;
export_variable_fit = 1;

C_LED = 0;
C1_LED = 1;
LED_power_segments(1) = 1;

for i_LED = 1:length(B.data(:,4))-1

    C_LED = C_LED + 1;

    if B.data(i_LED+1,4) ~= B.data(i_LED,4)
%     B.data( ,8) is the column containing LED power information
          C1_LED = C1_LED + 1;

          LED_power_segments(C1_LED) = C_LED;

    end

end
LED_power_segments(1) = 0;

%%%%%%%%%%%%%%%%%%%%%%%%%%%%%%%%%%%%%%%%%%%%%%%%%%%%%%%%%%%%%%%%%%%%%%%%%%%%%%%
%%%%%%%%%%%%%%%%%%%%%%%%%%%%%%%%%%%%%%%%%%%%%%%%%%%%%%%%%%%%%%%%%%%%%%%%%%%%%%%

counter_on = 1;
counter = 2;
counter_fig = 2;
counter_final_results = 1;
for i_dat2 =1:length(LED_power_segments)/2 - 1

    % selecting the photopotential evolution when the light is OFF
time_off                                                                =
B.data(LED_power_segments(counter)+1:LED_power_segments(counter+1),2);
photo_potential_off                                     =                                   -
B.data(LED_power_segments(counter)+1:LED_power_segments(counter+1),3);
time_off = time_off - time_off(1);

d_photopot_dt = derivada(time_off,photo_potential_off);

kr = -d_photopot_dt(1)./(photo_potential_off(1));
kt    =    kr.*    (photo_potential_off(end))    ./    (photo_potential_off(1)    -
photo_potential_off(end));

%-------------------------------------------------------------------------

% selecting the photopotential evolution when the light is ON
time_on                                                                 =
```

```
B.data(LED_power_segments(counter_on)+1:LED_power_segments(counter_on+1),2);
photo_potential_on                                =                                -
B.data(LED_power_segments(counter_on)+1:LED_power_segments(counter_on+1),3);
LED_Power =  B.data(LED_power_segments(counter_on)+1,4);

final_results_off(counter_final_results,1:2) = [kt kr];
final_results_on(counter_final_results,1:2)             =             [LED_Power
photo_potential_on(end)];

if export_variable == 1

    output_headers = {'time_off' 'photo_potential_off' 'd_ocpd_dt' 'time_on'
'photo_potential_on'};
    data1 = [time_off photo_potential_off d_photopot_dt'];
    data2 =  [time_on photo_potential_on];
        xlswrite('Results OCPD', output_headers(1),counter_fig - 1,'B5');
        xlswrite('Results OCPD', output_headers(2),counter_fig - 1,'C5');
        xlswrite('Results OCPD', output_headers(3),counter_fig - 1,'D5');
        xlswrite('Results OCPD', output_headers(4),counter_fig - 1,'E5');
        xlswrite('Results OCPD', output_headers(5),counter_fig - 1,'F5');
        xlswrite('Results OCPD', data1,counter_fig - 1,'B6');
        xlswrite('Results OCPD', data2,counter_fig - 1,'E6');
        clear data

end

figure(1)
plot(time_off,       photo_potential_off,       color_line,       'linewidth',
linewidth_show_lines)
title('PHOTOPOTENTIAL DECAY VS TIME')
hold on

figure(2)
plot(time_off, d_photopot_dt, color_line, 'linewidth', linewidth_show_lines)
title('dU/dt VS TIME')
hold on

figure(3)
plot(time_off,       d_photopot_dt./(photo_potential_off(1)),       color_line,
'linewidth', linewidth_show_lines)
title('[1/Uo][dU/dt] VS TIME')
hold on

figure(4)
plot(time_on,        photo_potential_on,        color_line,        'linewidth',
linewidth_show_lines)
title('PHOTOPOTENTIAL VS TIME')
hold on
xlabel('time, s', 'FontSize', font_size_show)
ylabel('Photopotential V', 'FontSize', font_size_show)
set(gca,'FontSize', font_size_show, 'linewidth',linewidth_show_lines)

figure(5)
plot(LED_Power,  photo_potential_on(end),  [color_line  'o--'],  'linewidth',
linewidth_show_lines)
title('PHOTOPOTENTIAL VS LED POWER')
hold on
xlabel('Led Power, mW/cm2', 'FontSize', font_size_show)
ylabel('Photopotential V', 'FontSize', font_size_show)
set(gca,'FontSize', font_size_show, 'linewidth',linewidth_show_lines)

counter = counter + 2;
counter_on = counter_on + 2;
counter_fig = counter_fig + 1;
counter_final_results = counter_final_results + 1;

clear time photo_potential d_photopot_dt k1 k2
```

```
end

figure(6)
plot(final_results_on(:,1),    final_results_off(:,1),    [color_line    'o-'],
'linewidth', linewidth_show_lines)
hold on
title('kt vs Led Power')
xlabel('Led Power, mW/cm2', 'FontSize', font_size_show)
ylabel('kt, s-1', 'FontSize', font_size_show)
legend('kt')
set(gca,'FontSize', font_size_show, 'linewidth',linewidth_show_lines)

figure(7)
plot(final_results_on(:,1),    final_results_off(:,2),    [color_line    'o-'],
'linewidth', linewidth_show_lines)
hold on
title('kr VS Led Power')
xlabel('Led Power, mW/cm2', 'FontSize', font_size_show)
ylabel('kr, s-1', 'FontSize', font_size_show)
legend('kr')
set(gca,'FontSize', font_size_show, 'linewidth',linewidth_show_lines)

disp('kt; kr')
disp(final_results_off)

disp('led power; Photopotential')
disp(final_results_on)

if export_variable_fit == 1

    output_headers = {'led power (mW/cm2)' 'photopotential (V)' 'kt (s-1)' 'kr
(s-1)' };
    data_fit = [final_results_on final_results_off];
         xlswrite('Results OCPD fit', output_headers(1),1,'B5');
         xlswrite('Results OCPD fit', output_headers(2),1,'C5');
         xlswrite('Results OCPD fit', output_headers(3),1,'D5');
         xlswrite('Results OCPD fit', output_headers(4),1,'E5');
        xlswrite('Results OCPD fit', data_fit,1,'B6');
    clear data

end

   if export_variable == 1
   disp('look for the output files in the folder')
   disp(pwd)
   end


function D = derivada(x,y)

Der = diff(y)./diff(x);

%plot(x,y)

D(1) = Der(1);

for i = 1:length(Der)-1

    D(i+1) = 0.5*(Der(i)+Der(i+1));

end

D(length(Der)+1)=Der(end);

end
```

ANNEX II. Kinetic parameters derived from the fitting of PEIS.

Table A1. Fit parameters of PEIS for the Rh:$SrTiO_3$ system under cathodic polarization.

k_t (s^{-1})	k_r (s^{-1})	C_{sc} (F)	I_0 (A)	η	E (V)	LED power (mW/cm^2)
0.023	0.005	2.70E-04	6.08E-05	0.82	-1.30	529.03
0.008	0.003	2.49E-04	2.54E-05	0.74	-1.25	294.13
0.022	0.006	2.43E-04	3.16E-05	0.78	-1.25	529.03
0.013	0.003	2.30E-04	1.76E-05	0.80	-1.20	0.49
0.023	0.006	2.24E-04	1.81E-05	0.78	-1.20	294.13

Table A2. Fit parameters of PEIS for the Rh:$SrTiO_3$ system under anodic polarization.

k_t (s^{-1})	k_r (s^{-1})	C_{sc} (F)	I_0 (A)	η	E (V)	LED power (mW/cm^2)
0.032	0.026	3.45E-05	3.30E-05	0.55	1.40	0.49
0.029	0.021	3.18E-05	2.26E-05	0.58	1.40	294.13
0.029	0.020	3.22E-05	2.64E-05	0.60	1.40	529.03
0.022	0.016	3.75E-05	8.23E-05	0.58	1.50	294.13

Table A3. Fitting results of PEIS for the Rh:$SrTiO_3$ – Ch photoelectrode under cathodic polarization.

k_t (s^{-1})	k_r (s^{-1})	C_{sc} (F)	I_0 (A)	η	E (V)	LED power (mW/cm^2)
0.28	0.09	1.18E-04	8.84E-05	0.76	-1.30	129.57
0.28	0.09	1.08E-04	4.90E-05	0.76	-1.30	529.03
0.15	0.12	1.05E-04	2.41E-05	0.56	-1.15	129.57
0.28	0.09	9.01E-05	2.98E-05	0.76	-1.25	529.03
0.19	0.09	8.71E-05	2.09E-05	0.68	-1.20	129.57
0.28	0.09	7.57E-05	1.84E-05	0.76	-1.20	529.03
0.16	0.09	7.69E-05	1.01E-05	0.62	-1.15	129.57
0.28	0.09	6.54E-05	1.17E-05	0.76	-1.15	529.03
0.28	0.09	5.74E-05	1.16E-05	0.76	-1.10	129.57

Table A4. Fitting results of PEIS for the Rh:$SrTiO_3$ – Ch photoelectrode under anodic polarization.

k_t (s^{-1})	k_r (s^{-1})	C_{sc} (F)	I_0 (A)	η	E (V)	LED power (mW/cm^2)
0.010	0.015	2.13E-05	9.91E-05	0.40	1.50	294.13
0.013	0.012	2.13E-05	7.38E-05	0.53	1.50	529.03
0.014	0.013	2.14E-05	2.09E-05	0.52	1.40	529.03
0.021	0.008	2.49E-05	3.30E-06	0.74	1.30	294.13
0.013	0.007	2.38E-05	5.00E-06	0.64	1.30	529.03

Table A5. Fitting results of PEIS data for the Rh:$SrTiO_3$ – Cu under cathodic polarization.

k_t (s^{-1})	k_r (s^{-1})	C_{sc} (F)	I_0 (A)	η	E (V)	LED power (mW/cm^2)
2.6	4.0	3.55E-07	1.13E-04	0.39	-1.30	67.39
4.1	5.1	3.35E-07	1.12E-04	0.45	-1.30	185.92
3.1	4.6	3.31E-07	1.06E-04	0.40	-1.30	294.13
3.1	4.8	3.20E-07	1.06E-04	0.39	-1.30	393.52
2.9	4.8	3.13E-07	1.06E-04	0.38	-1.30	485.34
3.0	5.0	3.04E-07	1.07E-04	0.37	-1.30	529.03
2.0	5.6	3.01E-07	9.49E-05	0.26	-1.25	67.39
1.9	5.5	2.96E-07	9.62E-05	0.26	-1.25	185.92
1.9	5.7	2.89E-07	9.75E-05	0.25	-1.25	294.13
1.9	5.7	2.82E-07	9.89E-05	0.25	-1.25	393.52
1.8	5.9	2.77E-07	9.89E-05	0.24	-1.25	485.34
1.8	5.9	2.70E-07	1.00E-04	0.23	-1.25	529.03
1.2	6.7	2.70E-07	9.28E-05	0.15	-1.20	67.39
1.2	6.8	2.65E-07	9.40E-05	0.15	-1.20	185.92
1.2	7.1	2.61E-07	9.50E-05	0.14	-1.20	294.13
1.2	6.9	2.58E-07	9.58E-05	0.14	-1.20	393.52
1.2	7.2	2.54E-07	9.63E-05	0.14	-1.20	485.34
1.1	7.1	2.52E-07	9.70E-05	0.14	-1.20	529.03
0.7	7.6	2.52E-07	9.13E-05	0.08	-1.15	67.39
0.7	7.7	2.50E-07	9.13E-05	0.08	-1.15	185.92
0.7	7.7	2.48E-07	9.13E-05	0.08	-1.15	294.13
0.7	7.7	2.46E-07	9.16E-05	0.08	-1.15	393.52
0.7	7.7	2.44E-07	9.16E-05	0.08	-1.15	485.34
0.7	7.8	2.43E-07	9.23E-05	0.08	-1.15	529.03
0.4	7.8	2.42E-07	8.91E-05	0.05	-1.10	67.39
0.4	7.8	2.40E-07	8.97E-05	0.04	-1.10	185.92
0.4	8.0	2.39E-07	9.12E-05	0.04	-1.10	294.13
0.4	8.3	2.38E-07	9.27E-05	0.04	-1.10	393.52
0.4	8.5	2.38E-07	9.61E-05	0.04	-1.10	485.34
0.4	8.8	2.38E-07	9.93E-05	0.04	-1.10	529.03
0.2	9.0	2.38E-07	1.03E-04	0.02	-1.05	67.39
0.2	9.3	2.37E-07	1.06E-04	0.02	-1.05	185.92
0.2	9.9	2.36E-07	1.09E-04	0.02	-1.05	294.13
0.2	9.8	2.35E-07	1.10E-04	0.02	-1.05	393.52
0.2	10.1	2.34E-07	1.11E-04	0.02	-1.05	485.34
0.2	10.1	2.33E-07	1.12E-04	0.02	-1.05	529.03

Table A6. Fitting results of PEIS data for the system Rh:$SrTiO_3$ – Cu under anodic polarization.

k_t (s^{-1})	k_r (s^{-1})	C_{sc} (F)	I_0 (A)	η	E (V)	LED power (mW/cm^2)
0.021	0.017	2.48E-05	5.43E-05	0.54	1.40	0.49
0.017	0.016	2.64E-05	6.21E-05	0.52	1.40	294.13

Table A7. Kinetic parameters obtained from the fitting of PEIS data under cathodic polarization for Rh:$SrTiO_3$ – Pt photoelectrodes.

k_t (s^{-1})	k_r (s^{-1})	C_{sc} (F)	I_0 (A)	η	E (V)	LED power (mW/cm^2)
9.0	10.6	9.53E-08	4.67E-05	0.46	-1.30	294.13
8.6	10.2	9.42E-08	4.63E-05	0.46	-1.30	393.52
8.0	9.9	9.22E-08	4.66E-05	0.45	-1.30	485.34
7.2	9.5	8.84E-08	4.62E-05	0.43	-1.30	529.03
6.4	11.2	8.47E-08	4.19E-05	0.36	-1.25	67.39
5.5	10.6	8.24E-08	4.10E-05	0.34	-1.25	185.92
5.8	10.8	8.06E-08	4.12E-05	0.35	-1.25	294.13
5.5	10.3	7.75E-08	4.23E-05	0.35	-1.25	393.52
5.6	10.2	7.59E-08	4.15E-05	0.35	-1.25	485.34
5.3	10.0	7.34E-08	4.09E-05	0.35	-1.25	529.03
4.0	11.4	6.95E-08	3.74E-05	0.26	-1.20	67.39
3.9	11.9	6.72E-08	3.76E-05	0.25	-1.20	185.92
4.1	11.6	6.61E-08	3.80E-05	0.26	-1.20	294.13
4.0	11.7	6.49E-08	3.77E-05	0.26	-1.20	393.52
4.1	11.4	6.43E-08	3.79E-05	0.26	-1.20	485.34
4.0	11.4	6.25E-08	3.80E-05	0.26	-1.20	529.03
3.0	12.9	6.17E-08	3.48E-05	0.19	-1.15	67.39
2.7	12.6	6.01E-08	3.39E-05	0.18	-1.15	185.92
2.8	12.8	6.02E-08	3.43E-05	0.18	-1.15	294.13
2.9	12.4	6.02E-08	3.46E-05	0.19	-1.15	393.52
2.9	12.4	6.02E-08	3.46E-05	0.19	-1.15	485.34
2.9	12.5	6.00E-08	3.48E-05	0.19	-1.15	529.03
2.0	13.7	5.81E-08	3.24E-05	0.13	-1.10	67.39
1.8	13.2	5.94E-08	3.24E-05	0.12	-1.10	185.92
1.9	13.3	5.91E-08	3.24E-05	0.12	-1.10	294.13
1.9	12.9	5.87E-08	3.20E-05	0.13	-1.10	393.52
2.0	13.4	5.90E-08	3.26E-05	0.13	-1.10	485.34
1.9	12.9	5.84E-08	3.24E-05	0.13	-1.10	529.03
1.2	13.7	5.73E-08	3.13E-05	0.08	-1.05	67.39
1.1	13.5	5.67E-08	3.12E-05	0.08	-1.05	185.92
1.2	13.1	5.80E-08	3.11E-05	0.08	-1.05	294.13

1.2	12.9	6.03E-08	3.06E-05	0.09	-1.05	393.52
1.2	13.5	5.95E-08	3.15E-05	0.08	-1.05	485.34
1.2	12.6	6.11E-08	3.05E-05	0.09	-1.05	529.03

Table A8. Kinetic parameters of the OER at the surface of $Rh:SrTiO_3$ – Pt photoelectrodes.

k_t (s^{-1})	k_r (s^{-1})	C_{sc} (F)	I_0 (A)	η	E (V)	LED power (mW/cm^2)
0.013	0.009	2.35E-05	3.90E-05	0.59	1.50	529.03
0.010	0.003	2.26E-05	8.71E-06	0.77	1.40	129.57
0.010	0.005	2.24E-05	1.07E-05	0.67	1.40	529.03
0.010	0.003	2.29E-05	3.62E-06	0.77	1.30	129.57
0.007	0.003	2.27E-05	3.88E-06	0.70	1.30	529.03
0.010	0.003	2.66E-05	1.51E-06	0.76	1.20	129.57
0.019	0.007	2.43E-05	1.49E-06	0.72	1.20	529.03
0.012	0.004	3.30E-05	9.20E-07	0.75	1.10	129.57
0.020	0.009	2.97E-05	7.95E-07	0.69	1.10	529.03

ANNEX III. Total energies from the DFT calculations

Table A9. Total energies for the species depicted in Figure 5 of the main text Level B3LYP/cc-pVTZ for Co and cc-pVDZ for all other atoms.

B3LYP/cc-pVTZ for Co, cc-pVDZ for all other		
Species	E (Hartree)	E (kJ/mol)
$[^5Co]^1$	-5280.884928	-13864963.38
$[^1Co]^1$	-5280.931263	-13865085.03
$[^4Co]^0$	-5281.111179	-13865557.4
$[^2Co]^0$	-5281.169864	-13865711.48
$[^3Co]^{-1}$	-5281.245364	-13865909.7
$[^1Co]^{-1}$	-5281.247299	-13865914.78
$[^3Co(Co)H]^0$	-5281.686192	-13867067.1
$[^1Co(Co)H]^0$	-5281.746202	-13867224.65
$[^2Co(Co)H]^{-1}$	-5281.820122	-13867418.73
$[^3Co(N)H]^0$	-5281.719053	-13867153.37
$[^1Co(N)H]^0$	-5281.70926	-13867127.66
$[^3Co(C)H]^0$	-5281.743185	-13867216.73
$[^1Co(C)H]^0$	-5281.736767	-13867199.88
$[^3Co(NN)HH]^1$	converged to	$[^3Co(CoN)HH]^1$
$[^1Co(NN)HH]^1$	-5282.069582	-13868073.69
$[^3Co(NC)HH]^1$	-5281.21786	-13865837.49
$[^1Co(NC)HH]^1$	-5281.217816	-13865837.38
$[^3Co(CoN)HH]^1$	-5281.265207	-13865961.8
$[^1Co(CoN)HH]^1$	-5281.308896	-13866076.51

Table A10. Total energies and relevant thermodynamic quantities (B3LYP/LANL2DZ, ECP for Co and Cl)

B3LYP/LANL2DZ (ECP for Co and Cl)							
Species	E (Hartree)	G_{corr} (kJ/mol)	E_{zpe} (kJ/mol)	$E_{thermal}$ (J/mol)	E + G_{corr} (kJ/mol)	E + G_{corr} + ZPE (kJ/mol)	E + G_{corr} + ZPE + $E_{thermal}$ (kJ/mol)
$[^5Co]^1$	-1371.51642	472.201	317.482	67689.549	-3600444	-3600126.677	-3600058.987
$[^1Co]^1$	-1371.536781	338.831	484.980567	64064.939	-3600631	-3600146.007	-3600081.942
$[^4Co]^0$	-1371.699747	313.751	471.23843	68467.571	-3601084	-3600612.696	-3600544.228
$[^2Co]^0$	-1371.47263	323.803	478.782055	67634.384	-3600478	-3599998.804	-3599931.169
$[^3Co]^{-1}$	-1371.901656	308.466	467.114069	69713.71	-3601619	-3601152.218	-3601082.504
$[^1Co]^{-1}$	-1371.612991	325.426	477.253622	66768.634	-3600844	-3600367.227	-3600300.459
$[^3Co(Co)H]^0$	-1372.257779	339.613	495.155695	68406.668	-3602523	-3602028.029	-3601959.622
$[^1Co(Co)H]^0$	-1372.317662	350.023	501.391676	67016.977	-3602670	-3602168.607	-3602101.590
$[^2Co(Co)H]^{-1}$	-1372.465417	330.997	488.708503	69747.172	-3603076.9	-3602588.245	-3602518.498
$[^3Co(N)H]^0$	-1372.32564	352.25	507.030175	67852.574	-3602689	-3602181.687	-3602113.834
$[^1Co(N)H]^0$	-1372.305906	358.809	506.866816	65606.023	-3602630	-3602123.48	-3602057.874
$[^3Co(C)H]^0$	-1372.348853	348.379	507.291709	68798.526	-3602754	-3602246.242	-3602177.443
$[^1Co(C)H]^0$	-1372.334165	358.139	508.980663	67104.276	-3602705	-3602196.23	-3602129.126
$[^3Co(NN)HH]^1$	Converged to $[^3Co(CoN)HH]^1$						
$[^1Co(NN)HH]^1$	-1372.712519	419.851	562.630564	63641.474	-3603637	-3603074.237	-3603010.595
$[^3Co(NC)HH]^1$	-1239.098958	503.63	635.070362	49814.392	-3252751	-3252115.613	-3252065.799
$[^1Co(NC)HH]^1$	-1239.092152	505.103	631.123561	47953.443	-3252731	-3252100.219	-3252052.266
$[^3Co(CoN)HH]^1$	-1239.063473	516.192	647.179458	48356.425	-3252645	-3251997.777	-3251949.42
$[^1Co(CoN)HH]^1$	-1239.101762	524.833	653.039086	47957.061	-3252737	-3252083.805	-3252035.848

B3LYP/LANL2DZ (ECP for Fe) for Ferrocene							
Species	E (Hartree)	G_{ccorr} (kJ/mol)	E_{zpe} (kJ/mol)	$E_{thermal}$ (J/mol)	E + G_{corr} (kJ/mol)	E + G_{corr} + ZPE (kJ/mol)	E + G_{corr} + ZPE + $E_{thermal}$ (kJ/mol)
$[^1Fe(Cp)_2]^0$	-510.1348768	353.698	442.354273	15886.585	-1339359.12	-1339005.42	-1338989.54
$[^2Fe(Cp)_2]^1$	-509.9728737	352.142	444.529323	16663.683	-1338933.78	-1338581.64	-1338564.97

ANNEX IV. Geometric coordinates from the DFT optimization

$[^5Co]^1$

Co	4.87620	4.10438	3.14823
Cl	9.14696	5.40776	1.82804
Cl	7.32511	8.03457	2.73002
Cl	3.10143	1.86451	-0.50390
Cl	1.21966	4.46091	0.33214
Cl	5.22586	1.14723	6.66751
Cl	3.52940	3.86727	7.54958
N	6.87032	4.07418	2.53409
N	5.43066	6.10627	3.10585
N	4.60744	2.74721	1.58435
N	3.16812	4.79879	2.20808
N	5.47035	2.51180	4.32536
N	4.02651	4.56393	4.96540
B	3.11688	6.61793	3.90607
B	6.65815	1.58361	2.35086
O	7.49763	2.91956	2.20409
O	4.56775	7.08513	3.47479
O	5.47109	1.69203	1.37746
O	2.49074	5.89824	2.69406
O	6.20812	1.46406	3.81332
O	3.27172	5.70761	5.13669
C	7.48656	5.23901	2.39412
C	6.67742	6.39711	2.76350
C	3.55346	2.92448	0.83646
C	2.26115	7.87998	4.27523
C	4.98830	2.48495	5.53652
C	2.71707	4.09933	1.20405
C	7.56312	0.36148	1.96562
C	4.19541	3.69282	5.92123
H	8.43970	0.29504	2.62319
H	2.18040	8.56518	3.42147
H	7.00413	-0.57946	2.05656
H	7.92098	0.44047	0.93088
H	1.24404	7.59012	4.57094
H	2.70895	8.43194	5.11179

$[^1Co]^1$

Co	4.92452	4.12938	3.09132
Cl	9.17511	5.29703	2.36271
Cl	7.13571	7.97138	2.59249
Cl	3.30909	2.01139	-0.49805
Cl	1.12592	4.28500	0.73146
Cl	5.11329	1.14690	6.41560
Cl	3.74440	4.06177	7.40753
N	6.84931	4.03324	2.94464
N	5.27827	5.99810	2.69554

N	4.84052	3.09036	1.45707
N	3.07844	4.48117	2.59845
N	5.02936	2.43034	4.03259
N	4.43702	4.73489	4.87616
B	3.19234	6.59462	3.85687
B	6.63621	1.66079	2.34332
O	7.51748	2.83099	2.86093
O	4.31601	6.97564	2.85611
O	5.83187	2.18927	1.12463
O	2.33959	5.48205	3.19603
O	5.61497	1.31905	3.45857
O	3.88094	5.97700	5.10199
C	7.45344	5.15902	2.67997
C	6.54390	6.31827	2.62754
C	3.67672	3.05286	0.86436
C	2.31057	7.82941	4.24126
C	4.82759	2.48685	5.32194
C	2.67781	3.94083	1.47848
C	7.51458	0.42509	1.95438
C	4.37474	3.80468	5.79108
H	8.23150	0.18376	2.75043
H	1.96965	8.36397	3.34436
H	6.89408	-0.46304	1.77692
H	8.08608	0.62556	1.03821
H	1.42034	7.51341	4.80234
H	2.86944	8.53837	4.86639

$[^2Co]^0$

Co	4.78073	4.02980	3.18284
Cl	9.11609	5.36575	1.90292
Cl	7.23596	7.99279	2.67028
Cl	3.28409	1.96577	-0.53026
Cl	1.33603	4.58004	0.30469
Cl	5.41095	1.25693	6.64922
Cl	3.63175	4.00042	7.48803
N	6.85705	4.02162	2.62723
N	5.35065	6.06171	3.03434
N	4.66609	2.84948	1.64242
N	3.13195	4.69507	2.35219
N	5.31736	2.49161	4.22063
N	4.09782	4.56369	4.86409
B	3.12795	6.62889	3.87343
B	6.68964	1.60951	2.35939
O	7.56673	2.86281	2.34637
O	4.48133	7.10168	3.33358
O	5.54097	1.81329	1.36459
O	2.42232	5.80045	2.79576
O	6.08390	1.43792	3.75500
O	3.38455	5.72626	5.08796
C	7.43511	5.17336	2.46010

C	6.58463	6.33826	2.73263
C	3.62291	3.00485	0.85852
C	2.24386	7.86138	4.29555
C	4.98395	2.52191	5.49257
C	2.75074	4.09477	1.25017
C	7.52911	0.33698	1.96507
C	4.26294	3.72108	5.86311
H	8.38719	0.20770	2.63826
H	2.12147	8.56107	3.45844
H	6.91545	-0.57205	2.01914
H	7.91508	0.42524	0.94037
H	1.24510	7.54045	4.61926
H	2.70938	8.40895	5.12572

$[^4Co]^0$

Co	4.91191	4.17984	2.94836
Cl	9.18794	5.31194	2.06153
Cl	7.41660	7.99495	3.06572
Cl	3.15428	1.90921	-0.55096
Cl	1.00000	4.21810	0.73257
Cl	5.51237	1.36194	6.67809
Cl	3.37265	3.84586	7.36170
N	6.86688	4.05898	2.74525
N	5.40074	6.15440	2.90125
N	4.78065	2.99318	1.42738
N	3.11399	4.55299	2.50028
N	5.20542	2.38853	4.15713
N	4.24812	4.69648	4.91477
B	3.20977	6.66841	3.88166
B	6.66080	1.60811	2.35981
O	7.51902	2.87509	2.42898
O	4.51353	7.16197	3.25346
O	5.51707	1.84556	1.30475
O	2.49369	5.72293	2.83457
O	6.00118	1.33843	3.70567
O	3.47760	5.83830	5.13071
C	7.49957	5.19287	2.59827
C	6.67820	6.39350	2.82365
C	3.50664	2.98559	0.81283
C	2.26821	7.88891	4.20102
C	4.96028	2.51571	5.42371
C	2.62347	3.88136	1.35812
C	7.53141	0.37339	1.91622
C	4.24575	3.75043	5.80445
H	8.30483	0.14936	2.66271
H	2.01349	8.43884	3.28529
H	6.90451	-0.52155	1.80252
H	8.02956	0.56131	0.95602
H	1.33223	7.55402	4.66681
H	2.75847	8.59049	4.88934

$[^1Co]^{-1}$

Co	4.59968	4.05763	3.22213
Cl	9.13533	5.65763	1.57443
Cl	7.09491	7.92683	2.79755
Cl	3.42387	2.04778	-0.61157
Cl	1.42937	4.68721	0.15179
Cl	5.60772	1.36378	6.67162
Cl	3.60077	3.94557	7.56292
N	7.11359	3.97912	2.48555
N	5.37608	5.86017	3.12864
N	4.64477	2.90453	1.71108
N	3.04462	4.65816	2.37511
N	5.42476	2.67420	4.25072
N	3.78990	4.41503	4.86540
B	3.04002	6.52376	3.92837
B	6.72169	1.65562	2.35797
O	7.74175	2.81905	2.10294
O	4.51300	6.88198	3.54897
O	5.51917	1.84072	1.45938
O	2.37801	5.83568	2.75255
O	6.28732	1.66794	3.80866
O	3.05208	5.58083	5.11687
C	7.53665	5.17671	2.32644
C	6.58186	6.21233	2.76379
C	3.65519	3.08153	0.82420
C	2.28969	7.86810	4.28922
C	5.07110	2.63277	5.53879
C	2.76953	4.12719	1.18412
C	7.44045	0.28481	2.01862
C	4.16790	3.66762	5.89877
H	8.31193	0.12982	2.67013
H	2.26852	8.54817	3.42719
H	6.75579	-0.56257	2.15556
H	7.79271	0.27539	0.97771
H	1.25207	7.66632	4.58967
H	2.78902	8.38799	5.11830

$[^3Co]^{-1}$

Co	9.17254	4.59357	3.12278
Cl	10.64204	0.75294	4.86601
Cl	13.22008	6.98593	5.09205
Cl	6.19985	7.62703	4.51307
Cl	6.71552	7.79849	1.19919
Cl	13.99968	5.85229	2.00018
Cl	10.74927	0.76572	1.47612
O	9.47709	3.41527	5.78935
O	10.62913	5.65456	5.82392
O	8.12648	5.56285	5.67563
O	9.97628	3.52853	0.50384

O	11.33404	5.62576	0.46735
O	8.81354	5.78106	0.43080
N	9.51721	3.23083	4.39197
N	10.92610	5.58945	4.46219
N	8.14267	5.70405	4.29599
N	8.47608	5.77513	1.77196
N	10.01957	3.39807	1.90865
N	11.22974	5.97362	1.81208
B	9.38490	4.85491	6.26188
B	10.04111	4.94868	-0.03005
C	10.08568	2.13840	3.86955
C	12.01053	6.13887	4.02190
C	7.37349	6.56929	3.67855
C	9.28158	4.89182	7.84362
C	7.57485	6.61812	2.22867
C	10.03090	4.91147	-1.61659
C	12.26408	6.06578	2.56884
C	10.27736	2.19717	2.45140
H	10.04513	5.92914	-2.03193
H	9.13196	4.40280	-1.99110
H	10.91074	4.37602	-2.00040
H	8.34688	4.42911	8.18850
H	10.11851	4.34540	8.29942
H	9.30874	5.92511	8.21541

$[^{1}Co(Co)H]^{0}$

Co	9.20646	4.59185	3.12605
Cl	10.46290	0.69466	4.86087
Cl	13.16394	6.94577	5.11780
Cl	6.44233	7.78578	4.53470
Cl	6.80485	7.81749	1.19640
Cl	13.77206	6.78057	1.89261
Cl	10.71042	0.72693	1.50807
O	9.42307	3.38572	5.76107
O	10.67282	5.55193	5.84107
O	8.18191	5.58876	5.65915
O	9.98901	3.47332	0.52901
O	11.31073	5.59918	0.46774
O	8.80757	5.71440	0.43517
N	9.59164	3.23103	4.40381
N	10.90710	5.55911	4.45947
N	8.20660	5.73018	4.29033
N	8.54650	5.80419	1.78196
N	9.91528	3.30421	1.89284
N	11.24644	5.69620	1.85093
B	9.39920	4.85034	6.27480
B	10.04699	4.91774	-0.03880
C	10.04209	2.11634	3.89702
C	11.97667	6.14550	4.02729
C	7.50295	6.64884	3.68842

C	9.25691	4.84050	7.84479
C	7.68476	6.67934	2.22781
C	10.03015	4.83937	-1.61414
C	12.20812	6.16032	2.56010
C	10.19984	2.14833	2.43261
H	10.07159	5.84447	-2.05537
H	9.11805	4.34736	-1.97669
H	10.89459	4.27371	-1.98662
H	8.31651	4.36432	8.15357
H	10.08347	4.28522	8.30814
H	9.26885	5.86258	8.24571
H	7.95619	3.89928	2.89143

$[^3Co(Co)H]^0$

Co	9.14086	4.58395	3.12017
Cl	10.45010	0.68407	4.87939
Cl	13.22186	6.85187	5.10978
Cl	6.38145	7.77084	4.54277
Cl	6.75197	7.81820	1.20418
Cl	13.93147	6.18855	1.93115
Cl	10.94129	0.81979	1.50382
O	9.49882	3.41315	5.73245
O	10.63196	5.62115	5.82054
O	8.13143	5.56086	5.66123
O	10.06777	3.52607	0.58215
O	11.28797	5.67023	0.45960
O	8.76454	5.71676	0.43813
N	9.56466	3.26551	4.38608
N	10.88288	5.59447	4.44280
N	8.14579	5.71289	4.28812
N	8.49490	5.80277	1.78688
N	9.97242	3.39016	1.92768
N	11.18885	5.89776	1.83082
B	9.38009	4.90155	6.26831
B	10.02817	4.99751	-0.03777
C	10.10420	2.08230	3.85382
C	11.98859	6.12189	4.01850
C	7.44064	6.63487	3.69395
C	9.25754	4.86662	7.83689
C	7.62700	6.67214	2.23067
C	10.00275	4.86496	-1.60654
C	12.23069	6.09827	2.55741
C	10.30602	2.14007	2.49232
H	9.97391	5.85547	-2.08095
H	9.12150	4.30371	-1.94478
H	10.89827	4.34416	-1.97120
H	8.32679	4.37560	8.15133
H	10.09760	4.31749	8.28249
H	9.26030	5.88310	8.25231
H	7.92354	3.85609	2.84463

[^{1}Co(C)H]^{0}

Co	9.41835	4.74397	3.00387
Cl	10.27411	0.68873	4.79724
Cl	13.25068	7.39832	5.00194
Cl	7.60288	8.23044	4.27198
Cl	6.28903	7.31103	1.13372
Cl	13.47511	6.79114	1.78638
Cl	10.47003	0.65677	1.45054
O	9.79073	3.47636	5.70192
O	10.75737	5.75010	6.07872
O	8.30161	5.46952	5.53992
O	9.76542	3.39355	0.42442
O	11.18264	5.41999	0.70756
O	8.70810	5.66591	0.34368
N	9.85682	3.34553	4.33316
N	11.08454	5.69155	4.73990
N	8.33188	5.54390	4.16285
N	8.44075	5.74651	1.69419
N	9.72744	3.25114	1.79897
N	11.10644	5.51954	2.10551
B	9.51761	4.87475	6.29059
B	9.97092	4.85355	-0.02604
C	10.04672	2.15557	3.82466
C	12.04941	6.31160	4.17511
C	7.30234	6.43862	3.64861
C	9.17966	4.75156	7.82542
C	7.44277	6.43140	2.14869
C	10.19130	4.91387	-1.58537
C	12.09101	6.13277	2.70453
C	10.02998	2.11428	2.35977
H	10.33308	5.94982	-1.92064
H	9.32709	4.49911	-2.12170
H	11.07906	4.33855	-1.87936
H	8.27987	4.14366	7.98675
H	10.00904	4.28305	8.37255
H	9.00369	5.74162	8.26713
H	6.29881	6.19225	4.01094

[^{3}Co(C)H]^{0}

Co	9.21047	4.54926	3.13029
Cl	10.57593	0.65725	4.83178
Cl	13.01492	7.12472	5.14633
Cl	7.85363	8.32707	4.25141
Cl	6.50289	7.47969	1.10569
Cl	13.73409	6.82816	1.93813
Cl	10.79846	0.70824	1.48649
O	9.45816	3.31774	5.76342
O	10.60805	5.55272	5.85683
O	8.12628	5.47965	5.61857

O	10.08660	3.46534	0.51586
O	11.26124	5.68010	0.48746
O	8.74063	5.61372	0.42153
N	9.61867	3.17091	4.39831
N	10.87533	5.55875	4.47770
N	8.12944	5.55961	4.26811
N	8.44814	5.69494	1.76942
N	9.98373	3.28059	1.87818
N	11.17494	5.80460	1.86814
B	9.39152	4.76608	6.27734
B	10.04675	4.92321	-0.03446
C	10.09659	2.07357	3.88286
C	11.89947	6.22697	4.05410
C	7.27322	6.55922	3.67442
C	9.21066	4.76379	7.84106
C	7.49463	6.47556	2.18222
C	10.05751	4.85726	-1.61149
C	12.13818	6.25285	2.58706
C	10.26125	2.12106	2.41277
H	9.99818	5.86536	-2.04381
H	9.20674	4.27477	-1.98926
H	10.98062	4.38725	-1.97707
H	8.29450	4.23337	8.13299
H	10.05855	4.26781	8.33194
H	9.14835	5.78826	8.23107
H	6.22794	6.53061	3.99274

$[^{1}Co(N)H]^{0}$

Co	9.33748	4.64766	3.18709
Cl	10.12905	0.58496	4.85755
Cl	13.12971	6.75036	5.12341
Cl	6.69691	7.99918	4.51157
Cl	7.16721	7.91545	1.14031
Cl	13.22891	7.67853	1.93763
Cl	10.66021	0.68259	1.53979
O	9.23054	3.34548	5.76117
O	10.71133	5.33871	5.74853
O	8.24021	5.68924	5.71551
O	10.17456	3.46378	0.57208
O	11.34728	5.67947	0.40221
O	8.86478	5.62122	0.50544
N	9.49267	3.19490	4.41082
N	10.81800	5.54554	4.36865
N	7.94205	5.51300	4.30016
N	8.62229	5.66903	1.86209
N	10.00335	3.30641	1.93113
N	11.43210	5.57784	1.77832
B	9.36535	4.82240	6.25582
B	10.11643	4.87774	-0.02949
C	9.90398	2.06361	3.90604

C	11.89840	6.16104	3.96501
C	7.52896	6.72026	3.62925
C	9.33279	4.83695	7.83520
C	7.79181	6.70517	2.28103
C	10.03089	4.78745	-1.60231
C	12.12644	6.35602	2.52125
C	10.17421	2.12042	2.46184
H	10.03484	5.78981	-2.05160
H	9.11536	4.27442	-1.92486
H	10.89054	4.23557	-2.00692
H	8.42569	4.34474	8.21078
H	10.20263	4.30864	8.24795
H	9.34431	5.86517	8.22034
H	7.17400	4.80735	4.25353

$[^{3}Co(N)H]^{0}$

Co	9.15815	4.50475	3.14566
Cl	10.44091	0.61556	4.88023
Cl	13.14537	6.77873	5.09876
Cl	6.61772	7.94311	4.52852
Cl	7.50679	8.22851	1.30024
Cl	13.20195	7.60688	1.87114
Cl	10.85816	0.69569	1.55047
O	9.35801	3.32186	5.77522
O	10.64209	5.46271	5.76236
O	8.13646	5.57097	5.70582
O	10.05711	3.42295	0.54193
O	11.37554	5.56525	0.40441
O	8.91396	5.72877	0.49300
N	9.54234	3.14400	4.42105
N	10.76910	5.63493	4.37899
N	7.79756	5.43049	4.27696
N	8.67105	5.79509	1.83752
N	9.94377	3.24079	1.90541
N	11.42784	5.48868	1.79299
B	9.34062	4.82972	6.23992
B	10.11052	4.84670	-0.03745
C	10.02182	2.04140	3.91626
C	11.87004	6.19206	3.96828
C	7.53079	6.71186	3.64488
C	9.29750	4.84694	7.82304
C	7.93126	6.83325	2.32311
C	9.99412	4.76458	-1.60827
C	12.10528	6.30407	2.51326
C	10.21899	2.08503	2.44724
H	10.04615	5.76471	-2.05909
H	9.04378	4.30433	-1.91070
H	10.81036	4.16186	-2.02963
H	8.40819	4.32489	8.20025
H	10.18657	4.35509	8.24083

H	9.27345	5.87798	8.20044
H	6.93194	4.85587	4.28326

[^{1}Co(CoN)HH]^{1}

Co	9.29330	4.67626	3.22077
Cl	10.07037	1.06118	4.93845
Cl	12.60960	6.39673	5.16861
Cl	6.49375	7.41563	4.48320
Cl	7.52396	7.73725	1.21687
Cl	13.81108	6.92312	2.18075
Cl	11.05866	1.35785	1.69507
O	8.93446	3.31744	5.66451
O	10.36983	5.32921	5.45881
O	7.90262	5.52301	5.71327
O	10.31603	3.66701	0.78202
O	11.50168	5.79272	0.17943
O	9.10438	5.76710	0.74241
N	9.28070	3.58182	4.28210
N	10.48521	5.31596	3.90583
N	8.28722	5.37097	4.26567
N	8.92406	5.54949	2.11187
N	9.94025	3.77081	2.16544
N	11.32641	5.74278	1.65497
B	9.14985	4.74364	6.21211
B	10.18048	4.96004	-0.01780
C	9.86938	2.40377	3.97827
C	11.69877	5.92404	3.83278
C	7.58702	6.47383	3.65722
C	9.38691	4.85276	7.80799
C	8.01850	6.61924	2.33736
C	9.78850	4.74509	-1.56854
C	12.31259	6.21420	2.47943
C	10.29957	2.52762	2.61582
H	9.67330	5.77599	-2.13080
H	8.78832	4.13896	-1.71586
H	10.64544	4.15568	-2.12933
H	8.46676	4.39608	8.39540
H	10.35195	4.28183	8.17145
H	9.49121	5.97500	8.15517
H	8.07795	3.93246	2.74319
H	7.34767	4.79672	3.94756

[^{3}Co(CoN)HH]^{1}

Co	9.27319	4.65907	3.20911
Cl	10.04327	1.04279	4.89734
Cl	12.52031	6.58453	5.14458
Cl	6.55155	7.50497	4.49024
Cl	7.58241	7.78849	1.23636
Cl	13.79069	6.97817	2.15432
Cl	10.96166	1.33603	1.59669

O	9.02838	3.36232	5.59871
O	10.35115	5.39903	5.43107
O	7.87310	5.50383	5.70529
O	10.22459	3.69742	0.74810
O	11.54229	5.71299	0.17823
O	9.12151	5.85153	0.70341
N	9.29890	3.59180	4.22725
N	10.45739	5.37385	3.87649
N	8.26402	5.36603	4.24487
N	8.92807	5.57461	2.09301
N	9.88592	3.78860	2.12023
N	11.33044	5.72907	1.64065
B	9.14224	4.81803	6.18640
B	10.13504	5.01633	-0.04873
C	9.85696	2.36725	3.91365
C	11.66069	6.02278	3.80757
C	7.60187	6.51758	3.65506
C	9.37504	4.83941	7.78617
C	8.05375	6.63422	2.34337
C	9.82662	4.76473	-1.61238
C	12.30145	6.25674	2.46271
C	10.24799	2.49976	2.55762
H	9.77615	5.78701	-2.20124
H	8.81679	4.18685	-1.80136
H	10.69547	4.13923	-2.11151
H	8.43205	4.36389	8.32194
H	10.32291	4.24231	8.14699
H	9.47219	5.94617	8.18168
H	7.31882	4.81258	3.99974
H	8.02276	3.95099	2.73582

[^{1}Co(NN)HH]^{1}

Co	9.65881	4.81725	3.15315
Cl	9.74530	0.70117	4.82971
Cl	13.24444	6.65022	5.13731
Cl	7.28601	8.34273	4.14942
Cl	6.78363	7.35019	0.90585
Cl	13.15859	7.32504	1.82779
Cl	10.50345	0.75108	1.52540
O	8.83661	3.52317	5.58477
O	10.91591	4.88985	5.77527
O	8.73888	6.06221	5.62142
O	10.62803	3.65767	0.67228
O	10.67020	6.17103	0.70943
O	8.51530	4.97835	0.40002
N	9.27173	3.31353	4.28206
N	11.04456	5.23369	4.44637
N	8.32069	5.74811	4.27107
N	8.11814	5.06348	1.81299
N	10.34369	3.42164	1.99297

N	10.78094	6.04737	2.07834
B	9.43877	4.83896	6.24153
B	9.96914	4.96290	0.05286
C	9.72089	2.16396	3.85774
C	11.98627	6.05411	4.06763
C	7.79563	6.82016	3.42920
C	9.34391	4.78563	7.80294
C	7.62018	6.42118	2.15090
C	10.17469	4.96545	-1.50593
C	11.87714	6.45936	2.66087
C	10.23770	2.20830	2.47386
H	9.95762	5.95886	-1.92205
H	9.50523	4.24495	-1.99296
H	11.20757	4.70528	-1.77147
H	8.32621	4.53591	8.13228
H	10.02919	4.03016	8.21164
H	9.61239	5.75554	8.24562
H	7.56282	5.05680	4.41134
H	7.38203	4.34006	1.82926

$[^{1}Co(NC)HH]^{1}$

Co	9.39771	4.77393	3.21927
Cl	8.80058	1.09835	4.86085
Cl	12.49517	6.61492	5.32303
Cl	6.63450	7.97883	4.27232
Cl	7.21505	7.21526	0.81932
Cl	13.27011	7.90603	2.32408
Cl	10.66349	1.08639	1.88751
O	8.42367	3.77861	5.37710
O	10.80292	4.45451	5.11545
O	9.15155	6.22633	5.51678
O	10.55666	3.66876	0.96687
O	11.44008	5.98470	0.32800
O	8.97141	5.48891	0.71847
N	8.99761	3.70317	4.04697
N	10.54640	5.42812	3.79542
N	8.40307	5.77951	4.28672
N	8.76356	5.47104	2.15337
N	10.03552	3.75448	2.26371
N	11.36191	5.90786	1.78448
B	9.60397	4.78147	5.99578
B	10.23693	4.95889	0.12593
C	9.24620	2.35722	3.90027
C	11.63066	6.17295	3.97036
C	7.28645	6.55669	3.56776
C	9.78199	4.58585	7.59976
C	7.86236	6.48905	2.16768
C	10.12943	4.59830	-1.44921
C	12.11257	6.72255	2.64120

C	10.00611	2.38133	2.70334
H	9.97833	5.58460	-2.08194
H	9.24850	3.86530	-1.71845
H	11.13716	4.11436	-1.83098
H	8.76607	4.23854	8.09301
H	10.60785	3.77892	7.85432
H	10.11736	5.59628	8.11516
H	7.78355	4.97343	4.81913
H	6.49874	5.66935	3.36898

$[^{3}Co(NC)HH]^{1}$

Co	9.42518	4.80463	3.22917
Cl	8.72967	1.11678	4.80661
Cl	12.68609	6.46564	5.24155
Cl	6.77765	8.11262	4.19329
Cl	7.09660	7.07129	0.79016
Cl	13.20765	7.96968	2.32251
Cl	10.71631	1.10257	1.92763
O	8.34871	3.84887	5.31577
O	10.75730	4.49286	5.15497
O	9.16783	6.29590	5.59402
O	10.74534	3.73487	1.03310
O	11.27598	6.16909	0.28217
O	8.89848	5.34771	0.73210
N	8.99496	3.71469	4.01536
N	10.60171	5.42019	3.80841
N	8.51553	5.88874	4.29383
N	8.75026	5.41650	2.15794
N	10.12246	3.77511	2.28824
N	11.23835	6.05698	1.76392
B	9.52735	4.81417	5.99563
B	10.26125	4.98410	0.14626
C	9.22629	2.37945	3.88120
C	11.68192	6.13587	3.96636
C	7.38188	6.63407	3.57369
C	9.71396	4.47949	7.58224
C	7.84126	6.45715	2.14265
C	10.13495	4.52080	-1.40483
C	12.04005	6.78711	2.62432
C	10.03643	2.41143	2.70565
H	9.79636	5.43644	-2.07221
H	9.35848	3.65464	-1.58960
H	11.18224	4.17153	-1.82401
H	8.70399	4.11795	8.07341
H	10.53155	3.64565	7.76246
H	10.08840	5.45274	8.14163
H	7.84517	5.10453	4.77848
H	6.55760	5.75293	3.46771

TRANSITION STATE

Co	4.36331	3.70341	3.26209
Cl	8.97869	5.31449	1.82326
Cl	7.18544	7.89485	2.75704
Cl	3.85629	2.54583	-1.00767
Cl	1.88508	5.11737	-0.15502
Cl	6.22737	1.79814	6.84135
Cl	4.38259	4.46249	7.66142
N	6.74453	3.93106	2.53338
N	5.26695	6.00826	3.14213
N	4.57069	2.74722	1.59699
N	3.15429	4.78219	2.21609
N	5.44355	2.51440	4.35033
N	4.02498	4.54428	4.97603
B	3.06002	6.60779	3.93541
B	6.62656	1.52779	2.37041
O	7.44318	2.78150	2.19152
O	4.43851	7.05740	3.52139
O	5.36707	1.64377	1.44670
O	2.43306	5.81976	2.73616
O	6.14201	1.44913	3.84919
O	3.20695	5.62979	5.14093
C	7.30781	5.08440	2.40950
C	6.48586	6.25407	2.79711
C	3.83711	3.20954	0.61970
C	2.11082	7.79086	4.33222
C	5.38986	2.75775	5.63208
C	2.99202	4.36591	0.98876
C	7.42120	0.22339	2.01340
C	4.57227	3.93509	5.99291
H	8.29907	0.11306	2.66409
H	1.99598	8.49645	3.49911
H	6.79695	-0.67159	2.13469
H	7.77530	0.25161	0.97436
H	1.11254	7.42383	4.60486
H	2.51326	8.34478	5.19028
H	2.78772	2.98087	3.65633
H	3.24330	2.35212	3.53850

$[^1Fe(Cp)_2]^0$

Fe	0.01481	0.05574	0.02141
C	-0.31006	-2.03397	0.23540
C	-1.18019	-1.30592	1.12844
C	-2.02369	-0.44696	0.33026
C	-1.67440	-0.63989	-1.05794
C	-0.61493	-1.62110	-1.11434
C	1.60190	1.06709	-0.95220
C	0.56334	2.01041	-0.60787
C	2.08628	0.46309	0.26737
C	0.40160	1.98402	0.82685

C	1.34047	1.02894	1.36691
H	0.45047	-2.74718	0.52575
H	-1.18989	-1.38326	2.20808
H	-2.78205	0.22652	0.70810
H	-2.12443	-0.13853	-1.90463
H	-0.12787	-1.97833	-2.01216
H	1.96015	0.85530	-1.95140
H	0.00034	2.62056	-1.30212
H	2.86152	-0.28785	0.34389
H	-0.30963	2.57048	1.39497
H	1.45605	0.77585	2.41301

$[^{2}Fe(Cp)_{2}]^{1}$

Fe	0.01346	0.05931	0.02088
C	-0.33448	-2.04338	0.24435
C	-1.25495	-1.35389	1.11534
C	-2.09875	-0.51739	0.30496
C	-1.70466	-0.67772	-1.07077
C	-0.61332	-1.62487	-1.11210
C	1.60352	1.07350	-0.95450
C	0.57717	2.02831	-0.59249
C	2.12787	0.49844	0.26267
C	0.47026	2.03177	0.84632
C	1.42464	1.09105	1.36967
H	0.42638	-2.74982	0.54918
H	-1.29081	-1.43260	2.19434
H	-2.87673	0.14052	0.67139
H	-2.15105	-0.18058	-1.92157
H	-0.10464	-1.97055	-2.00144
H	1.93896	0.84786	-1.95860
H	0.00249	2.63959	-1.27585
H	2.89999	-0.25615	0.33146
H	-0.22280	2.62359	1.43004
H	1.56726	0.84799	2.41451

université PARIS-SACLAY

ÉCOLE DOCTORALE
Sciences chimiques : molécules, matériaux, instrumentation et biosystèmes

Titre : Cinétique photo-électrochimique de la photo-dissociation de l'eau assistée par lumière visible sur électrodes à base de Rh:$SrTiO_3$

Mots clés : Photo-électrochimie, cinétique, dissociation de l'eau

Résumé : L'étude de la cinétique de la photodissociation de l'eau assistée par lumière visible a été l'objectif principal de ce travail. En tant que matériau photo-excitable, le semi-conducteur $SrTiO_3$ dopé au Rh a été utilisé. Le dopage permet l'absorption de lumière visible et donc la transformation d'énergie solaire en combustibles chimiques. Le 1er Chapitre de cette thèse est consacré à une étude bibliographique couvrant les méthodes de caractérisation et les modèles de la cinétique photo-électrochimique. Le 2ème Chapitre traite la description des matériaux et méthodes expérimentaux. Le 3ème Chapitre concerne la caractérisation de la cinétique de la photodissociation de l'eau sur photo-électrodes à base de Rh:$SrTiO_3$, modifiées en surface par ajout d'un clathrochélate modèle, ou avec du Cu ou du Pt métalliques. Le 4ème Chapitre décrit une étude théorique du mécanisme de la réaction de dégagement d'hydrogène, catalysée par un clathrochélate modèle. Le spectre EXAFS du complexe a été analysé et modélisé, et les intermédiaires importants du mécanisme ont été mis en évidence. Le 5ème Chapitre est consacré à l'étude dynamique de photo-électrodes à base de Rh:$SrTiO_3$ en utilisant la technique de la photo-tension à lumière modulée. Ce Chapitre présente des résultats inattendus, qui sont rapportés pour la première fois. Ce comportement bizarre a été modélisé par un système d'équations différentielles usuellement utilisées pour décrire ce type de système photo-électrochimique.

Title : Photoelectrochemical kinetics of visible-light driven water splitting at Rh:$SrTiO_3$ based electrodes

Keywords: Photoelectrochemistry, kinetics, water splitting

Abstract: The kinetics of water photo-dissociation assisted by visible light was the main topic of this work. The Rh doped $SrTiO_3$ semiconductor was employed as photo-excitable material. It can absorb visible light and therefore transform solar energy into useful chemical fuels. In this manuscript, a wide bibliographic overview is provided in the 1st Chapter, covering a description of the characterization methods and current models for photoelectrochemical kinetics. The 2nd Chapter is devoted to the description of the materials and methods. The 3rd Chapter deals with the full photoelectrochemical kinetic characterization of water splitting with Rh:$SrTiO_3$ photoelectrodes, surface-modified by addition of a model clathrochelate or with metallic Cu or Pt. In the 4th Chapter, a theoretical study of the mechanism of hydrogen evolution catalyzed by a model clathrochelate is provided. During the discussion, the EXAFS spectrum of the organometallic complex was thoroughly analyzed and modelled, and the relevant protonated intermediates involved in the mechanism were identified. The 5th Chapter deals with the photoelectrochemical dynamics of illuminated Rh:$SrTiO_3$-based photo-electrodes, characterized by the light-modulated photovoltage technique. Unusual results were obtained and are reported in this thesis for the first time. This unexpected dynamic behavior has been modelled by a set of classical differential equations usually used to describe such photo-processes.